

EFFECT OF A BAFFLE ON PSEUDOSTEADY-STATE
NATURAL CONVECTION INSIDE
SPHERICAL CONTAINERS

Except where reference is made to the work of others, the work described in this thesis is my own or was done in collaboration with my advisory committee. This thesis does not include proprietary or classified information

Yuping Duan

Certificate of Approval:

Amnon J. Meir
Professor
Mathematics

Jay M. Khodadadi, Chair
Professor
Mechanical Engineering

Daniel W. Mackowski
Associate Professor
Mechanical Engineering

Joe F. Pittman
Interim Dean
Graduate School

EFFECT OF A BAFFLE ON PSEUDOSTEADY-STATE
NATURAL CONVECTION INSIDE
SPHERICAL CONTAINERS

Yuping Duan

A Thesis

Submitted to

the Graduate Faculty of

Auburn University

in Partial Fulfillment of the

Requirements for the

Degree of

Master of Science

Auburn, Alabama
August 4, 2007

EFFECT OF A BAFFLE ON PSEUDOSTEADY-STATE
NATURAL CONVECTION INSIDE
SPHERICAL CONTAINERS

Yuping Duan

Permission is granted to Auburn University to make copies of this thesis at its discretion, upon the request of individuals or institutions and at their expense. The author reserves all publication rights.

Signature of Author

Date of Graduation

VITA

Yuping Duan, son of Wen Duan and Shouxian Ding, was born on April 20, 1981, in Zhangjiayao Village, Shanxi Province, the P. R. China. He graduated from Kangjie High School in 2000 and then was admitted to Zhejiang University. He studied at Zhejiang University for four years and graduated with a Bachelor of Science degree in Mechanical and Energy Engineering in June, 2004. In January 2005, he enrolled at the University of Nebraska-Lincoln as a graduate student in Mechanical Engineering. After one year study there, he transferred to Auburn University to complete his MS in Mechanical Engineering.

THESIS ABSTRACT
EFFECT OF A BAFFLE ON PSEUDOSTEADY-STATE
NATURAL CONVECTION INSIDE
SPHERICAL CONTAINERS

Yuping Duan

Master of Science, August 4, 2007
(Bachelor of Science, Zhejiang University, 2004)

226 Typed Pages

Directed by Jay M. Khodadadi

Pseudosteady-state natural convection within spherical containers with and without thin baffles was studied computationally. Insulated or isothermal baffles were considered for passive management of the flow and thermal fields. For Rayleigh numbers of 10^4 , 10^5 , 10^6 and 10^7 , baffles with 3 lengths positioned at 5 different locations were investigated. Elaborate grid size and time step size independence tests were performed. The solution of the governing equations was obtained by use of a commercial computational fluid dynamics (CFD) package. For the case of no baffle, computational results were validated successfully to previous data available in the literature by comparing the heat transfer correlations, temperature distribution and streamline patterns.

Both thermally stable and unstable layers are present in this problem and for the higher Rayleigh numbers, the onset of instabilities was observed in this system.

Regardless of the thermal status of the thin baffle, placing it on the inner wall of the spherical container directly leads to modification of the velocity field. It can generally be stated that the resulting “confinement” or “compartmentalization” causes the fluid above the baffle to be characterized by stable constant-temperature layers that are slow moving and dominated by heat conduction. In contrast, the fluid below the baffle is subjected to strong natural convection currents. Regardless of the Ra number, the modifications of the flow and temperature fields for short baffles are limited to the vicinity of the baffle and a possible interaction with the eye of the primary clockwise rotating vortex. The modifications of the flow and thermal fields were more pronounced for the longest baffle for which two clockwise rotating vortices are clearly observed when the baffle is positioned at or in the vicinity of the mid-plane. The Nusselt numbers and maximum stream function of the primary vortex were generally lower than the reference cases with no baffle. The degree of degradation of the Nusselt number has a strong dependence on the position and length of the insulated baffle. In contrast to the general reduction of heat transfer trends exhibited by the insulated or isothermal baffles, placing a baffle near the top of the sphere for high Ra number cases can lead to heat transfer enhancement in comparison to the reference case with no baffle. The extra heat that is brought in the fluid through the surface of the sphere is linked to the disturbance of the thermal boundary layer by the thin baffle. Some differences are observed due to the thermal status of the baffle. Due to the extra heating afforded by a thin isothermal baffle, the velocity and temperature fields were more complicated than the case with a thin insulated

baffle. In addition to confinement, a strong counterclockwise rotating vortex was created due to the extra heating of the baffle for high Ra numbers and baffle positions on or below the mid-plane. The hot fluid in this vortex was observed to be transported toward the center of the sphere, thus disturbing the stable stratified layers. In contrast to insulated baffles, placing isothermal baffles near the bottom for high Ra number cases also gave rise to heat transfer enhancement due to disturbance of the stratified layers by the CCW rotating vortex that is energized by the heated baffle.

ACKNOWLEDGMENTS

The author would like to express his special gratitude to his major professor, Dr. Jay M. Khodadadi, for his academic guidance, encouragement and patience towards the completion of this thesis and all the help he provided during my study at Auburn University. Dr. Khodadadi has offered all the academic help that a major professor could possibly provide. Personally, Dr. Khodadadi has gone way beyond the coverage of a major professor. It is hard to fully express my gratitude in words.

The author would like to express his gratitude to his other committee members, Drs. Mackowski and Meir. They provided some helpful suggestions to the thesis. The author acknowledges the Department of Mechanical Engineering at Auburn University for supporting his graduate assistantship. Mr. Seyed Farid Hosseinizadeh provided valuable technical help early in this project. Many thanks also go to the Alabama Supercomputer Center for their technical support and CPU time.

Many friends in Auburn also gave me a lot of help.

Finally, I would like to sincerely thank my parents for their support and inspiration. My siblings, Yanping Duan, Yiping Duan, Liping Duan and Yaping Duan are greatly appreciated for their support and encouragement. I also wish to thank my sister-in-law Lifan Zhao and my girl friend Lijin Yao for their encouragement.

Style manual or journal used:

Guide to Preparation and Submission of Thesis and Dissertation 2007

Computer software used:

MS Word 2003, MS Excel 2003, TECPLOT 9.0

TABLE OF CONTENTS

LIST OF TABLES.....	xiv
LIST OF FIGURES.....	xvi
NOMENCLATURE.....	xxx
CHAPTER 1 INTRODUCTION.....	1
CHAPTER 2 LITERRATURE REVIEW OF NATURAL CONVECTION INSIDE SPHERICAL CONTAINER.....	7
CHAPTER 3 COMPUTATIONAL METHODOLOGY AND BENCHMARKING.....	21
3.1 Mathematical Formulation for the Pseudosteady-State Natural Convection inside A Spherical Container without Baffles.....	21
3.1.1 Modeling Assumptions.....	21
3.1.2 Governing Equations.....	22
3.1.3 Boundary and Initial Conditions.....	23
3.1.4 Dimensionless Form of Governing Equations.....	23
3.2 Computational Details.....	26

3.2.1	Mesh Generation	26
3.2.2	FLUENT Configuration.....	27
3.3	Results and Discussion.....	28
3.3.1	Definition of the Nusselt Numbers.....	28
3.3.2	Stream Function	31
3.3.3	Fluid Flow and Thermal Fields	32
3.3.4	Code Validation.....	36
3.3.5	Correlation of the Pseudosteady-state Nusselt Numbers.....	38
3.4	Closure.....	40
CHAPTER 4 EFFECT OF AN INSULATED BAFFLE ON PSEUDOSTEADY-STATE NATURAL CONVECTION INSIDE SPHERICAL CONTAINERS.....		62
4.1	Mathematical Formulation for Pseudosteady-State Natural Convection inside Spherical Containers with a Thin Insulated Baffle.....	63
4.1.1	Governing Equations and Boundary Initial Conditions.....	63
4.1.2	Computational Details.....	64
4.1.3	Code Validation	65
4.2	Grid and Time Step Size Independence Study	66
4.3	Results and Discussion	69
4.3.1	PSS Fluid Flow and Thermal Fields for $Ra=10^4$, 10^5 and 10^6	70
4.3.2	Time-Dependent Fluid Flow and Thermal Fields for $Ra=10^7$	74
4.4	Nusselt Number Definitions and Other Parameters.....	75

4.4.1	Definitions of the Nusselt Numbers.....	75
4.4.2	Time-Averaged Nusselt Number.....	76
4.4.3	Strength of Fluctuations of Nusselt Numbers.....	78
4.4.4	Stream Function	79
4.5	Variation of the Time-Average Nusselt Number and Stream Function	80
4.6	Closure	87
CHAPTER 5 EFFECT OF AN ISOTHERMAL BAFFLE ON PSEUDOSTEADY-STATE NATURAL CONVECTION INSIDE SPHERICAL CONTAINERS.....		125
5.1	Mathematical Formulation for Pseudosteady-State Natural Convection inside Spherical Container with A Thin Isothermal Baffle.....	125
5.1.1	Governing Equations and Boundary Initial Conditions.....	125
5.1.2	Computational Details.....	127
5.1.3	Code Validation	128
5.2	Grid and Time Step Size Independence Study	128
5.3	Result and Discussion	131
5.3.1	PSS Fluid Flow and Thermal Fields for $Ra=10^4$, 10^5 and 10^6	131
5.3.2	Time-Dependent Fluid Flow and Thermal Field for $Ra= 10^7$	136
5.4	Nusselt Number Definitions and Other Parameters.....	137
5.4.1	Definition of the Nusselt Numbers.....	137
5.4.2	Time-Averaged Nusselt Numbers for Time-Dependent Cases.....	143
5.4.3	Oscillation Strength of the Nusselt Number.....	144

5.4.4 Stream Function Field.....	144
5.5 Variation of Time-Average Nusselt Numbers and Stream Function.....	145
5.6 Closure	153
CHAPTER 6 CONCLUSIONS AND RECOMMENDATION.....	188
6.1 Conclusions.....	188
6.2 Recommendations for Future Work.....	191
REFERENCES.....	192

LIST OF TABLES

Table 3.1	Radial and polar angle positions of the eye of the recirculating vortex for the cases with no baffles.....	34
Table 3.2	RMS and relative RMS of Nusselt Number.....	36
Table 3.3	Comparison of the pseudosteady-state Nusselt numbers	37
Table 3.4	Dimensionless maximum stream function (ψ_{\max}^*) values	38
Table 4.1	Dependence of the time-averaged and RMS values of the Nusselt numbers on the number of cells for an insulated case with $Ra=10^7$, $Pr=0.7$, $L=0.25$, $\theta_b = 90^\circ$ and $\Delta\tau = 1.57 \times 10^{-4}$	68
Table 4.2	Dependence of the time-averaged and RMS values of the Nusselt numbers on the time step size for an insulated case with $Ra=10^7$, $Pr=0.7$, $L=0.25$, $\theta_b = 90^\circ$ and 13,868 cells.....	69
Table 4.3	Nusselt numbers (Nu_c) and relative RMS ($RMS _{rNu_c}$) for all 60 cases with thin insulated baffles.....	84
Table 4.4	Nusselt numbers (Nu_m) and relative RMS ($RMS _{rNu_m}$) for all 60 cases with thin insulated baffles.....	85

Table 4.5	Maximum stream function (ψ_{\max}) of the primary vortex and relative RMS ($RMS _{r\psi_{\max}}$) for all 60 cases with thin insulated baffles.....	86
Table 5.1	Dependence of the time-averaged and RMS values of the Nusselt numbers on the number of cells for an isothermal case with $Ra=10^7$, $Pr=0.7$, $L=0.25$, $\theta_b = 90^\circ$ and $\Delta\tau = 1.57 \times 10^{-4}$	130
Table 5.2	Dependence of the time-averaged Nusselt numbers on the time step size for an isothermal case with $Ra=10^7$, $Pr=0.7$, $L=0.25$, $\theta_b = 90^\circ$ and 13,868 cells.....	131
Table 5.3	Nusselt numbers (Nu_c) and relative RMS (r-RMS) for all 60 cases with thin isothermal baffles.....	150
Table 5.4	Nusselt numbers (Nu_m) and relative RMS (r-RMS) for all 60 cases with thin isothermal baffles.....	151
Table 5.5	Maximum stream function (ψ_{\max}) of the primary vortex and relative RMS ($RMS _{r\psi_{\max}}$) for all 60 cases with thin isothermal baffles.....	152

LIST OF FIGURES

Figure 1.1	Typical external natural convection flow next to a hot vertical plate at temperature T_{wall} , with the motionless fluid faraway at temperature T_{∞}	4
Figure 1.2	Internal natural convection in a differentially-heated heated cavity.....	5
Figure 1.3	Schematic relations between heat addition/extraction and bulk temperature trends in a container.....	6
Figure 2.1	Natural convection flow pattern in a sphere for $Ra=2 \times 10^3$ (Pustovolt, 1958).....	12
Figure 2.2	Natural convection streamlines in a sphere at dimensionless time $\tau=0.03$ (Left) and 0.10 (Right) (Whitley and Vachon, 1972).....	13
Figure 2.3	Natural convection flow pattern in a sphere for $Ra=2.8 \times 10^6$ (Chow and Akins, 1975).....	14
Figure 2.4	Dependence of location of the eye of the recirculation pattern on Rayleigh number (Chow and Akins, 1975).....	15
Figure 2.5	Location of eye of recirculation (a) and mean Nusselt number variation (b) for natural convection in sphere (Hutchins and Marschall, 1989).....	16

Figure 2.6	Streamline patterns and temperature contours in spherical for different Rayleigh number (Hutchins and Marschall, 1989).....	17
Figure 2.7	Streamline patterns and temperature contours in spherical for different Rayleigh number (Shen et al., 1995).....	18
Figure 2.8	Dependence of the recirculation vortex center position on Rayleigh number (Shen et al., 1995).....	19
Figure 2.9	Streamlines and temperature field contours for composite systems (Zhang et al., 1999).....	20
Figure 3.1	Schematic diagram of the problem.....	41
Figure 3.2	Hybrid mesh created in GAMBIT.....	42
Figure 3.3	Boundary layer mesh system.....	43
Figure 3.4	Detailed view of the boundary layer mesh.....	44
Figure 3.5	Magnified view of part of the adopted hybrid mesh.....	45
Figure 3.6	Solution controls in FLUENT.....	46
Figure 3.7	Solver settings in FLUENT.....	47
Figure 3.8	Operating conditions in FLUENT.....	48
Figure 3.9	Fluid properties in FLUENT.....	49
Figure 3.10	Thermal boundary conditions in FLUENT supplied by a user-defined function (UDF).....	50
Figure 3.11	Momentum boundary conditions in FLUENT.....	51
Figure 3.12	Residual monitors in FLUENT.....	52

Figure 3.13	Pseudosteady-state streamline patterns (left half) and corresponding temperature contours (right half) for cases with no baffles ($Ra = 10^4, 10^5, 10^6$ and 10^7).....	53
Figure 3.14	Thermally stable and unstable structures.....	54
Figure 3.15	Nusselt number as a function of dimensionless time for $Ra=10^4$ with no baffle.....	55
Figure 3.16	Nusselt number as a function of dimensionless time for $Ra=10^5$ with no baffle.....	56
Figure 3.17	Nusselt number as a function of dimensionless time for $Ra=10^6$ with no baffle.....	57
Figure 3.18	Nusselt number as a function of dimensionless time for $Ra=10^7$ with no baffle.....	58
Figure 3.19	Nusselt numbers relative differences between two different approaches.....	59
Figure 3.20	Nusselt number (Nu_c) correlations.....	60
Figure 3.21	Nusselt number (Nu_m) correlations.....	61
Figure 4.1	Schematic diagram of a spherical container with a thin insulated baffle.....	88
Figure 4.2	3-D View of the system	89
Figure 4.3	Grid systems with the same baffle ($L=0.25$) located at (a) $\theta_b = 30^\circ$, (b) $\theta_b = 60^\circ$, (c) $\theta_b = 90^\circ$ and (d) $\theta_b = 120^\circ$	90

Figure 4.4	The Nusselt number Nu_m (based on $\Delta T = T_w - T_m$) as a function of grid size.....	91
Figure 4.5	The Nusselt number Nu_c (based on $\Delta T = T_w - T_c$) as a function of grid size.....	92
Figure 4.6	Nusselt number ($\Delta T = T_w - T_m$) as a function of time step size.....	93
Figure 4.7	Nusselt number ($\Delta T = T_w - T_c$) as a function of time step size.....	94
Figure 4.8	Pseudosteady-state streamline patterns and temperature contours for three insulated baffles ($L = 0.05, 0.10$ and 0.25) placed at various locations ($\theta_b = 30^\circ, 60^\circ, 90^\circ, 120^\circ$ and 150°) for $Ra = 10^4$	95
Figure 4.9	Pseudosteady-state streamline patterns and temperature contours for three insulated baffles ($L = 0.05, 0.10$ and 0.25) placed at various locations ($\theta_b = 30^\circ, 60^\circ, 90^\circ, 120^\circ$ and 150°) for $Ra = 10^5$	96
Figure 4.10	Pseudosteady-state streamline patterns and temperature contours for three insulated baffles ($L = 0.05, 0.10$ and 0.25) placed at various locations ($\theta_b = 30^\circ, 60^\circ, 90^\circ, 120^\circ$ and 150°) for $Ra = 10^6$	97
Figure 4.11	Pseudosteady-state streamline patterns and temperature contours with an insulated baffle ($L = 0.25$) placed at various locations ($\theta_b = 30^\circ, 90^\circ$ and 150°) for $Ra = 10^4, 10^5, 10^6$ and 10^7	98
Figure 4.12	Streamline patterns and temperature contours in one cycle (a→h) for case with a thin insulated baffle ($L=0.25, \theta_b = 60^\circ$) for $Ra=10^7$	99

Figure 4.13	Cyclic variation of the instantaneous area-averaged Nusselt number for case with a thin insulated baffle ($L=0.25, \theta_b=60^\circ$) for $Ra=10^7$ (Corresponding to Figure 4.12).....	100
Figure 4.14	Nusselt numbers $Nu_c(\tau)$ oscillation with dimensionless time for case (a) with thin insulated baffle ($L=0.10, \theta_b = 60^\circ$) and case (b) with thin insulated baffle ($L=0.05, \theta_b = 150^\circ$).....	101
Figure 4.15	Strength of Nusselt number (Nu_c) oscillation with dimensionless time for case with thin insulated baffle ($L=0.25, \theta_b = 120^\circ$).....	102
Figure 4.16	Strength (RMS) of Nusselt number (Nu_c) oscillation with dimensionless time for case with thin insulated baffle ($L=0.25, \theta_b = 30^\circ$).....	103
Figure 4.17	Dependence of the time-averaged Nusselt number (Nu_c) on Ra among cases with a fixed thin insulated baffle ($L=0.05$) at various locations ($\theta_b = 30^\circ, 60^\circ, 90^\circ, 120^\circ$ and 150°) and the case without baffle	104
Figure 4.18	Dependence of the time-averaged Nusselt number (Nu_c) on Ra among cases with a fixed thin insulated baffle ($L=0.10$) at various locations ($\theta_b = 30^\circ, 60^\circ, 90^\circ, 120^\circ$ and 150°) and the case without baffle	105

Figure 4.19	Dependence of the time-averaged Nusselt number (Nu_c) on Ra among cases with a fixed thin insulated baffle ($L=0.25$) at various locations ($\theta_b = 30^\circ, 60^\circ, 90^\circ, 120^\circ$ and 150°) and the case without baffle	106
Figure 4.20	Dependence of the time-averaged Nusselt number (Nu_m) on Ra among cases with a fixed thin insulated baffle ($L=0.05$) at various locations ($\theta_b = 30^\circ, 60^\circ, 90^\circ, 120^\circ$ and 150°) and the case without baffle	107
Figure 4.21	Dependence of the time-averaged Nusselt number (Nu_m) on Ra among cases with a fixed thin insulated baffle ($L=0.10$) at various locations ($\theta_b = 30^\circ, 60^\circ, 90^\circ, 120^\circ$ and 150°) and the case without baffle	108
Figure 4.22	Dependence of the time-averaged Nusselt number (Nu_m) on Ra among cases with a fixed thin insulated baffle ($L=0.25$) at various locations ($\theta_b = 30^\circ, 60^\circ, 90^\circ, 120^\circ$ and 150°) and the case without baffle	109
Figure 4.23	Dependence of the Maximum stream function ψ_{max} on Ra among cases with a fixed thin insulated baffle ($L=0.05$) at various locations ($\theta_b = 30^\circ, 60^\circ, 90^\circ, 120^\circ$ and 150°) and the case without baffle	110

Figure 4.24	Dependence of the Maximum stream function ψ_{\max} on Ra among cases with a fixed thin insulated baffle (L=0.10) at various locations ($\theta_b = 30^\circ, 60^\circ, 90^\circ, 120^\circ$ and 150°) and the case without baffle	111
Figure 4.25	Dependence of the Maximum stream function ψ_{\max} on Ra among cases with a fixed thin insulated baffle (L=0.25) at various locations ($\theta_b = 30^\circ, 60^\circ, 90^\circ, 120^\circ$ and 150°) and the case without baffle	112
Figure 4.26	Dependence of the Nusselt number (Nu_c) on θ_b among case without baffle and the cases with a thin insulated baffle of different lengths (L=0.05, 0.10 and 0.25) for Ra=10 ⁴	113
Figure 4.27	Dependence of the Nusselt number (Nu_m) on θ_b among case without baffle and the cases with a thin insulated baffle of different lengths (L=0.05, 0.10 and 0.25) for Ra=10 ⁴	114
Figure 4.28	Dependence of the Maximum stream function ψ_{\max} on θ_b among case without baffle and the cases with a thin insulated baffle of different lengths (L=0.05, 0.10 and 0.25) for Ra=10 ⁴	115
Figure 4.29	Dependence of the Nusselt number (Nu_c) on θ_b among case without baffle and the cases with a thin insulated baffle of different lengths (L=0.05, 0.10 and 0.25) for Ra=10 ⁵	116

Figure 4.30	Dependence of the Nusselt number (Nu_m) on θ_b among case without baffle and the cases with a thin insulated baffle of different lengths ($L=0.05, 0.10$ and 0.25) for $Ra=10^5$	117
Figure 4.31	Dependence of the Maximum stream function ψ_{max} on θ_b among case without baffle and the cases with a thin insulated baffle of different lengths ($L=0.05, 0.10$ and 0.25) for $Ra=10^5$	118
Figure 4.32	Dependence of the Nusselt number (Nu_c) on θ_b among case without baffle and the cases with a thin insulated baffle of different lengths ($L=0.05, 0.10$ and 0.25) for $Ra=10^6$	119
Figure 4.33	Dependence of the Nusselt number (Nu_m) on θ_b among case without baffle and the cases with a thin insulated baffle of different lengths ($L=0.05, 0.10$ and 0.25) for $Ra=10^6$	120
Figure 4.34	Dependence of the Maximum stream function ψ_{max} on θ_b among case without baffle and the cases with a thin insulated baffle of different lengths ($L=0.05, 0.10$ and 0.25) for $Ra=10^6$	121
Figure 4.35	Dependence of the Nusselt number (Nu_c) on θ_b among case without baffle and the cases with a thin insulated baffle of different lengths ($L=0.05, 0.10$ and 0.25) for $Ra=10^7$	122
Figure 4.36	Dependence of the Nusselt number (Nu_m) on θ_b among case without baffle and the cases with a thin insulated baffle of different lengths ($L=0.05, 0.10$ and 0.25) for $Ra=10^7$	123

Figure 4.37	Dependence of the Maximum stream function ψ_{\max} on θ_b among case without baffle and the cases with a thin insulated baffle of different lengths ($L=0.05, 0.10$ and 0.25) for $Ra=10^7$	124
Figure 5.1	Schematic diagram of a spherical container with a thin isothermal baffle.....	154
Figure 5.2	The Nusselt number Nu_m (based on $\Delta T = T_w - T_m$) as a function of grid size.....	155
Figure 5.3	The Nusselt number Nu_c (based on $\Delta T = T_w - T_c$) as a function of grid size.....	156
Figure 5.4	The Nusselt number Nu_m (based on $\Delta T = T_w - T_m$) as a function of time step size.....	157
Figure 5.5	The Nusselt number Nu_c (based on $\Delta T = T_w - T_c$) as a function of time step size.....	158
Figure 5.6	Pseudosteady-state streamline patterns and temperature contours for three isothermal baffles ($L = 0.05, 0.10$ and 0.25) placed at various locations ($\theta_b = 30^\circ, 60^\circ, 90^\circ, 120^\circ$ and 150°) for $Ra = 10^4$	159
Figure 5.7	Pseudosteady-state streamline patterns and temperature contours for three isothermal baffles ($L = 0.05, 0.10$ and 0.25) placed at various locations ($\theta_b = 30^\circ, 60^\circ, 90^\circ, 120^\circ$ and 150°) for $Ra = 10^5$	160
Figure 5.8	Pseudosteady-state streamline patterns and temperature contours for three isothermal baffles ($L = 0.05, 0.10$ and 0.25) placed at various locations ($\theta_b = 30^\circ, 60^\circ, 90^\circ, 120^\circ$ and 150°) for $Ra = 10^6$	161

Figure 5.9	Pseudosteady-state streamline patterns and temperature contours with an isothermal baffle ($L = 0.25$) placed at various locations ($\theta_b = 30^\circ, 90^\circ$ and 150°) for $Ra = 10^4, 10^5, 10^6$ and 10^7	162
Figure 5.10	Streamline patterns and temperature contours in one cycle (a \rightarrow i) for case with a thin isothermal baffle ($L=0.25, \theta_b = 60^\circ$) for $Ra=10^7$	163
Figure 5.11	Cyclic variation of the instantaneous area-averaged Nusselt number for case with a thin isothermal baffle ($L=0.25, \theta_b = 60^\circ$) for $Ra=10^7$ (Corresponding to Figure 5.10).....	164
Figure 5.12	Detailed drawing of an isothermal baffle surface	165
Figure 5.13	Nusselt number (Nu_c) oscillation with dimensionless time for a case (a) with a thin isothermal baffle ($L=0.25, \theta_b = 60^\circ, Ra=10^7$) and case (b) with a thin isothermal baffle ($L=0.05, \theta_b = 150^\circ, Ra=10^7$).....	166
Figure 5.14	Dependence of the time-average Nusselt number (Nu_c) on Ra among cases with a fixed thin isothermal baffle ($L=0.05$) at various locations ($\theta_b = 30^\circ, 60^\circ, 90^\circ, 120^\circ$ and 150°) and the case without baffle	167

Figure 5.15	Dependence of the time-average Nusselt number (Nu_c) on Ra among cases with a fixed thin isothermal baffle ($L=0.10$) at various locations ($\theta_b = 30^\circ, 60^\circ, 90^\circ, 120^\circ$ and 150°) and the case without baffle	168
Figure 5.16	Dependence of the time-average Nusselt number (Nu_c) on Ra among cases with a fixed thin isothermal baffle ($L=0.25$) at various locations ($\theta_b = 30^\circ, 60^\circ, 90^\circ, 120^\circ$ and 150°) and the case without baffle	169
Figure 5.17	Dependence of the time-average Nusselt number (Nu_m) on Ra among cases with a fixed thin isothermal baffle ($L=0.05$) at various locations ($\theta_b = 30^\circ, 60^\circ, 90^\circ, 120^\circ$ and 150°) and the case without baffle.....	170
Figure 5.18	Dependence of the time-average Nusselt number (Nu_m) on Ra among cases with a fixed thin isothermal baffle ($L=0.10$) at various locations ($\theta_b = 30^\circ, 60^\circ, 90^\circ, 120^\circ$ and 150°) and the case without baffle.....	171
Figure 5.19	Dependence of the time-average Nusselt number (Nu_m) on Ra among cases with a fixed thin isothermal baffle ($L=0.25$) at various locations ($\theta_b = 30^\circ, 60^\circ, 90^\circ, 120^\circ$ and 150°) and the case without baffle.....	172

Figure 5.20	Dependence of the Maximum stream function ψ_{\max} on Ra among cases with a fixed thin isothermal baffle (L=0.05) at various locations ($\theta_b = 30^\circ, 60^\circ, 90^\circ, 120^\circ$ and 150°) and the case without baffle.....173
Figure 5.21	Dependence of the Maximum stream function ψ_{\max} on Ra among cases with a fixed thin isothermal baffle (L=0.10) at various locations ($\theta_b = 30^\circ, 60^\circ, 90^\circ, 120^\circ$ and 150°) and the case without baffle.....174
Figure 5.22	Dependence of the Maximum stream function ψ_{\max} on Ra among cases with a fixed thin isothermal baffle (L=0.25) at various locations ($\theta_b = 30^\circ, 60^\circ, 90^\circ, 120^\circ$ and 150°) and the case without baffle.....175
Figure 5.23	Dependence of the Nusselt number (Nu_c) on θ_b among case without baffle and cases with a thin isothermal baffle of different lengths (L=0.05, 0.10 and 0.25) for $Ra=10^4$176
Figure 5.24	Dependence of the Nusselt number (Nu_m) on θ_b among case without baffle and cases with a thin isothermal baffle of different lengths (L=0.05, 0.10 and 0.25) for $Ra=10^4$177
Figure 5.25	Dependence of the Maximum stream function (ψ_{\max}) on θ_b among case without baffle and cases with a thin isothermal baffle of different lengths (L=0.05, 0.10 and 0.25) for $Ra=10^4$178

Figure 5.26	Dependence of the Nusselt number (Nu_c) on θ_b among case without baffle and cases with a thin isothermal baffle of different lengths ($L=0.05, 0.10$ and 0.25) for $Ra=10^5$	179
Figure 5.27	Dependence of the Nusselt number (Nu_m) on θ_b among case without baffle and cases with a thin isothermal baffle of different lengths ($L=0.05, 0.10$ and 0.25) for $Ra=10^5$	180
Figure 5.28	Dependence of the Maximum stream function (ψ_{max}) on θ_b among case without baffle and cases with a thin isothermal baffle of different lengths ($L=0.05, 0.10$ and 0.25) for $Ra=10^5$	181
Figure 5.29	Dependence of the Nusselt number (Nu_c) on θ_b among case without baffle and cases with a thin isothermal baffle of different lengths ($L=0.05, 0.10$ and 0.25) for $Ra=10^6$	182
Figure 5.30	Dependence of the Nusselt number (Nu_m) on θ_b among case without baffle and cases with a thin isothermal baffle of different lengths ($L=0.05, 0.10$ and 0.25) for $Ra=10^5$	183
Figure 5.31	Dependence of the Maximum stream function (ψ_{max}) on θ_b among case without baffle and cases with a thin isothermal baffle of different lengths ($L=0.05, 0.10$ and 0.25) for $Ra=10^6$	184
Figure 5.32	Dependence of the Nusselt number (Nu_c) on θ_b among case without baffle and cases with a thin isothermal baffle of different lengths ($L=0.05, 0.10$ and 0.25) for $Ra=10^7$	185

Figure 5.33	Dependence of the Nusselt number (Nu_m) on θ_b among case without baffle and cases with a thin isothermal baffle of different lengths ($L=0.05, 0.10$ and 0.25) for $Ra=10^7$	186
Figure 5.34	Dependence of the Maximum stream function (ψ_{max}) on θ_b among case without baffle and cases with a thin isothermal baffle of different lengths ($L=0.05, 0.10$ and 0.25) for $Ra=10^7$	187

NOMENCLATURE

English Symbols

a	constant in approximated linear equation
b	slope of approximated linear equation
c	constant value in correlation
c_p	specific heat at constant pressure, J/(kgK)
C	constant temperature difference between wall and container center, °C
D	diameter of the sphere, m
g	gravitational acceleration, m/s ²
g_r	radial component of the gravitational acceleration, m/s ²
g_r^*	dimensionless radial component of the gravitational acceleration
g_θ	polar component of the gravitational acceleration, m/s ²
g_θ^*	dimensionless polar component of the gravitational acceleration
Gr	Grashof number, $g\beta\rho^2D^3(T_w - T_c)/\mu^2$
h	heat transfer coefficient, W/m ² K
k	thermal conductivity, W/mK
l	length of baffle, m
L	dimensionless length of baffle, l/D
Nu_c	time-averaged Nusselt number, $qD/k(T_w - T_c)$

$Nu_c(\tau)$	area-averaged Nusselt number
Nu_m	time-averaged Nusselt number, $qD/k(T_w - T_m)$
$Nu_m(\tau)$	area-averaged Nusselt number
p	pressure, Pa
p_0	initial static pressure, Pa
p^*	dimensionless pressure, $(p-p_0)R^2/\rho\alpha^2$
Pr	Prandtl number of the fluid, ν/α
q	heat flux, W/m^2
r	radial coordinate within the sphere, m
r^*	dimensionless radial position, defined as r/R
r_e	radial position of vortex eye, m
r_e^*	dimensionless radial position of vortex eye, r_e/R
R	radius of the sphere, m
Ra	Rayleigh number, $Gr Pr$
t	time, s
T	temperature, K
T_c	temperature at the center of sphere, K
T_m	mean or bulk temperature of the fluid, K
T_w	temperature of the spherical container inner surface, K
T_0	initial temperature of the fluid, K
T^*	dimensionless temperature, defined as $(T - T_0) / (T_w - T_c)$
V_r	radial component of the fluid velocity, m/s
V_θ	polar component of the fluid velocity, m/s

V_r^* dimensionless radial component of the fluid velocity, $V_r R/\alpha$

V_θ^* dimensionless polar component of the fluid velocity, $V_\theta R/\alpha$

Greek Symbols

α thermal diffusivity of the fluid, m^2/s

β coefficient of thermal expansion, K^{-1}

θ polar angle in the sphere, degrees

θ_b polar angle location of the baffle, degrees

θ_e polar angle of the vortex eye, degrees

μ fluid viscosity, $kg/(ms)$

ν kinematic viscosity, m^2/s

ξ generic variable

σ cross-correlation coefficient

ρ density of the fluid, kg/m^3

τ dimensionless time, $\alpha t/R^2$

Ψ stream function, m^3/s

Ψ^* dimensionless stream function, $\Psi/\alpha R$

Ψ_{\max} maximum stream function, m^3/s

Ψ_{\max}^* dimensionless maximum stream function, $\Psi_{\max}/\alpha R$

Subscripts

b related to baffle

- e related to vortex eye
- r related to the radial direction
- θ related to the polar direction

Superscripts

- * dimensionless value

CHAPTER 1 INTRODUCTION

Buoyancy-driven or natural convection is a very important thermal transport mechanism that has been studied for many decades. In natural convection flows, the buoyancy effect due to the strong dependence of the fluid density on temperature plays the key role. Natural convection problems can generally be categorized in two broad classes, namely: (1) external and (2) internal. In the external group of problems, an infinite amount of fluid is of interest such as the one shown in Figure 1.1. In this figure, an infinite body of fluid is shown next to a vertical wall. The temperature of the wall (T_{wall}) and the temperature of quiescent fluid far away ($T_{\infty} < T_{\text{wall}}$) are the two distinct temperature scales that are generally taken to be constants. Development of thin momentum and thermal boundary layers next to the wall plays the key role in this problem. Accordingly, a variety of analytical/computational and experimental tools have been utilized for solving this and problems related to it.

In contrast, for internal natural convection problems, a finite amount of fluid is under consideration. The idealized problem of a differentially-heated cavity (Figure 1.2) is the simplest example of an internal natural convection problem in which a fluid is placed between two vertical walls with constant temperatures T_{cold} and T_{hot} , whereas the two horizontal walls are insulated. One can generally state that external flows are characterized by simpler phenomenon related to uni-directional boundary layer flow, whereas internal flows may exhibit further complications such as multiple recirculating

vortices. In spite of these complications, it is possible to formulate a steady formulation for both problems mentioned so far.

In practice, internal natural convection problems involve geometries which are more complicated than the idealized differentially-heated cavity problem. For instance, cylindrical or spherical containers that hold fluids are commonly utilized in industrial applications. Besides the more complicated geometry, these problems are such that one can not generally specify a steady formulation for them. For instance, consider a fluid that is held in an arbitrary-shaped container such that it has reached a motionless state and has a constant temperature. If the container is suddenly exposed to a new environment such that the temperature of the surface is lowered or increased, a transient process will ensue. This behavior is due to presence of just one temperature scale in the problem (i.e. T_{wall}). The temperature difference between that of the wall and the initial fluid temperature will give rise to buoyancy-driven convection. As shown in Figure 1.3, any heat that is added or extracted from the fluid will cause the bulk fluid temperature to rise or decline, respectively. In effect, one will be faced to solve an unsteady multi-dimensional formulation to recover the complex phenomena in this class of problems.

Given this background, a computational study of pseudosteady-state natural convection within spherical containers without and with baffles was performed. Spherical containers are widely used in different industries to store, transport and process fluids. The pseudosteady-state condition is distinct from a transient problem. In a transient problem, a motionless fluid will be perturbed early on and will finally settle down to a motionless state with a higher or lower temperature. In a pseudosteady-state

formulation, the flow and thermal fields will indefinitely evolve with time. However, bulk quantities such as the Nusselt number will be independent of time.

Following a review of literature in Chapter 2, the mathematical formulation and benchmarking are presented in Chapter 3. Pseudosteady-state natural convection due to presence of insulated and isothermal thin baffles placed on the inner wall of a sphere are discussed in great detail in Chapters 4 and 5, respectively. General conclusions are finally given in Chapter 6.

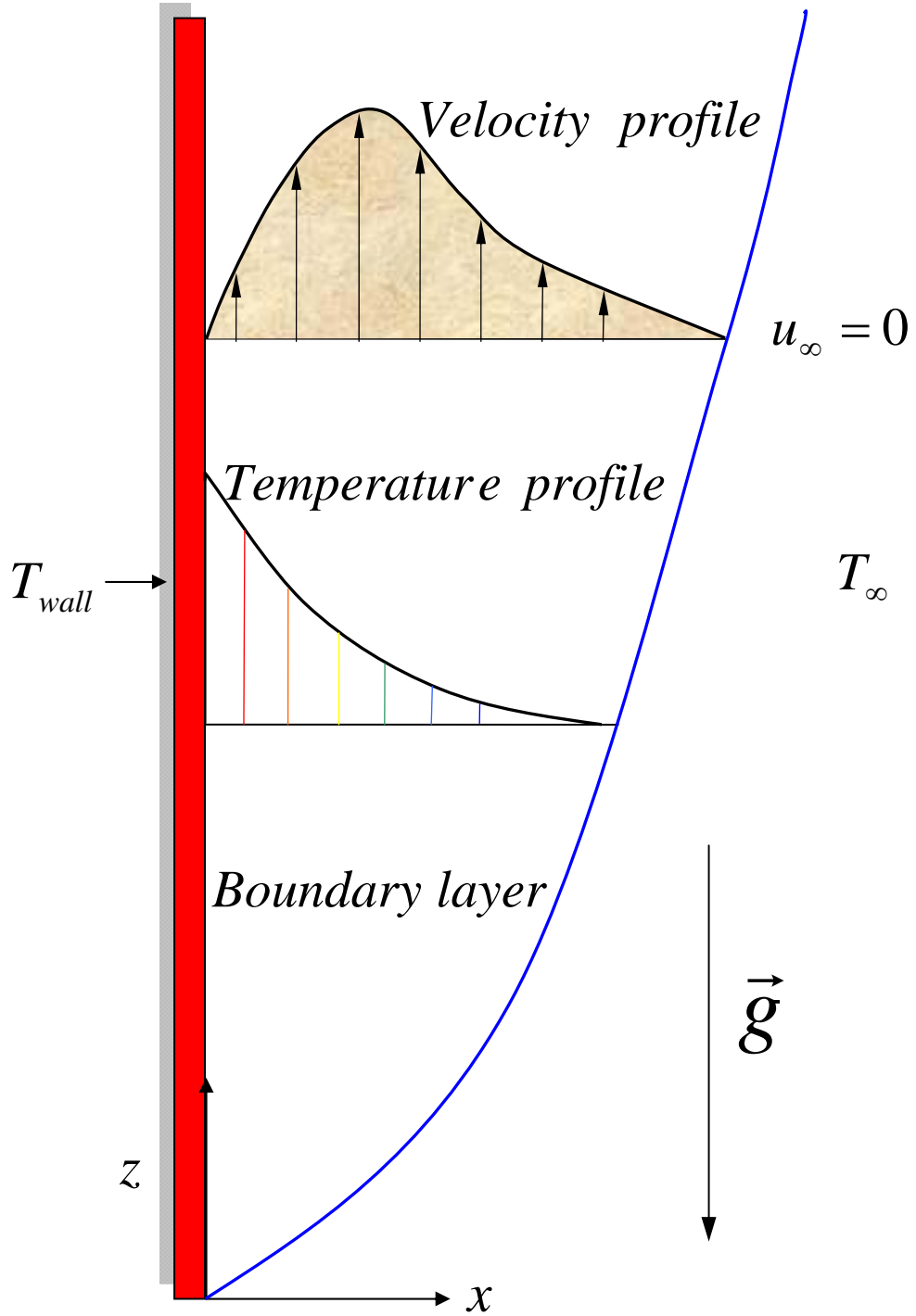


Figure 1.1 Typical external natural convection flow next to a hot vertical plate at temperature T_{wall} , with the motionless fluid far away at temperature T_{∞} .

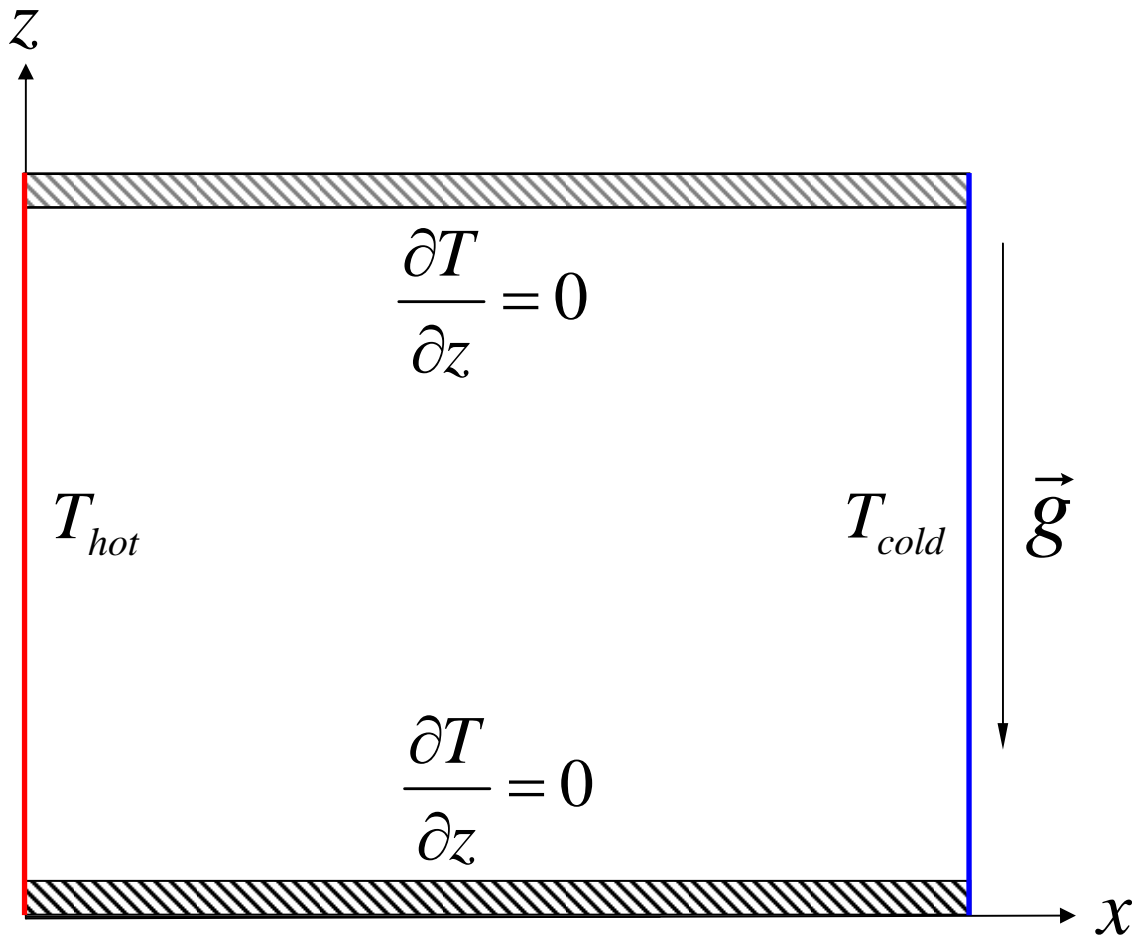


Figure 1.2 Internal natural convection in a differentially-heated cavity

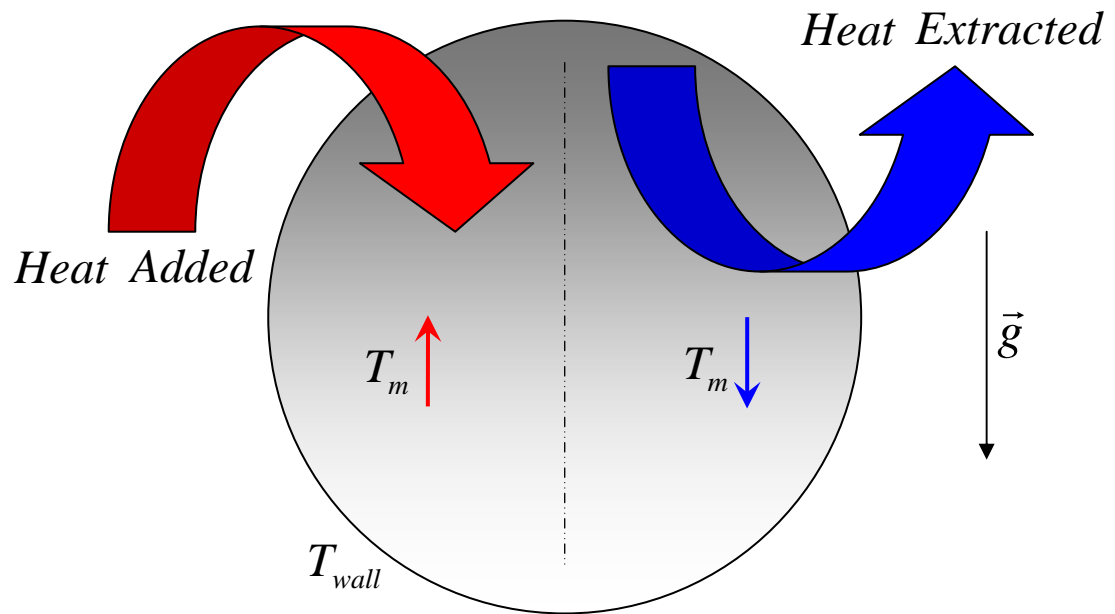


Figure 1.3 Schematic relations between heat addition/extraction and bulk temperature trends in a container

CHAPTER 2 LITERRATURE REVIEW OF NATURAL CONVECTION INSIDE SPHERICAL CONTAINERS

Containment of fluids within spherical vessels is very common in industrial applications in relation to storage and transport of cryogenic liquids and propellants. Research on natural convection within spherical containers at both applied and fundamental levels has been reported for some time. A review of the relevant literature is given in this Chapter.

Schmidt (1956) can be credited as the first researcher to have reported on unsteady heat transfer inside spherical containers subject to a step change in wall temperature. Measurements were carried out for five different diameters ranging from 100 to 500 mm. By utilizing water and three alcohols (methyl, ethyl and butyl) with different properties, a wide range of Rayleigh numbers ($2 \times 10^9 - 5 \times 10^{11}$) was covered.

Pustovoit (1958) reported results of an approximate method to solve the coupled equations governing slowly-varying axisymmetric natural convection inside a spherical container by expanding the dependent variables (velocity, pressure and temperature) in terms of the Grashof number. Streamlines and temperature contours were given for water ($Pr = 6.75$) and $Gr = 300$ for the case of a step change in the wall temperature (Figure 2.1). With the initial liquid temperature being higher than the constant surface temperature, the theoretical results suggested that the liquid that was being cooled sank near the surface replacing the hot liquid that rose vertically in the middle of the sphere.

The upper part of the sphere was at a higher temperature compared to the lower section. It was observed that the liquid was cooled least in a region located at about one third of the radius above the center, where molecular conduction was dominant.

Whitley and Vachon (1972) presented their numerical solutions of transient, laminar natural convection heat transfer inside spheres (Figure 2.2). The flow field was assumed to be axisymmetric, thus the dependent variables were functions of time and two spatial variables (two-dimensional flow). A finite-difference-based vorticity-stream function numerical procedure employing an implicit formulation of the temporal derivatives was employed. Subjecting the wall temperature to a sudden step change, the quiescent air in the sphere was set in motion and after a long period of time attained a new equilibrium state with zero motion. In this configuration, air being heated next the surface rose upward, replacing the cooler air which sank vertically to the bottom of the sphere.

Chow and Akins (1975) presented their experimental investigation of the pseudosteady-state natural convection inside spheres (Figure 2.3). The main feature of the *pseudosteady-state* treatment is that the driving force for convection is continuously maintained, i.e. the temperature outside the sphere was increased so that the temperature difference between the outside and the center of the sphere remained constant. During the flow visualization phase of the study, the motion of hollow glass spheres was monitored and the location of the eye of the recirculation pattern was quantified (Figure 2.4). Comparisons with the analytical results of Pustovoit (1958) and computational data of Whitley and Vachon (1972) were attempted. However, previous mathematical analyses treated a transient phenomenon, whereas Chow and Akins (1975) strived to

maintain pseudosteady-state conditions. In view of this, direct comparisons should be considered unwarranted. They also provided an empirical correlation for the mean Nusselt number in the laminar regime (Rayleigh number below 10^7).

Val'tsiferov and Polezhaev (1975) refer to a number of articles directed at theoretical and experimental studies of natural convection in spherical vessels filled with a liquid. Among them, only the work of Pustovoit (1958) and Whitley and Vachon (1972) are widely available. They also refer to experimental data for given surface heat flux values with relatively high Rayleigh (10^9 – 10^{11}) and Prandtl numbers (3–1500), for which the characteristics of convection were found to be contradictory. They continued to present a computational study of natural convection in a sphere with a thin-walled shell for a range of the Rayleigh and Fourier numbers that covered the principal conditions of time-dependent laminar convection due to given heat flux on the surface of the sphere.

Transient natural convection within a thin-walled copper sphere filled with three liquids was investigated by Owen and Jalil (1986) both experimentally and computationally. For the experimental study, the sphere was suddenly immersed in a bath of boiling water and allowed to reach equilibrium. Temperature readings along the diameter of the sphere at various inclination angles were obtained. The key observation was that the temperature measurements at the bottom of the sphere exhibited oscillating behavior indicative of the interaction of sinking cold liquid with the rising hot liquid.

Detailed computational results for pseudosteady-state, two-dimensional, natural convection inside spheres were reported by Hutchins and Marschall (1989). Similar to Whitley and Vachon (1972), they utilized a finite-difference-based vorticity-stream function numerical procedure to simulate the flow and temperature fields in the laminar

regime ($10^5 < Ra < 10^8$) and two different Prandtl numbers of 0.7 and 8. In order to compare to the experimental results of Chow and Akins (1975), a case of $Pr = 4$ and $Ra = 5.2 \times 10^7$ was also simulated. The general trends of their computed eye of the recirculation zone and mean Nusselt number variation were similar to the findings of Chow and Akins (1975) (Figure 2.5). The heat transfer data were found to be independent of the Prandtl number. Both streamline and temperature contours were presented, showing their dependence on the Rayleigh number (Figure 2.6). Finally, they proposed a mean Nusselt number correlation applicable for the Rayleigh number range of 10^5 to 10^8 .

Research at Auburn University concentrated on repeating the work of Hutchins and Marschall (1989) with the objective of benchmarking a CFD code in the spherical coordinate system (Shen et al., 1995). Their findings were generally in concert with the predictions of Hutchins and Marschall (1989) and experimental observations of Chow and Akins (1975) (Figures 2.7 and 2.8).

Transient natural convection in a spherical composite system that was partially filled with a porous medium was studied by Nguyen, Paik and Pop (1997). Using a hybrid spectral method, they numerically simulated the unsteady flow and thermal fields. They concluded that heat transfer results were not sensitive to the variation of the Prandtl number for the range considered (0.5 to 10). It was established that the overall heat transfer rate was primarily controlled by the transport characteristics in the porous medium and the thermal conductivity ratio.

Zhang et al. (1999) extended the work of Nguyen et al. (1997) by studying the pseudosteady-state behavior of composite systems (Figure 2.9). A parametric study was

performed for a range of values of the Rayleigh number (Ra), Darcy number (Da) and the thermal conductivity ratio. The local Nusselt number on the surface and interface temperature exhibited nearly uniform variations for low Ra and Da numbers, signifying little deviation from the limiting pure conduction case. For high Ra and Da numbers, significant heat transfer was observed on the bottom of the sphere. The interface temperature was also seen to deviate from uniform variation for high Ra and Da numbers. The intensity of the recirculating flow in the central fluid core region was observed to depend on the thermal conductivity ratio. The thermal conductivity ratio modified the time scale of the thermal transport and only the relative magnitudes of the monitored quantities were affected. A recent study by Khodadadi et al. (1999) focused on analysis of pseudosteady-state natural convection within rotating spheres. Their results for the limiting case of no rotation were obtained for Ra numbers different than a previous study by Shen et al. (1995).

In extending the breadth of previous work, the present study was initiated to explore the utilization of baffles within spherical containers in order to control the flow field and consequently heat transfer, through its enhancement and/or degradation. In analyzing the limiting cases for the thermal state of the baffle, the pseudosteady-state natural convection within spherical containers due to presence of both insulated and isothermal baffles are discussed in this thesis.

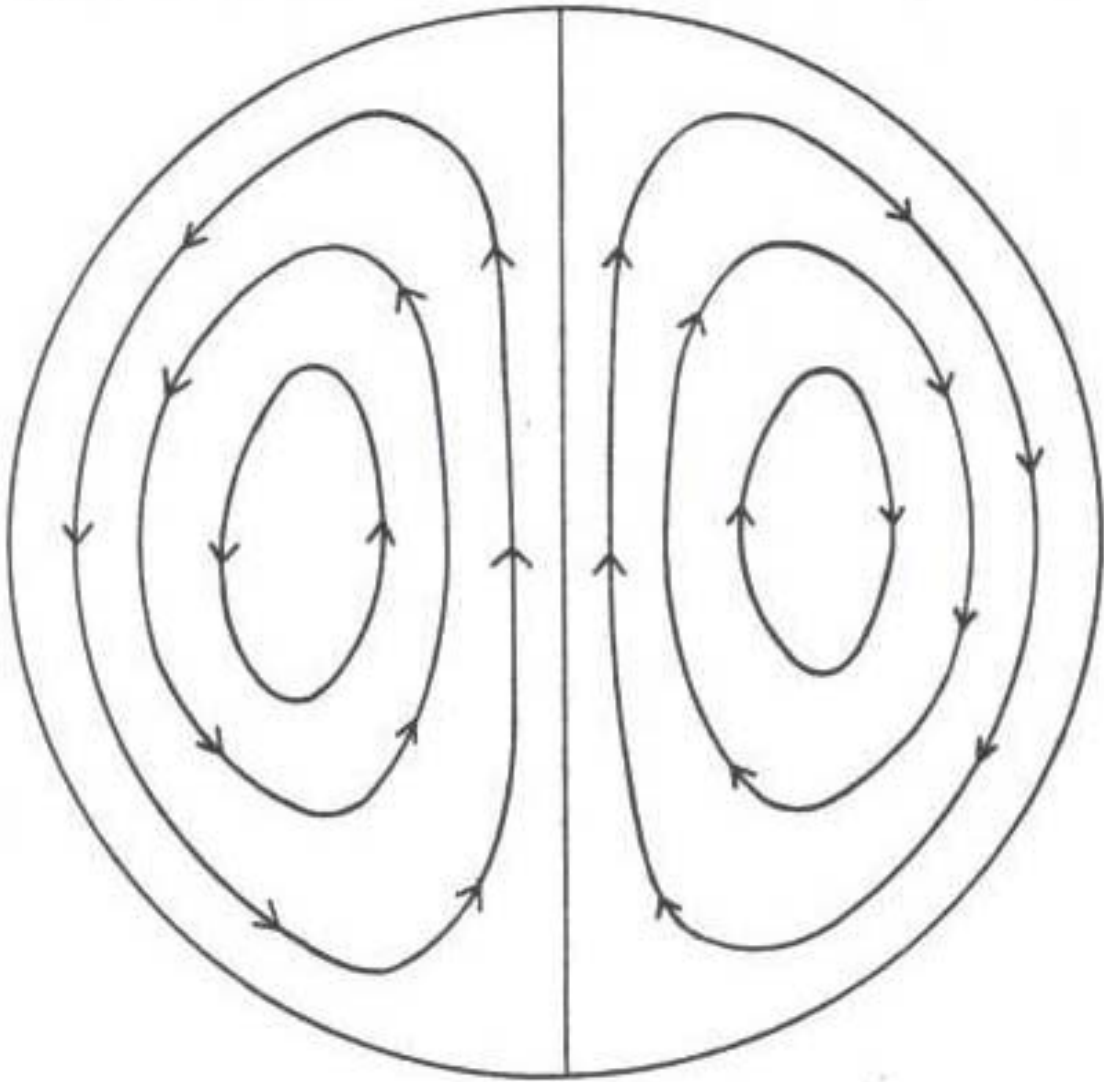


Figure 2.1 Natural convection flow pattern in a sphere for $Ra=2 \times 10^3$ (Pustovoit, 1958)

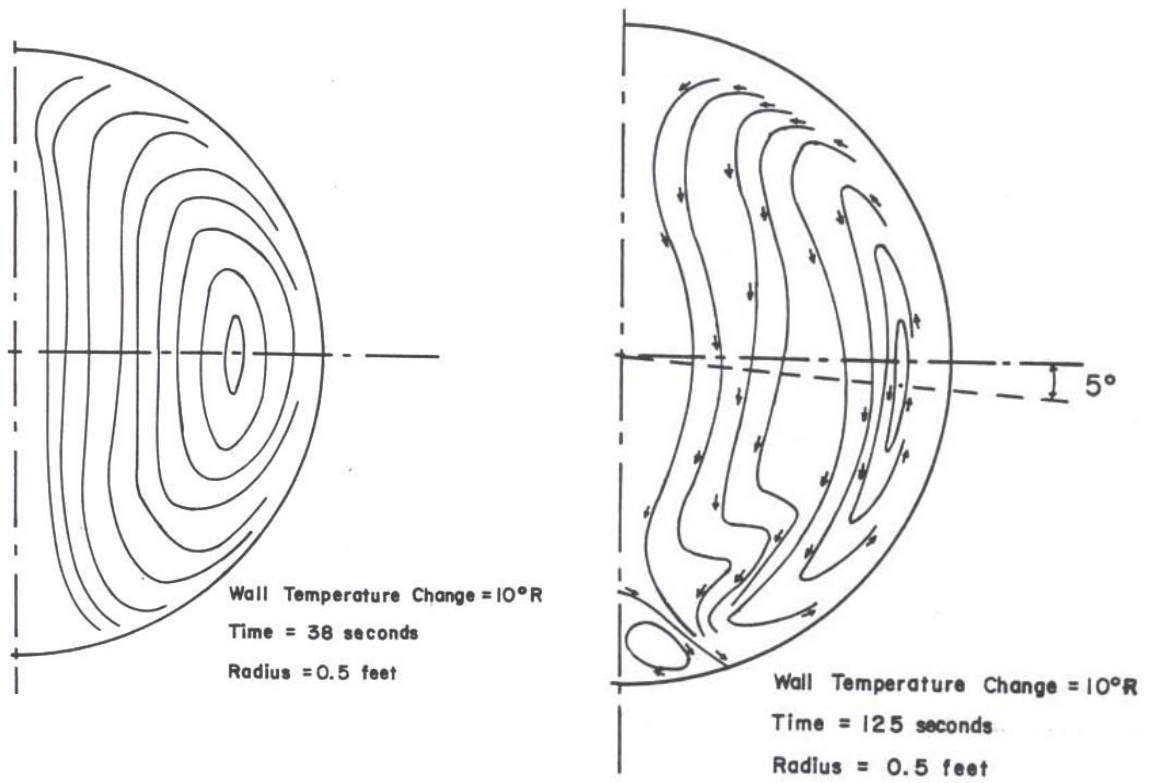


Figure 2.2 Natural convection streamlines in a sphere at dimensionless time $\tau=0.03$ (Left) and 0.10 (Right) (Whitley and Vachon, 1972)

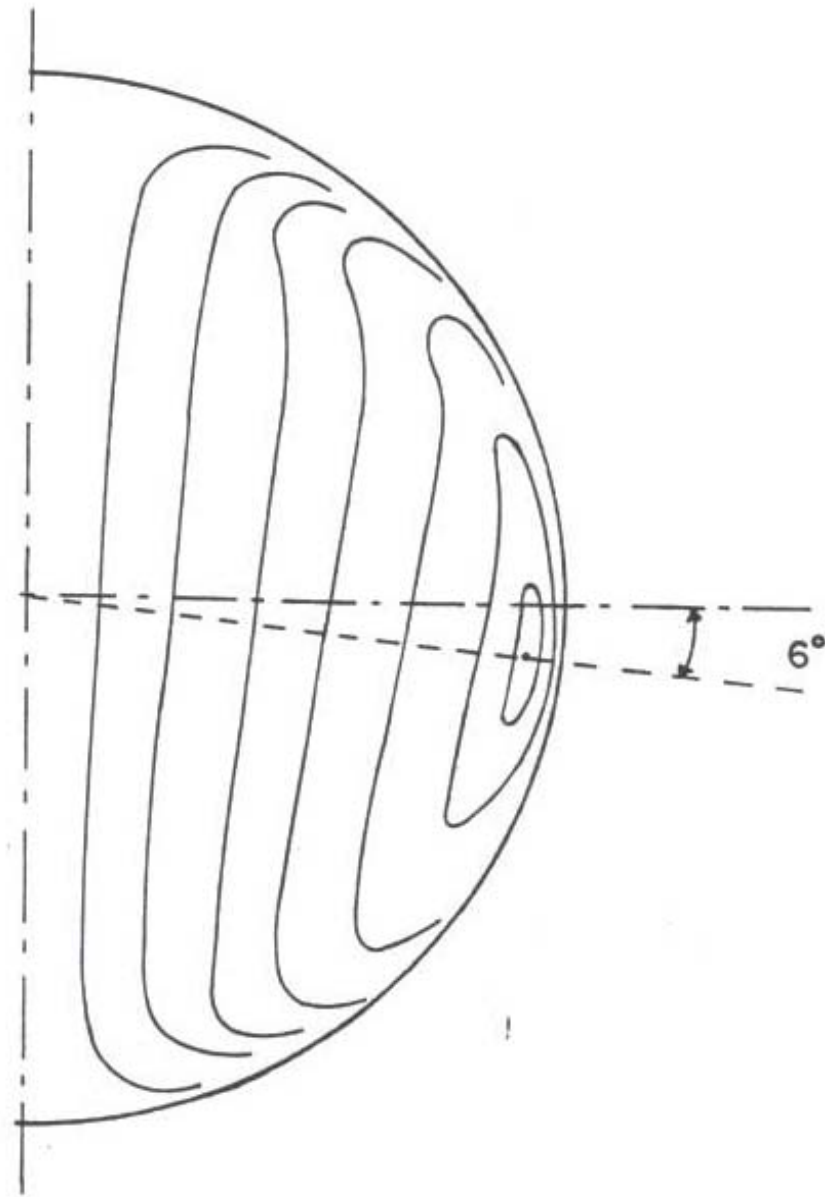


Figure 2.3 Natural convection flow pattern in a sphere for $Ra=2.8 \times 10^6$ (Chow and Akins, 1975)

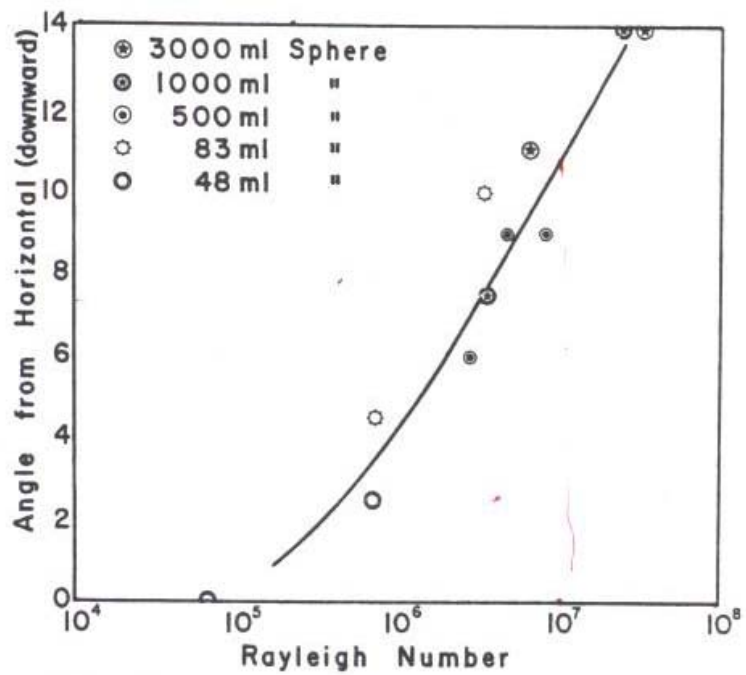
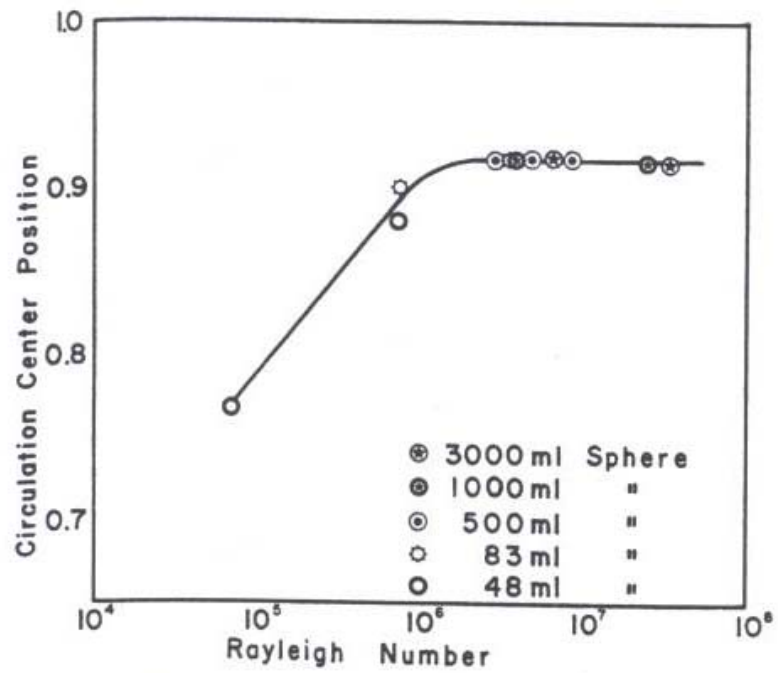
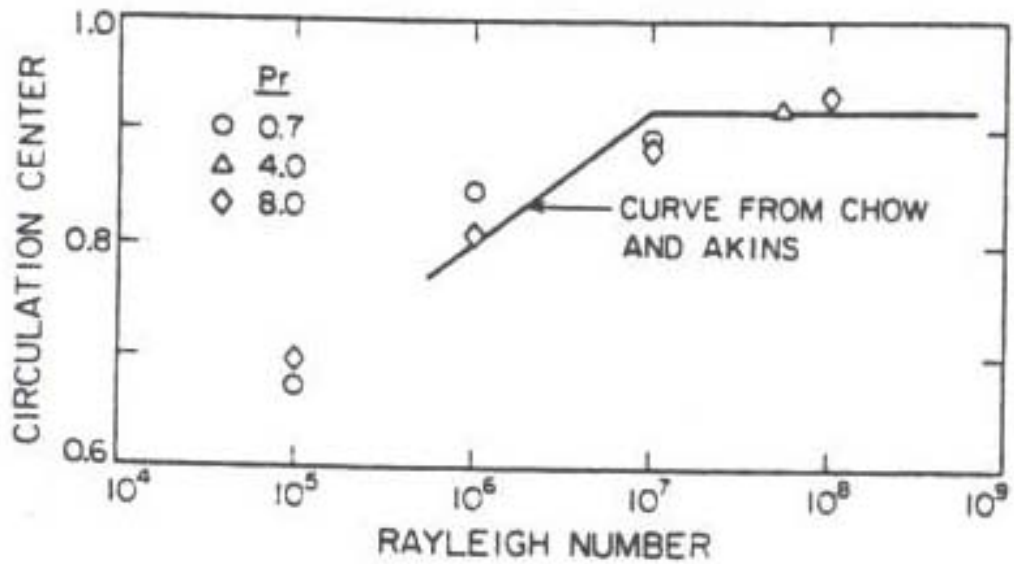
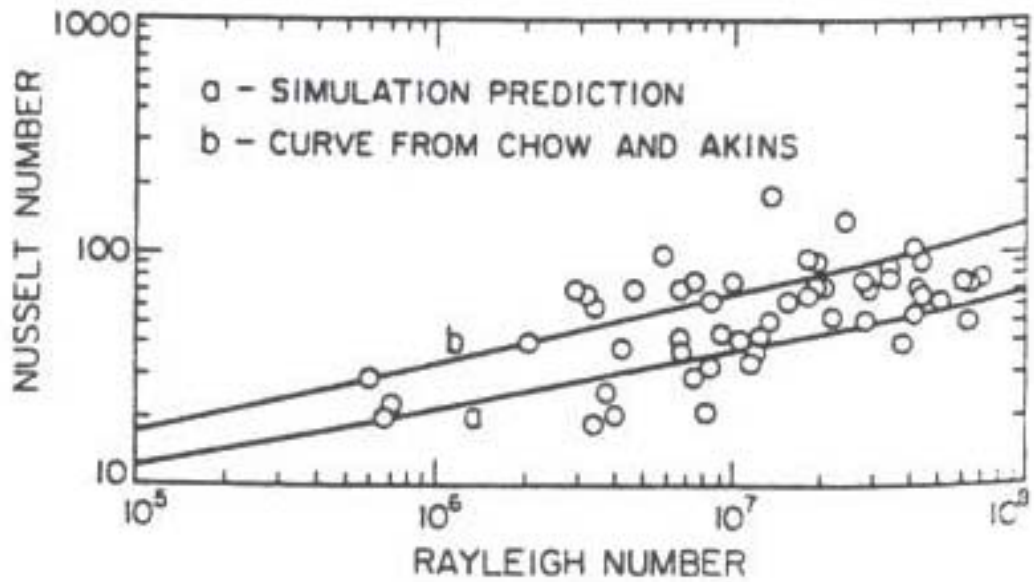


Figure 2.4 Dependence of the location of the eye of the recirculation pattern on the Rayleigh number (Chow and Akins, 1975)

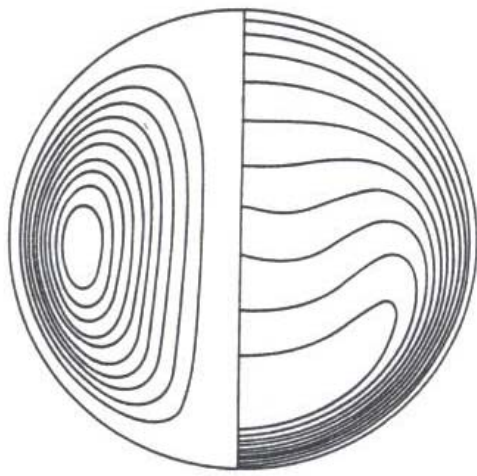


(a)

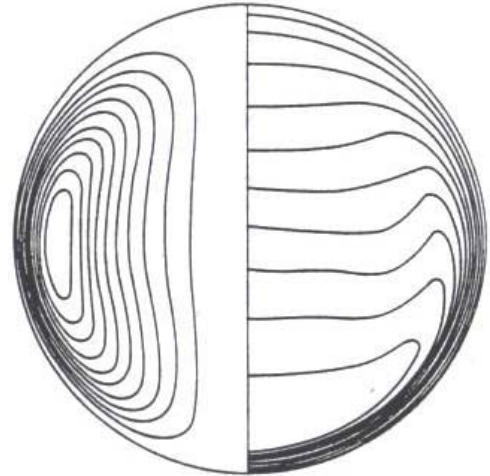


(b)

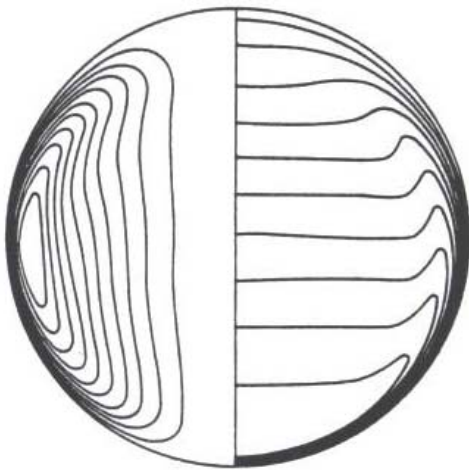
Figure 2.5 Location of the eye of recirculation (a) and mean Nusselt number variation (b) for natural convection in a sphere (Hutchins and Marschall, 1989)



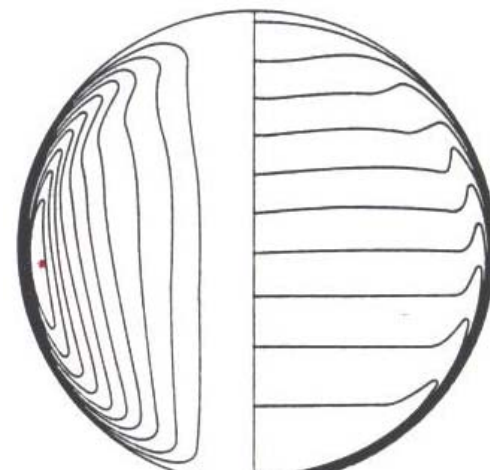
$Ra = 10^5$



$Ra = 10^6$



$Ra = 10^7$



$Ra = 10^8$

Figure 2.6 Streamline patterns and temperature contours in a sphere for different Rayleigh numbers (Hutchins and Marschall, 1989)

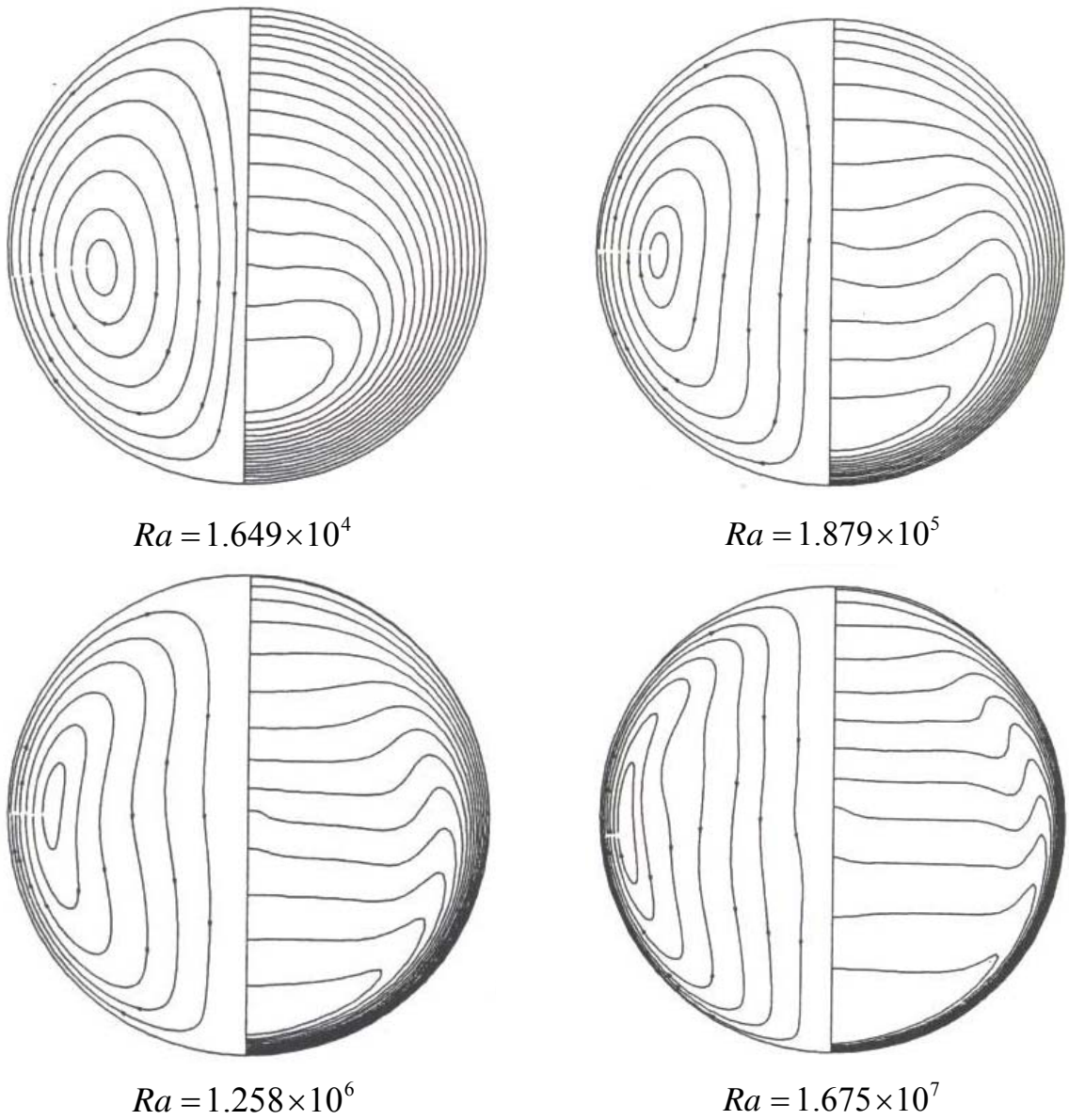


Figure 2.7 Streamline patterns and temperature contours in a sphere for different Rayleigh numbers (Shen et al., 1995)

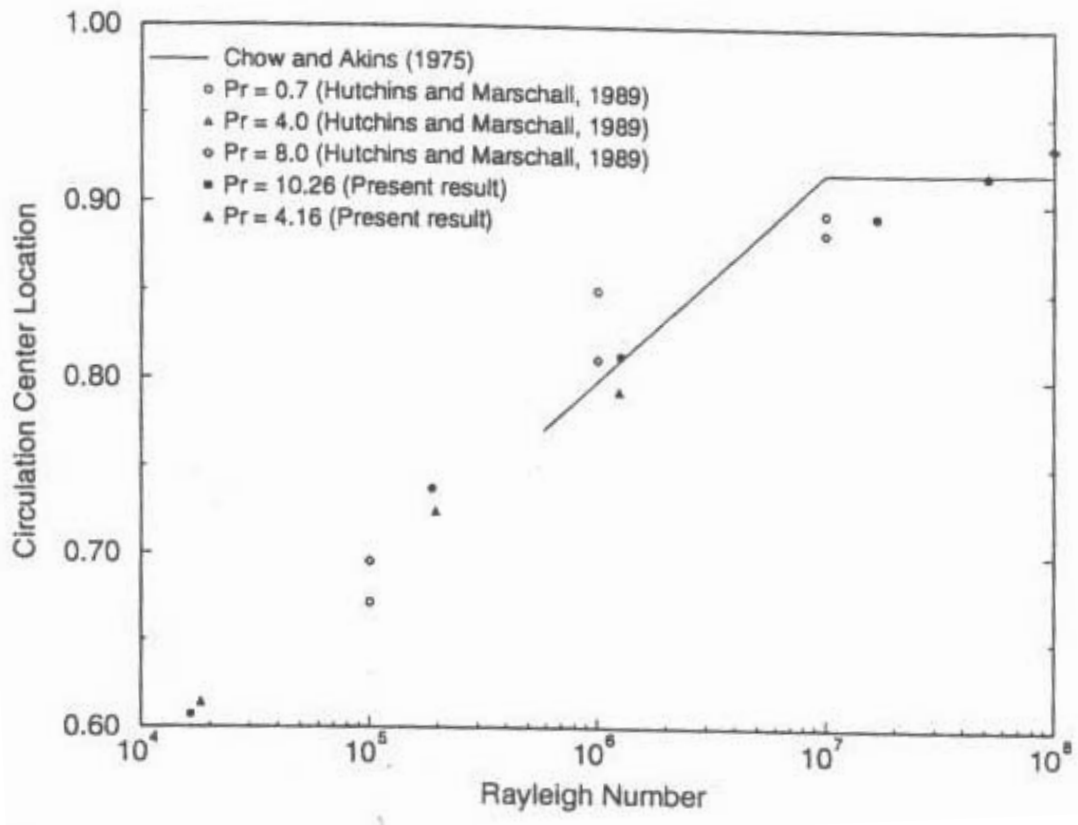


Figure 2.8 Dependence of recirculating vortex center position on the Rayleigh number (Shen et al., 1995)

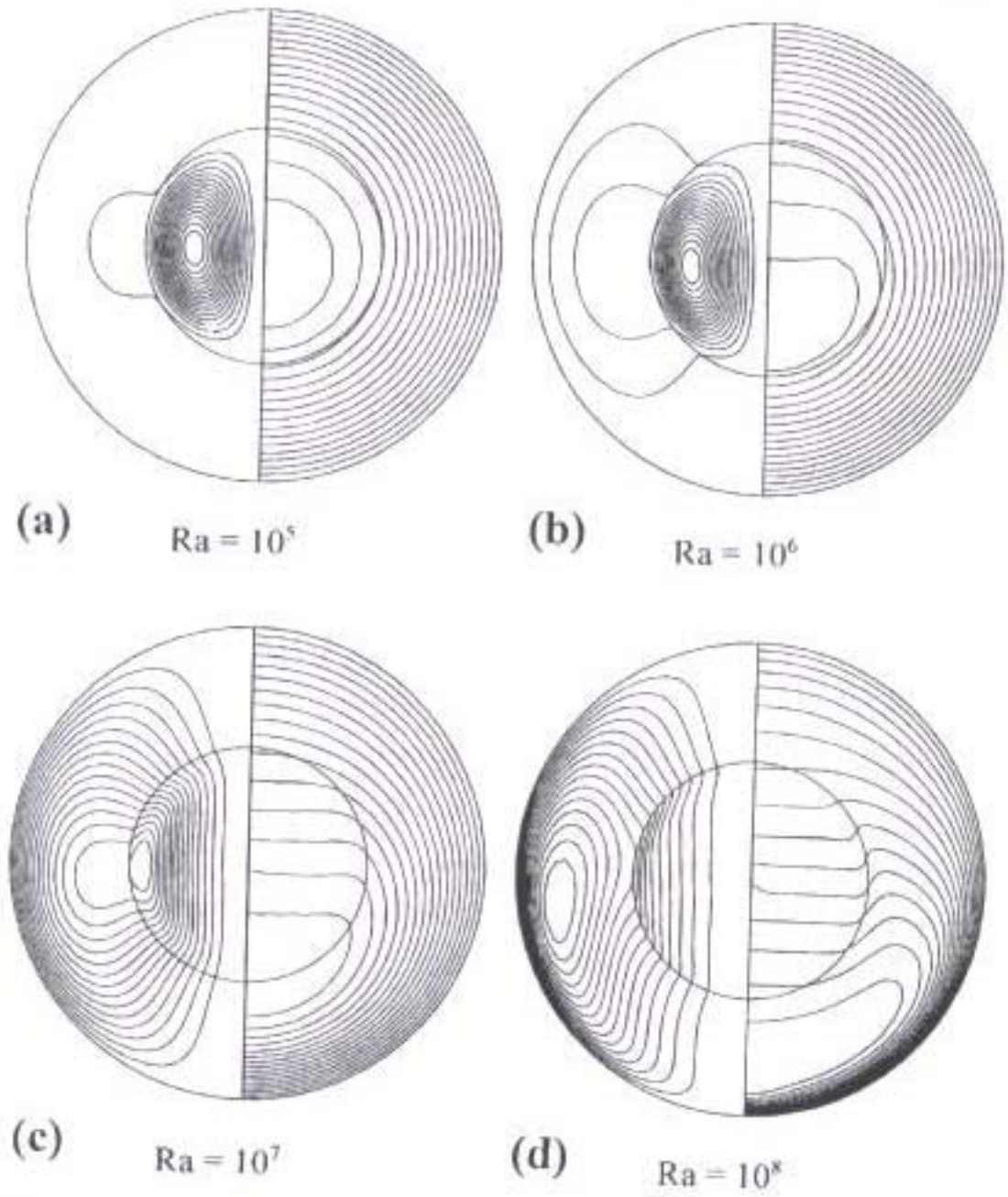


Figure 2.9 Streamlines and temperature field contours for composite systems (Zhang et al., 1999)

CHAPTER 3 COMPUTATIONAL METHODOLOGY AND BENCHMARKING

The limiting case of pseudosteady-state natural convection within spheres with no baffles is presented in this Chapter. Time-dependent computations were performed for the case of a motionless fluid at a constant temperature subjected to a step change of the wall temperature at time $t = 0$. By varying the wall temperature such that it is always greater than the temperature at the center of the sphere by a constant value, the system will attain the pseudosteady-state condition after some time period.

In this Chapter, details of the computational methodology are presented and the results corresponding to the pseudosteady-state natural convection within spherical containers with no baffles are presented. The predictions are then compared to the available data in literature.

3.1 Mathematical Formulation for the Pseudosteady-State Natural Convection inside A Spherical Container without Baffles

3.1.1 Modeling Assumptions

Consider a spherical container with a diameter of $D = 2R$ that is completely filled with a fluid. In view of the spherical shape, the orthogonal spherical coordinate system is adopted. A schematic diagram for the posed problem is shown in Figure 3.1 in which a typical computational mesh is shown on the left side. In deriving the governing equations, the following assumptions are invoked:

- I. The dependent variables (velocity, pressure and temperature) are symmetric with respect to the azimuthal direction (ϕ). Therefore, they are functions of only two spatial coordinates, i.e. radial coordinate (r) and θ . Thus, the flow field is two-dimensional. The gravitational acceleration points downward along the symmetry axis.
- II. The fluid is viscous and Newtonian with constant properties, except for variation of density that is modeled using the Boussinesq approximation.
- III. Viscous heating effects are ignored.

3.1.2 Governing Equations

Based on these assumptions, the appropriate governing equations in the spherical coordinate system can be developed (Bird, Stewart and Lightfoot, 1960). The continuity equation is:

$$\frac{1}{r^2} \frac{\partial}{\partial r} (r^2 V_r) + \frac{1}{r \sin \theta} \frac{\partial}{\partial \theta} (V_\theta \sin \theta) = 0. \quad (3.1)$$

The momentum equations in the radial (r) and polar (θ) directions are:

$$\begin{aligned} & \rho \left(\frac{\partial V_r}{\partial t} + V_r \frac{\partial V_r}{\partial r} + \frac{V_\theta}{r} \frac{\partial V_r}{\partial \theta} - \frac{V_\theta^2}{r} \right) \\ &= - \frac{\partial(p - p_0)}{\partial r} - \rho \beta g_r (T - T_0) + \mu \left[\nabla^2 V_r - \frac{2}{r^2} V_r - \frac{2}{r^2} \frac{\partial V_\theta}{\partial \theta} - \frac{2 \cot \theta}{r^2} V_\theta \right], \end{aligned} \quad (3.2)$$

and:

$$\begin{aligned} & \rho \left(\frac{\partial V_\theta}{\partial t} + V_r \frac{\partial V_\theta}{\partial r} + \frac{V_\theta}{r} \frac{\partial V_\theta}{\partial \theta} + \frac{V_r V_\theta}{r} \right) \\ &= - \frac{1}{r} \frac{\partial(p - p_0)}{\partial \theta} - \rho \beta g_\theta (T - T_0) + \mu \left[\nabla^2 V_\theta + \frac{2}{r^2} \frac{\partial V_r}{\partial \theta} - \frac{V_\theta}{r^2 \sin^2 \theta} \right], \end{aligned} \quad (3.3)$$

with:

$$\nabla^2 = \frac{1}{r^2} \frac{\partial}{\partial r} \left(r^2 \frac{\partial}{\partial r} \right) + \frac{1}{r^2 \sin \theta} \frac{\partial}{\partial \theta} \left(\sin \theta \frac{\partial}{\partial \theta} \right). \quad (3.4)$$

Finally, the energy equation is:

$$\rho c_p \left(\frac{\partial T}{\partial t} + V_r \frac{\partial T}{\partial r} + \frac{V_\theta}{r} \frac{\partial T}{\partial \theta} \right) = k \nabla^2 T. \quad (3.5)$$

3.1.3 Boundary and Initial Conditions

The no-slip boundary condition is applied on the solid wall. Therefore, on the solid surface of the sphere ($r = R$) the boundary condition can be described as:

$$V_\theta = V_r = 0. \quad (3.6)$$

The wall temperature of the sphere (T_w) was allowed to vary with time so that it was always above the temperature of the center (T_c) of the sphere by a constant value, i.e.:

$$T_w(t) = T_c(t) + C. \quad (3.7)$$

The boundary conditions on the symmetry axis of the sphere ($\theta = 0$ and π) are:

$$V_\theta = \frac{\partial V_r}{\partial \theta} = \frac{\partial T}{\partial \theta} = 0. \quad (3.8)$$

At the beginning of the computations ($t=0$), the fluid velocity was set to zero and the fluid temperature was initialized to a constant value (T_0).

3.1.4 Dimensionless Form of the Governing Equations

In order to analyze this natural convection problem, it is necessary to determine the dimensionless parameters that influence the solution. Therefore, the governing equations can be rewritten by introducing appropriate dimensionless variables. The appropriate length scale is the radius of the spherical container (R). There is no free-

stream velocity in this natural convection problem, thus the reference velocity is taken to

be $V = \frac{\alpha}{R}$. The resulting dimensionless variables that are denoted by an asterisk

superscript are listed as follows:

$$\begin{aligned}
 r^* &= \frac{r}{R} & g_r^* &= \frac{g_r}{g} & g_\theta^* &= \frac{g_\theta}{g} \\
 \tau &= \frac{\alpha t}{R^2} & T^* &= \frac{T - T_0}{T_w - T_c} & V_r^* &= \frac{V_r R}{\alpha} \\
 V_\theta^* &= \frac{V_\theta R}{\alpha} & p^* &= \frac{(p - p_0) R^2}{\rho \alpha^2}. & & (3.9)
 \end{aligned}$$

Substituting these dimensionless variables into equations 3.1-3.5, the dimensionless governing equations can be obtained. These are:

Dimensionless continuity equation:

$$\frac{1}{r^{*2}} \frac{\partial}{\partial r^*} (r^{*2} V_r^*) + \frac{1}{r^* \sin \theta} \frac{\partial}{\partial \theta} (V_\theta^* \sin \theta) = 0. \quad (3.10)$$

Dimensionless momentum equation in the radial (r) direction:

$$\begin{aligned}
 &\frac{\partial V_r^*}{\partial \tau} + V_r^* \frac{\partial V_r^*}{\partial r^*} + \frac{V_\theta^*}{r^*} \frac{\partial V_r^*}{\partial \theta} - \frac{V_\theta^{*2}}{r^*} \\
 &= -\frac{\partial p^*}{\partial r^*} - \frac{1}{8} Ra Pr g_r^* T^* + Pr \left[\nabla^{*2} V_r^* - \frac{2}{r^{*2}} V_r^* - \frac{2}{r^{*2}} \frac{\partial V_\theta^*}{\partial \theta} - \frac{2 \cot \theta}{r^{*2}} V_\theta^* \right]. \quad (3.11)
 \end{aligned}$$

Dimensionless momentum equation in the polar (θ) direction:

$$\begin{aligned}
 &\frac{\partial V_\theta^*}{\partial \tau} + V_r^* \frac{\partial V_\theta^*}{\partial r^*} + \frac{V_\theta^*}{r^*} \frac{\partial V_\theta^*}{\partial \theta} + \frac{V_r^* V_\theta^*}{r^*} \\
 &= -\frac{1}{r^*} \frac{\partial p^*}{\partial \theta} - \frac{1}{8} Ra Pr g_\theta^* T^* + Pr \left[\nabla^{*2} V_\theta^* + \frac{2}{r^{*2}} \frac{\partial V_r^*}{\partial \theta} - \frac{V_\theta^*}{r^{*2} \sin^2 \theta} \right]. \quad (3.12)
 \end{aligned}$$

With the dimensionless Laplacian operator defined as:

$$\nabla^{*2} = \frac{1}{r^{*2}} \frac{\partial}{\partial r^*} \left(r^{*2} \frac{\partial}{\partial r^*} \right) + \frac{1}{r^{*2} \sin \theta} \frac{\partial}{\partial \theta} \left(\sin \theta \frac{\partial}{\partial \theta} \right). \quad (3.13)$$

Finally, the dimensionless energy equation is:

$$\frac{\partial T^*}{\partial \tau} + V_r^* \frac{\partial T^*}{\partial r^*} + \frac{V_\theta^*}{r^*} \frac{\partial T^*}{\partial \theta} = \nabla^{*2} T^*. \quad (3.14)$$

The dimensionless boundary conditions are:

$$V_\theta^* = V_r^* = 0 \quad \text{for } r^* = 1, \quad (3.15)$$

$$T_w^*(\tau) = T_c^*(\tau) + 1, \quad (3.16)$$

$$V_\theta^* = \frac{\partial V_r^*}{\partial \theta} = \frac{\partial T^*}{\partial \theta} = 0 \quad \text{for } \theta = 0 \text{ and } \pi. \quad (3.17)$$

Finally, the initial conditions at $\tau = 0$ are:

$$V_r^* = V_\theta^* = T^* = 0. \quad (3.18)$$

Inspecting the dimensionless governing equations, it is found that the pseudosteady-state behavior of this system is characterized by the Rayleigh number

$$(Ra = \frac{g\beta D^3(T_w - T_c)}{\alpha\nu}) \text{ and Prandtl number } (Pr = \frac{\nu}{\alpha}).$$

The Rayleigh number is a measure of the strength of buoyancy force in comparison to viscous force, whereas the Prandtl number is a ratio of momentum diffusivity over thermal diffusivity. Previous findings have established the weak dependence of the results on the Prandtl number. Therefore, a single Prandtl number equal to 0.7 was used. The Rayleigh number is varied with $Ra = 10^4, 10^5, 10^6$ and 10^7 (mainly in the laminar regime).

3.2 Computational Details

The formulated problem above and variations of it were solved by Shen et al. (1995) and Khodadadi et al. (1999) who used a research code. In view of the anticipated difficulty associated with presence of baffles in a sphere, the solution of the governing equations in the present study was handled by use of a commercial computational fluid dynamic (CFD) package. The computational mesh was generated using GAMBIT (version 2.2.30) and the commercial code FLUENT (version 6.2.16) was utilized for solving the governing equations. The computations are based on an iterative, finite-volume numerical procedure using primitive dependent variables, whereby the time-dependent, two-dimensional axisymmetric form of the governing continuity, momentum and energy equations are solved. All the computations were performed on the Cray XD1 supercomputer of the Alabama Supercomputer Authority (Huntsville, Alabama).

3.2.1 Mesh Generation

In view of strong convective heat transfer that is expected next to the wall, a hybrid mesh (Figure 3.2) that consists of a “boundary layer” mesh (Figure 3.3) and an “interior mesh” was employed. The “boundary layer” mesh next to the wall is much denser than the “interior” mesh. The details of the grid system provided next are not specific to the cases with no baffles and similar steps with minor changes were taken for cases with baffles (Chapters 4 and 5). A more detailed discussion in relation to the grid and time step size independence tests will be given in Chapter 4.

Combining theoretical estimates of the thickness of a boundary layer next to a vertical heated wall and numerical tests, the “boundary layer” thickness in the radial

direction is set to be 4% of diameter. The thickness of the first row of the “boundary layer” mesh in the radial direction is set to be 0.1% of diameter. In going from the first row to last row of the “boundary layer” mesh, the radial grid spacing expanded with a growth factor equal to 1.1. A total of 17 radial rows are created in the “boundary layer” mesh. The spacing of the adjacent nodes in the polar direction on the first row of the “boundary layer” mesh is set to be 0.98% of diameter and a total of 160 polar nodes are laid on the first row (Figure 3.4). For the “interior” mesh, unstructured grids were created. A close-up view of both mesh systems is shown in Figure 3.5. The spacing between any two adjacent nodes in the “interior mesh” is less than 1.15% of diameter. Thus, there are 6,610 nodes and 10,222 cells in the grid network, whereas there were about 900 cells in the entire mesh network of previous studies (e.g. Hutchins and Marschall (1989), Shen et al. (1995)).

3.2.2 FLUENT Configuration

The SIMPLE method (Patankar, 1980) was utilized for solving the governing equations. The QUICK differencing scheme was used for solving the momentum and energy equations, whereas the PRESTO scheme was adopted for the pressure correction equation. The under-relaxation factors for the velocity components, pressure correction and thermal energy were 0.7, 0.3 and 1, respectively (Figure 3.6). Second-order accurate implicit discretization was utilized for the unsteady term (Figure 3.7). The operating pressure and temperature were 0.1 MPa and 288.16 K, respectively. The effect of gravity is applied using the Boussinesq approximation (Figure 3.8). Air is selected as the working fluid and all the material properties, except density, were assumed to be

independent of temperature (Figure 3.9). The Rayleigh number was varied by adjusting the thermal expansion coefficient. A UDF (User-Defined Function) file is utilized to apply the thermal boundary condition (Figure 3.10) and the settings for applying the momentum boundary conditions are shown in Figure 3.11.

The time step size is 2 seconds ($\Delta\tau = 1.57 \times 10^{-4}$). At each time step, the continuity and velocity residuals were monitored. An iteration was terminated and solution was forwarded in time when all the three residuals were less than 10^{-6} (Figure 3.12). At each time step, the number of iterations varied between 100 and 200.

3.3 Results and Discussion

3.3.1 Definitions of the Nusselt Numbers

The Nusselt number can be considered as a dimensionless heat transfer coefficient and a significant parameter that is used to describe the strength of the pseudosteady-state natural convection inside spherical containers without baffles. Similar to the work done by Hutchins and Marschall (1989), the Nusselt numbers either can be derived from:

- (a) the temperature gradient on the wall (direct approach), or
- (b) performing a lumped energy balance for the fluid within the container (indirect approach).

Theoretically, these two approaches should give the same values when the pseudosteady-state is reached. The accuracy and verification of computational solution can be evaluated by inspecting the difference between the Nusselt numbers values that are determined by two different approaches.

(a) Direct Approach

In order to obtain the instantaneous area-averaged Nusselt number over the entire wall surface, the area-averaged heat flux can be expressed as:

$$\bar{q}(t) = \frac{\int_0^\pi k \frac{\partial T}{\partial r} \Big|_{r=R} dA}{\int_0^\pi dA} = \frac{\int_0^\pi k \frac{\partial T}{\partial r} \Big|_{r=R} R \sin \theta 2\pi R d\theta}{\int_0^\pi R \sin \theta 2\pi R d\theta} = \frac{1}{2} \int_0^\pi k \frac{\partial T}{\partial r} \Big|_{r=R} \sin \theta d\theta. \quad (3.19)$$

This quantity might depend on time due to:

1. transient behavior during the establishment of the flow early on, and/or
2. instability issues for high Rayleigh number cases.

The area-averaged Nusselt number can be calculated employing the general definition:

$$Nu(t) = \frac{hD}{k} = \frac{\bar{q}(t)D}{k\Delta T} = \frac{D}{2\Delta T} \int_0^\pi \frac{\partial T}{\partial r} \Big|_{r=R} \sin \theta d\theta. \quad (3.20)$$

The quantity ΔT can be an arbitrary value. Generally, the term ΔT is taken as $\Delta T = T_w - T_m$. This is a quantity that depends on time for this problem and serves as the driving force for natural convection. The above definition can be simplified by introducing expressions for r^* and T^* :

$$Nu_m(\tau) = \frac{I}{(T_w^* - T_m^*)} \int_0^\pi \frac{\partial T^*}{\partial r^*} \Big|_{r^*=1} \sin \theta d\theta. \quad (3.21)$$

Note that a subscript “m” is used for this area-averaged Nusselt number meaning that T_m (mean or bulk temperature) is used in the ΔT expression.

However, in this specific pseudosteady-state natural convection work, the temperature difference between the wall and center is maintained as a constant value. This boundary condition can introduce another logical Nusselt number that is based upon a constant driving force $\Delta T = T_w - T_c$. Then, another Nusselt number can be obtained:

$$Nu_c(\tau) = \int_0^\pi \frac{\partial T^*}{\partial r^*} \Big|_{r^*=1} \sin \theta d\theta. \quad (3.22)$$

Note that a subscript “c” is used for this area-averaged Nusselt number meaning that T_c (container’s center temperature) is used in the ΔT expression.

(b) Indirect Approach

As mentioned above, another approach to get the Nusselt number is to perform a lumped energy balance for the fluid within the container. The heat transferred into the container must be exactly equal to the enthalpy change of the fluid inside the container, i.e.:

$$\frac{\bar{q}(t)}{A} = \frac{mc_p \frac{dT_m}{dt}}{A} = \frac{\rho \frac{4}{3} \pi R^3 c_p \frac{dT_m}{dt}}{4\pi R^2} = \frac{\rho R c_p \frac{dT_m}{dt}}{3}. \quad (3.23)$$

Thus, the Nusselt number can be expressed as:

$$Nu(t) = \frac{hD}{k} = \frac{\bar{q}(t)D}{k\Delta T} = \frac{\rho R c_p D}{3k\Delta T} \frac{dT_m}{dt} = \frac{D^2}{6\alpha\Delta T} \frac{dT_m}{dt}. \quad (3.24)$$

Similar to the above derivations for the direct approach, term ΔT can either be taken as $(T_w - T_m)$ or $(T_w - T_c)$. Correspondingly, two definitions of the Nusselt numbers are obtained by introducing dimensionless time, which are:

$$Nu_m(\tau) = \frac{2}{3} \frac{1}{(T_w^* - T_m^*)} \frac{dT_m^*}{d\tau}, \quad (3.25)$$

$$Nu_c(\tau) = \frac{2}{3} \frac{dT_m^*}{d\tau}. \quad (3.26)$$

The two Nusselt numbers that are obtained by the two approaches and are based on the driving force of $\Delta T = T_w - T_m$ should equal each other. Similarly, the two Nusselt

numbers that are based on the driving force of $\Delta T = T_w - T_c$ should be identical. These four Nusselt numbers were evaluated for each case. The Nusselt number based on the constant driving force $\Delta T = T_w - T_c$ is uniquely proportional to the time rate of change of the bulk temperature, while the Nusselt number based on the varying driving force $\Delta T = T_w - T_m$ is also dependent on this driving force besides the time rate of change of the bulk temperature. It is clear that Nu_c can be used as a direct indicator of the variation of the bulk temperature with time.

3.3.2 Stream Function

The difference between the maximum and minimum stream function values of a primary vortex is a convenient parameter to measure the strength of a recirculating flow field. This quantity can also be used to monitor the convergence of the pseudosteady-state natural convection within spheres with no baffles. If the difference between the maximum and minimum time-averaged stream function values remains smaller than 10^{-6} , then it is declared that pseudosteady-state natural convection is reached. The minimum stream function value is taken by FLUENT as zero at the eye of the vortex. The maximum stream function is the value on the wall. Both dimensional and dimensionless stream function values are presented. The dimensionless stream function is defined as:

$$\psi^* = \frac{\psi}{\alpha R}. \quad (3.27)$$

3.3.3 Fluid Flow and Thermal Fields

Composite diagrams of the streamline patterns and temperature contours under the pseudosteady-state condition for the Rayleigh numbers of 10^4 , 10^5 , 10^6 and 10^7 with no baffles are presented in Figure 3.13. The solution was declared to be the pseudosteady-state when the Nusselt number and stream function values satisfied the requirement to be discussed in Chapter 4. Streamlines are shown on the left half of the sphere, whereas the temperature contours are shown on the right half of the sphere. For the limiting case of $Ra = 0$ (pure conduction within the fluid), perfectly concentric rings for the temperature contours would have been observed, indicating one-dimensional heat diffusion independent of the polar angle. For the lowest Rayleigh number studied, the temperature contours are observed to be skewed from a concentric ring distribution suggesting that natural convection effects are important. As buoyancy-induced convection effects become more dominant, deviations of the temperature contours from concentric ring patterns become more pronounced and the temperature gradients on the bottom of the sphere become stronger. For higher Ra numbers, the region around the symmetry axis of the sphere is composed of constant-temperature stratified layers. The spatial extent of this region is observed to increase as the Rayleigh number is raised and natural convection is strengthened next to the wall. This observation on thermal stratification does not hold strongly for the highest Ra number studied due to the unsteady flow behavior to be discussed below. In observing the trends of the flow field, the fluid that is heated adjacent to the hot wall becomes less dense and rises, replacing the colder fluid that sinks slowly downward along the symmetry axis of the sphere. As the Rayleigh number rises, fluid flow is intensified and the velocity gradient next to the

surface becomes stronger. The location of the eye of the clockwise (CW) rotating recirculating vortex is strongly dependent on the Rayleigh number. The radial and polar angle positions of the eye of the recirculating vortex are summarized in Table 3.1, suggesting that the eye travels radially toward the wall of the sphere as the Rayleigh number is raised. At the same time, its polar position is lifted from the bottom half to the top half. There are contradictions between the present results and those of Shen et al. (1995) who reported streamline and temperature contours for Ra numbers that were higher by factors of 1.3~1.9 (Figure 2.7). Those data are also summarized in Table 3.1 showing similar trends for the radial coordinate of the eye of the vortex. However, according to Shen et al. (1995) the polar angle position of the vortex shows almost no sensitivity to the change of the Ra. Whereas the polar angle changes 50 degrees upon raising the Ra number by 3 orders of magnitude in the present study, Shen et al. (1995) only observed 11 degrees, with the eye always remaining in the lower half. The observations of Shen et al. (1995) were generally supportive of findings of Hutchins and Marschall (1989) that reported data on the eye of the vortex for similar Rayleigh numbers reported here (Table 3.1). Interestingly, Khodadadi et al. (1999) reported streamline and temperature contours for a higher Rayleigh number of 10^8 , with the vortex eye located at $r_e^* = 0.824$ and $\theta_e = 54^\circ$. This observation is in concert with the data for the present study for a Ra number of 10^7 , whereas the data of Hutchins and Marschall (1989) for Ra = 10^8 exhibits no sensitivity to the Ra number for the polar angle position of the vortex. In view of the commonality of the computational procedure used by these investigators, the contradictions can be attributed to the differences in spatial grid resolutions among

the three studies (about 10,000 cells for the present study compared to ~900 cells for the earlier studies).

Table 3.1 Radial and polar angle positions of the eye of the recirculating vortex for the cases with no baffles

Ra	10^4	10^5	10^6	10^7	10^8
r_e^*					
Present Study	0.605	0.651	0.768	0.814	-----
Shen, Khodadadi and Zhang (1995)*	0.617	0.733	0.8	0.9	-----
Hutchins and Marschall (1989)	-----	0.727	0.910	0.850	0.912
θ_e (degrees)					
Present Study	104.3	91.5	68.5	54.8	-----
Shen, Khodadadi and Zhang (1995)*	100	92	89	94	-----
Hutchins and Marschall (1989)	-----	93	94	92	95

* The reported Rayleigh numbers were higher than the values shown at the top of the columns by a factor of 1.3~1.9. Refer to Figure 2.7 for streamlines and temperature contours.

Natural convection within spherical enclosures exhibits a variety of flow structures that interact constantly. These include developing momentum and temperature boundary layers over concave and convex surfaces and a massive recirculating flow that is directly linked to the confinement of the fluid in the vessel. A very interesting feature of natural convection in a spherical container is the simultaneous existence of thermally stable and unstable fluid layers in the vicinity of the symmetry axis. This is illustrated schematically in Figure 3.14 that shows enlarged views of these two fluid layers. For the greater portion of the symmetry axis, horizontal stratified fluid layers are observed with the hot lighter fluid sitting on top of cooler dense layers. Such a system is denoted to be thermally stable, where fluid motion is negligible and heat conduction dominates. In

contrast, the remaining portion of the symmetry axis near the bottom is composed of cold fluid layers on top of hotter dense layers. This type of system is denoted to be thermally unstable and will feature recirculating cells. In the present study, the onset of instabilities through creation of a small counter CW (CCW) rotating vortex near the bottom of the sphere was observed for the Rayleigh number of 10^7 (Figure 3.13). The strength of this vortex is dictated by the dynamic interaction of the rising hot fluid along the symmetry line with the sinking cooler fluid that originates from the top of the sphere. In connection with this finding, Owen and Jalil (1986) have reported temperature measurements at the bottom of the sphere exhibiting an oscillating behavior.

The instantaneous area-averaged Nusselt numbers ($Nu_c(\tau)$) as functions of dimensionless time are presented in Figures 3.15-3.18 for $Ra=10^4$, 10^5 , 10^6 and 10^7 , respectively. Marked variations of the values of the Nusselt number is observed during the early transient period ($\tau \leq 0.12$) as the flow perturbs starting from a motionless state. The oscillations observed during the early transient period gain in their frequency as the Rayleigh number is raised. Beyond the early transient period, the Nusselt number tends toward its final pseudosteady-state value. Even then, it is observed that the oscillating behavior persists regardless of the Rayleigh number. The RMS and relative RMS values of the Nusselt numbers are given in Table 3.2. It is clearly observed that the oscillations are weak and the pseudosteady-state was established for the cases that were investigated.

Table 3.2 RMS and relative RMS of the Nusselt Number under pseudo-steady state condition

Ra	$RMS _{Nu_c}$	$RMS _{rNu_c}$
10^4	1.76×10^{-3}	3.06×10^{-4}
10^5	2.09×10^{-3}	1.62×10^{-4}
10^6	1.87×10^{-3}	7.35×10^{-5}
10^7	3.22×10^{-3}	3.22×10^{-5}

3.3.4 Code Validation

Due to the steady rise of computing power in recent years, numerical simulation of processes and machinery is becoming more important for engineering applications. Even so, it is not foreseen that numerical simulation will completely replace experiments. However, its low-cost and smart-adoption advantages are elevating CFD to play an important role in wide engineering applications. Ensuring code and solution correctness is critical for any computational study. Code verification and validation allow one to quantitatively evaluate the correctness of code and model, respectively. Before final results are obtained, code verification and validation should be carried out to ensure that the simulation can represent reality within the required accuracy. Code verification concentrates on the mathematical formulation, while the code validation deals with comparison against experimental data (Roy, 2006). The CFD code FLUENT is a widely-adopted commercial computational fluid dynamic (CFD) package that has been widely tested by others. Therefore, in this section we mainly focus on code validation that is accomplished by comparing the present results with prior known data.

Four Nusselt numbers were calculated according to different definitions discussed earlier. The Nusselt numbers obtained from the temperature gradient on the wall were computed by FLUENT and this approach is called “Direct”. The Nusselt number obtained from the lumped energy balance is calculated in Matlab using the temperature data file output of FLUENT. In this thesis, this method is called “Indirect”. The computed Nusselt number results in comparison to those of Hutchins and Marschall (1989) are given in Table 3.3. First of all, the results of the direct and indirect approaches that were adopted for evaluating the specific Nusselt numbers matched almost perfectly. Present results are a little higher than the predictions of Hutchins and Marschall (1989). The relative differences are within 8 percentage for all the Rayleigh numbers.

Table 3.3 Comparison of the pseudosteady-state Nusselt numbers

Pr	Ra	Direct Approach*		Indirect Approach**		Hutchins and Marschall (1989)	
		Nu_m	Nu_c	Nu_m	Nu_c	Nu_m	Nu_c
0.7	10^4	11.224	5.7556	11.2246	5.7559	-----	-----
0.7	10^5	16.129	12.8698	16.1298	12.8705	15.8	11.5
0.7	10^6	25.3452	25.4938	25.3465	25.495	23.8	23.5
0.7	10^7	40.1974	37.1717	40.1993	37.1735	40.8	36.7

The relative difference of Nu_m and Nu_c using two different approaches can be employed to examine the accuracy of simulations. Defining relative differences of Nu_m and Nu_c as $\frac{|Nu_m^* - Nu_m^{**}|}{Nu_m^*}$ and $\frac{|Nu_c^* - Nu_c^{**}|}{Nu_c^*}$, respectively, the relative difference values for different Rayleigh numbers are shown in Figure 3.19. Note that the Nusselt number with a single star stands for the “direct” value, while double stars stand for the “indirect” value. It can be seen clearly that both relative difference of Nu_m and that of

Nu_c are of the order of magnitude of 10^{-5} , regardless of the Rayleigh number. Considering the truncation error in the discretization, the relative differences can not be exactly zero. Thus, these negligible relative differences indicate the good accuracy of the FLUENT in simulating the pseudosteady-state natural convection inside spherical containers.

Another approach for code validation is carried out by comparing the maximum dimensionless stream function (ψ_{\max}^*) with those of Hutchins and Marschall (1989). The data of dimensionless stream function reported by Hutchins and Marschall (1989) is for $Pr=8$, while our computational results are for $Pr=0.7$. It has been reported that the Prandtl number has negligible effect on the solution when Pr lies in the range of 0.7 to 8. The tabulated results can be found in Table 3.4. In view of the discrepancies that were discussed in relation to the location of the eye of vortex, it is shown that the current data (ψ_{\max}^*) match the results of Hutchins and Marschall (1989) well.

Table 3.4 Dimensionless maximum stream function (ψ_{\max}^*) values

Pr	Ra	Current Results	Hutchins and Marschall (1989)
0.7	10^4	1.554137939	-----
0.7	10^5	7.64067724	6.01
0.7	10^6	19.61292939	14.51
0.7	10^7	41.42771552	33.47

3.3.5 Correlations of the Pseudosteady-State Nusselt Numbers

Assume that the dependence of the Nusselt numbers on the Rayleigh number takes the form:

$$Nu_{\zeta} = CRa^b, \quad (3.28)$$

with ζ standing for m or c depending on the use of temperature difference ΔT . The following correlations were constructed for both Nu_m and Nu_c using the least-squares fitting method:

$$Nu_m = 1.96934Ra^{0.185844}, \quad (3.29)$$

$$Nu_c = 0.514756Ra^{0.272723} \text{ for } 10^4 < Ra < 10^7. \quad (3.30)$$

The cross-correlation coefficient (σ) is a quantity that describes the divergence between the least-squares fitting curve and the original data. It is defined as:

$$\sigma = bb', \quad (3.31)$$

with:

$$\ln(Nu_{\zeta}) = \ln(C) + b \ln(Ra), \quad (3.32)$$

that is a rearrangement of Equation 3.28. Equation 3.28 can also be solved for Ra, thus leading to:

$$\ln(Ra) = \ln(C') + b' \ln(Nu_{\zeta}). \quad (3.33)$$

The cross-correlation coefficients are 0.997 and 0.977 for Nu_m and Nu_c , respectively. These values are very close to unity that indicates good accuracy of the least-squares fitting.

Chow and Akins (1975) reported correlation of their experimental data using the least-squares fitting method as:

$$Nu_c = 0.54Ra^{0.3} \text{ for } 7.74 \times 10^4 < Ra < 1.13 \times 10^7. \quad (3.34)$$

Hutchins and Marschall (1989) reported correlation of their numerical data using the least-squares fitting method as:

$$Nu_m = 1.19Ra^{0.2215}, \quad (3.35)$$

$$Nu_c = 0.655Ra^{0.2521} \text{ for } 10^5 < Ra < 10^8. \quad (3.36)$$

Shen et al. (1995) reported correlation of their numerical data (using different dimensionless form) using the least- squares fitting method as:

$$Nu_m = 0.78055Ra^{0.2013} \text{ for } 1.649 \times 10^4 < Ra < 1.675 \times 10^7. \quad (3.37)$$

The various correlations of the two Nusselt numbers (Nu_c and Nu_m) were drawn in Figures 3.20 and 3.21, respectively.

3.4 Closure

The solution of the pseudosteady-state natural convection in a sphere was obtained by using a commercial CFD package. The code validation was done by comparing the Nusselt numbers and stream functions against prior known data. A thermally unstable structure near the bottom of the sphere is observed in a spherical container for $Ra=10^7$. The correlations for the Nusselt numbers were established.

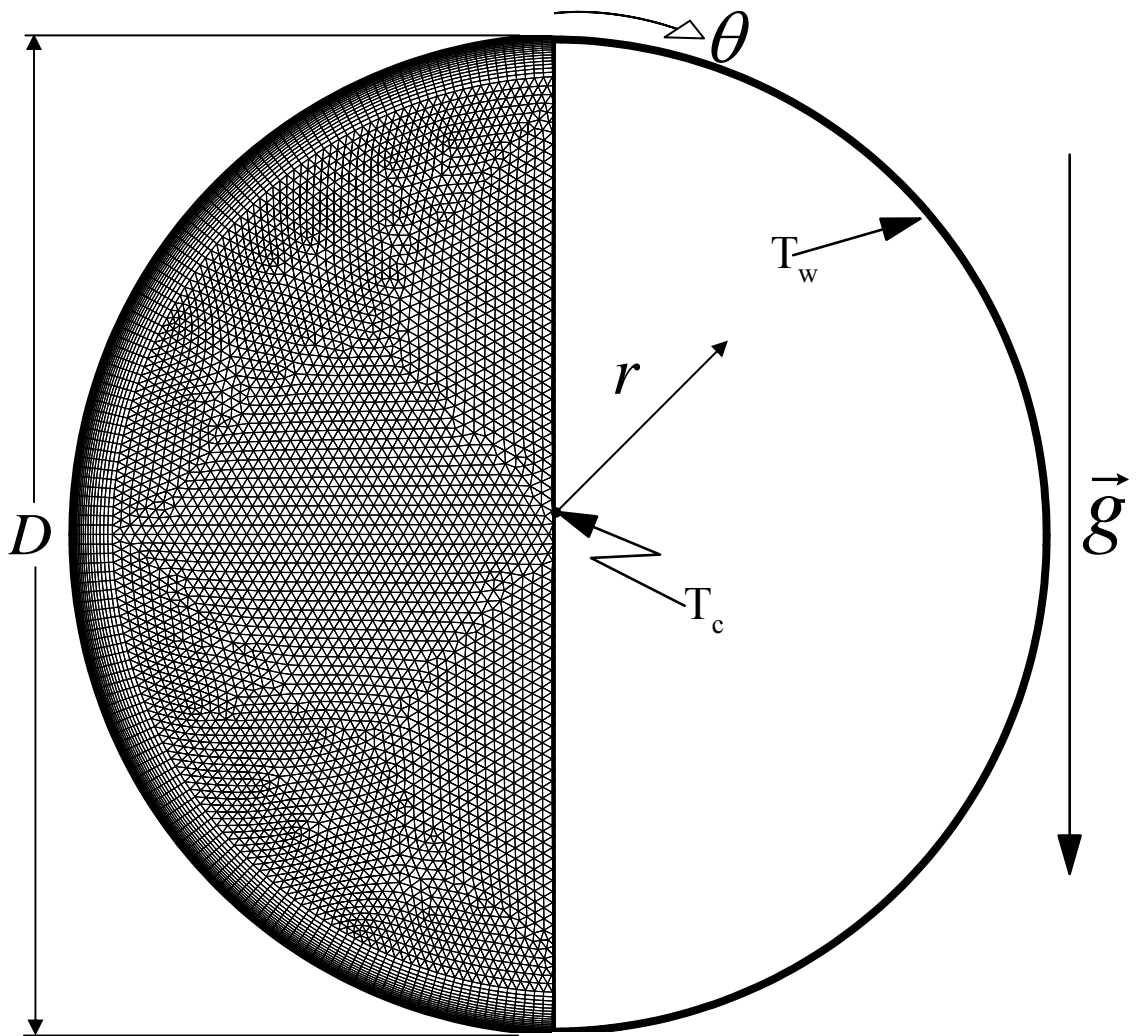


Figure 3.1 Schematic diagram of the problem

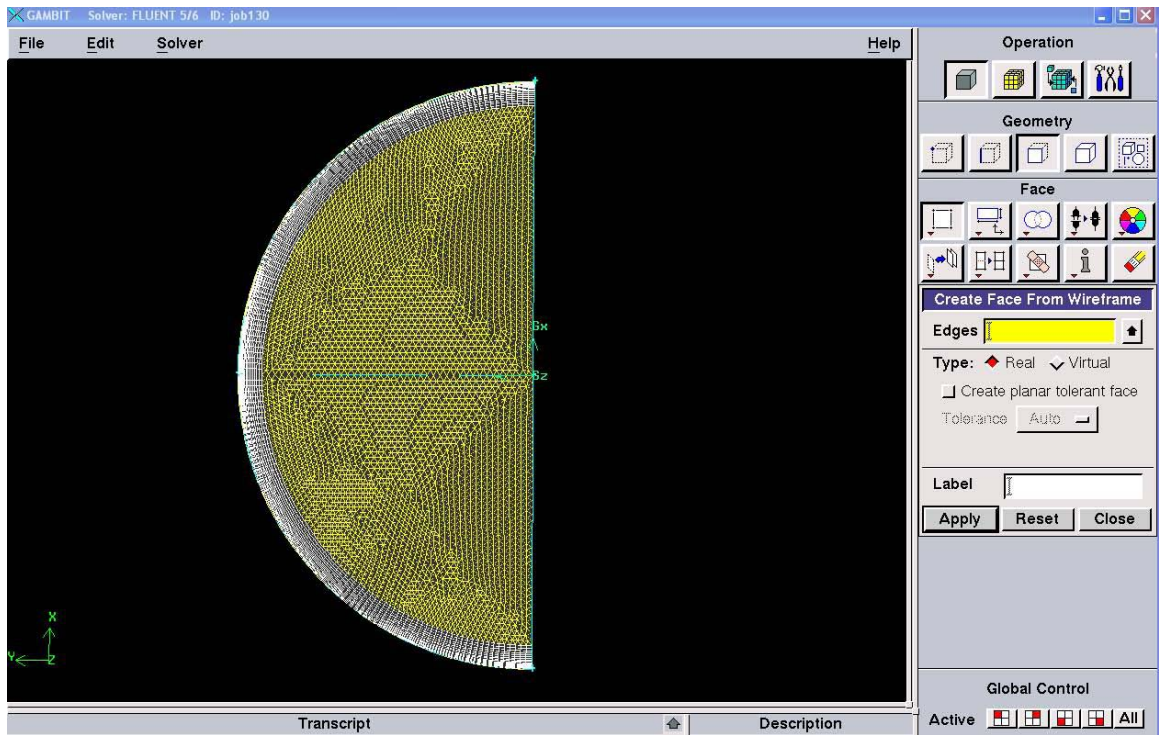


Figure 3.2 Hybrid mesh created in GAMBIT



Figure 3.3 Boundary layer mesh system

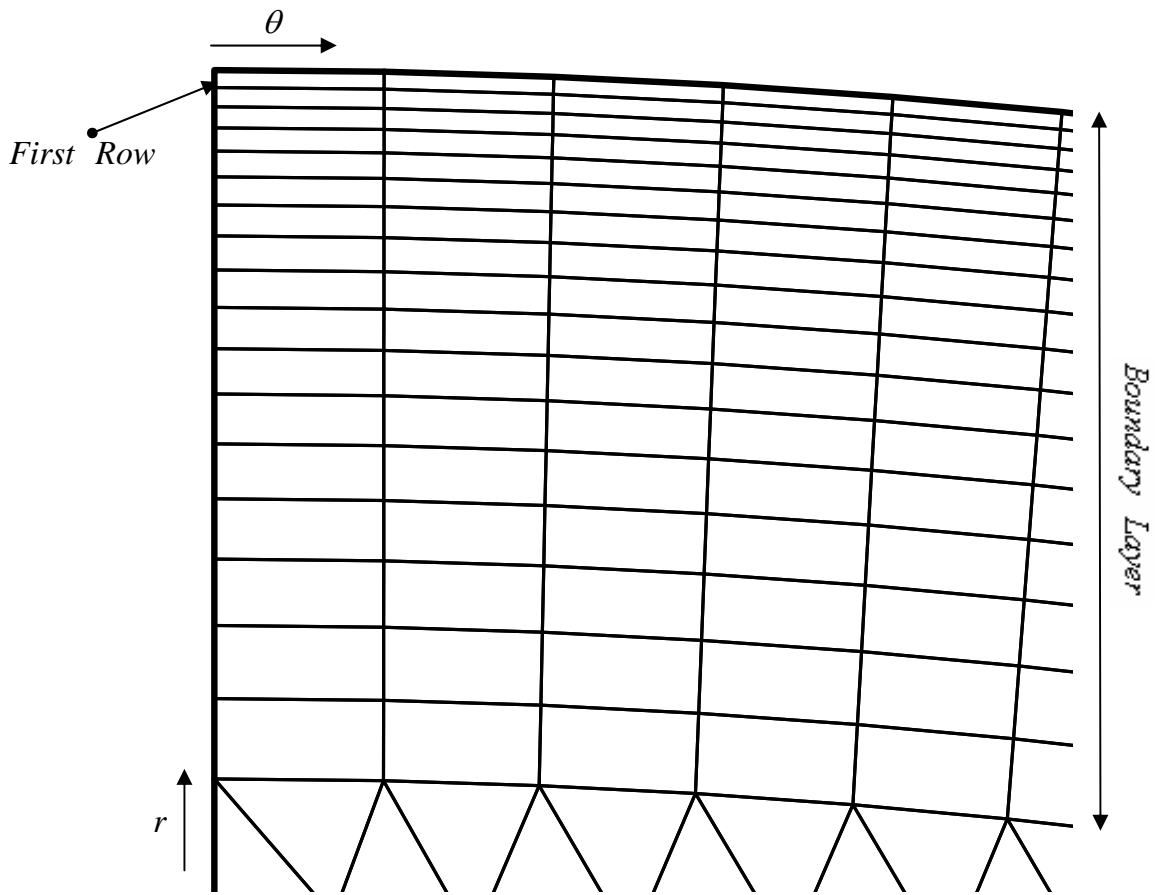


Figure 3.4 Detailed view of the boundary layer mesh

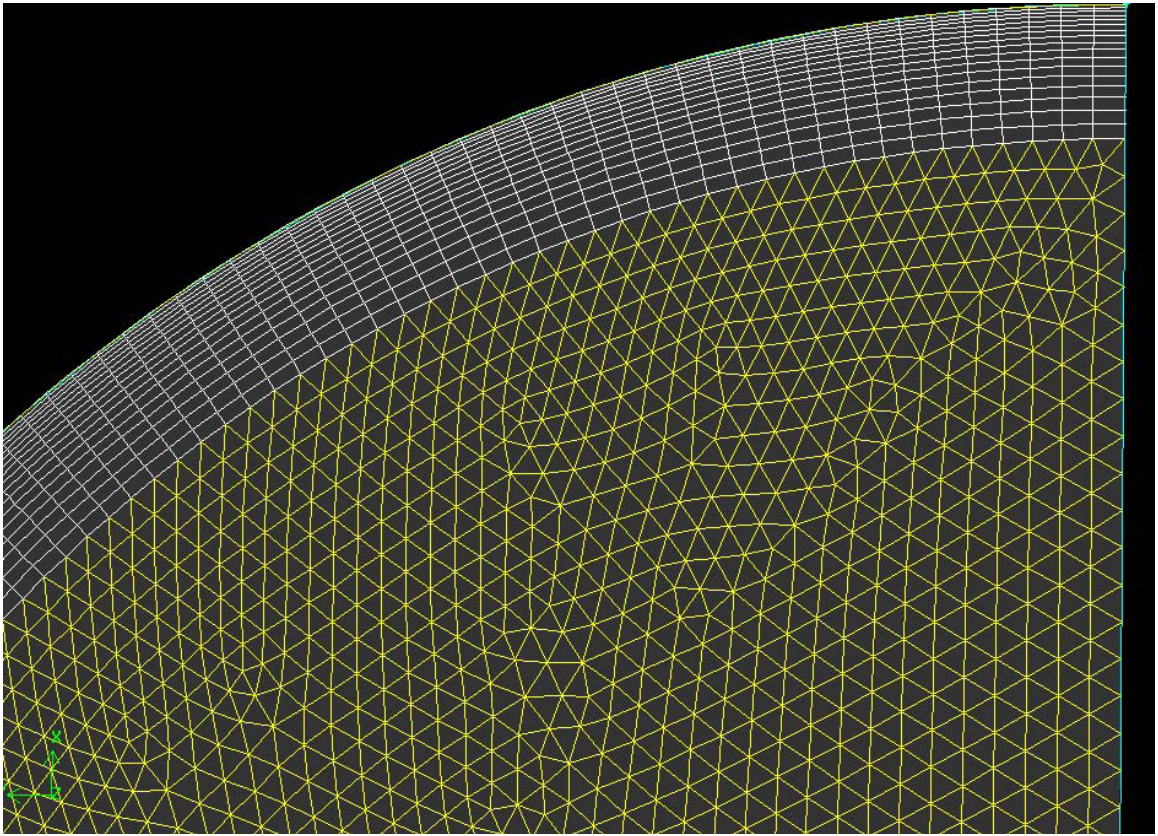


Figure 3.5 Magnified view of part of the adopted hybrid mesh

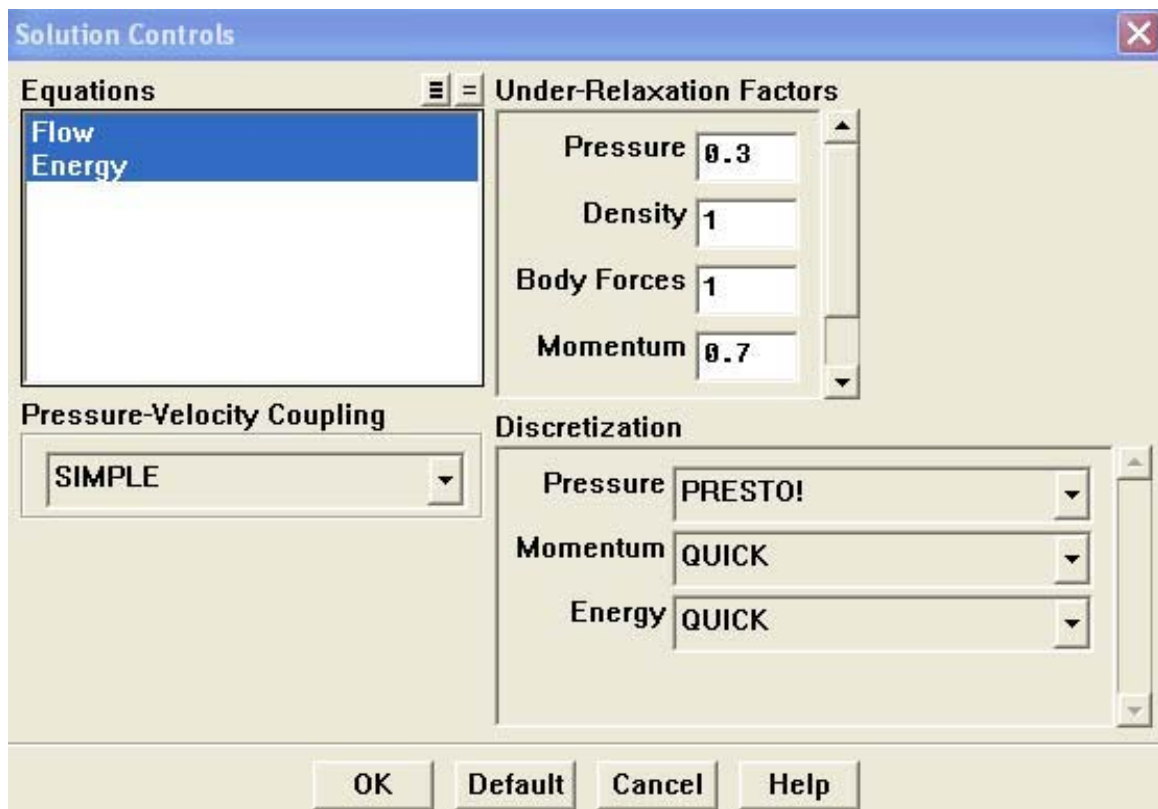


Figure 3.6 Solution controls in FLUENT

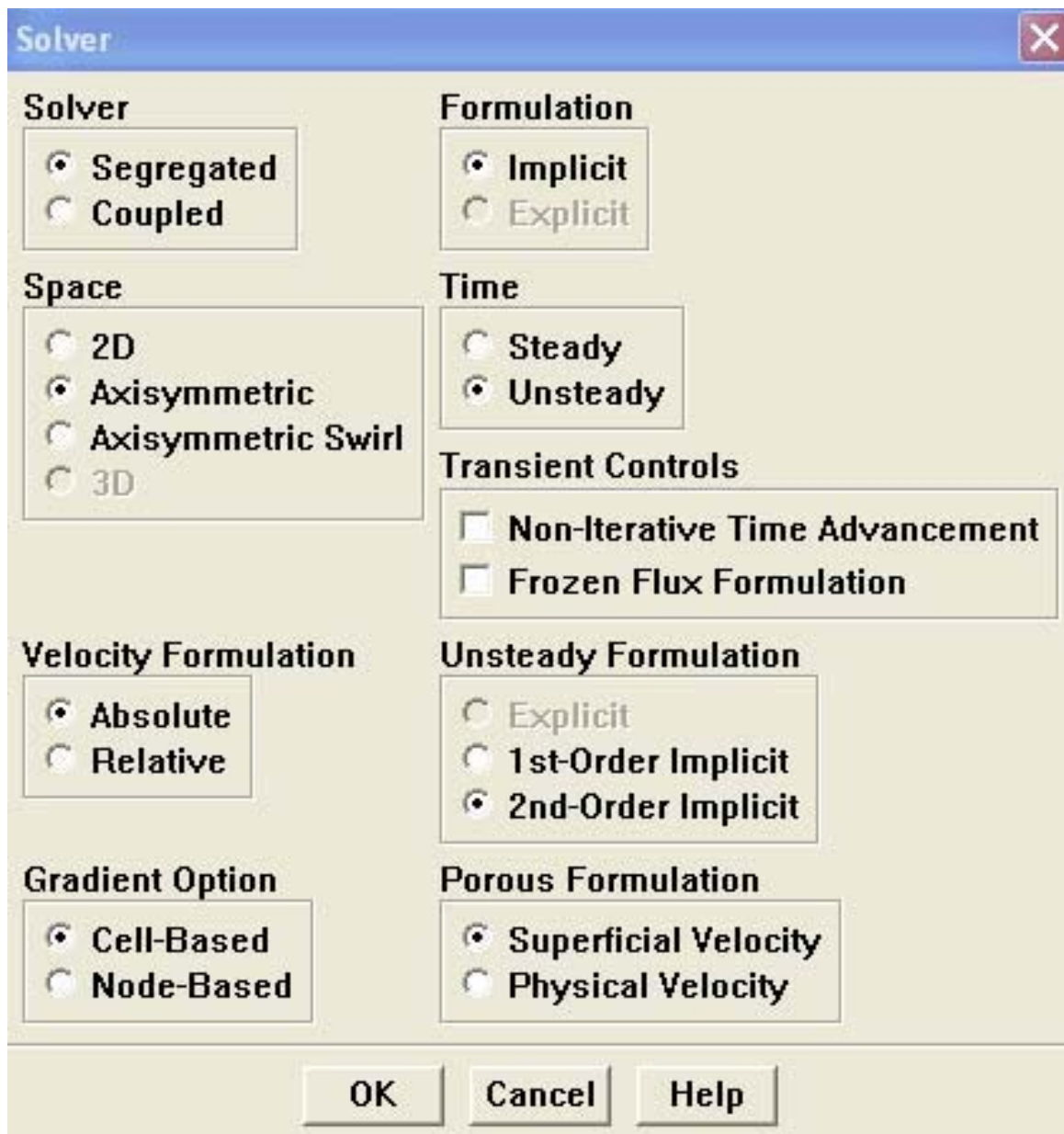


Figure 3.7 Solver settings in FLUENT

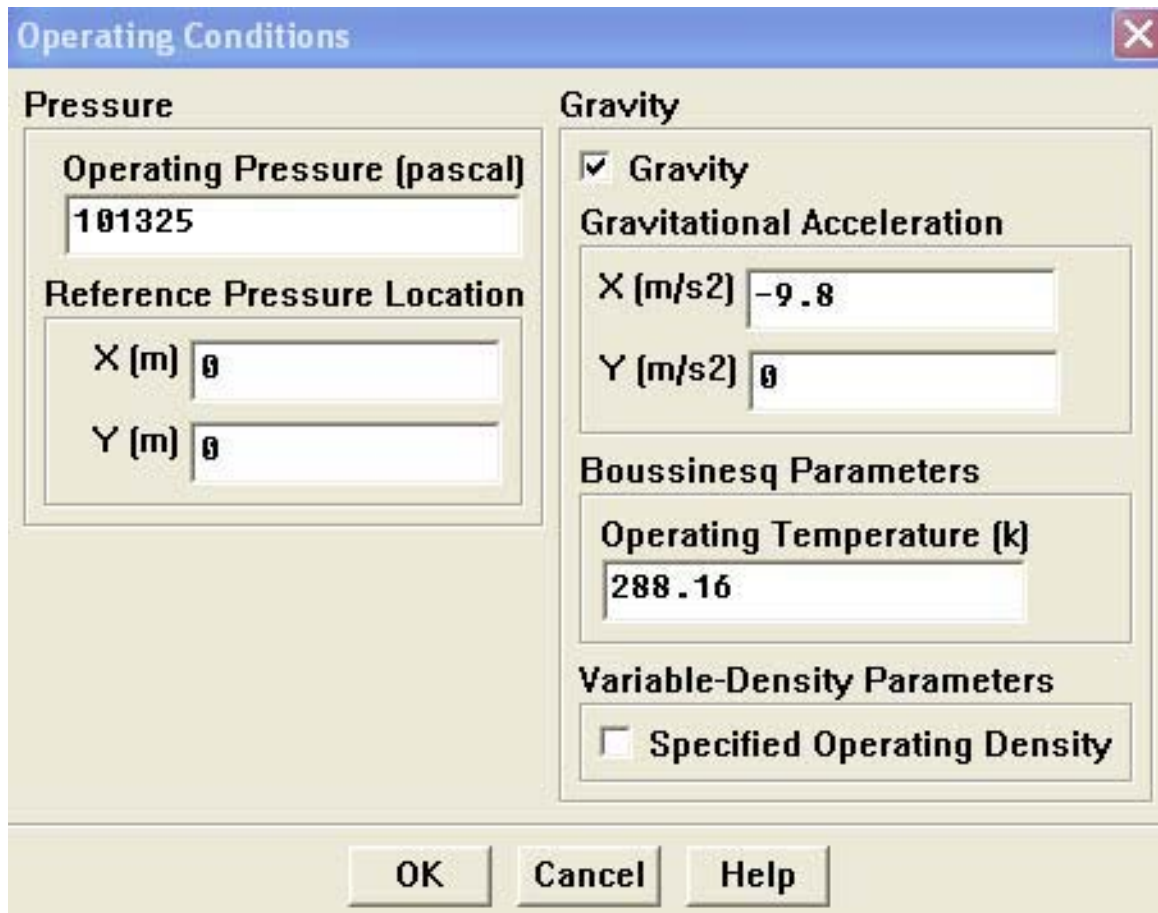


Figure 3.8 Operating conditions in FLUENT

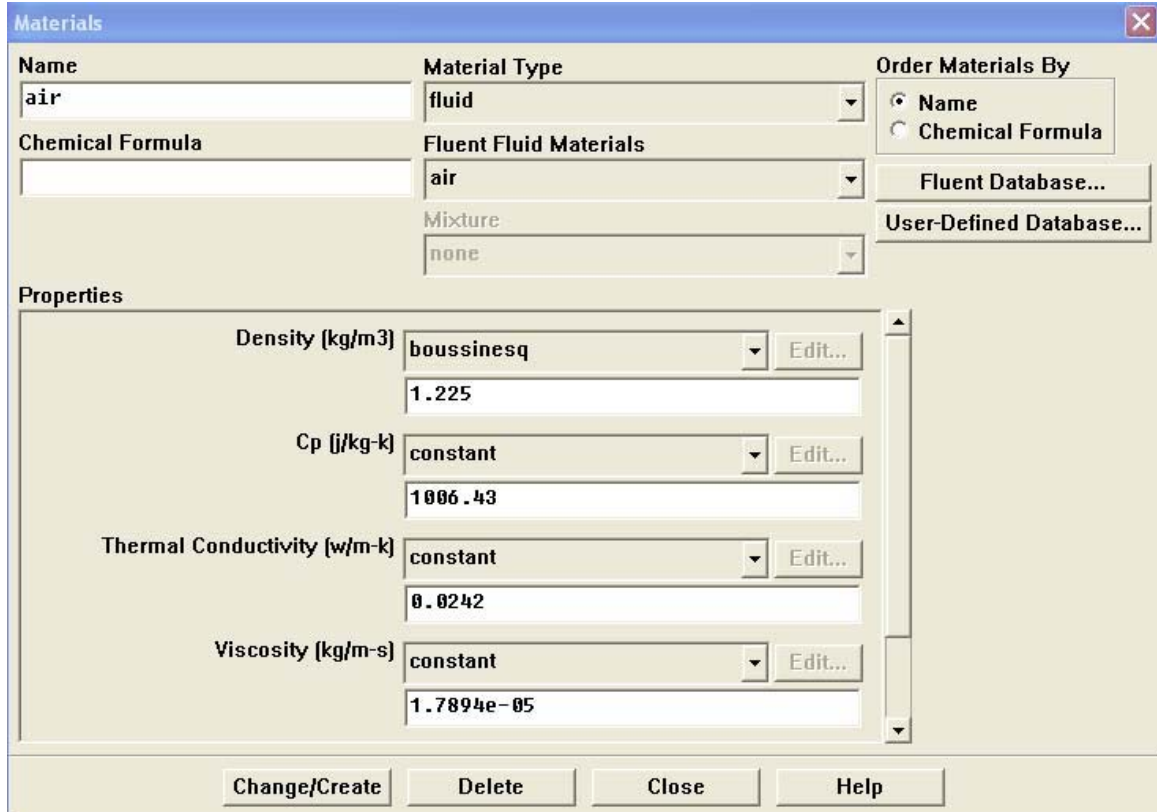


Figure 3.9 Fluid properties in FLUENT

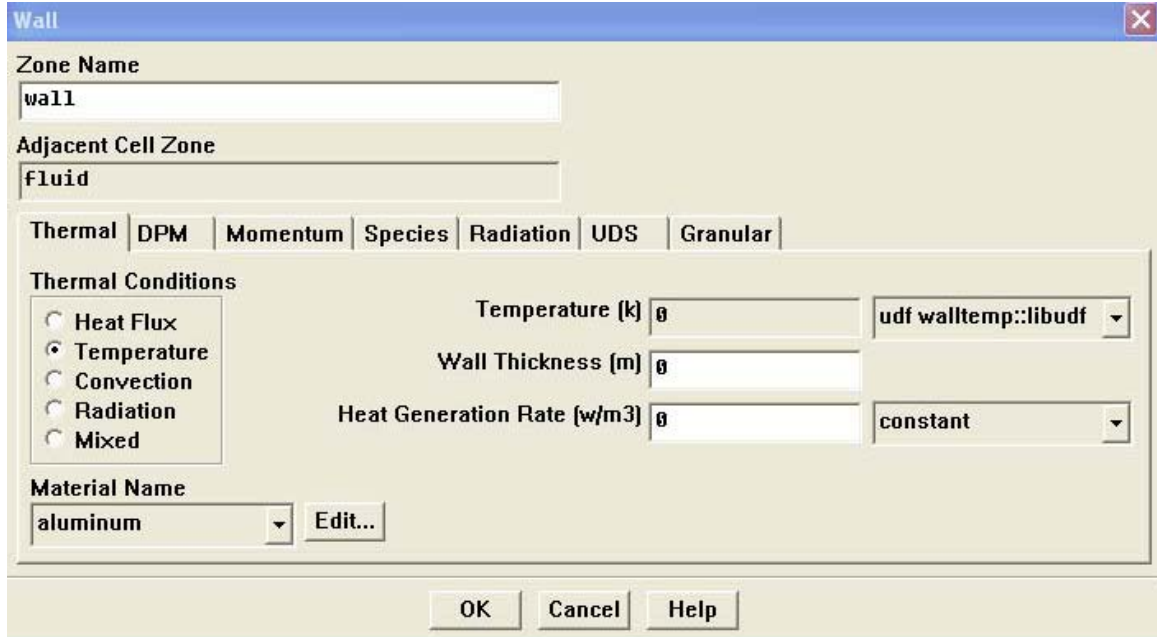


Figure 3.10 Thermal boundary conditions in FLUENT supplied by a user-defined function (UDF)

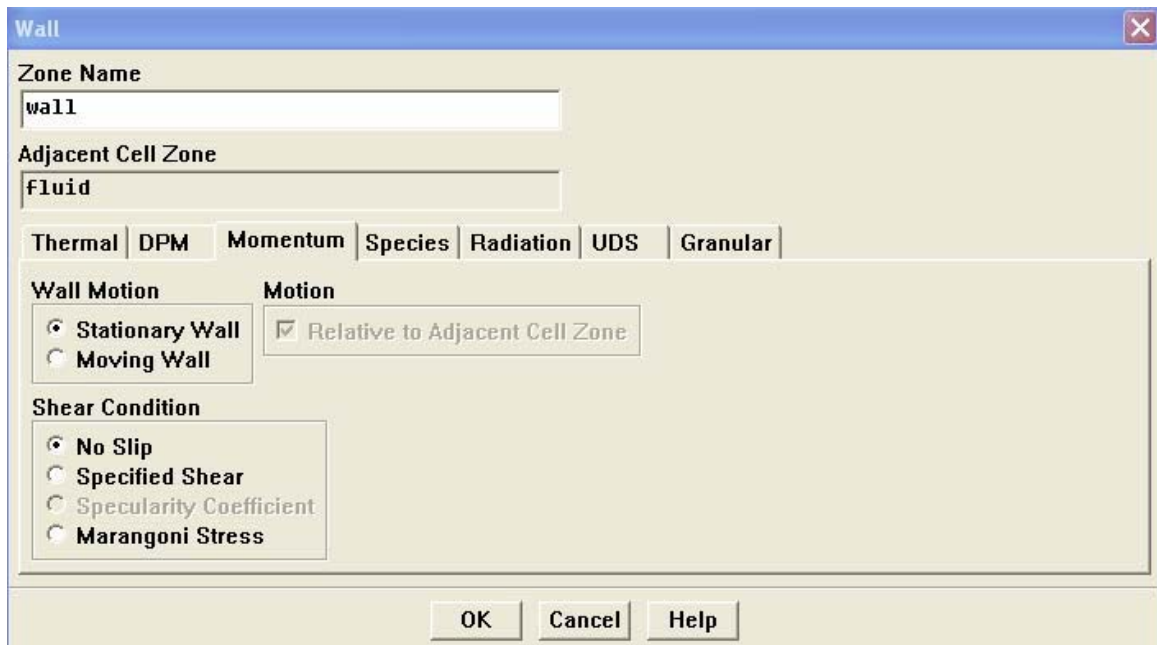


Figure 3.11 Momentum boundary conditions in FLUENT

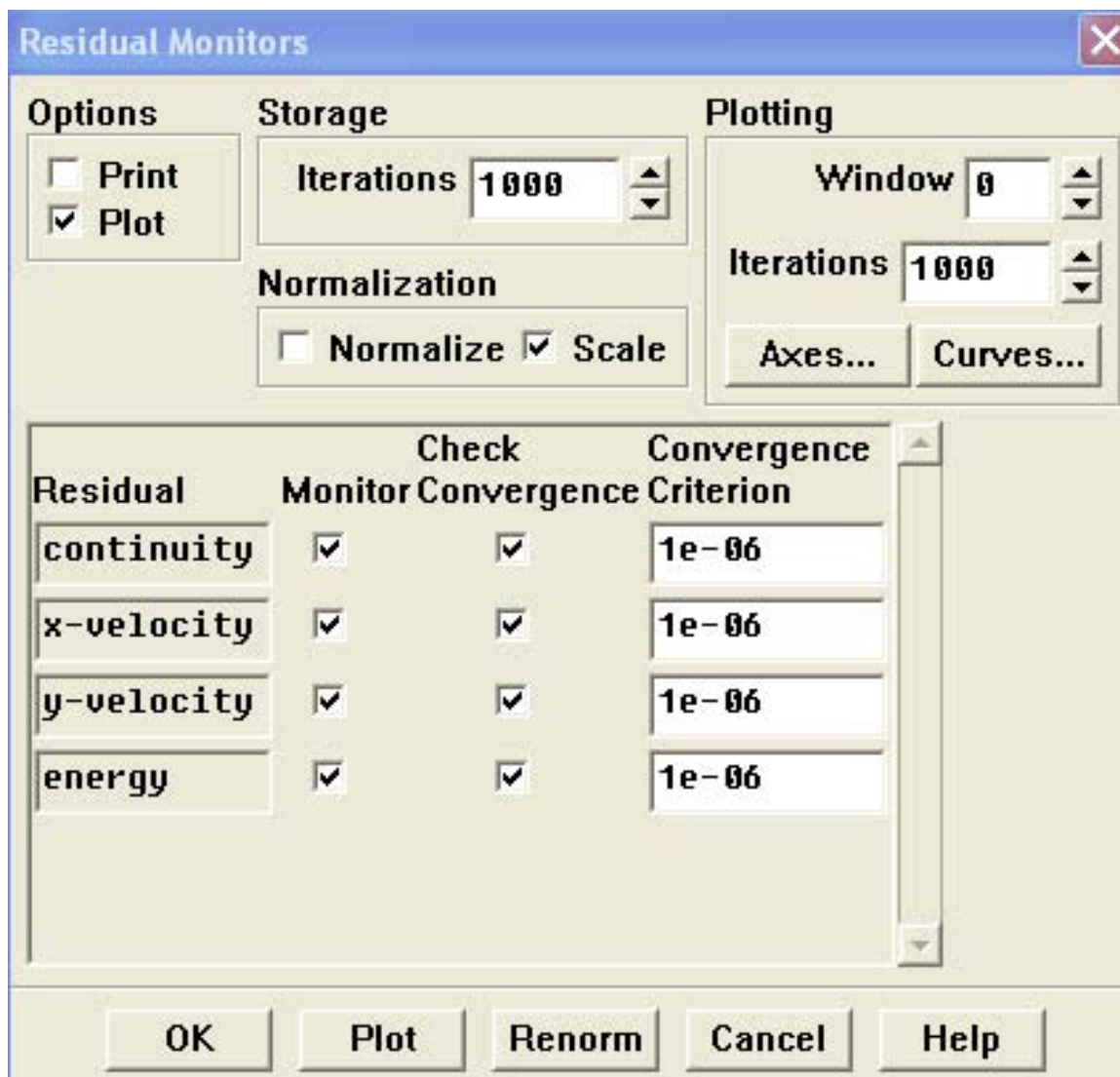


Figure 3.12 Residual monitors in FLUENT

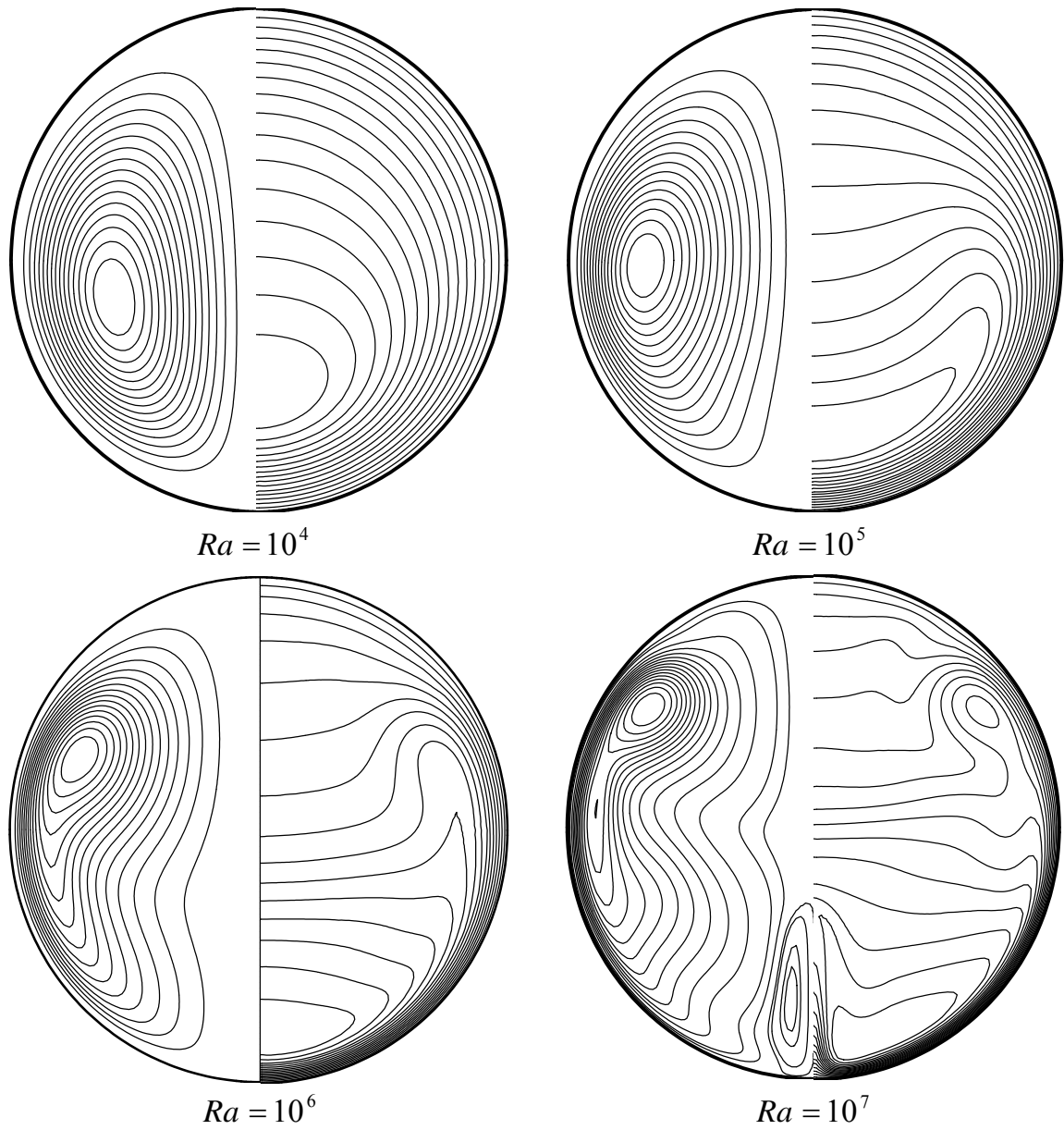


Figure 3.13 Pseudosteady-state streamline patterns (left half) and corresponding temperature contours (right half) for cases with no baffles ($Ra = 10^4$, 10^5 , 10^6 and 10^7)

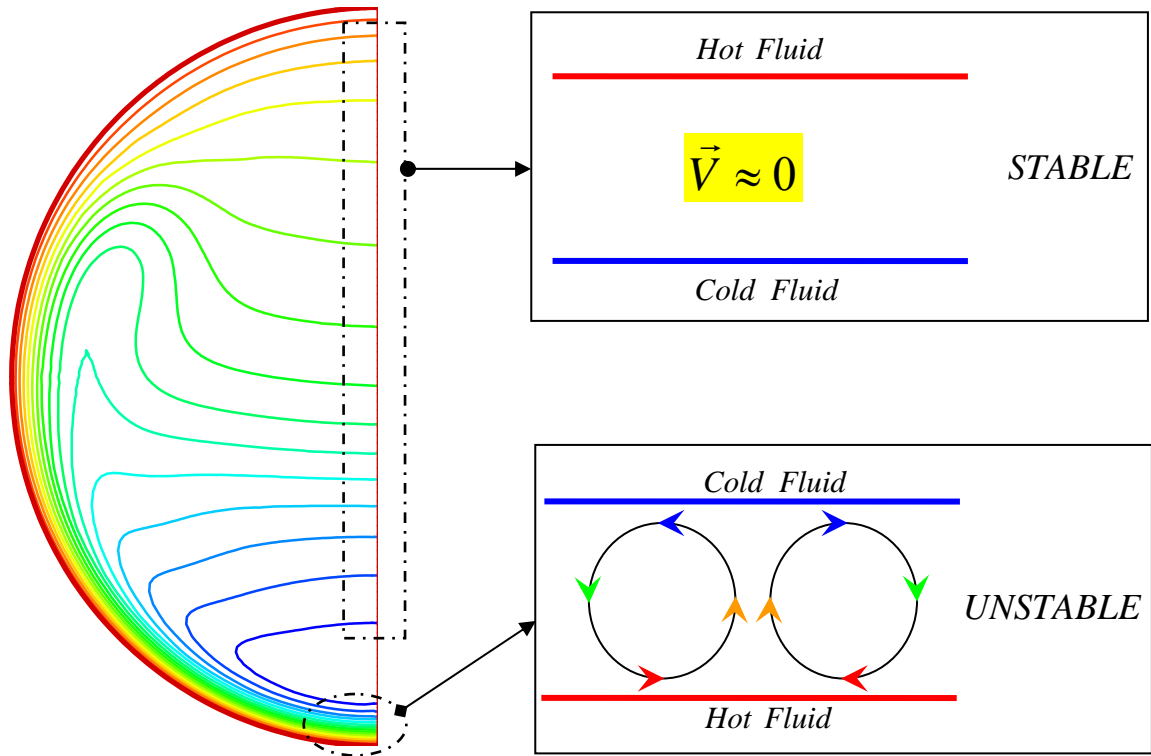


Figure 3.14 Thermally stable and unstable structures

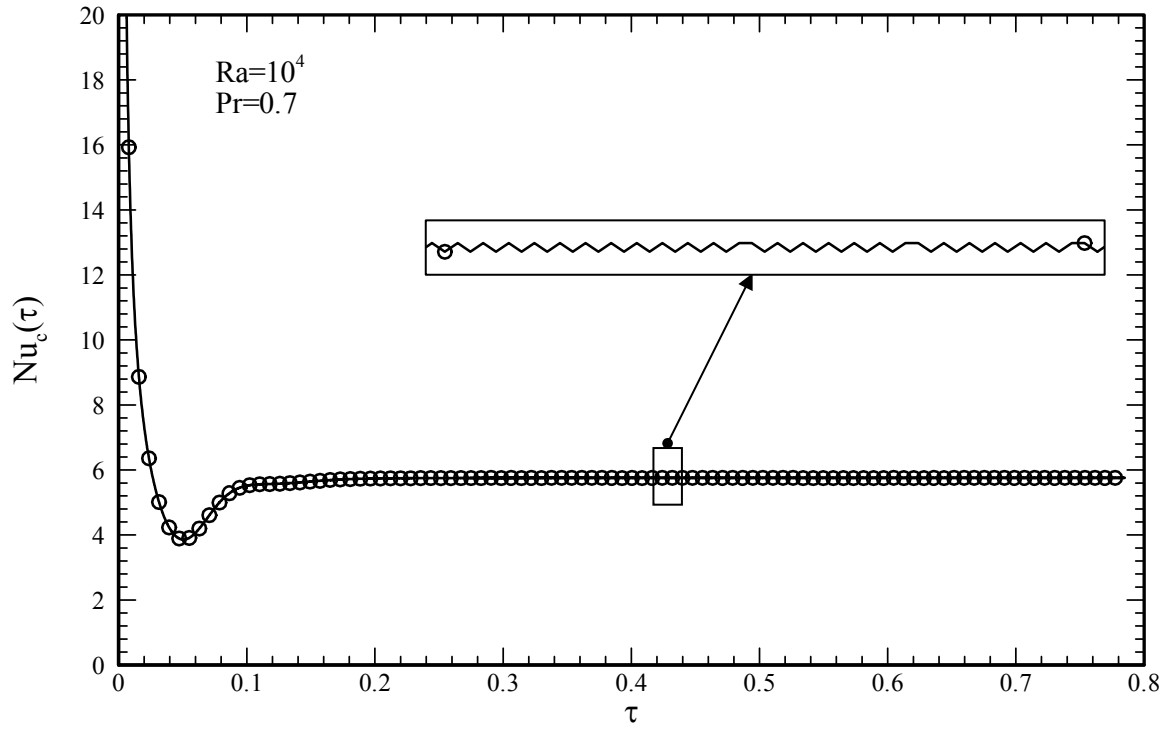


Figure 3.15 Instantaneous Nusselt number as a function of dimensionless time for $Ra=10^4$ with no baffle

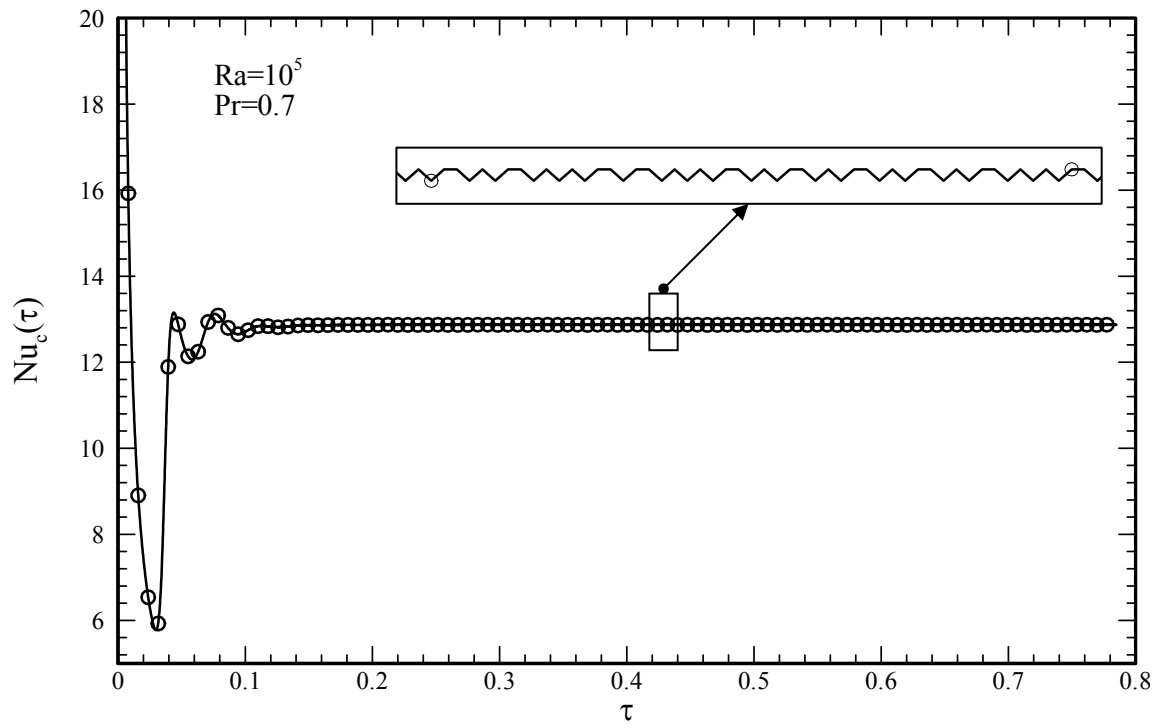


Figure 3.16 Instantaneous Nusselt number as a function of dimensionless time for $Ra=10^5$ with no baffle

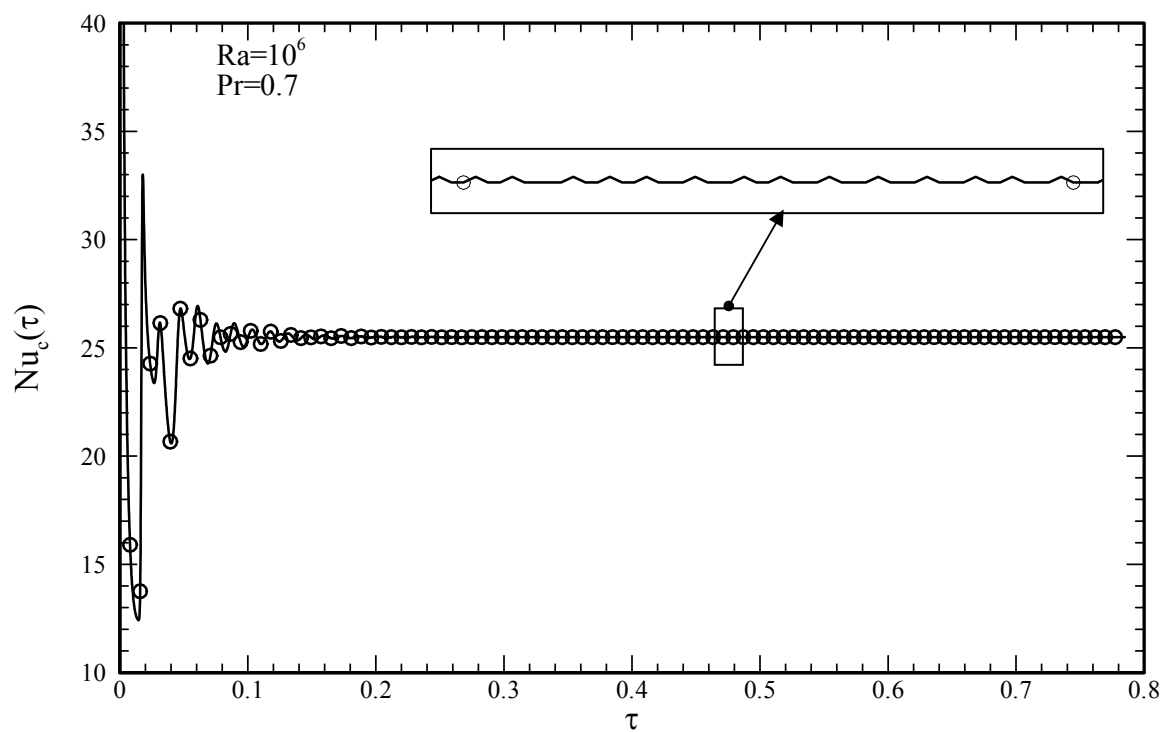


Figure 3.17 Instantaneous Nusselt number as a function of dimensionless time for $Ra=10^6$ with no baffle

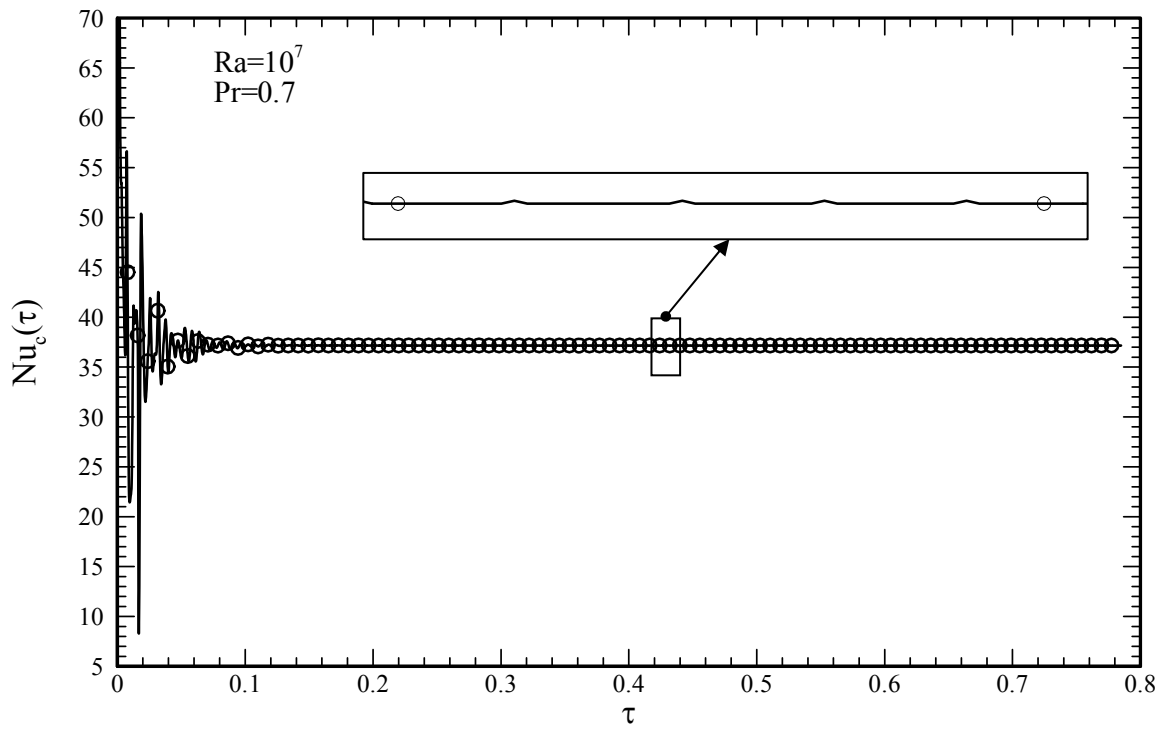


Figure 3.18 Instantaneous Nusselt number as a function of dimensionless time for $Ra=10^7$ with no baffle

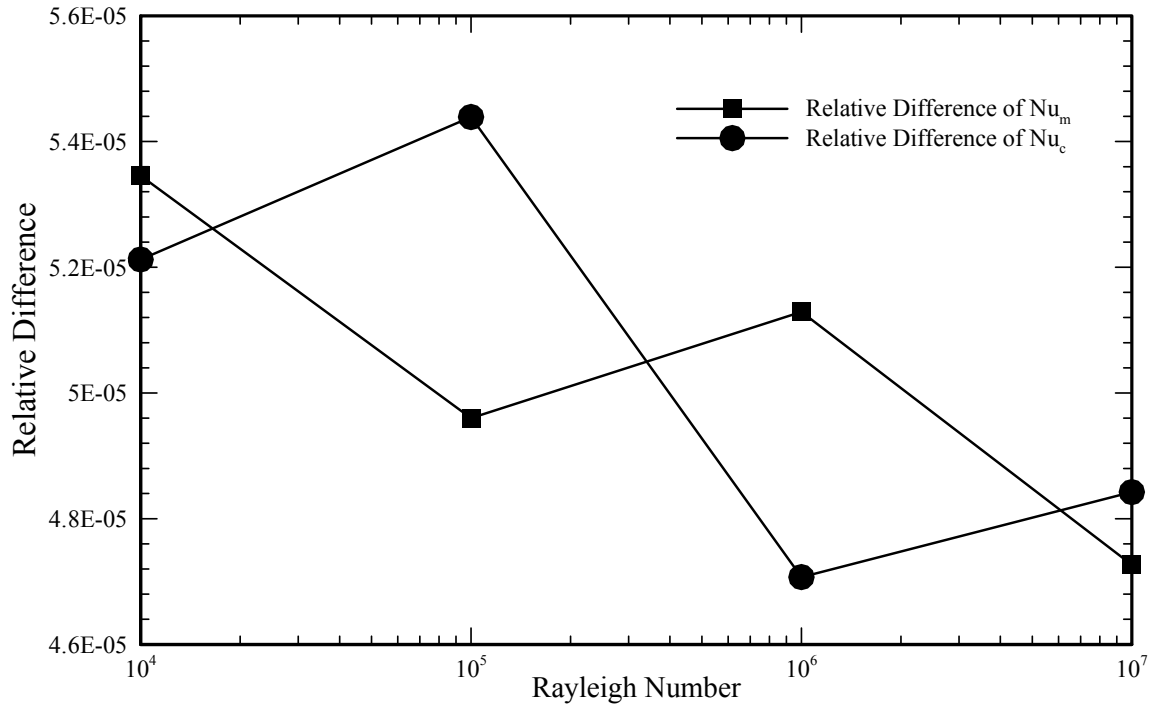


Figure 3.19 Relative differences of the Nusselt numbers between two different approaches

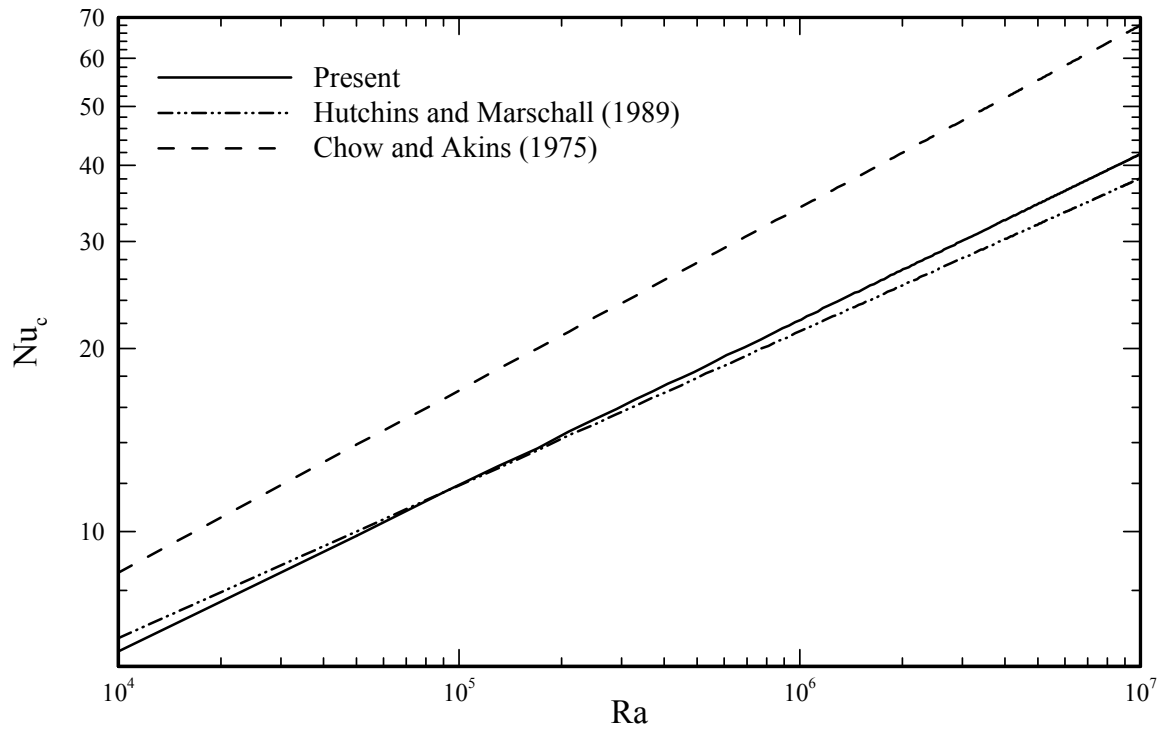


Figure 3.20 Nusselt number (Nu_c) correlations

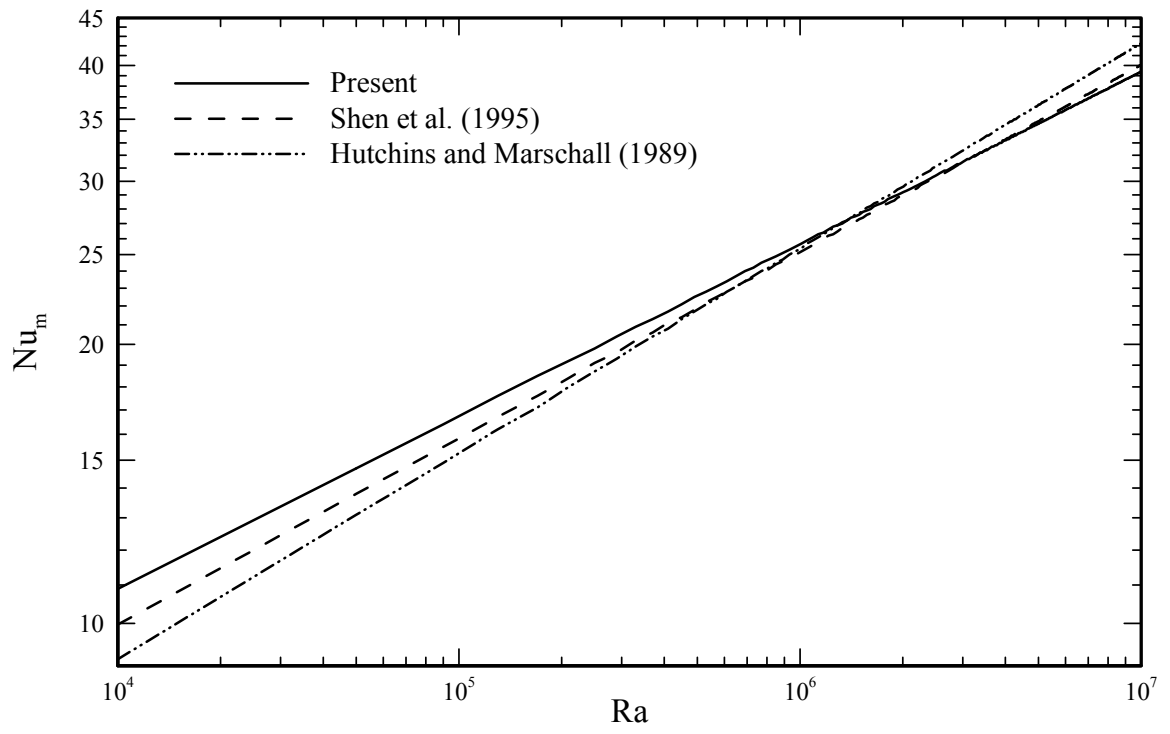


Figure 3.21 Nusselt number (Nu_m) correlations

CHAPTER 4 EFFECT OF AN INSULATED BAFFLE ON PSEUDOSTEADY- STATE NATURAL CONVECTION INSIDE SPHERICAL CONTAINERS

Pseudosteady-state natural convection inside spherical containers has been studied using a computational fluid dynamic package (FLUENT) in Chapter 3. The phenomenon associated with this problem has been widely studied over several decades in relation to transport and storage of liquefied natural gas (LNG). During these operations, it is desired that convection be reduced, whereas in other applications, enhancement of convection may be sought. Detailed knowledge related to control of heat transfer and management of the flow field due to natural convection inside spherical containers is still not available. At the same time, interest in such knowledge is increasing due to its relevance to numerous engineering applications.

Pseudosteady-state natural convection inside spherical containers is an appropriate model to investigate the effect of a baffle inside a container on flow field and heat transfer. Due to the relatively complicated geometry, it is impossible to get an analytical solution of the governing equations. Alternately, conducting proper numerical simulation is a good way to study the effect of a baffle on the flow and thermal fields. The objective of this Chapter is to investigate how a perpendicular-to-wall insulated thin baffle modifies the flow field as well as heat transfer. Parametric studies were performed for a Prandtl number of 0.7. For Rayleigh numbers of 10^4 , 10^5 , 10^6 and 10^7 , baffles with

3 lengths positioned at 5 different locations were investigated. In effect, a parametric study involving 60 cases was performed.

4.1 Mathematical Formulation for the Pseudosteady-State Natural Convection inside Spherical Containers with a Thin Insulated Baffle

A thin insulated baffle with length (l) is attached on the inside wall of a spherical container at polar angle (θ_b). It is positioned along the radial direction and points to the center. A schematic diagram of the posed problem is illustrated in Figure 4.1, in which a typical computational mesh is also shown on the left half. As for mathematical formulation for this problem, the presence of a thin insulated baffle introduces an extra boundary condition, while the modeling assumptions are same as Chapter 3.

4.1.1 Governing Equations and Boundary/Initial Conditions

Further analysis was performed on the basis of Chapter 3 by adding a thin insulated baffle. The governing equations are same as those stated in Chapter 3 (Equations 3.1-3.5) and are not repeated here. Concerning the orientation of the baffle, a 3-D schematic drawing is shown in Figure 4.2. The thickness of the insulated baffle is exaggerated and in reality the baffle is assumed to be very thin. Therefore, it can not contribute any heat flux to the fluid in the spherical container.

The no-slip boundary condition is applied on the wall of the sphere and the two sides of baffle, i.e.:

$$V_{\theta}^* = V_r^* = 0. \tag{4.1}$$

The driving force of natural convection is a constant temperature difference between the wall and center:

$$T_w^*(\tau) = T_c^*(\tau) + 1 \quad \text{for } \tau \geq 0. \quad (4.2)$$

On the symmetry axis ($\theta = 0$ and π):

$$V_\theta^* = \frac{\partial V_r^*}{\partial \theta} = \frac{\partial T^*}{\partial \theta} = 0. \quad (4.3)$$

On both sides of the thin insulated baffle ($(1-2L) \leq r^* < 1$ and $\theta = \theta_b$) with $L = \frac{l}{D}$:

$$\frac{\partial T^*}{\partial \theta} = 0. \quad (4.4)$$

The governing equations are characterized by the Rayleigh and Prandtl numbers, dimensionless baffle length (L) and position (θ_b). Previous work has shown that the Prandtl number has negligible effect on the numerical solution within the 0.7-8 range. Therefore, the Prandtl number is not treated as a variable but a constant that is equal to 0.7. Various Rayleigh numbers are investigated for different baffle parameters (L and θ_b).

4.1.2 Computational Details

Similar to the cases with no baffles, strong convective heat transfer is expected next to the wall of the container due to steep temperature gradients there. The flow and thermal fields next to the baffle are also expected to be highly perturbed. Specific grid generation information for the “boundary layer” mesh can be found in Chapter 3 and is not repeated here. For cases with baffles ($L > 0.04$), the segment of the baffle outside the “boundary layer” mesh was discretized with about 50 or less nodes. Then, the “interior”

grid was generated using an unstructured mesh. In effect, the number of cells for cases with baffles is higher than 10,222 that was utilized in Chapter 3. For baffles with different lengths and locations, the total number of cells varies between 10,476 and 13,868. Schematic diagrams of the grid systems for a $L=0.25$ baffle at different locations are shown in Figure 4.3. Each grid system is very dense next to the inner wall of the container, whereas both sides of the baffle are also refined with a dense mesh.

The solutions of the governing equations were obtained following the same procedure outlined in Section 3.2.2 and the pertinent details are not repeated here. The governing equations were solved by combining the commercial codes GAMBIT (version 2.2.30) and FLUENT (version 6.2.16). All the computations (60 cases) were performed on a Cray XD1 supercomputer of the Alabama Supercomputer Authority (Huntsville, Alabama).

4.1.3 Code Validation

Code verification and validation should be performed to provide confidence in the accuracy of numerical simulation. The code verification procedure is omitted due to the use of commercial CFD package (FLUENT) which has been verified repeatedly by others. The code validation procedure of pseudosteady-state natural convection inside spherical containers without baffles is discussed in detail in Chapter 3. Mathematically, the presence of a thin insulated baffle introduces an extra boundary condition in the problem formulation, while the governing equations are the same as the case without a baffle. Therefore, it is considered that the code validation reported in Chapter 3 has provided enough confidence in the appropriateness of the adopted model for the

pseudosteady-state natural convection inside spherical containers with insulated thin baffles.

4.2 Grid and Time Step Size Independence Study

The accuracy of a numerical solution is highly dependent on both the adopted grid density over the physical domain and the proper choice of the time step size. Numerical solutions of the pseudosteady-state natural convection within spheres have been presented by Hutchins and Marschall (1989) and Shen et al. (1995). However, a detailed study on grid and time step size sensitivity was not reported. Considering different geometries due to the presence of a baffle and the dynamic strength of convection in the system, the specific case with $L=0.25$ and $\theta_b = \frac{\pi}{2}$ for an insulated thin baffle for the Rayleigh number of 10^7 is selected for the sensitivity test. The schematic geometry employed for the grid independence study is illustrated in Figure 4.3.c. Values of the time-averaged Nu_m and Nu_c are selected as representative quantities to determine the accuracy of the numerical solution. It was already indicated in Chapter 3 that this case with no baffle does exhibit flow patterns suggestive of a thermally unstable fluid layer at the bottom of the sphere. The time-averaged Nusselt number after a long time duration (2,000 time steps with $\Delta t = 2$ seconds, that is equivalent to dimensionless time period 0.314062213) is observed to be almost constant. The oscillating strength of a time-varying dynamic flow can be characterized by the Root Mean Square (RMS) of a monitored quantity. The grid spacing and time step size are two independent variables, thus these two studies can not be carried out at the same time. The grid size independence is tested first, while the time step size is fixed to 2 seconds

($\Delta\tau = 1.57 \times 10^{-4}$). The effects of the spacing of the first row of the “boundary layer” mesh, number of nodes on the baffle and the density of the “interior” nodes are studied. For convenience, a parameter referred as the “number of cells” is utilized to describe the overall grid density. The dependence of the time-averaged Nusselt numbers (Nu_m and Nu_c) on the overall grid density are illustrated in Figures 4.4 and 4.5, respectively. Note that the time-averaged Nusselt number values are presented along with the RMS values. The tabulated values of these Nusselt numbers are also presented in Table 4.1. It is observed that the time-averaged Nusselt number values are nearly identical when the number of cells is greater than 10^4 . Taking the accuracy of the solution and the computational time into account, the grid system with 13,868 cells is considered as a “proper” grid system. All the other grid systems were created based on the parameters of this “proper” mesh.

Table 4.1 Dependence of the time-averaged and RMS values of the Nusselt numbers on the number of cells for an insulated case with $Ra=10^7$, $Pr=0.7$, $L=0.25$, $\theta_b = 90^\circ$ and

$$\Delta\tau = 1.57 \times 10^{-4}$$

Number of Cells	Nu_c	$RMS _{Nu_c}$	Nu_m	$RMS _{Nu_m}$
108	21.2572	0.000932596	26.9184	0.001177357
318	25.3077	1.13378496	38.32	0.701256
962	31.0297	3.84147686	44.4273	2.03921307
2,084	31.6797	6.19338135	46.1072	4.25569456
5,200	29.1629	6.52374073	40.7615	6.2120526
6,790	28.7735	6.2438495	39.5513	6.16209254
8,972	28.7477	6.39923802	40.4279	6.28653845
9,500	28.6351	6.52593929	40.3671	6.41029548
10,998	28.5143	6.35298604	40.297	6.3225993
13,868	29.0071	6.671633	40.7759	6.49560087
15,618	28.5983	6.40887903	40.7881	6.12637262
23,584	27.8505	5.737203	40.7732	5.5655418
29,218	28.9628	6.7193696	40.7989	6.51966422
35,744	28.8631	6.73376123	40.7489	6.54019845

The grid and time step size independence tests for the pseudosteady-state natural convection inside spherical containers without baffles in Chapter 3 were not performed separately, and those grid systems were generated using the same parameters mentioned in this Section.

Once the proper mesh was selected, the sensitivity of the solution on the time step size can be studied. The dependence of the time-averaged Nusselt numbers (Nu_m and Nu_c) on the time step size for the same insulated thin baffle discussed above are shown in Figures 4.6 and 4.7, respectively. The tabulated data is given in Table 4.2. The predicted Nusselt numbers exhibit little sensitivity when the time step size is less than 6 seconds ($\Delta\tau = 4.71 \times 10^{-4}$). Considering both the accuracy of the solution and the

computational time, a time step size of 2 seconds ($\Delta\tau = 1.57 \times 10^{-4}$) is selected as a proper time step size for all 60 cases with thin insulated baffles.

Table 4.2 Dependence of the time-averaged and RMS values of the Nusselt numbers on the time step size for an insulated case with $Ra=10^7$, $Pr=0.7$, $L=0.25$, $\theta_b = 90^\circ$ and 13,868 cells

Δt (s)	Nu_c	$RMS _{Nu_c}$	Nu_m	$RMS _{Nu_m}$
0.1	28.7095	6.5256694	40.7459	5.8307383
0.2	28.4083	6.1930094	40.7709	5.5611508
1	28.9655	6.719996	40.7783	6.2472356
2	29.0071	6.67163	40.7759	6.4956
3	28.3995	6.1655315	40.834	6.0475154
5	28.928	6.1819136	40.9624	6.775181
7	28.0715	5.1735775	40.7907	6.3919027
8	26.2092	3.8081968	40.4022	4.8886662
10	25.2688	2.7745142	40.1154	3.8831707
15	23.9587	1.5453362	39.5984	2.5580566
30	22.3371	0.4668454	38.9356	1.0901968

4.3 Results and Discussion

Pseudosteady-state fluid flow field streamlines and temperature contours are presented for 45 cases for fixed Rayleigh numbers (10^4 , 10^5 and 10^6). Through examination of the pertinent information for these cases, one will be able to understand how the presence of a thin insulated baffle modifies the flow and thermal fields. The criterion used to declare that the pseudosteady-state has been achieved will be discussed in detail later. In short, once the time-averaged Nusselt numbers (Nu_m and Nu_c) do not change with time, the pseudosteady-state is achieved. For the Rayleigh number equal to 10^7 , strong oscillations occurred except the case with dimensionless baffle length of 0.25

located at $\theta_b = 150^\circ$. Therefore, the time-dependent flow field streamlines and temperature contours for $Ra = 10^7$ are plotted and discussed separately. The dependence of the time-averaged Nusselt numbers (Nu_m and Nu_c) for all 60 cases are given.

4.3.1 Pseudosteady-State Fluid Flow and Thermal Fields for $Ra = 10^4$, 10^5 and 10^6

The composite diagrams of the streamlines and temperature contours under the pseudosteady-state condition for three baffles with lengths ($L = 0.05, 0.1$ and 0.25) placed at various polar angle locations ($\theta_b = 30^\circ, 60^\circ, 90^\circ, 120^\circ$ and 150°) for a Rayleigh number of 10^4 are presented in Figure 4.8. Diagrams in each row correspond to baffles of various lengths positioned at a fixed location, whereas for each column the effects of a baffle with a fixed length at various positions are given. By comparing the streamline patterns and temperature fields in this figure to the limiting case of no baffle in Figure 3.13 for the same Ra , the effect of a thin insulated baffle can be elucidated. Focusing on the left column of Figure 4.8, it is clear that the presence of the shortest baffle ($L = 0.05$) does not alter the flow and thermal fields significantly, regardless of the angular position of the baffle. The distortions are restricted to minor alteration of the streamlines next to the short baffles, whereas the temperature contours are generally unchanged with minor radial shifting of the contours next to the adiabatic baffle. For the cases corresponding to the $L = 0.1$ baffle that are shown in the middle column, the modifications to the flow and thermal fields are a bit more marked than the cases with the shortest baffle, however the changes are still observed to be next to the baffle. In contrast, marked changes to the flow field are observed in the right column of Figure 4.8 that correspond to the longest baffle ($L = 0.25$), specially for the cases when the baffle is located at $\theta_b = 60^\circ, 90^\circ$ and

120°. For these cases, two distinct recirculating vortices are observed on both sides of the baffle. These vortices rotate in the clockwise (CW) direction lifting heated fluid next to the wall to a higher elevation and bringing down colder fluid. The temperature fields have also been affected by the longer length of the baffle that directly perturbs the flow field, however the general pseudo-concentric ring contour patterns are preserved. It can clearly be stated that due to the adiabatic nature of the baffle, this structure does not directly participate in perturbation of the thermal field. The presence of the baffle appears to be generally directed at modifying the flow paths for $Ra=10^4$ cases.

For the Rayleigh number of 10^5 , streamlines patterns and temperature contours for three baffles with lengths ($L = 0.05, 0.1$ and 0.25) placed at various locations ($\theta_b = 30^\circ, 60^\circ, 90^\circ, 120^\circ$ and 150°) are shown in Figure 4.9. Diagrams are plotted going from left column to right column with the dimensionless baffle length increasing from 0.05 to 0.25. Comparing the streamline patterns and temperature fields on the left column of Figure 4.9 ($L = 0.05$) with the case of no baffle (Figure 3.13), the presence of the shortest thin insulated baffle ($L=0.05$) modifies the thermal fields to some extent for various angular positions of the baffle. The flow field modifications are not very significant that is similar to the cases in Figure 4.8 ($Ra=10^4$), while modification of the thermal fields can be observed easily. In general, the flow and thermal fields exhibit features similar to those discussed above for Figure 4.8.

Streamlines and temperature contours for three baffles with lengths ($L = 0.05, 0.1$ and 0.25) placed at various locations ($\theta_b = 30^\circ, 60^\circ, 90^\circ, 120^\circ$ and 150°) for a Rayleigh number of 10^6 are presented in Figure 4.10. Comparing the streamline patterns and temperature fields on the left column of Figure 4.10 ($L = 0.05$) with the case of no baffle

(Figure 3.13), the presence of the shortest baffle modifies the flow and thermal fields to some extent for various angular positions of the baffle. The flow modifications are confined to streamlines next to the short baffle through its interaction with the eye of the vortex that is closer to the wall compared to similar cases in Figures 4.8 and 4.9. For some positions of the short baffle, two eyes within the CW rotating vortex are observed. As for the effect of the shortest baffle on the temperature contours, the changes are more pronounced in comparison to similar cases of Figures 4.8 and 4.9, however they are still localized in the vicinity of the baffle. The flow modifications are more noticeable for a $L = 0.1$ baffle that are shown in the middle column of Figure 4.10, particularly when the baffle is located at $\theta_b = 60^\circ, 90^\circ$ and 120° . For these cases, the double CW rotating vortex structure is further complicated by appearance of a smaller counter CW rotating vortex that is located very near the open end of the baffle. This vortex does not draw energy from the adiabatic thin baffle. Therefore, it is the lifting of the hot fluid below the baffle into the zone above the baffle that is creating this vortex. One can also note that the multi-vortex structure can clearly rearrange the thermal field when compared to the case of the shortest baffle that exhibited constant-temperature stratified layers in the vicinity of the symmetry axis of the sphere. In assessing the effect of the long baffle on the flow fields in the right column of Figure 4.10, modifications that are very similar to the cases of $Ra = 10^4$ and 10^5 in Figures 4.8 and 4.9 are observed. In general, two CW rotating vortices are clearly observed for the cases when the baffle is located at $\theta_b = 60^\circ, 90^\circ, 120^\circ$ and 150° . As for the thermal field, when the baffle is positioned such that $\theta_b \leq 90^\circ$, the space above the baffle is clearly composed of stable stratified constant-temperature layers. This suggests that the flow within the top portion is not strong and

conduction dominates, whereas the thermal field in the lower half is dominated by natural convection. As a general statement, note that when the long baffle is positioned in the bottom half including the mid-plane, the thermal field is clearly divided into two zones. Both zones have areas of intense wall heat transfer that are located at the bottom of the sphere and angular positions $\theta \approx \theta_b$, respectively. A portion of the top zone is a region of stable constant-temperature layers suggesting weak natural convection and dominance of heat diffusion, whereas the bottom zone is where natural convection is very prominent.

The effects of the Rayleigh number (10^4 , 10^5 , 10^6 and 10^7) and baffle's position ($\theta_b = 30^\circ$, 90° and 150°) on streamlines and temperature contours for the case of the longest baffle ($L = 0.25$) are presented in Figure 4.11. With the baffle positioned near the top at $\theta_b = 30^\circ$ (left column), the increase of the Rayleigh number brings about stronger convection and fluid flow within the CW rotating vortex as indicated by the denser packing of the streamlines next to the surface. This is accompanied by lifting of the eye of the vortex and its migration outward. At the highest Ra number studied, a weak vortex is observed near the top within the cone, part of which is the baffle. Simultaneously, a CCW rotating vortex at the bottom that is driven by the thermally unstable stratified layer is still active. The temperature contours exhibit greater deviation from the concentric ring patterns as natural convection strengthens and diffusion is observed to be limited to the small space between the baffle and the symmetry axis. With the baffle located at $\theta_b = 90^\circ$ (middle column), two CW rotating vortices occupy the two hemispherical regions with the lower half of the sphere being the site of stronger convection. As the Ra number is raised, the stronger vortex is observed to penetrate into the top hemisphere and even a third counter-CW rotating vortex is created next to the free end of the baffle for $Ra=10^6$

and 10^7 . The top hemisphere is clearly stratified with stable constant-temperature layers occupying it, whereas the thermal field within the bottom hemisphere is heavily affected by the stronger rotating vortex that occupies it. The flow fields for the cases with the longest baffle positioned near the bottom at $\theta_b = 150^\circ$ (right column) exhibit many of the features with the baffle located at $\theta_b = 30^\circ$, but in reverse. A CW-rotating recirculating vortex that occupies the small space between the baffle and the symmetry line of the sphere is clearly observed. As for the temperature contours, the alterations appear to be generally confined to the region between the baffle and the symmetry axis. The remainder of the sphere appears to be generally unaffected by the presence of the longest baffle. The reader is reminded that the last row of Figure 4.11 with $Ra=10^7$ is a snapshot of the instantaneous flow and thermal fields. Detailed discussion of a typical case with $Ra=10^7$ is given in the next Section.

4.3.2 Time-Dependent Fluid Flow and Thermal Fields for $Ra=10^7$

In order to illustrate the unsteady nature of the flow, a representative case of $Ra=10^7$, $L=0.25$ and $\theta_b = 60^\circ$ was selected. The instantaneous composite diagrams of the streamlines and temperature contour fields for this case during a “cycle” are shown in Figures 4.12 (a)-(h). In order to aid the reader, a companion diagram showing the variation of the instantaneous area-averaged Nusselt number is also shown in Figure 4.13. The cyclic nature of the instantaneous Nusselt number is clearly shown and the instants at which the composite streamlines and temperature contours of Figure 4.12 were shown are marked by letters a-h. A dynamic flow field is observed within the cycle with distinct growth and decay of a multitude of vortices. The temperature gradients next to the wall

of the sphere and the baffle vary dramatically during the cycle and are clearly linked to the variation of the Nusselt number shown in Figure 4.13.

4.4 Nusselt Number Definitions and Other Parameters

It is necessary to present and explain the definitions of different parameters that are employed in the remainder of this Chapter. These include two definitions of the Nusselt number and stream function.

4.4.1 Definitions of the Nusselt Numbers

The Nusselt number represents the ratio of convection heat transfer to conduction heat transfer. Therefore, it is employed to evaluate the strength of the pseudosteady-state natural convection inside spherical containers with a thin insulated baffle. Based on the results presented so far, there is no doubt that the presence of a thin insulated baffle can dramatically change the flow field. However, the insulated baffle does not contribute any heat flux to the fluid within the spherical container. In the absence of heat addition from the baffle, it is logical that the presence of the baffle can lead to increased or reduced heat transfer from the surface of the sphere. For both of these possibilities, the effective heat transfer area is the container wall area that is exactly the same as the case without the baffle. The area-weighted heat flux expression is the same as the case without the baffle. The specific derivation can be found in Chapter 3.

The Nusselt numbers based on the temperature gradient at the wall are:

$$Nu_m(\tau) = \frac{I}{(T_w^* - T_m^*)} \int_0^\pi \frac{\partial T^*}{\partial r^*} \Big|_{r^*=1} \sin \theta d\theta, \quad (4.5)$$

$$Nu_c(\tau) = \int_0^\pi \frac{\partial T^*}{\partial r^*} \Big|_{r^*=1} \sin \theta \, d\theta. \quad (4.6)$$

The Nusselt numbers that are obtained by performing a lumped energy balance are:

$$Nu_m(\tau) = \frac{2}{3} \frac{1}{(T_w^* - T_m^*)} \frac{dT_m^*}{d\tau}, \quad (4.7)$$

$$Nu_c(\tau) = \frac{2}{3} \frac{dT_m^*}{d\tau}. \quad (4.8)$$

Note that a subscript “c” is used for one of the surface-averaged Nusselt numbers meaning that T_c (temperature at the center) is used in the ΔT expression. Similarly, subscript “m” is used for the other surface-averaged Nusselt number meaning that T_m (mean or bulk temperature) is used in the ΔT expression. The validity of these expressions were verified by comparing the “direct” output of FLUENT against post-processed “indirect” values.

4.4.2 Time-Averaged Nusselt Numbers

In general, the flow field is disturbed due to the presence of the insulated baffle and the Nusselt number fluctuates with time depending on the location of the baffle, its length and the Rayleigh number. Determining whether the pseudosteady-state natural convection inside a spherical container with a thin insulated baffle is reached is a critical factor for our analysis. For some cases, the fitting curve can be easily estimated due to the simple oscillating behavior of the Nusselt number (Figure 4.14 (a)), whereas for other cases a disorderly and random variation of the Nusselt number was recorded (Figure 4.14 (b)). A lengthy analysis can be performed to recover the frequency content of these time-dependent quantities. However, in view of our focus on the pseudosteady-state behavior

of this system, it was decided that time-averaging of the Nusselt numbers is sufficient for this investigation.

A straight line curve-fitting equation of the fluctuating Nusselt number can be employed to determine whether the statistical stationary pseudosteady-state natural convection inside the spherical container with a thin insulated baffle is reached. Let us focus on $Nu_m(\tau)$ first. The fitting straight line is assumed to be:

$$Nu_m(\tau) = a + b\tau, \quad (4.9)$$

where a and b are constants. The constant b is the slope of the straight line that will be equal zero after the system has reached the pseudosteady-state. In reality, for statistical stationary state the value of b can be employed quantitatively to evaluate whether the pseudosteady-state has been reached. If the coefficient b satisfies the requirement, then constant a is the time-averaged Nusselt number that is denoted by Nu_m .

Considering the statistical distribution error, the least-squares approach is utilized to determine values of coefficients a and b in the linear equation. The sum of the squares of the differences ($L(a,b)$) between the Nusselt number on the approximated line and the discrete Nusselt number is defined as:

$$L(a,b) = \sum_{i=k}^N \{[a + b\tau_i] - Nu_m(\tau_i)\}^2. \quad (4.10)$$

Upon minimizing the least-squares error $L(a,b)$:

$$\frac{\partial L(a,b)}{\partial a} = \frac{\partial L(a,b)}{\partial b} = 0, \quad (4.11)$$

the values of a and b can be found immediately by solving the simple set of linear equations (Equations 4.12 and 4.13).

$$(N - k + 1)a + \sum_{i=k}^N b\tau_i = \sum_{i=k}^N Nu_m(\tau_i), \quad (4.12)$$

$$\sum_{i=k}^N a\tau_i + \sum_{i=k}^N b\tau_i^2 = \sum_{i=k}^N \tau_i Nu_m(\tau_i). \quad (4.13)$$

For determining the time-averaged Nusselt number Nu_c , the details are the same and are not repeated here.

At this point, the judgment of whether the statistical stationary pseudosteady-state natural convection inside spherical container with a thin insulated baffle is reached can be achieved by inspecting the approximated line equation. **For all the cases studied, when b is less than 10^{-6} , it is considered that the statistical stationary pseudosteady-state natural convection inside spherical containers with a thin insulated baffle is reached.** For many cases, the slope b can even be as low as 10^{-10} , which indicates a nearly perfect statistical stationary state.

4.4.3 Strength of Fluctuations of the Nusselt Numbers

Another parameter should be defined to characterize the strength of the fluctuating Nusselt numbers. There are several ways for doing this, such as the amplitude and the Root Mean Square (RMS). The amplitude is a good choice that indicates the largest deviation of the fluctuating Nusselt number from the time-averaged value (Figure 4.15). Taking the statistical distribution into account, the Root Mean Square (RMS) may be employed to characterize the strength of fluctuations (Figure 4.16). The Root Mean Square for the oscillating Nusselt numbers can be defined as:

$$RMS |_{Nu_\zeta} = \sqrt{\frac{\sum_{i=1}^N (Nu_\zeta(\tau_i) - Nu_\zeta)^2}{N}}, \quad (4.14)$$

with $\zeta = c$ or m depending on the choice of the ΔT .

In order to make comparison among all the cases, the relative RMS for the Nusselt numbers can be defined as:

$$RMS |_{rNu_\zeta} = \frac{1}{Nu_\zeta} \sqrt{\frac{\sum_{i=1}^N (Nu_\zeta(\tau_i) - Nu_\zeta)^2}{N}}, \quad (4.15)$$

with $\zeta = c$ or m depending on the choice of the ΔT .

4.4.4 Stream Function

The difference between the maximum and minimum values of the stream function of the primary vortex can be used to characterize the strength of the flow field, while the Nusselt number is generally considered for characterization of the thermal field. In view of the effect of the flow on the thermal field, it is appropriate to study the stream function fields in relation to the observed heat transfer modifications due to the presence of a thin insulated baffle. The stream function can also be employed to monitor whether the pseudosteady-state natural convection inside a spherical container with a thin insulated baffle has attained the statistical stationary state. Defining the minimum stream function at the center of vortex as zero, the maximum stream function ψ_{\max} (value on the wall) can be taken as a characteristic quantity for the flow field.

The computational results indicate that with increase of the Rayleigh number, the flow becomes time-dependent. Similar to the Nusslet numbers, the stream function ψ_{\max} is not a constant value but exhibits a fluctuating behavior. Thus, the time-averaged stream function ψ_{\max} can be utilized.

For the 60 cases studied in this project, when tolerance of statistical stationary state is less than 10^{-6} , it is considered that the statistical stationary pseudosteady-state natural convection inside spherical containers with a thin insulated baffle is reached. For many cases, the tolerance can even be as low as 10^{-10} , which indicates a nearly perfect statistical stationary state. Therefore, there are two different approaches to declare whether the statistical stationary state is reached during the course of the computations.

The time-averaged stream function ψ_{\max} is defined to describe the mean magnitude of the fluctuating stream function $\psi_{\max}(\tau)$. The RMS and relative RMS are also defined to characterize the strength of the fluctuating stream function $\psi_{\max}(\tau)$ as follow:

$$RMS |_{\psi_{\max}} = \sqrt{\frac{\sum_{i=1}^N (\psi_{\max}(\tau_i) - \psi_{\max})^2}{N}}, \quad (4.16)$$

$$RMS |_{r\psi_{\max}} = \frac{1}{\psi_{\max}} \sqrt{\frac{\sum_{i=1}^N (\psi_{\max}(\tau_i) - \psi_{\max})^2}{N}}. \quad (4.17)$$

4.5 Variations of the Time-Averaged Nusselt Numbers and Stream Function

In Section 4.3, the streamline patterns and temperature contours were presented for different Rayleigh numbers varying from 10^4 to 10^7 with various baffle lengths and locations. The presence of a thin insulated baffle modifies the flow field directly and consequently affects the temperature field. In order to describe these modifications quantitatively, variations of the time-averaged Nusslet numbers and maximum stream function are studied. The Nusselt number is directly associated with the temperature

field, while the stream function can characterize the flow field. Details about the definitions of the time-averaged Nusselt numbers can be found in Section 4.4.

The variations of the time-averaged Nusselt numbers (Nu_c and Nu_m) and maximum stream function of the primary vortex (ψ_{\max}) with Ra for a thin insulated baffle are presented in Figures 4.17 to 4.25. In each figure, the baffle length is fixed ($L=0.05, 0.10$ and 0.25) and its locations ($\theta_b = 30^\circ, 60^\circ, 90^\circ, 120^\circ$ and 150°) are identified with filled symbols, whereas the reference case with no baffle is shown with an open symbol. It must be emphasized that even though variations of the time-averaged Nusselt number (Nu_m) are presented, they will not be discussed in view of the complexity of their relation to the time rate of rise of the bulk temperature (Equation 4.7). The Nusselt numbers and maximum stream function strongly depend on the Rayleigh number and clearly exhibit the strengthening trend with the increase of Rayleigh number, irrespective of the baffle lengths and locations. For $Ra=10^4$, the flow and temperature fields do not change greatly due to presence of the thin insulated baffle. This is because conduction is dominant for this low range of the Rayleigh number and this is . With increase of Ra, the effects of the thin insulated baffle become more noticeable due to the increase of convective effects. For a given Ra, the extent of flow and thermal field modifications is directly related to the length of the thin insulated baffle. It is generally observed (56 out of 60 cases) that by adding a thin insulated baffle, the time-averaged Nusselt number Nu_c is lower than the reference case with no baffle. This Nusselt number is directly proportional to the heat that is transferred into the container and the time rate of rise of the bulk temperature according to Equation 4.8. Since there is no heat transfer through the surface of the baffle, the presence of the baffle has modified the heat input on the wall

of the sphere. This control utility is related to the observed flow and thermal fields presented earlier, where it was observed that presence of a baffle can lead to “confinement” or “compartmentalization” of the sphere. In other words, one can generally state that within the stable stratified layers that are formed in the zone above the baffle conduction dominates, whereas the lower region is dominated by convection. However, it can be observed that the Nusselt numbers and maximum stream function for four (4) cases for which the baffle is located at 30° and 60° are unexpectedly higher than the reference case for $Ra=10^6$ and 10^7 when $L=0.05$ and 0.10 . This is explained as follows. For all the cases with no baffle, the thermal boundary layer becomes thicker as the fluid from the bottom of the sphere rises along the inner wall of the sphere. For cases with high Rayleigh numbers, the presence of short baffles near the top is beneficial to disturbing the boundary layer, thus allowing extra heat to be drawn into the sphere. This effect can not be sustained if the length of the baffle is increased. Our computations show that for the case of $L=0.25$, the confinement effect of the baffle outweighs the disturbance of the boundary layer.

The behavior of the maximum stream function values that are shown in Figures 4.23-4.25 match the trends of the Nusselt number (Nu_c) that were discussed. This indicates that the presence of thin insulated baffles modifies the temperature field through modification of the flow field and it does not directly contribute energy to the system.

Dependence of the time-averaged Nusselt numbers (Nu_c and Nu_m) and maximum stream function of the primary vortex (ψ_{\max}) on the position of the baffles (θ_b) are presented in Figures 4.26-4.28, 4.29-4.31, 4.32-4.34 and 4.35-4.37 for $Ra= 10^4$, 10^5 , 10^6 and 10^7 , respectively. In each figure, the reference case with no baffle is

identified with a filled circle, whereas various baffle lengths ($L=0.05, 0.10$ and 0.25) are identified with non-circular filled symbols. Again, it must be emphasized that even though variations of the time-averaged Nusselt number (Nu_m) are presented, they will not be discussed in view of the complexity of their relation to the time rate of rise of the bulk temperature (Equation 4.7). For a given Ra number, as the location of baffle is lowered starting from the top of the sphere and moving toward the bottom, the Nusselt number Nu_c and maximum stream function exhibit trends suggesting that the confinement effect is minimal, when the baffle is placed near the two extremes. The location corresponding to the most marked confinement varies depending on the Ra and length of the baffle. For a fixed location of the baffle and Ra numbers lower than 10^7 , one can generally state that as the length of the baffle is raised, the confinement effect becomes more enhanced. This behavior is not observed for the highest Ra studied.

The tabulated data for the Nusselt numbers (Nu_c and Nu_m) and maximum stream function (ψ_{\max}) of the primary vortex are listed in Tables 4.3, 4.4 and 4.5, respectively. In general, the relative RMS values are low suggesting that the pseudosteady-state is established, except for $Ra=10^7$, indicating that unsteady effects are promoted as the Ra number is raised.

It is found that the relative RMS values of the Nusselt numbers have strong dependence on the Rayleigh number. This is not unusual, because the larger the Rayleigh number, the stronger the convection heat transfer. The results indicate that relative RMS values of the maximum stream function strongly depend on the Rayleigh number.

Table 4.3 Nusselt numbers (Nu_c) and relative RMS ($RMS|_{rNu_c}$) for all 60 cases with thin insulated baffles

Ra	θ_b	L=0.05		L=0.10		L=0.25	
		Nu_c	$RMS _{rNu_c}$	Nu_c	$RMS _{rNu_c}$	Nu_c	$RMS _{rNu_c}$
10^4	30°	5.7507	3.76E-04	5.6456	3.08E-04	5.336	3.06E-04
	60°	5.5848	3.94E-04	5.2843	3.58E-04	4.6973	4.50E-04
	90°	5.4883	3.21E-04	5.0689	3.32E-04	4.3069	4.93E-04
	120°	5.6264	4.18E-04	5.3355	3.34E-04	4.6715	4.37E-04
	150°	5.7492	4.12E-04	5.6944	4.29E-04	5.4687	4.54E-04
10^5	30°	12.6197	1.68E-04	11.9784	1.77E-04	10.4937	1.75E-04
	60°	11.9103	1.77E-04	10.4538	1.95E-04	8.0405	1.61E-04
	90°	11.9047	1.13E-04	10.5831	1.53E-04	7.8263	2.70E-04
	120°	12.4218	9.36E-05	11.7501	1.65E-04	10.9077	1.74E-04
	150°	12.7907	1.31E-04	12.674	1.57E-04	12.582	1.60E-04
10^6	30°	26.2174	7.97E-05	24.1578	7.88E-05	18.4589	6.33E-05
	60°	22.4345	9.17E-05	19.3234	1.09E-04	13.9664	1.33E-04
	90°	22.1206	9.51E-05	16.641	6.22E-04	14.8931	4.34E-05
	120°	22.8518	9.16E-04	18.8932	0.1405	20.5763	1.47E-04
	150°	24.9339	8.61E-05	24.8963	0.0115	24.9721	9.62E-05
10^7	30°	42.393	0.0958	48.2804	0.0245	33.6157	0.3067
	60°	38.5685	0.0355	35.6409	0.0454	29.1517	0.2621
	90°	31.997	0.1234	33.0963	0.1893	29.0071	0.23
	120°	32.9073	0.0253	28.2387	0.1085	29.5112	0.079
	150°	36.9014	0.0534	35.8857	0.0988	36.6353	0.004

Table 4.4 Nusselt numbers (Nu_m) and relative RMS ($RMS|_{rNu_m}$) for all 60 cases with thin insulated baffles

Ra	θ_b	L=0.05		L=0.10		L=0.25	
		Nu_m	$RMS _{rNu_m}$	Nu_m	$RMS _{rNu_m}$	Nu_m	$RMS _{rNu_m}$
10^4	30°	11.2168	3.16E-04	11.1841	2.33E-04	11.0597	2.53E-04
	60°	11.1416	3.43E-04	11.0078	3.09E-04	10.6936	4.43E-04
	90°	11.0255	2.68E-04	10.7733	2.90E-04	10.3361	4.88E-04
	120°	11.023	3.50E-04	10.7697	2.51E-04	10.4594	4.34E-04
	150°	11.1666	3.41E-04	11.0925	3.45E-04	10.9369	3.50E-04
10^5	30°	16.0937	1.67E-04	16.0216	1.76E-04	15.73	1.75E-04
	60°	15.947	1.76E-04	15.8	1.95E-04	15.0592	1.58E-04
	90°	15.5702	1.13E-04	15.6486	1.53E-04	15.0019	2.69E-04
	120°	15.6737	9.35E-05	15.7196	1.64E-04	15.9574	1.74E-04
	150°	16.0253	1.31E-04	15.9878	1.57E-04	15.994	1.60E-04
10^6	30°	25.4469	7.95E-05	25.0298	7.87E-05	23.5963	6.34E-05
	60°	24.0903	9.16E-05	23.701	1.09E-04	22.6813	1.33E-04
	90°	24.049	9.48E-05	24.1182	2.29E-04	24.3479	4.34E-05
	120°	24.2325	7.07E-04	24.8815	0.0594	26.0726	9.86E-05
	150°	24.9448	8.12E-05	25.4786	0.0078	25.9388	8.25E-05
10^7	30°	41.2438	0.014	42.3179	0.0192	38.6688	0.2812
	60°	41.1094	0.0262	40.7922	0.0381	38.3225	0.2079
	90°	38.6335	0.063	40.1324	0.0941	40.7759	0.1593
	120°	38.655	0.0257	39.787	0.0805	41.7251	0.0352
	150°	40.8409	0.043	40.7907	0.0817	41.8946	0.0065

Table 4.5 Maximum stream function (ψ_{\max}) of the primary vortex and relative RMS ($RMS|_{r\psi_{\max}}$) for all 60 cases with thin insulated baffles

Ra	θ_b	L=0.05		L=0.10		L=0.25	
		ψ_{\max}	$RMS _{r\psi_{\max}}$	ψ_{\max}	$RMS _{r\psi_{\max}}$	ψ_{\max}	$RMS _{r\psi_{\max}}$
10^4	30°	1.52E-05	4.39E-06	1.50E-05	1.57E-05	1.38E-05	5.58E-05
	60°	1.47E-05	2.06E-05	1.35E-05	6.61E-05	1.03E-05	8.74E-05
	90°	1.32E-05	1.75E-05	1.04E-05	1.18E-04	5.46E-06	3.30E-04
	120°	1.36E-05	8.01E-05	1.15E-05	2.04E-04	8.55E-06	2.01E-04
	150°	1.52E-05	2.54E-05	1.49E-05	6.44E-05	1.35E-05	5.71E-05
10^5	30°	7.47E-05	6.93E-06	7.33E-05	1.35E-05	6.82E-05	3.81E-07
	60°	7.48E-05	1.14E-05	7.04E-05	1.18E-05	5.49E-05	8.02E-07
	90°	7.05E-05	1.67E-05	6.38E-05	5.74E-06	3.93E-05	8.68E-06
	120°	6.60E-05	8.90E-07	5.50E-05	1.39E-06	4.96E-05	8.17E-07
	150°	7.29E-05	3.49E-06	7.10E-05	2.86E-06	6.98E-05	9.77E-07
10^6	30°	1.94E-04	6.60E-07	1.93E-04	3.18E-07	1.65E-04	3.76E-07
	60°	1.90E-04	8.50E-08	1.66E-04	6.47E-07	1.41E-04	3.53E-07
	90°	1.66E-04	1.14E-06	1.46E-04	0.0012	1.19E-04	1.31E-06
	120°	1.59E-04	0.0012	1.18E-04	0.1229	1.39E-04	9.05E-05
	150°	1.83E-04	5.64E-05	1.78E-04	0.0214	1.83E-04	5.74E-05
10^7	30°	4.23E-04	0.0818	4.46E-04	0.0164	3.72E-04	0.0454
	60°	4.43E-04	0.0777	3.88E-04	0.1062	3.16E-04	0.0136
	90°	2.84E-04	0.1719	3.00E-04	0.1937	2.84E-04	0.1272
	120°	3.35E-04	0.0284	3.70E-04	0.1516	2.88E-04	0.0698
	150°	4.22E-04	0.0803	3.65E-04	0.0672	3.77E-04	0.0028

4.6 Closure

The effect of a thin insulated baffle that is attached on the inner wall of a sphere on pseudosteady-state natural convection was investigated in this Chapter. For low Rayleigh numbers, pseudosteady-state with minimal fluctuations of the flow and thermal fields were observed. For $Ra=10^7$, strong fluctuations were promoted. In general, attaching an insulated baffle degrades the amount of heat that can be added to the stored fluid.

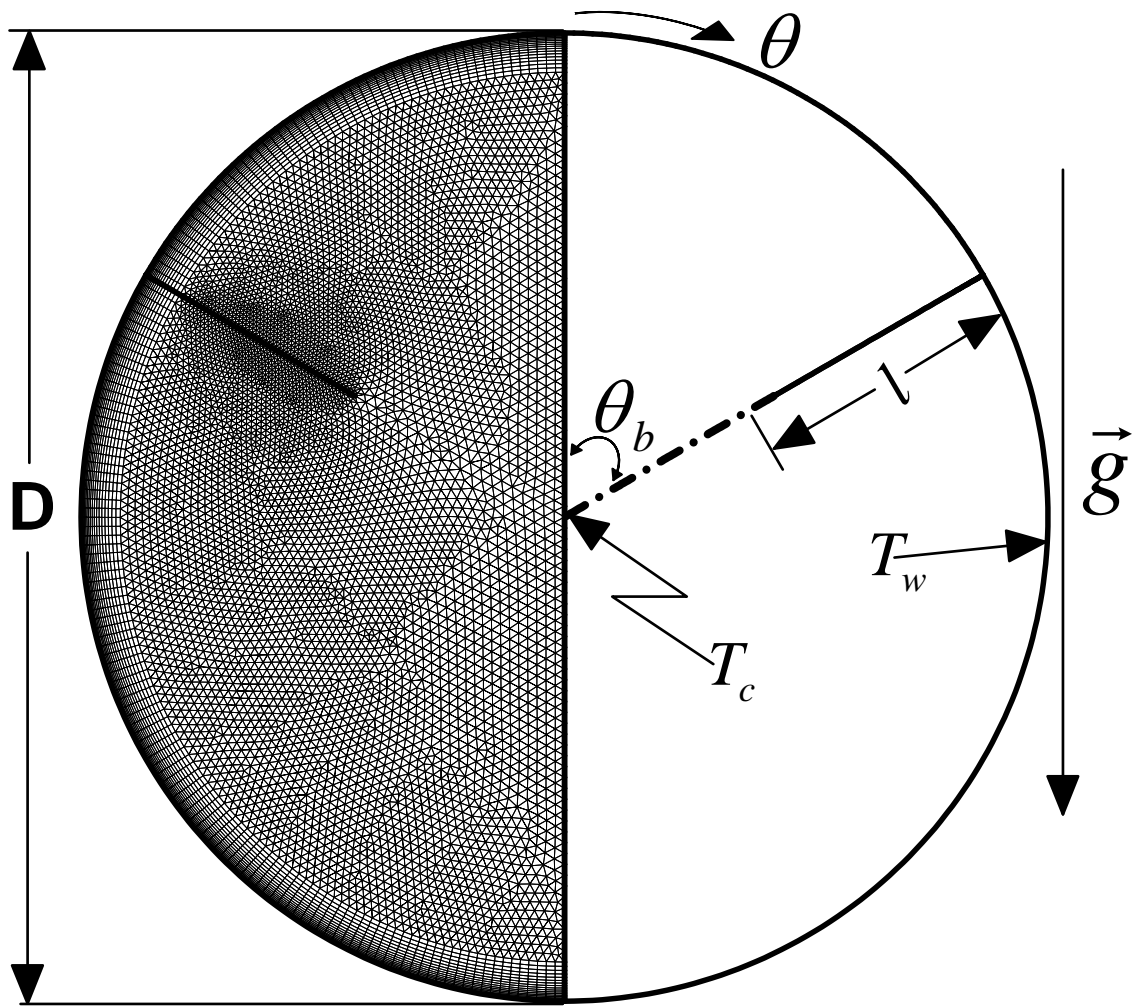


Figure 4.1 Schematic diagram of a spherical container with a thin insulated baffle

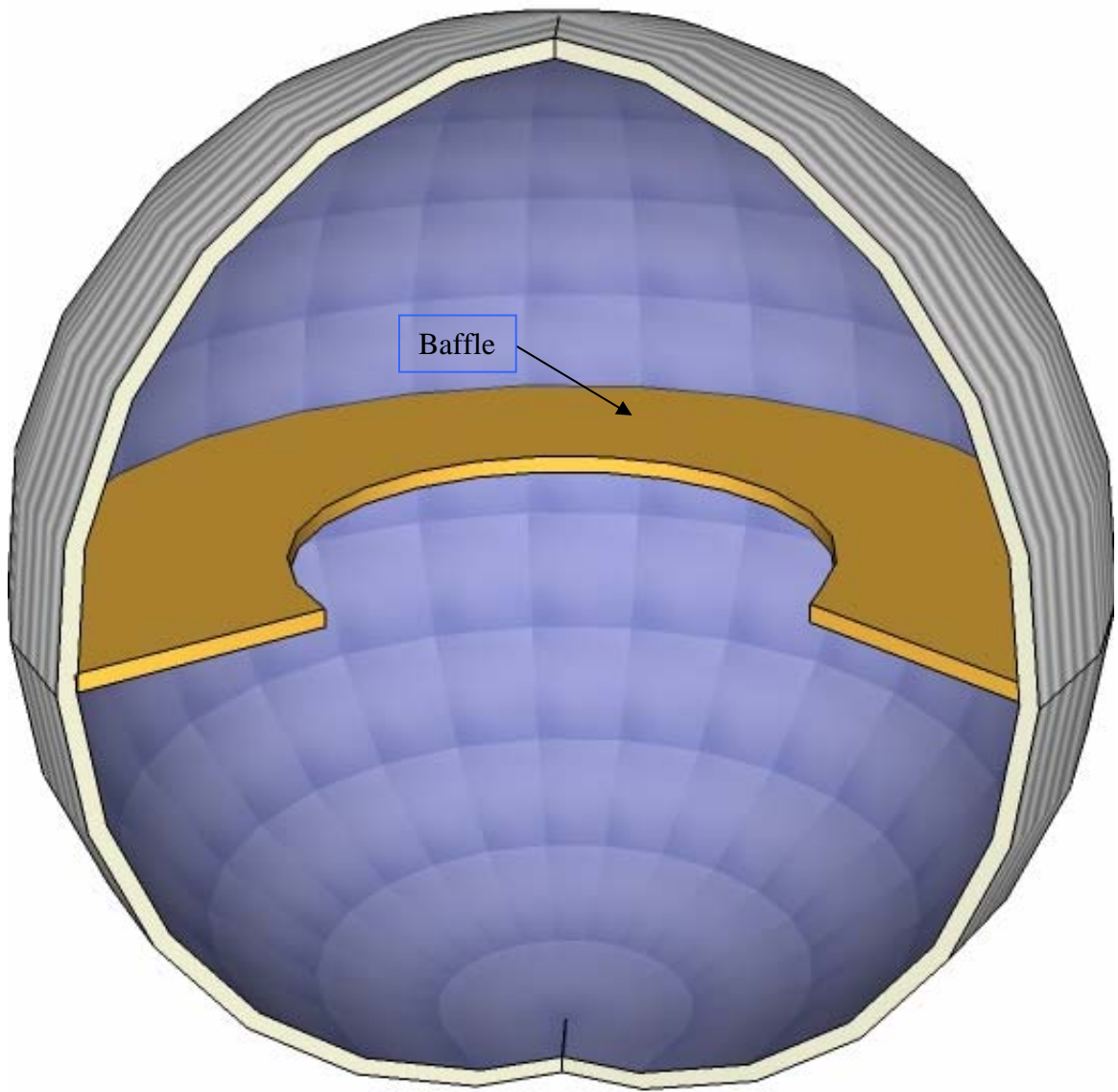


Figure 4.2 3-D view of the system

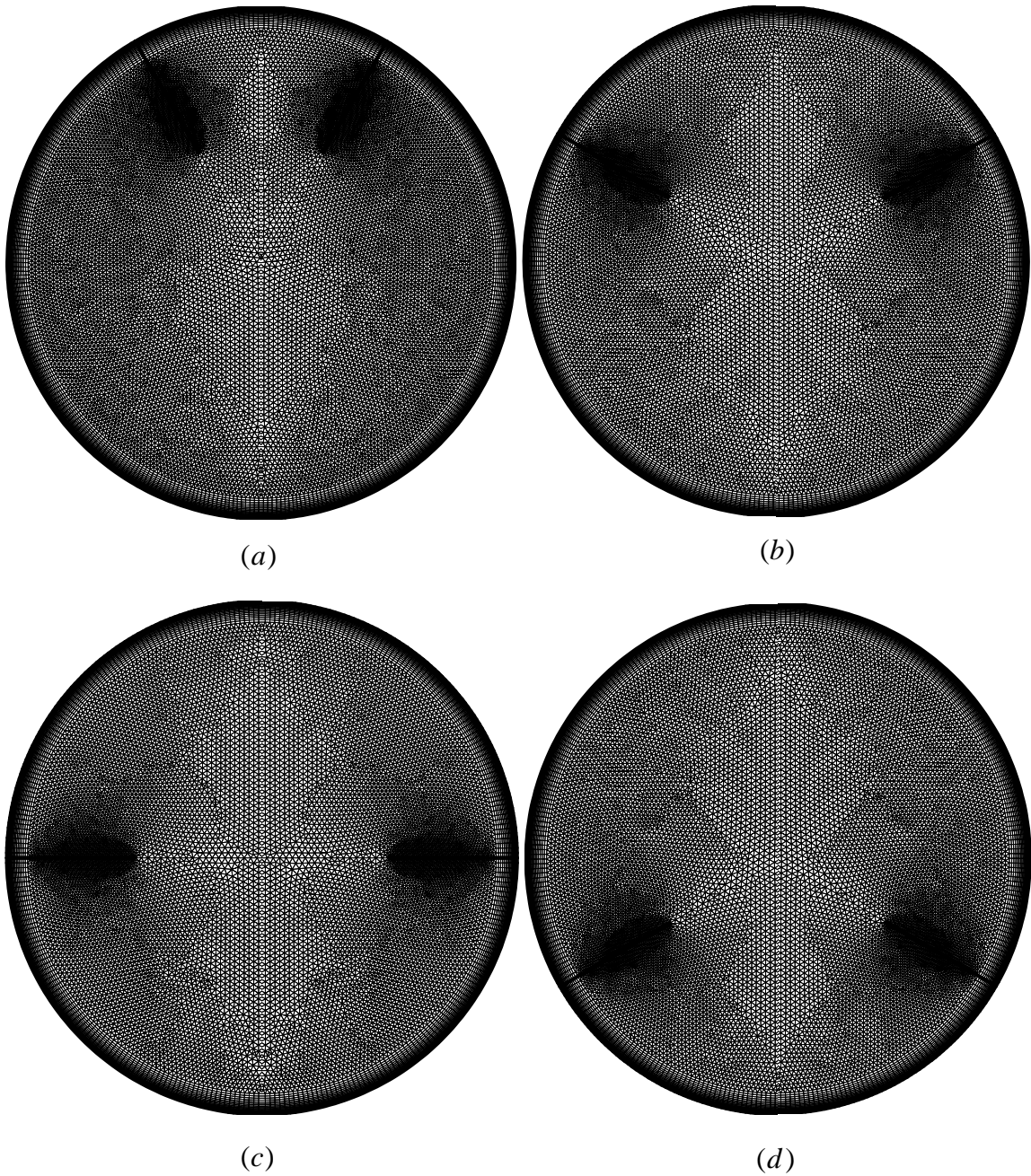


Figure 4.3 Grid systems with the same baffle ($L=0.25$) located at (a) $\theta_b = 30^\circ$,
(b) $\theta_b = 60^\circ$, (c) $\theta_b = 90^\circ$ and (d) $\theta_b = 120^\circ$

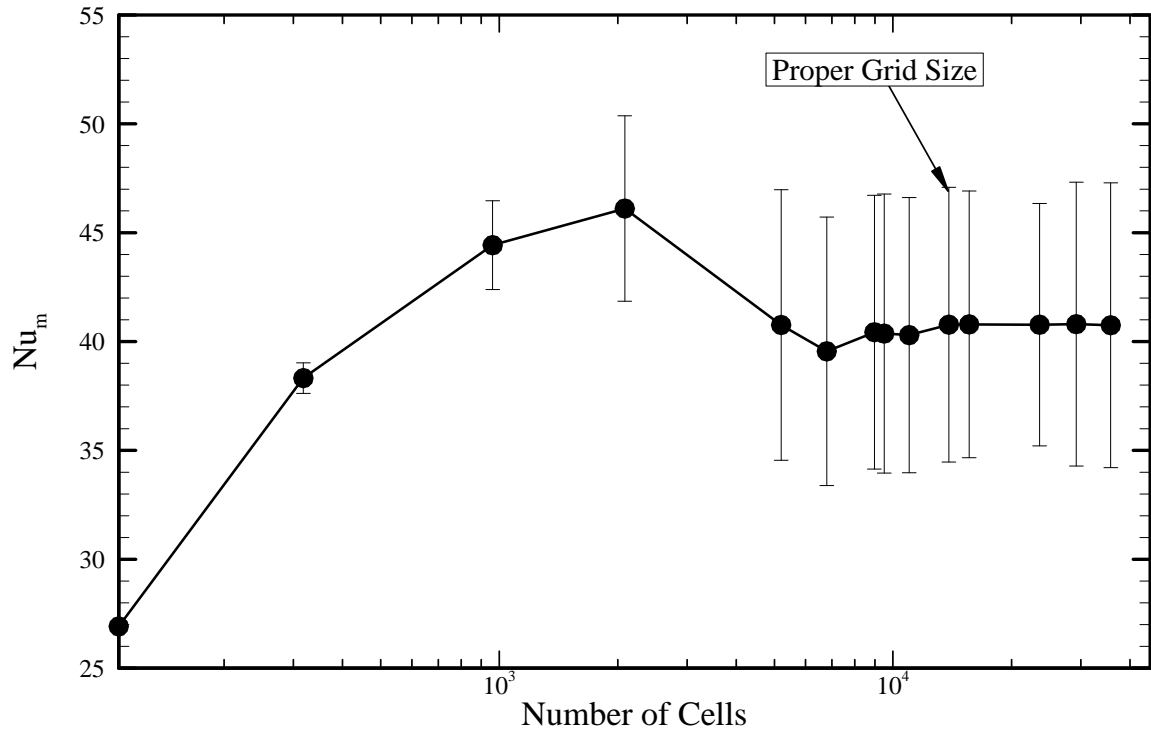


Figure 4.4 The time-averaged and RMS values of the Nusselt number Nu_m (based on $\Delta T = T_w - T_m$) as a function of grid size for a case with insulated baffle ($L=0.25$, $\theta_b = 90^\circ$ and $Ra=10^7$)

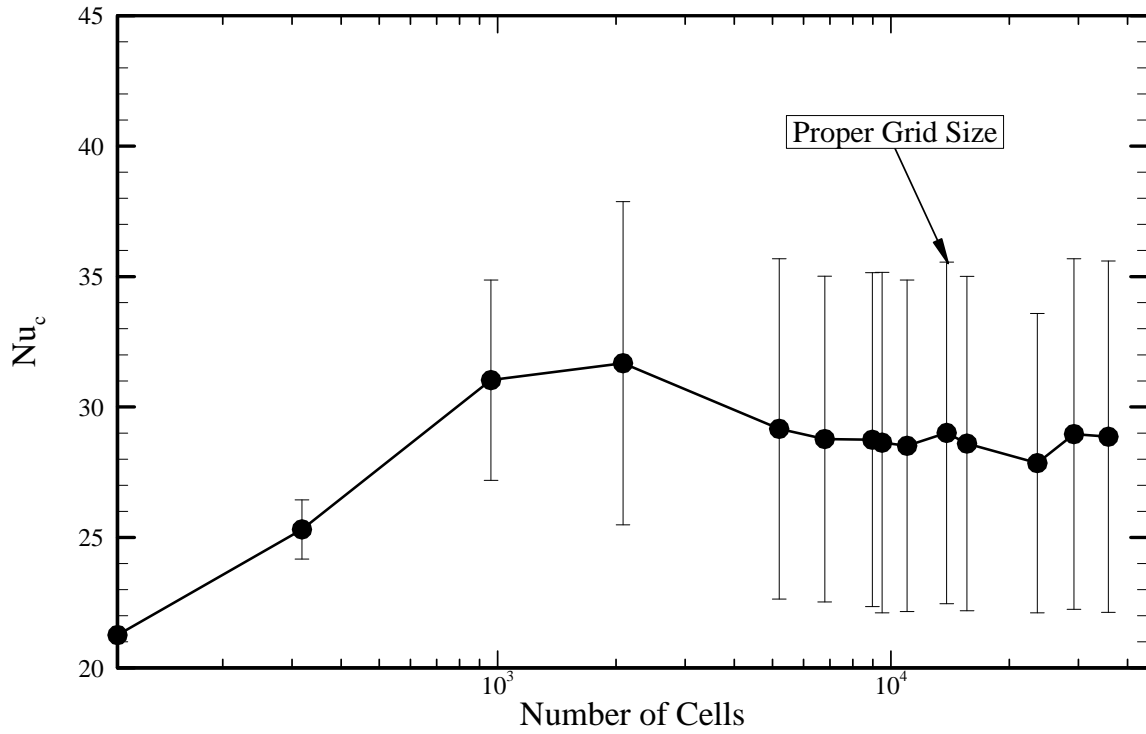


Figure 4.5 The time-averaged and RMS values of the Nusselt number Nu_c (based on $\Delta T = T_w - T_c$) as a function of grid size for a case with insulated baffle ($L=0.25$, $\theta_b = 90^\circ$ and $Ra=10^7$)

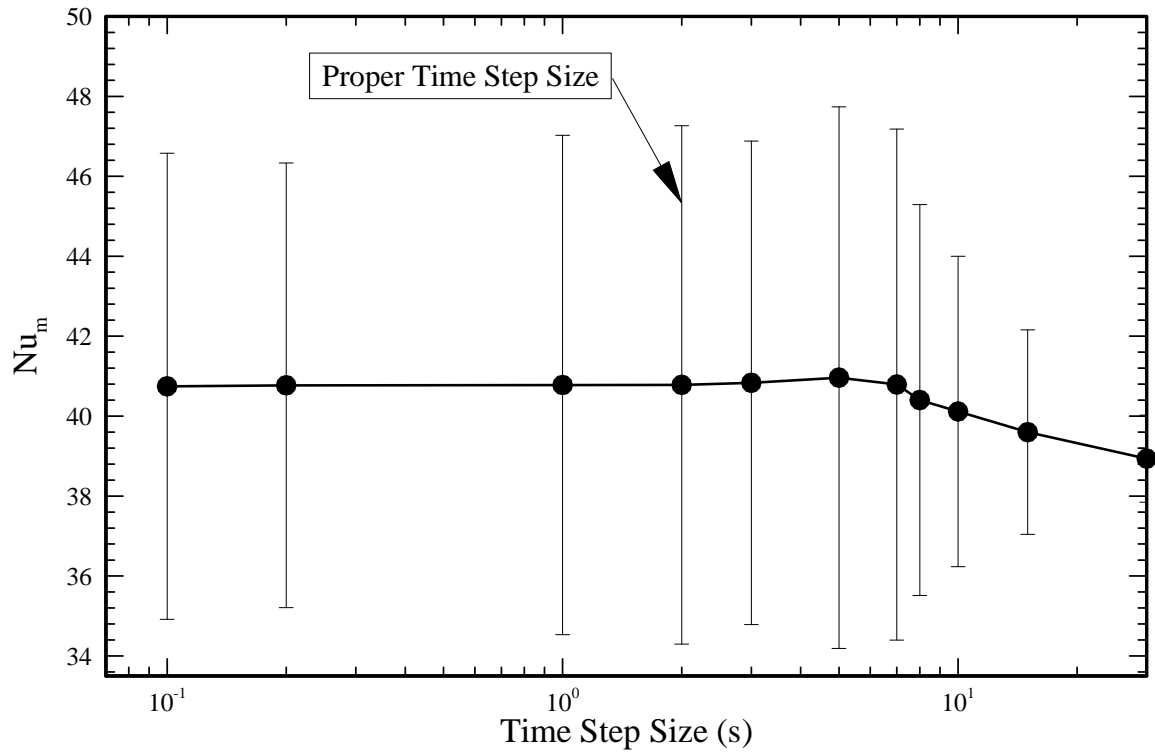


Figure 4.6 The time-averaged and RMS values of the Nusselt number Nu_m (based on $\Delta T = T_w - T_m$) as a function of time step size for a case with insulated baffle ($L=0.25$, $\theta_b = 90^\circ$ and $Ra=10^7$)

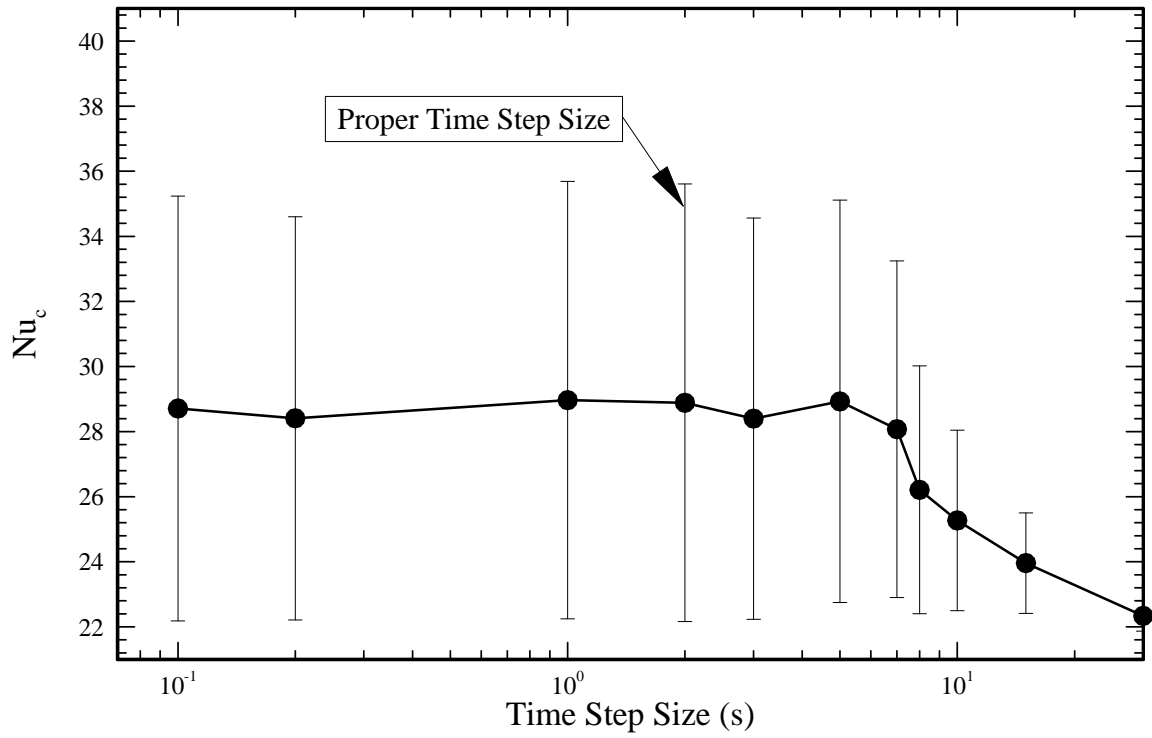


Figure 4.7 The time-averaged and RMS values of the Nusselt number Nu_c (based on $\Delta T = T_w - T_c$) as a function of time step size for a case with insulated baffle ($L=0.25$, $\theta_b = 90^\circ$ and $Ra=10^7$)

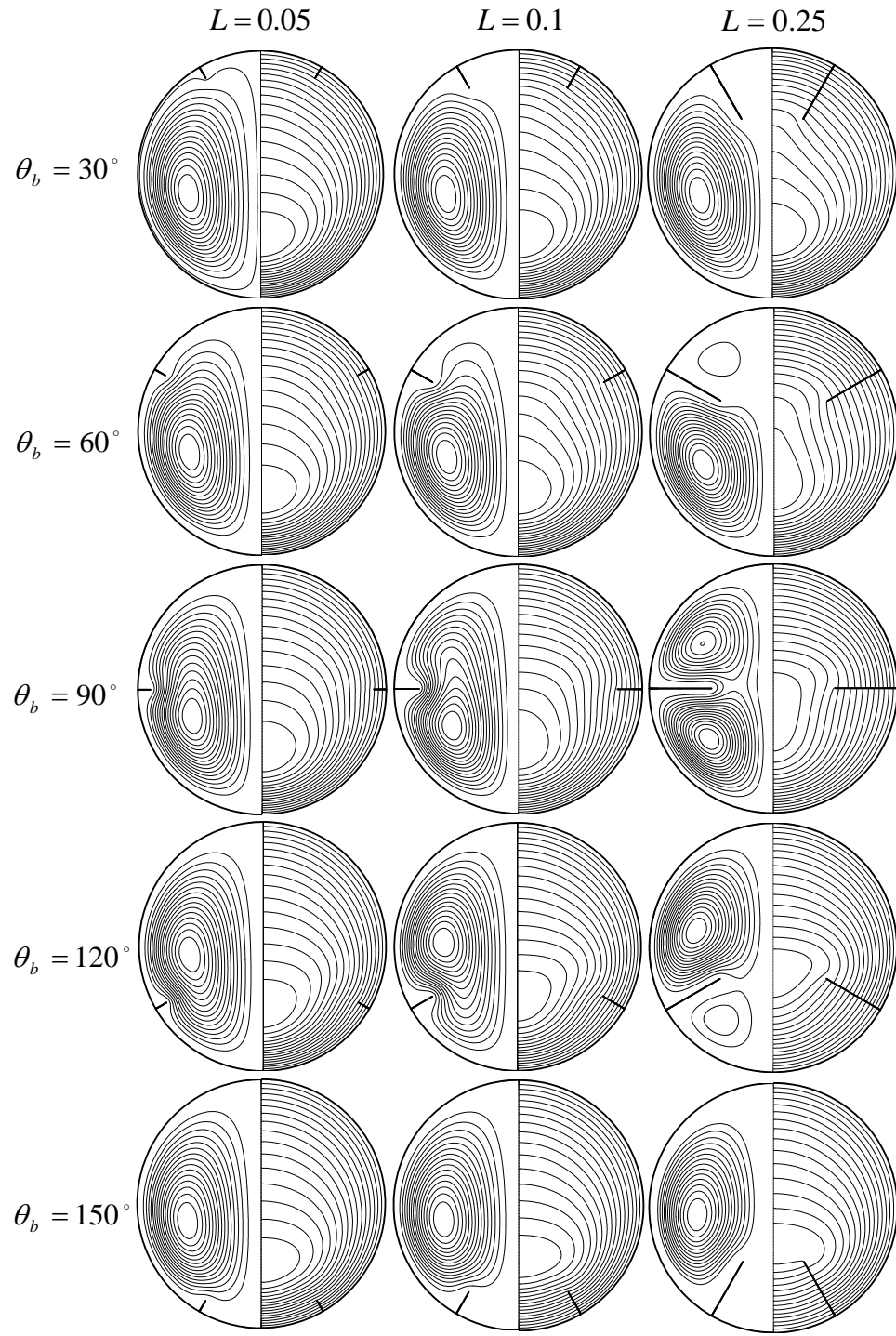


Figure 4.8 Pseudosteady-state streamline patterns and temperature contours for three insulated baffles ($L = 0.05, 0.10$ and 0.25) placed at various locations ($\theta_b = 30^\circ, 60^\circ, 90^\circ, 120^\circ$ and 150°) for $Ra = 10^4$

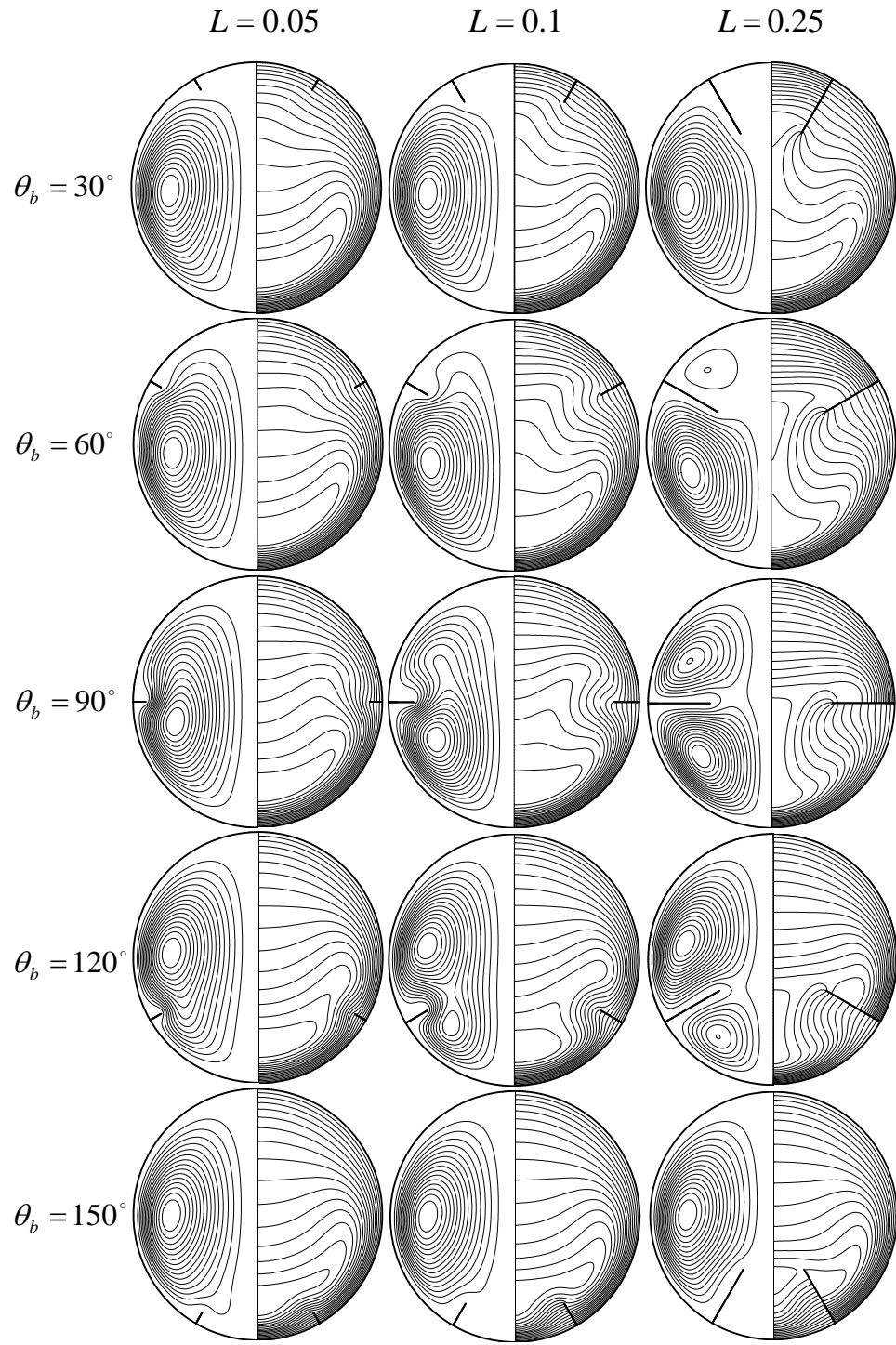


Figure 4.9 Pseudosteady-state streamline patterns and temperature contours for three insulated baffles ($L = 0.05, 0.10$ and 0.25) placed at various locations ($\theta_b = 30^\circ, 60^\circ, 90^\circ, 120^\circ$ and 150°) for $Ra = 10^5$

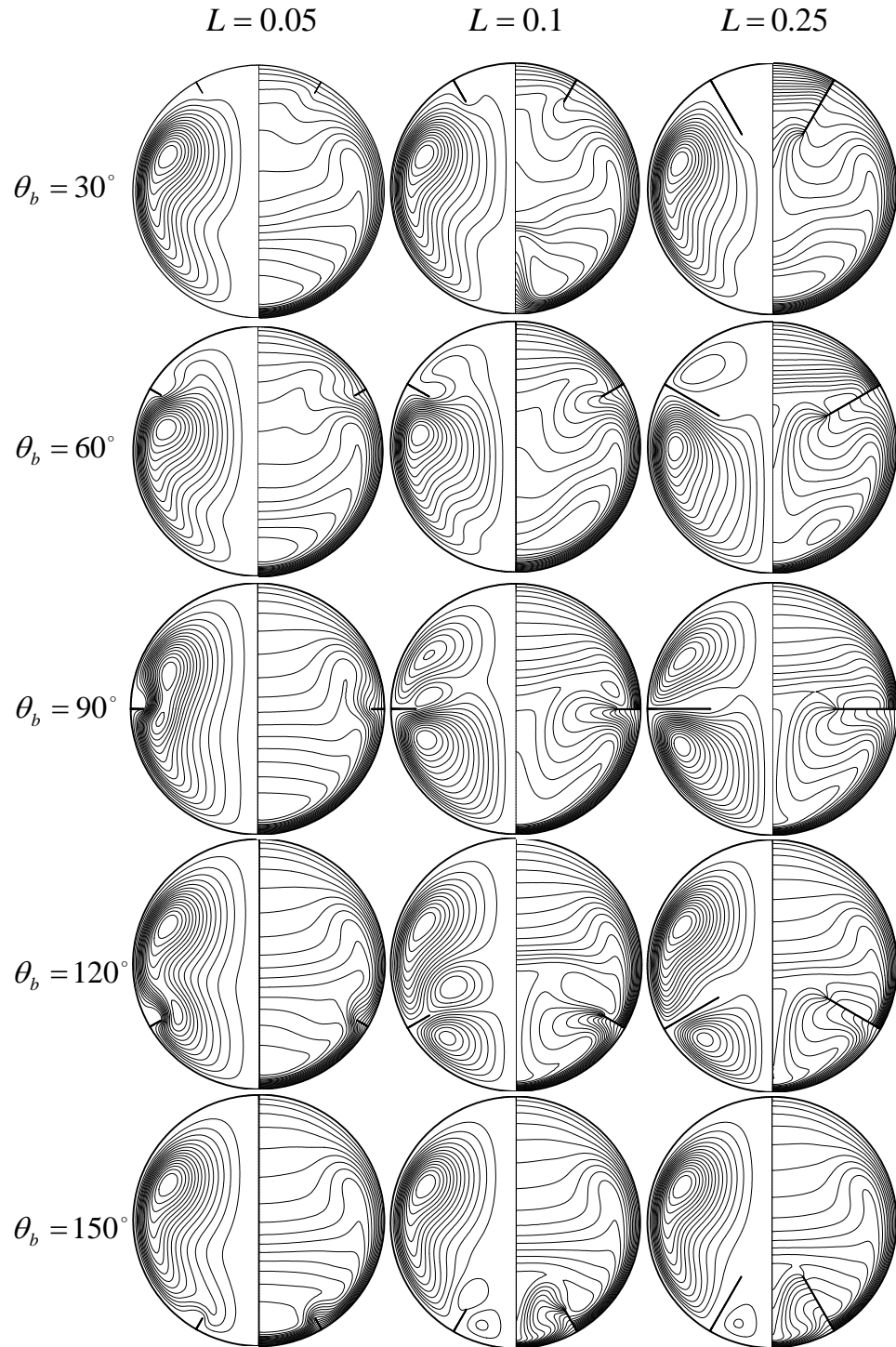


Figure 4.10 Pseudosteady-state streamline patterns and temperature contours for three insulated baffles ($L = 0.05, 0.10$ and 0.25) placed at various locations ($\theta_b = 30^\circ, 60^\circ, 90^\circ, 120^\circ$ and 150°) for $Ra = 10^6$

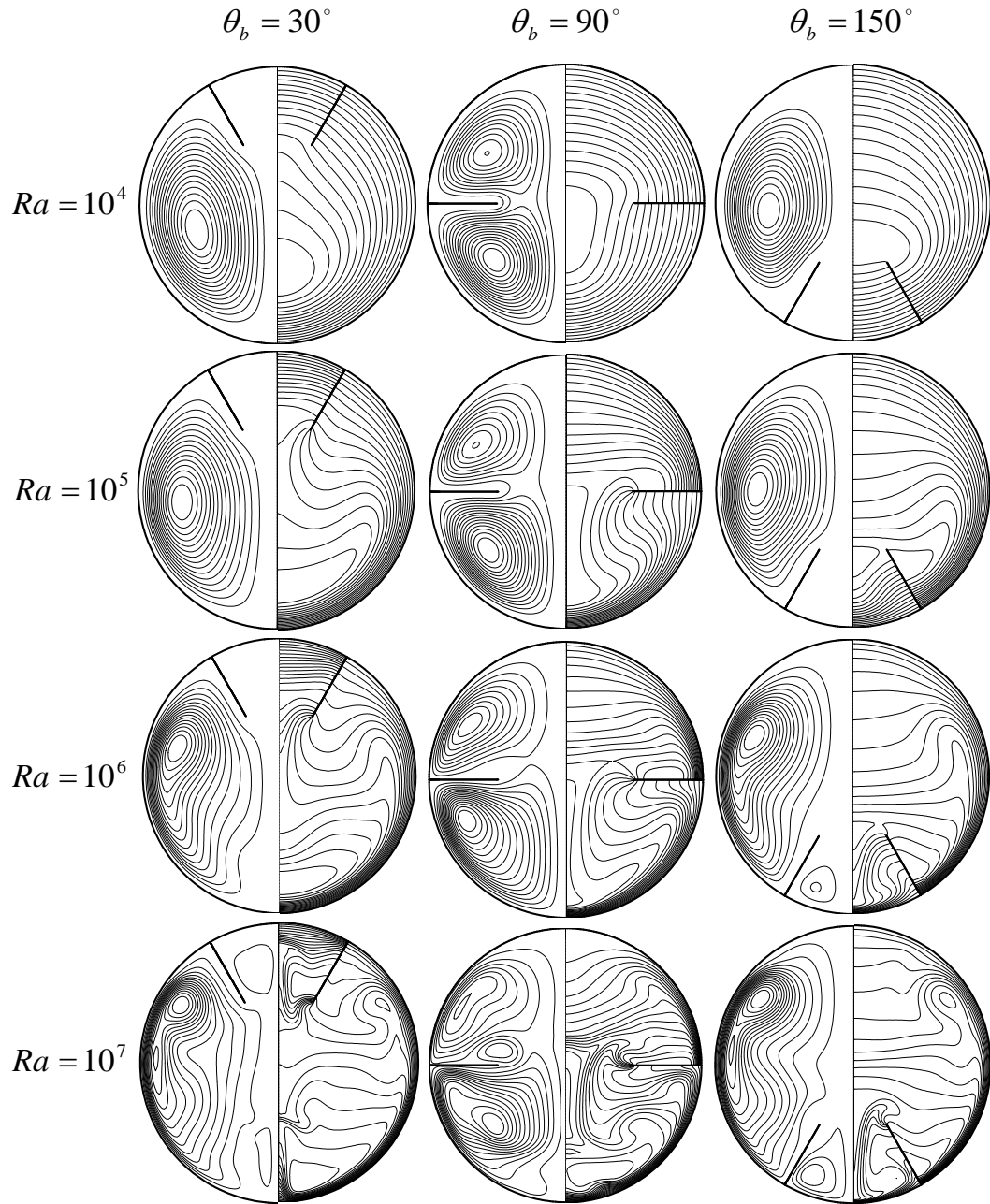


Figure 4.11 Pseudosteady-state streamline patterns and temperature contours with an insulated baffle ($L = 0.25$) placed at various locations ($\theta_b = 30^\circ, 90^\circ$ and 150°) for

$$Ra = 10^4, 10^5, 10^6 \text{ and } 10^7$$

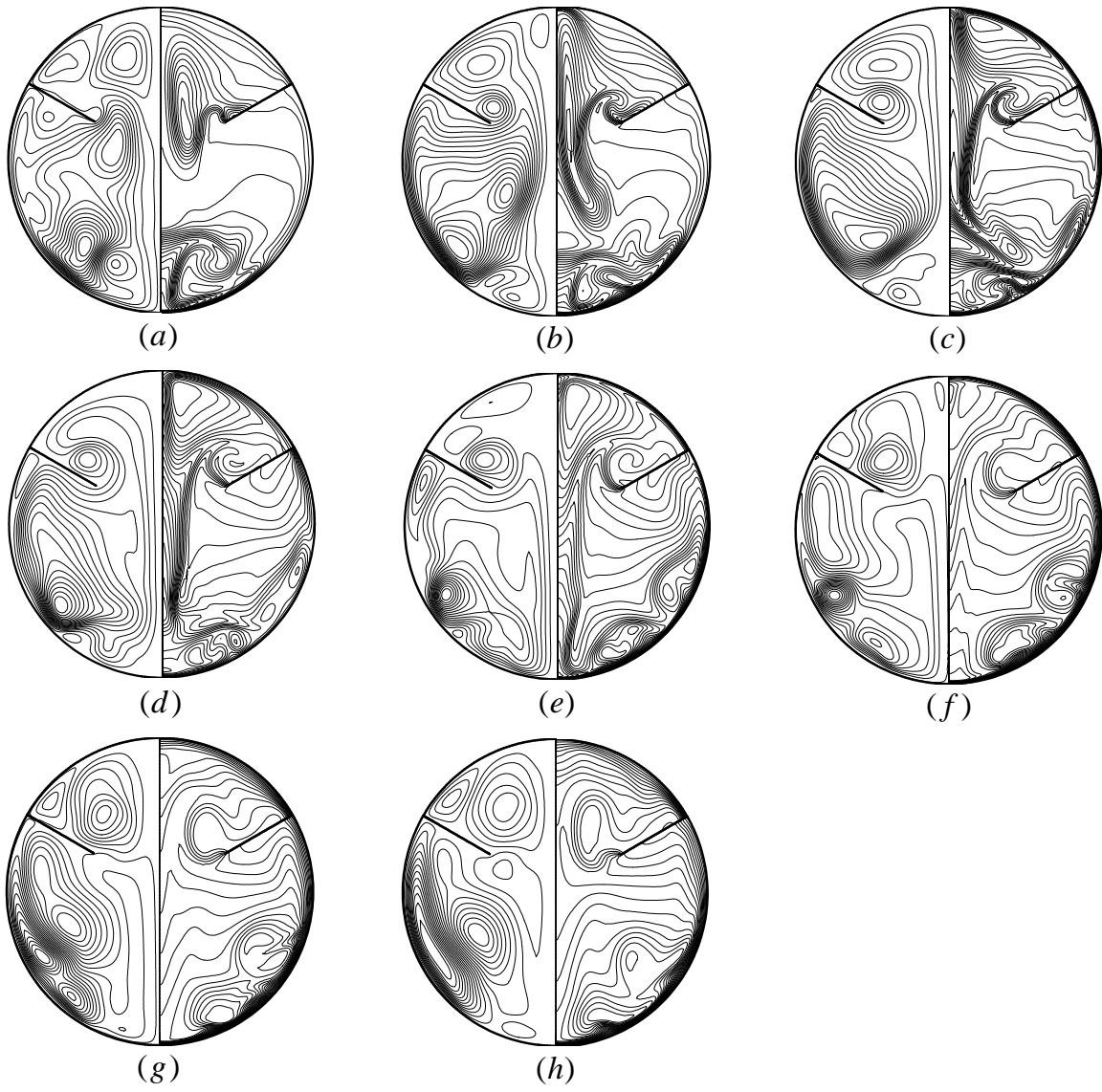


Figure 4.12 Streamline patterns and temperature contours in one cycle (a→h) for case with a thin insulated baffle ($L=0.25$, $\theta_b=60^\circ$) for $Ra=10^7$

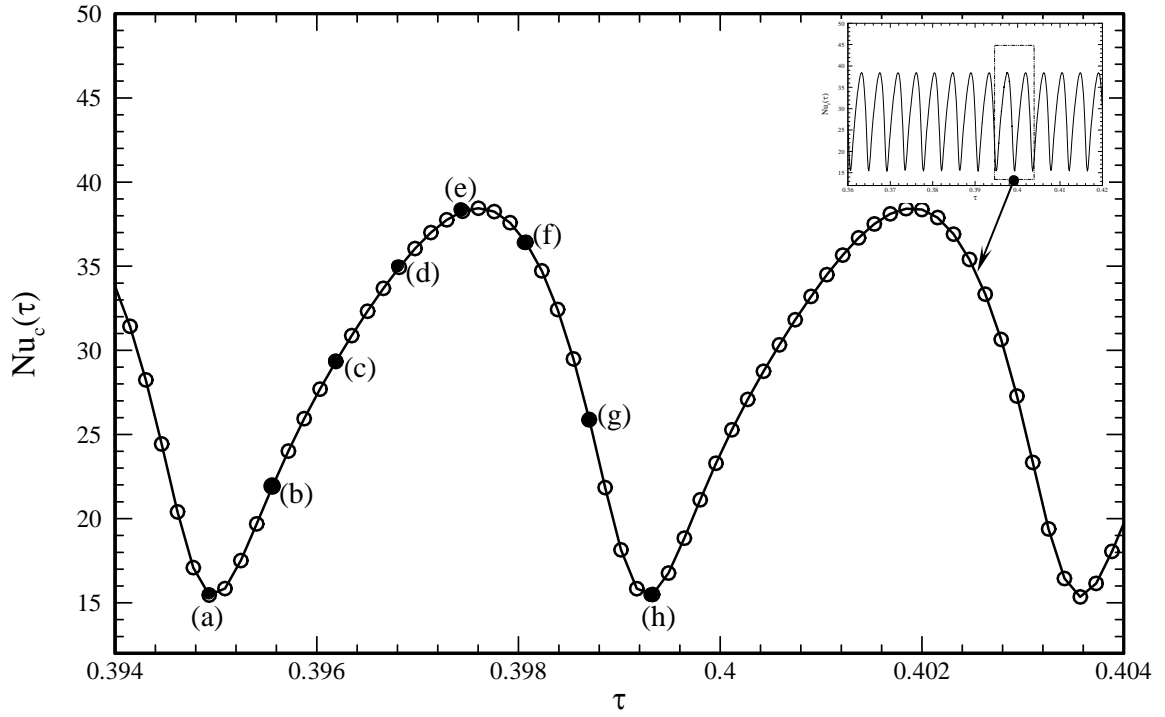
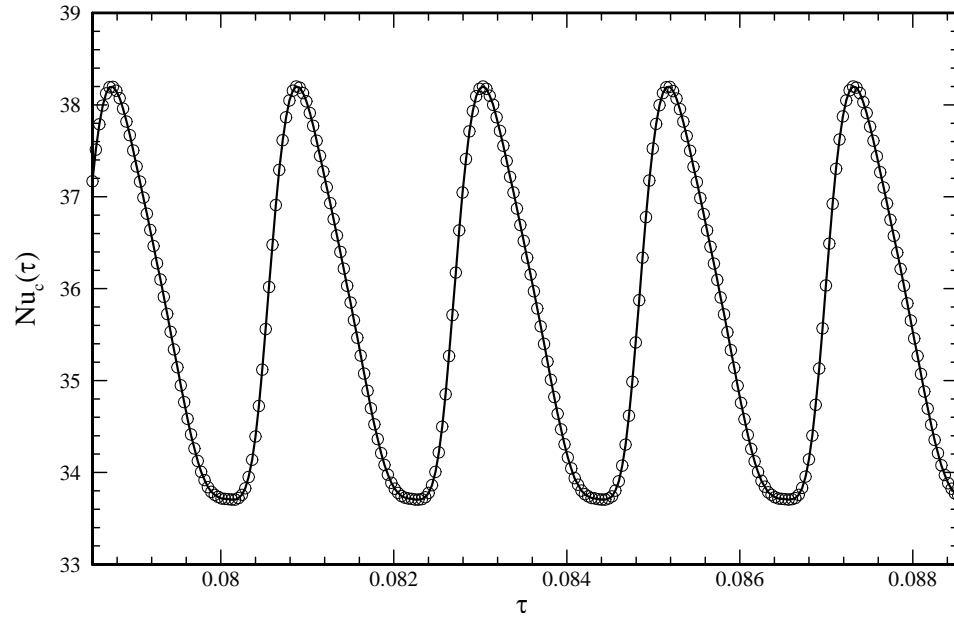
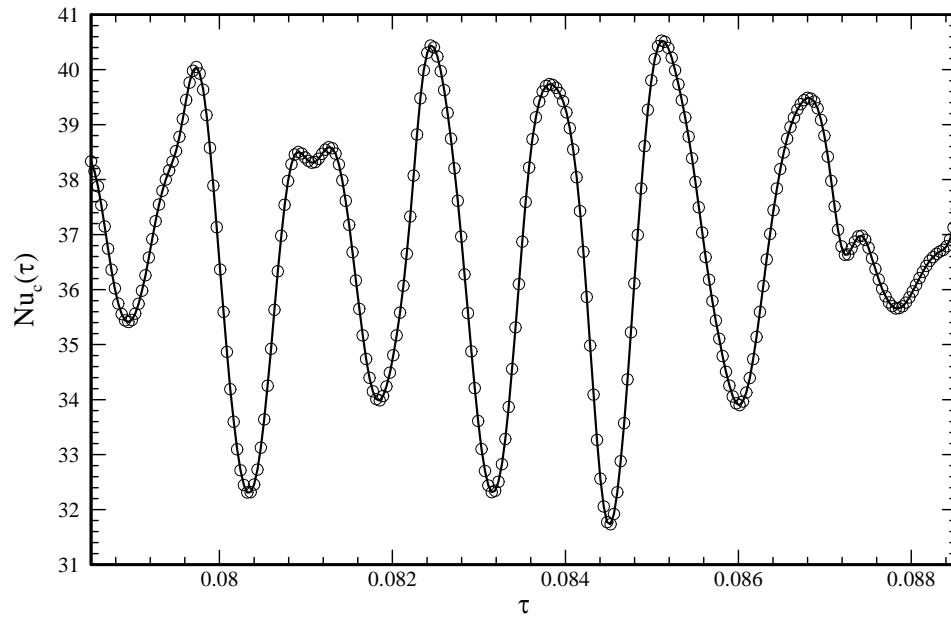


Figure 4.13 Cyclic variation of the instantaneous area-averaged Nusselt number for case with a thin insulated baffle ($L=0.25$, $\theta_b=60^\circ$) for $Ra=10^7$ (Corresponding to Figure 4.12)



(a)



(b)

Figure 4.14 Dependence of the instantaneous surface-averaged Nusselt number $Nu_c(\tau)$ with dimensionless time for case (a) with a thin insulated baffle ($L=0.10$, $\theta_b = 60^\circ$ and $Ra=10^7$) and case (b) with a thin insulated baffle ($L=0.05$, $\theta_b = 150^\circ$ and $Ra=10^7$)

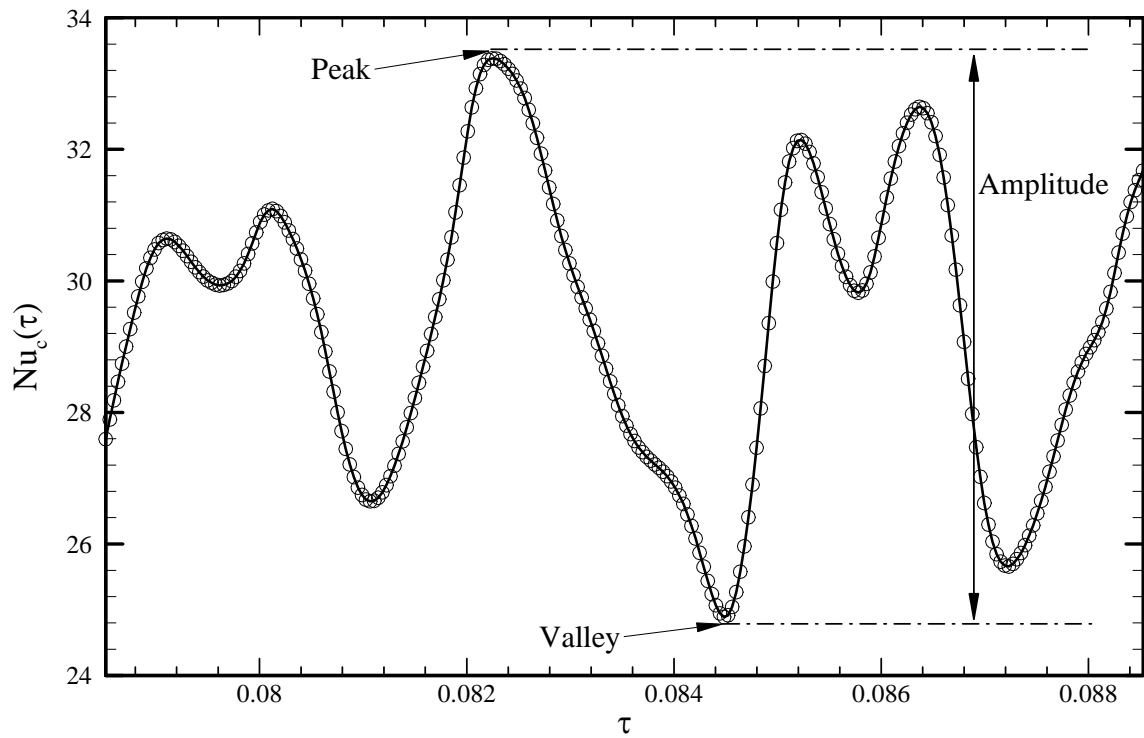


Figure 4.15 Strength of oscillations of the Nusselt number (Nu_c) with dimensionless time for a case with a thin insulated baffle ($L=0.25, \theta_b = 120^\circ$ and $Ra=10^7$)

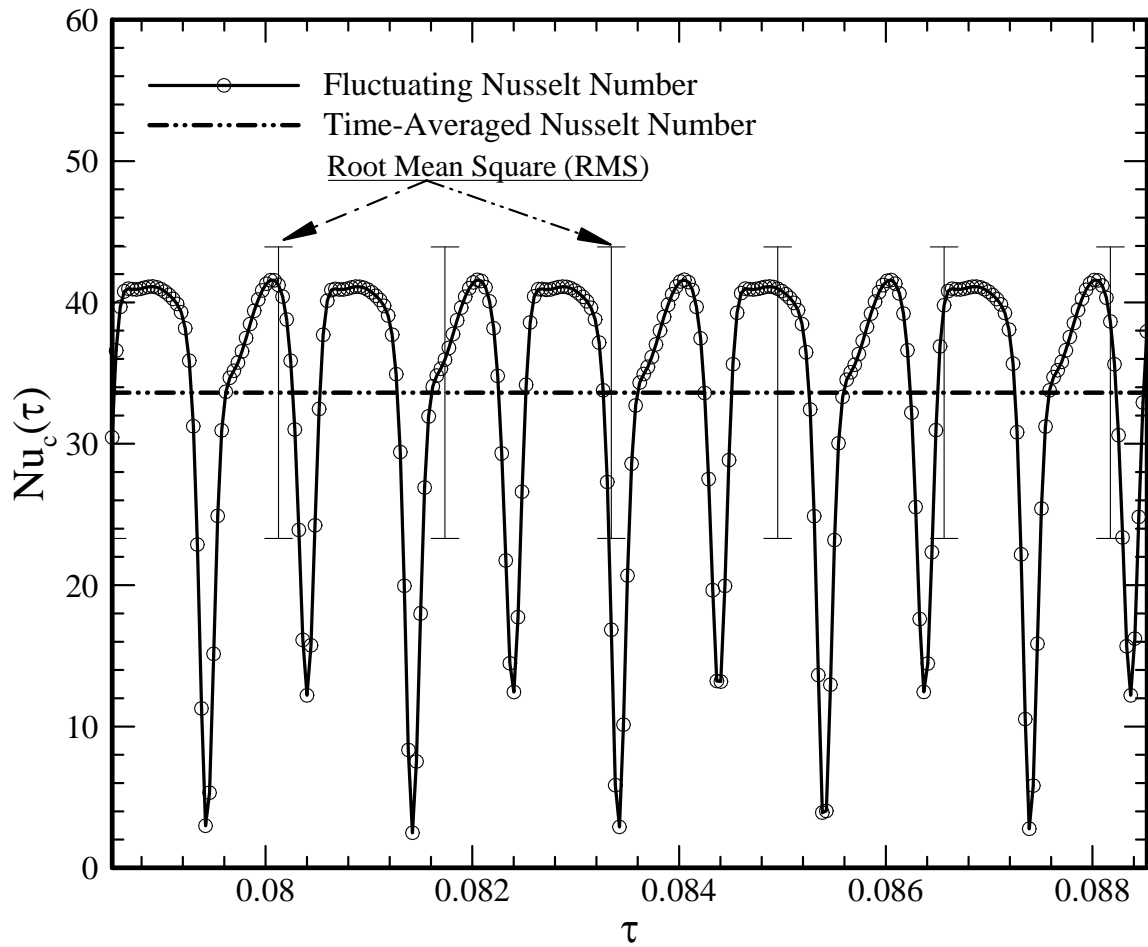


Figure 4.16 Strength (RMS) of oscillations of the Nusselt number (Nu_c) with dimensionless time for case with thin insulated baffle ($L=0.25, \theta_b = 30^\circ, Ra=10^7$)

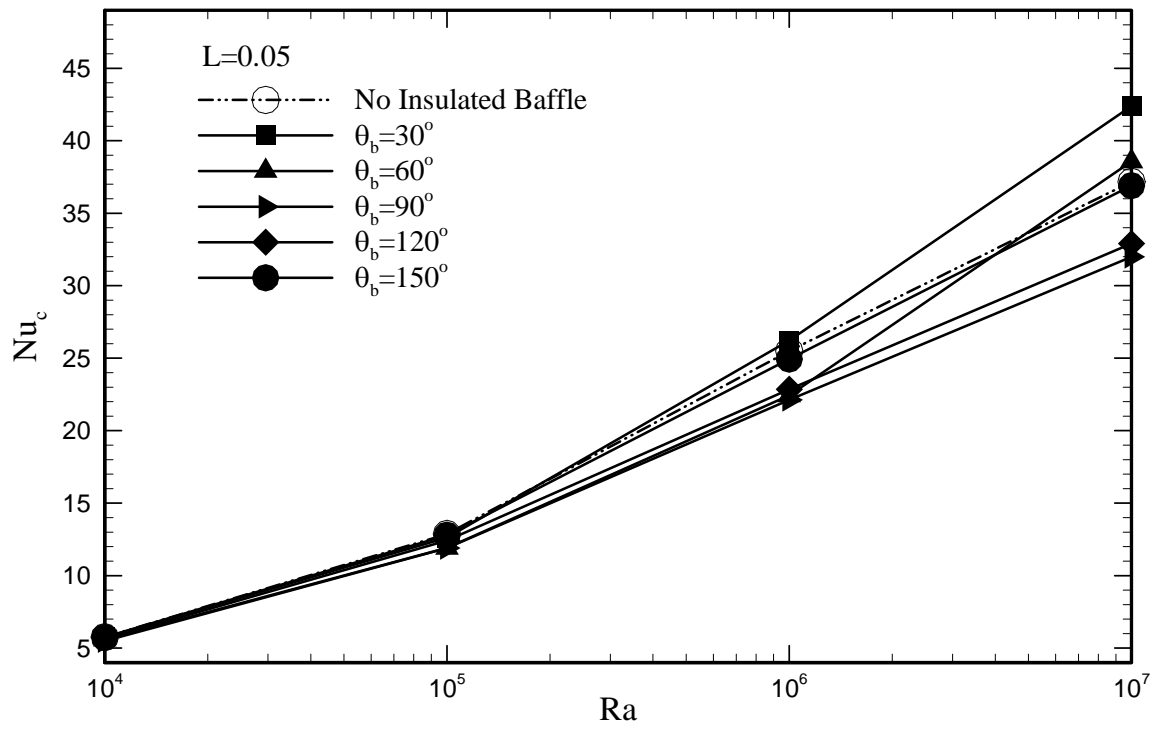


Figure 4.17 Dependence of the time-averaged Nusselt number (Nu_c) on Ra among cases with a fixed thin insulated baffle ($L=0.05$) at various locations ($\theta_b = 30^\circ, 60^\circ, 90^\circ, 120^\circ$ and 150°) and the case without baffle

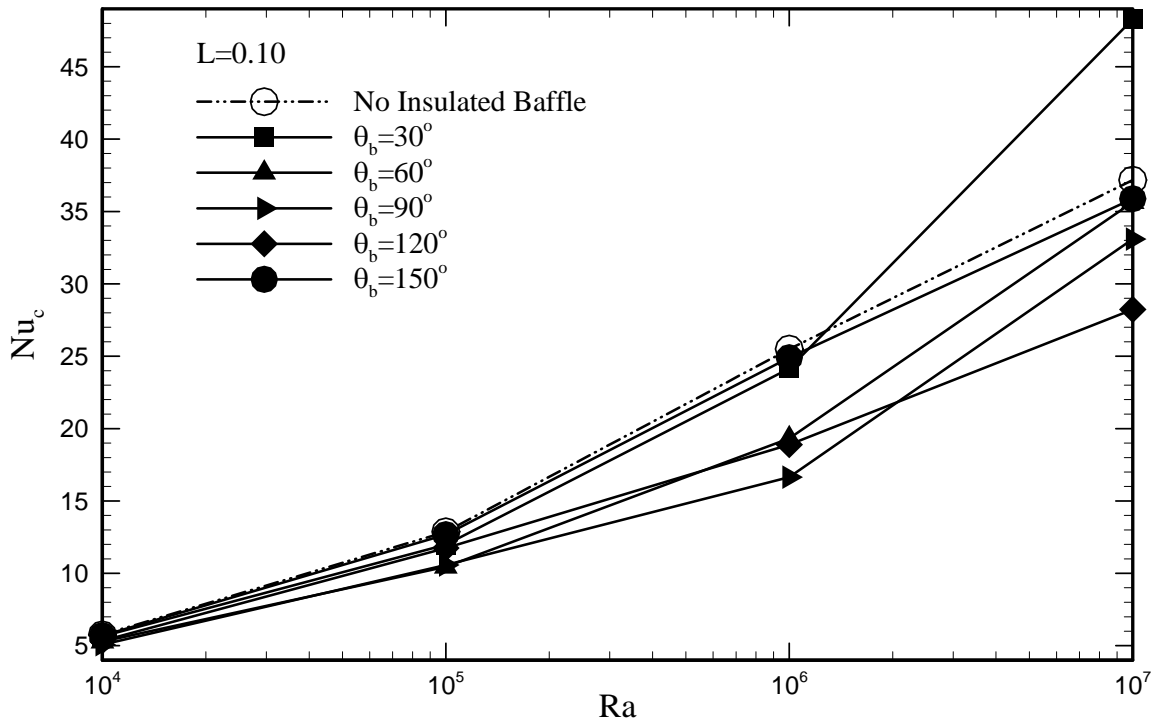


Figure 4.18 Dependence of the time-averaged Nusselt number (Nu_c) on Ra among cases with a fixed thin insulated baffle ($L=0.10$) at various locations ($\theta_b = 30^\circ, 60^\circ, 90^\circ, 120^\circ$ and 150°) and the case without baffle

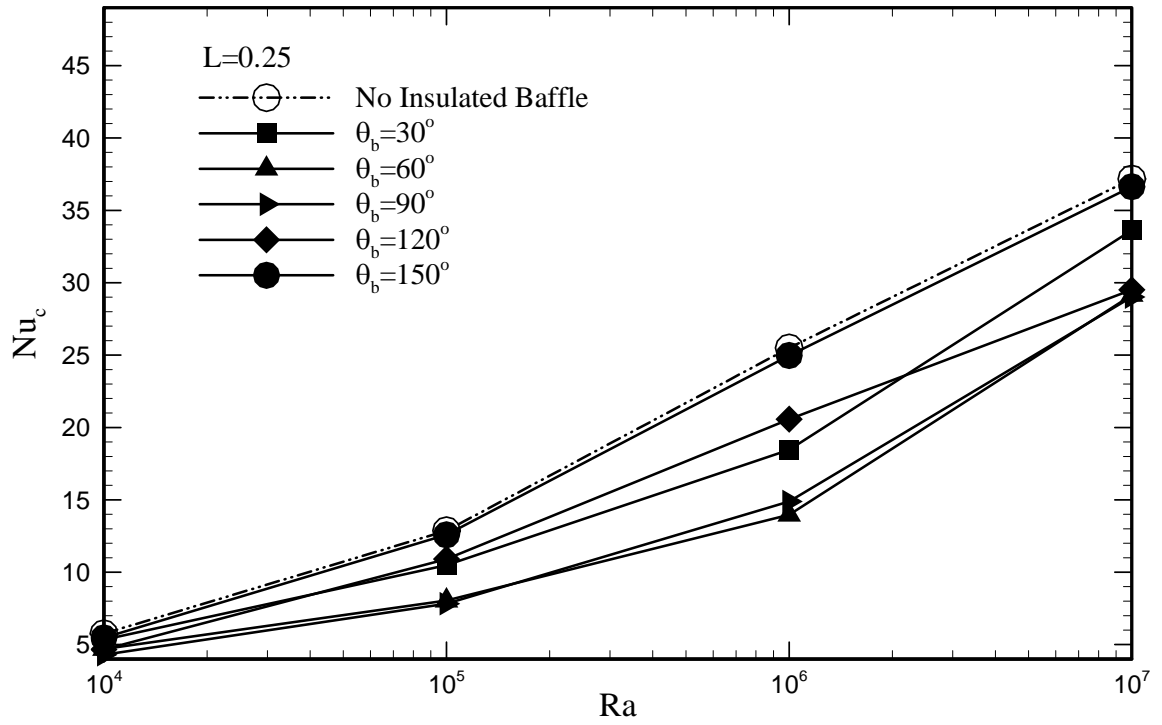


Figure 4.19 Dependence of the time-averaged Nusselt number (Nu_c) on Ra among cases with a fixed thin insulated baffle ($L=0.25$) at various locations ($\theta_b = 30^\circ, 60^\circ, 90^\circ, 120^\circ$ and 150°) and the case without baffle

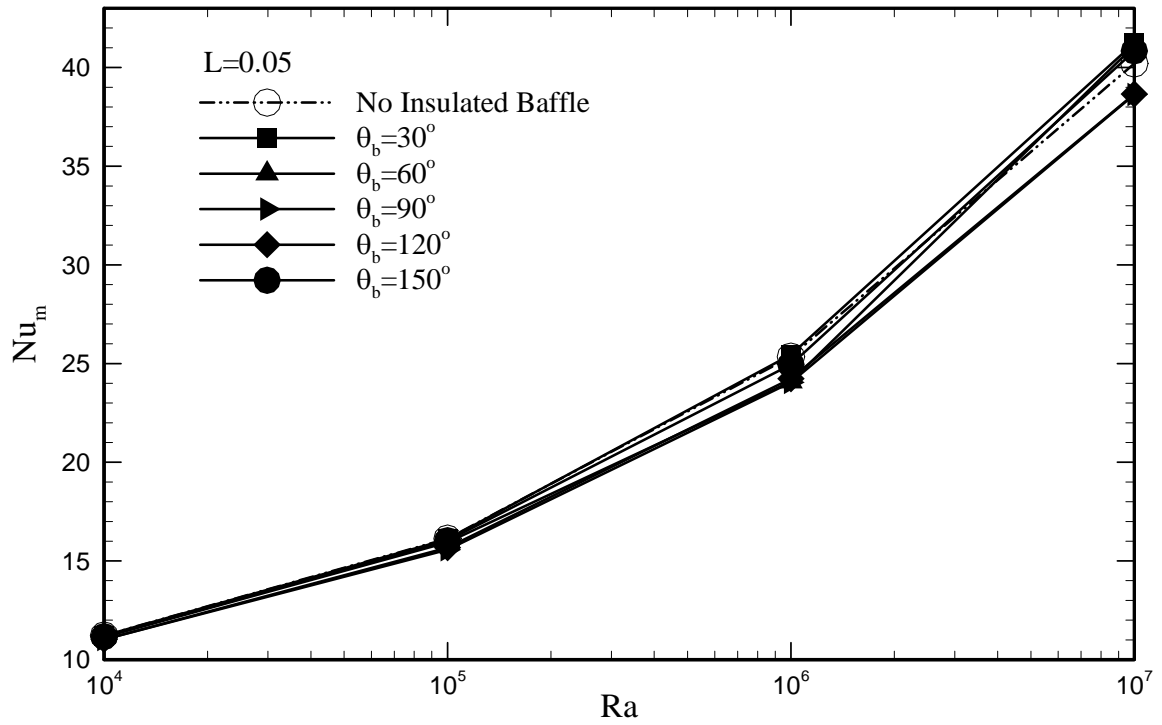


Figure 4.20 Dependence of the time-averaged Nusselt number (Nu_m) on Ra among cases with a fixed thin insulated baffle ($L=0.05$) at various locations ($\theta_b = 30^\circ, 60^\circ, 90^\circ, 120^\circ$ and 150°) and the case without baffle

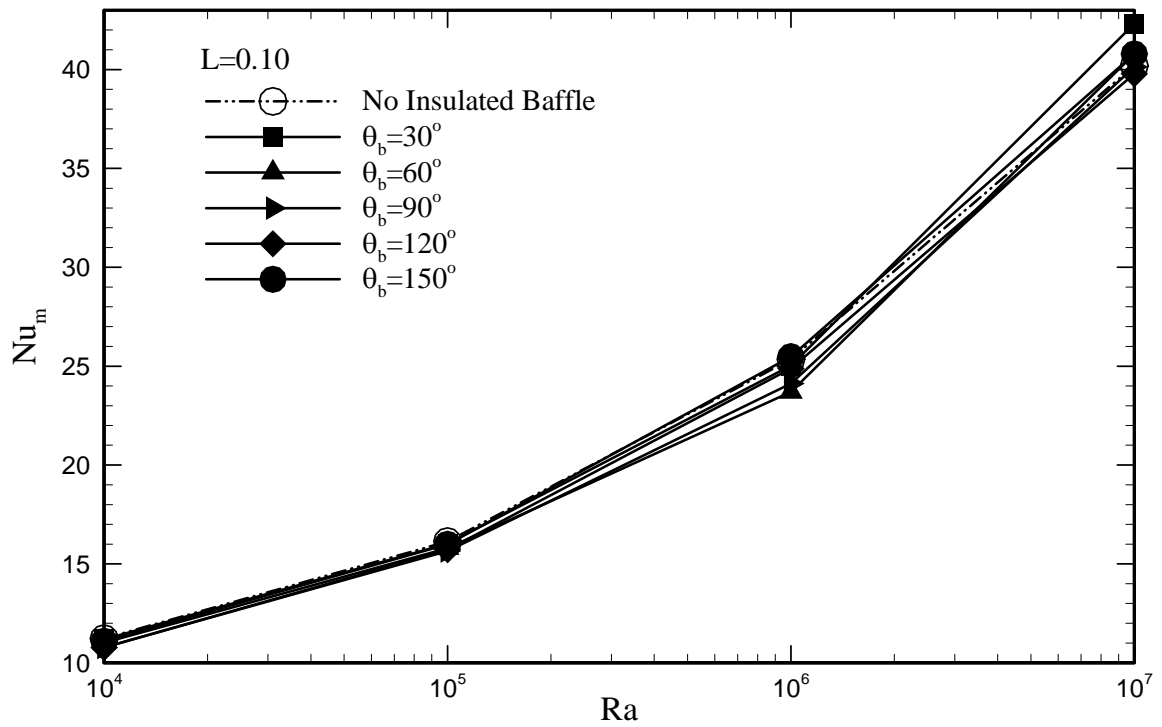


Figure 4.21 Dependence of the time-averaged Nusselt number (Nu_m) on Ra among cases with a fixed thin insulated baffle ($L=0.10$) at various locations ($\theta_b = 30^\circ, 60^\circ, 90^\circ, 120^\circ$ and 150°) and the case without baffle

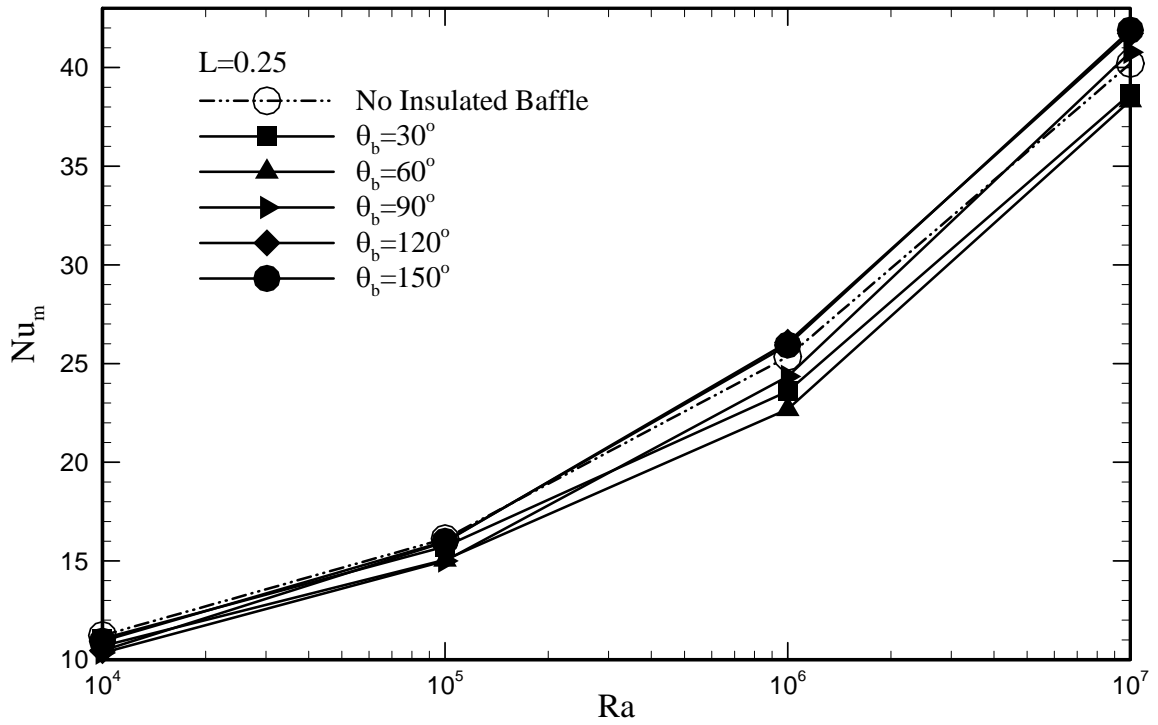


Figure 4.22 Dependence of the time-averaged Nusselt number (Nu_m) on Ra among cases with a fixed thin insulated baffle ($L=0.25$) at various locations ($\theta_b = 30^\circ, 60^\circ, 90^\circ, 120^\circ$ and 150°) and the case without baffle

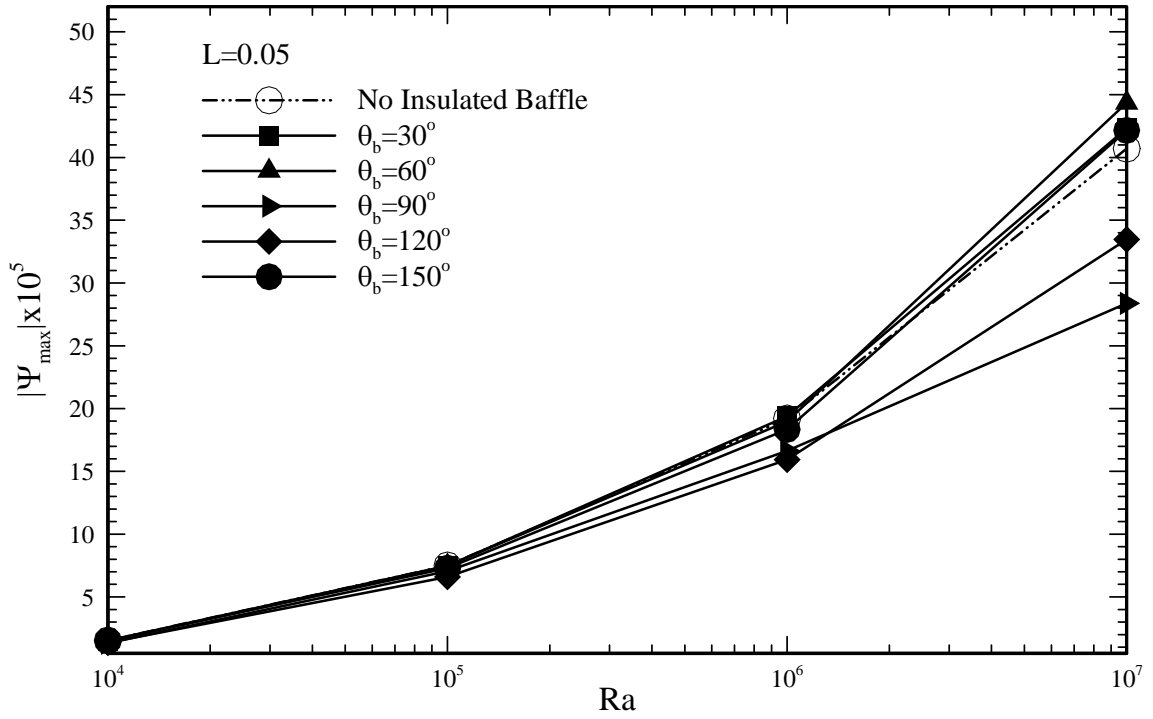


Figure 4.23 Dependence of the maximum stream function ψ_{\max} on Ra among cases with a fixed thin insulated baffle ($L=0.05$) at various locations ($\theta_b = 30^\circ, 60^\circ, 90^\circ, 120^\circ$ and 150°) and the case without baffle

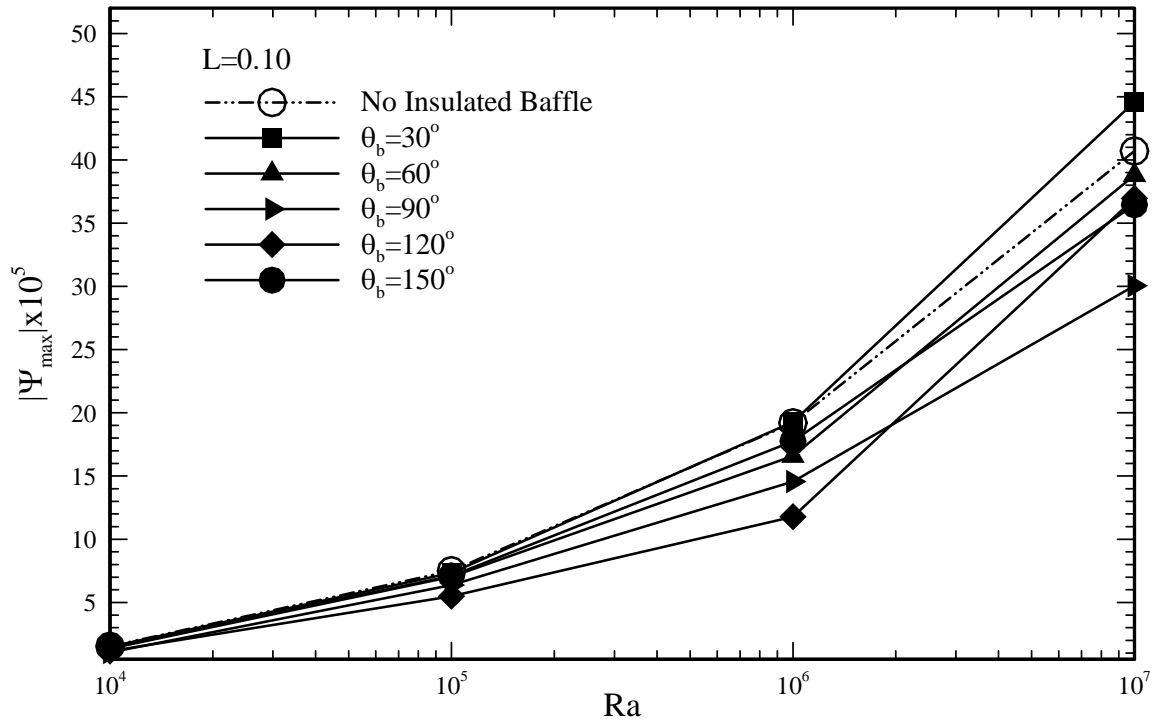


Figure 4.24 Dependence of the maximum stream function ψ_{\max} on Ra among cases with a fixed thin insulated baffle ($L=0.10$) at various locations ($\theta_b = 30^\circ, 60^\circ, 90^\circ, 120^\circ$ and 150°) and the case without baffle

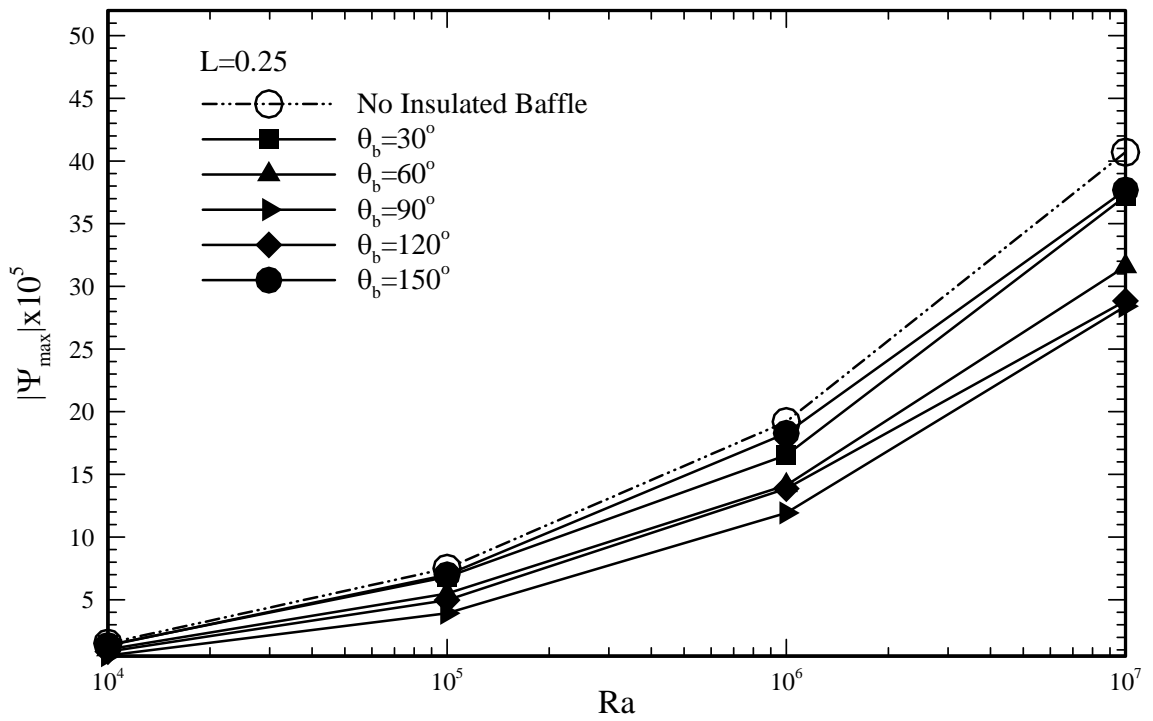


Figure 4.25 Dependence of the maximum stream function ψ_{\max} on Ra among cases with a fixed thin insulated baffle ($L=0.25$) at various locations ($\theta_b = 30^\circ, 60^\circ, 90^\circ, 120^\circ$ and 150°) and the case without baffle

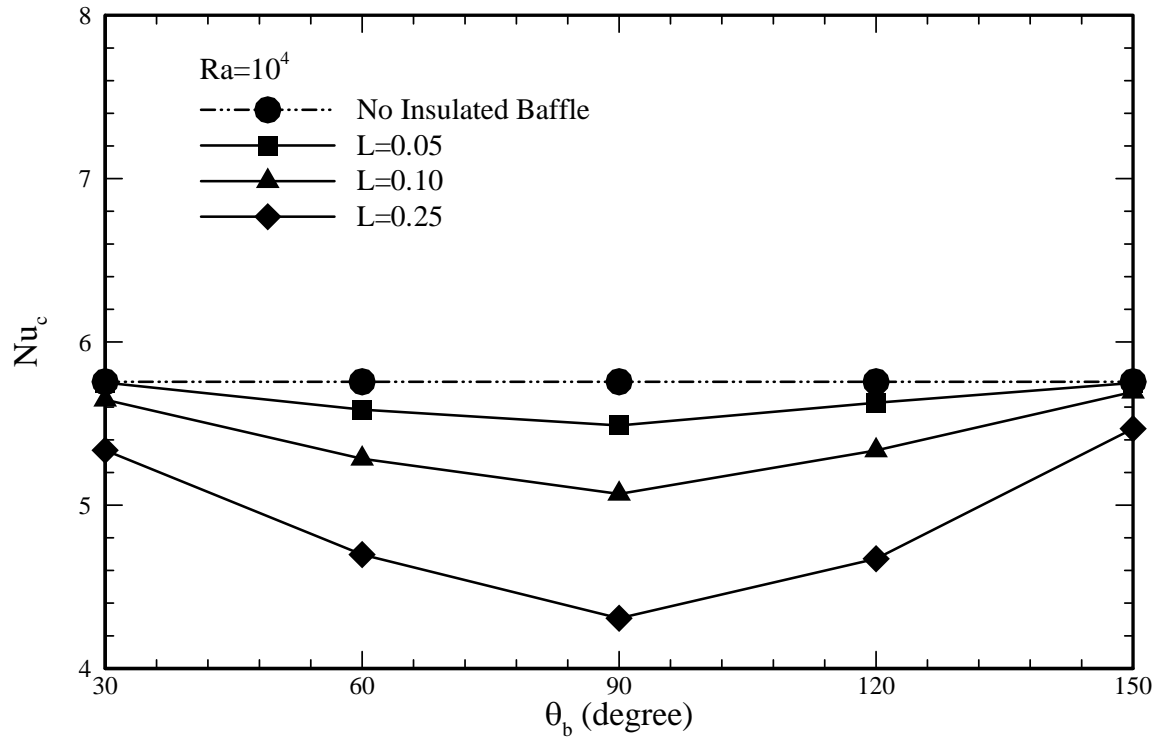


Figure 4.26 Dependence of the Nusselt number (Nu_c) on θ_b among a case without baffle and the cases with a thin insulated baffle of different lengths ($L=0.05, 0.10$ and 0.25) for $Ra=10^4$

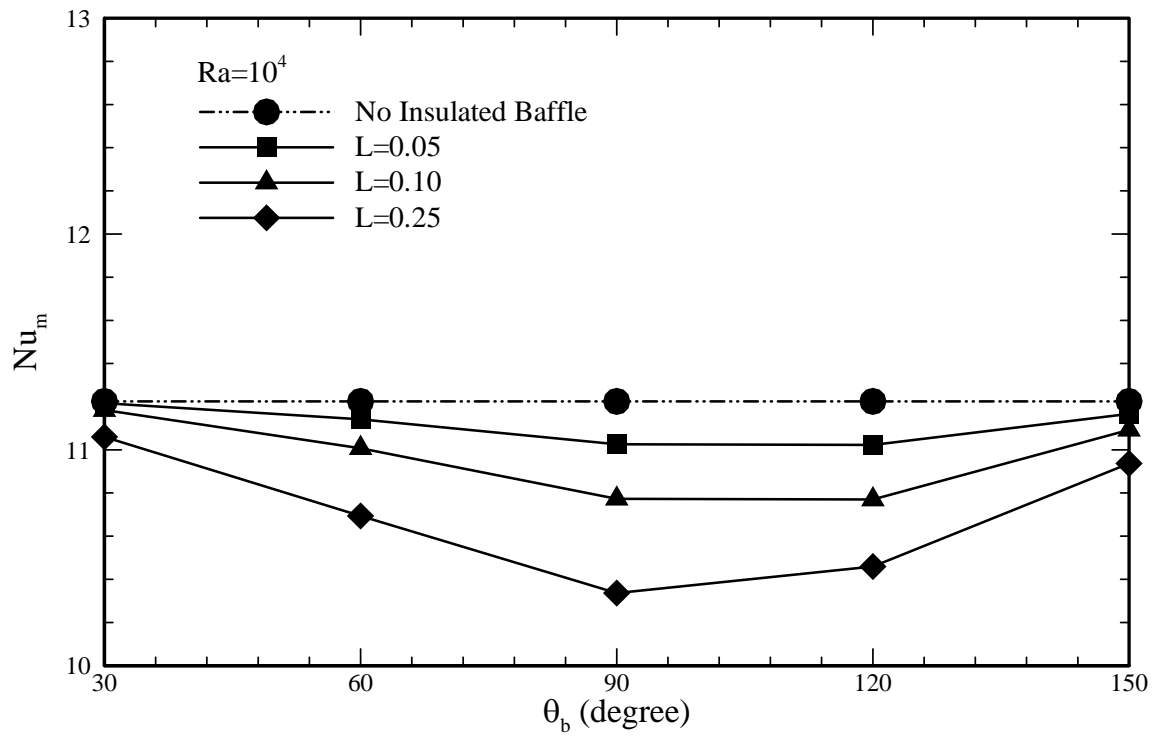


Figure 4.27 Dependence of the Nusselt number (Nu_m) on θ_b among a case without baffle and the cases with a thin insulated baffle of different lengths ($L=0.05$, 0.10 and 0.25) for $Ra=10^4$

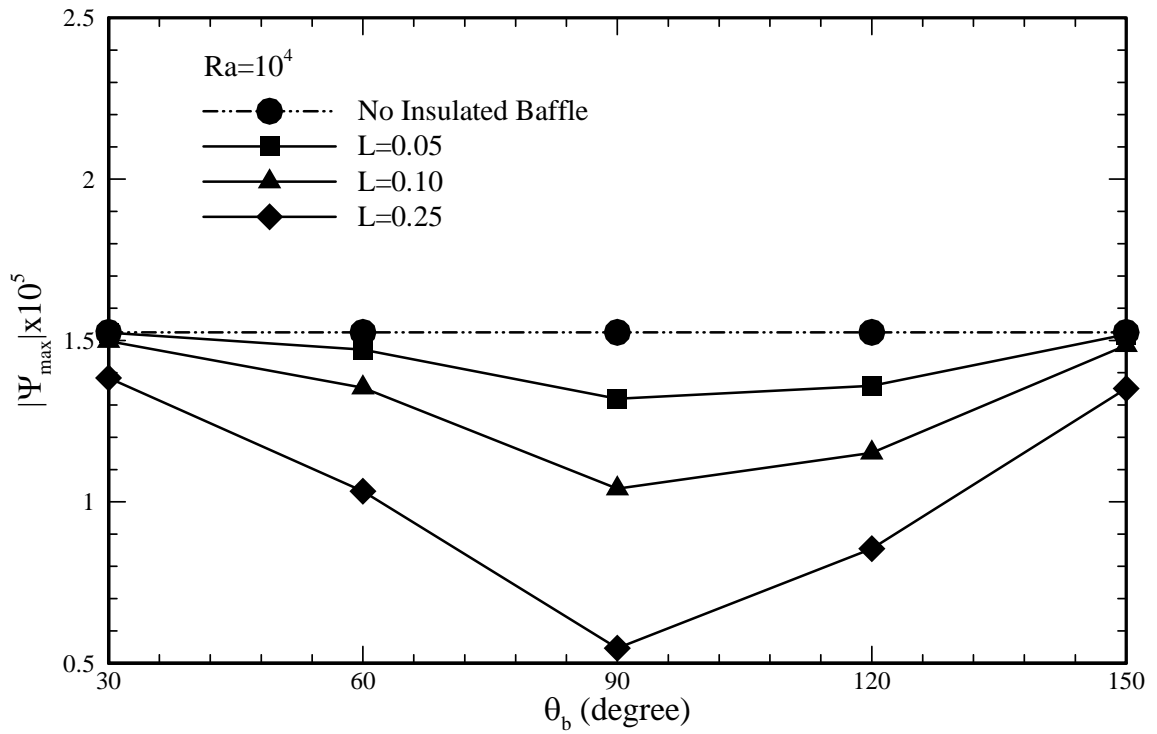


Figure 4.28 Dependence of the maximum stream function ψ_{\max} on θ_b among a case without baffle and the cases with a thin insulated baffle of different lengths ($L=0.05, 0.10$ and 0.25) for $Ra=10^4$

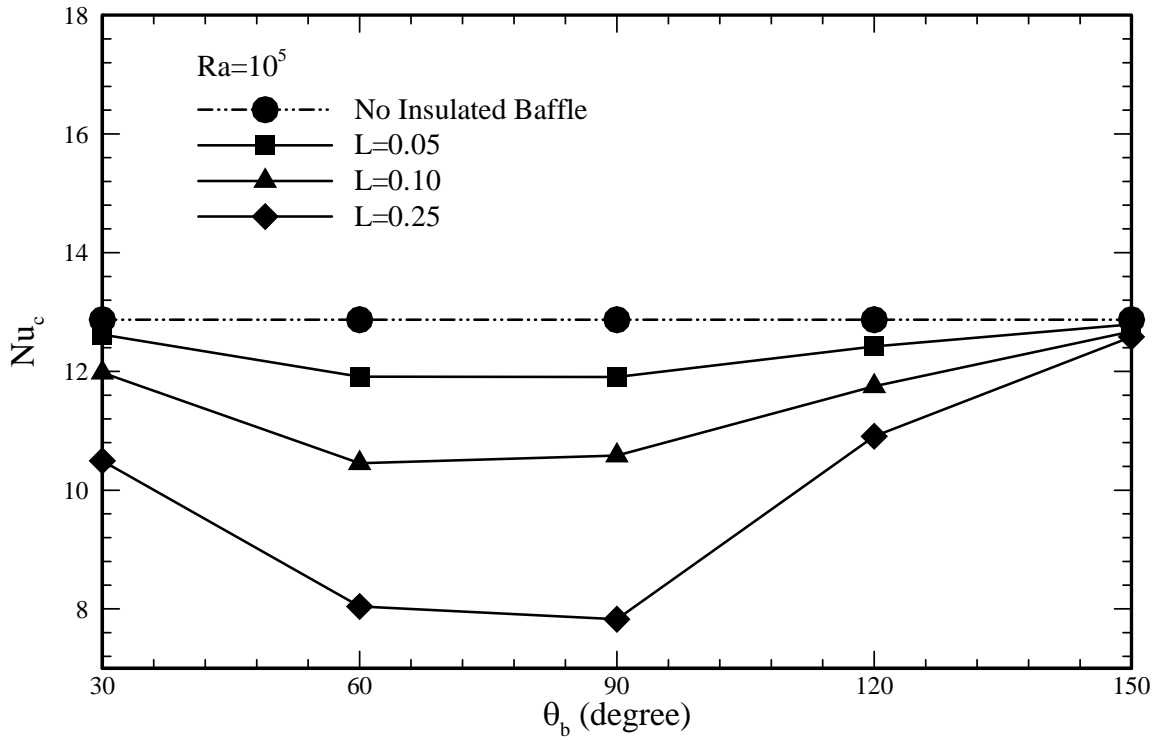


Figure 4.29 Dependence of the Nusselt number (Nu_c) on θ_b among a case without baffle and the cases with a thin insulated baffle of different lengths ($L=0.05, 0.10$ and 0.25) for $Ra=10^5$

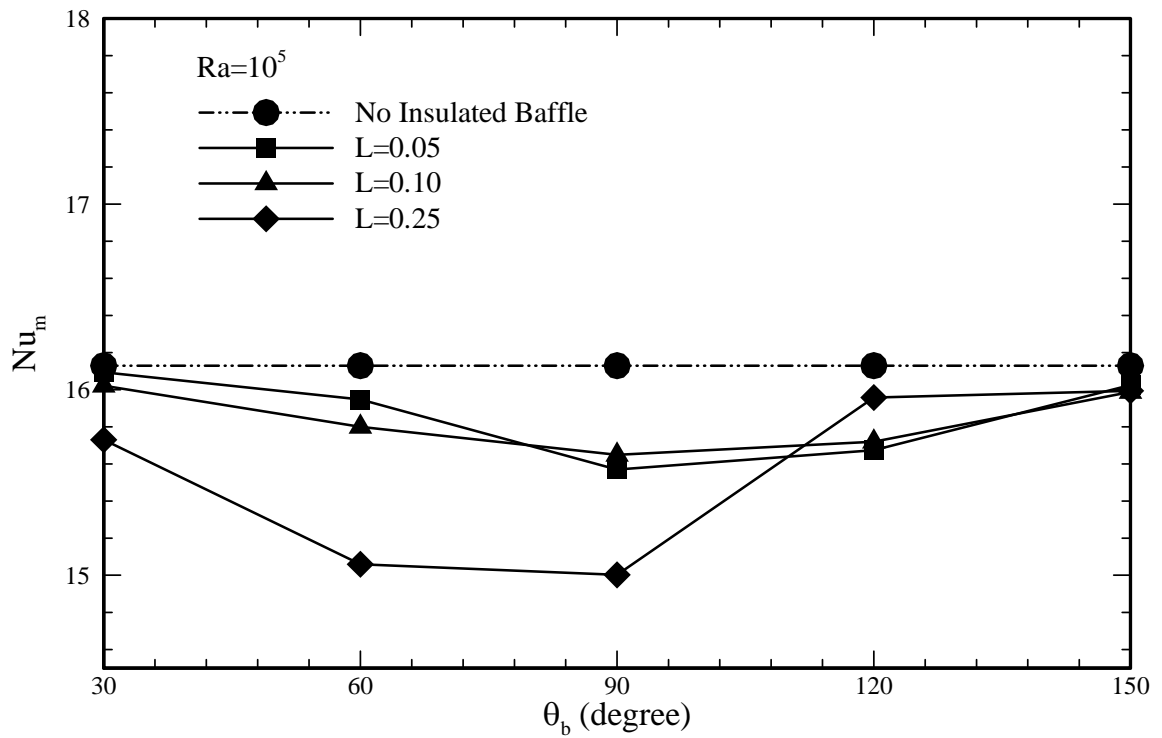


Figure 4.30 Dependence of the Nusselt number (Nu_m) on θ_b among a case without baffle and the cases with a thin insulated baffle of different lengths ($L=0.05$, 0.10 and 0.25) for $Ra=10^5$

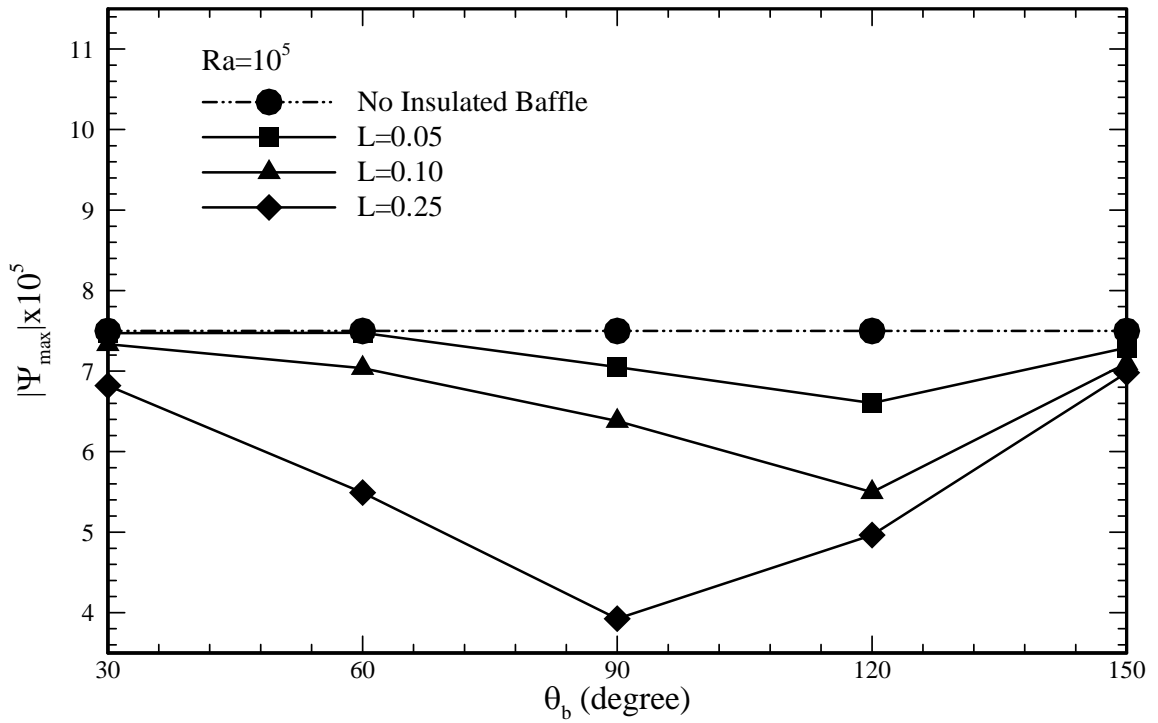


Figure 4.31 Dependence of the maximum stream function ψ_{\max} on θ_b among a case without baffle and the cases with a thin insulated baffle of different lengths ($L=0.05, 0.10$ and 0.25) for $Ra=10^5$

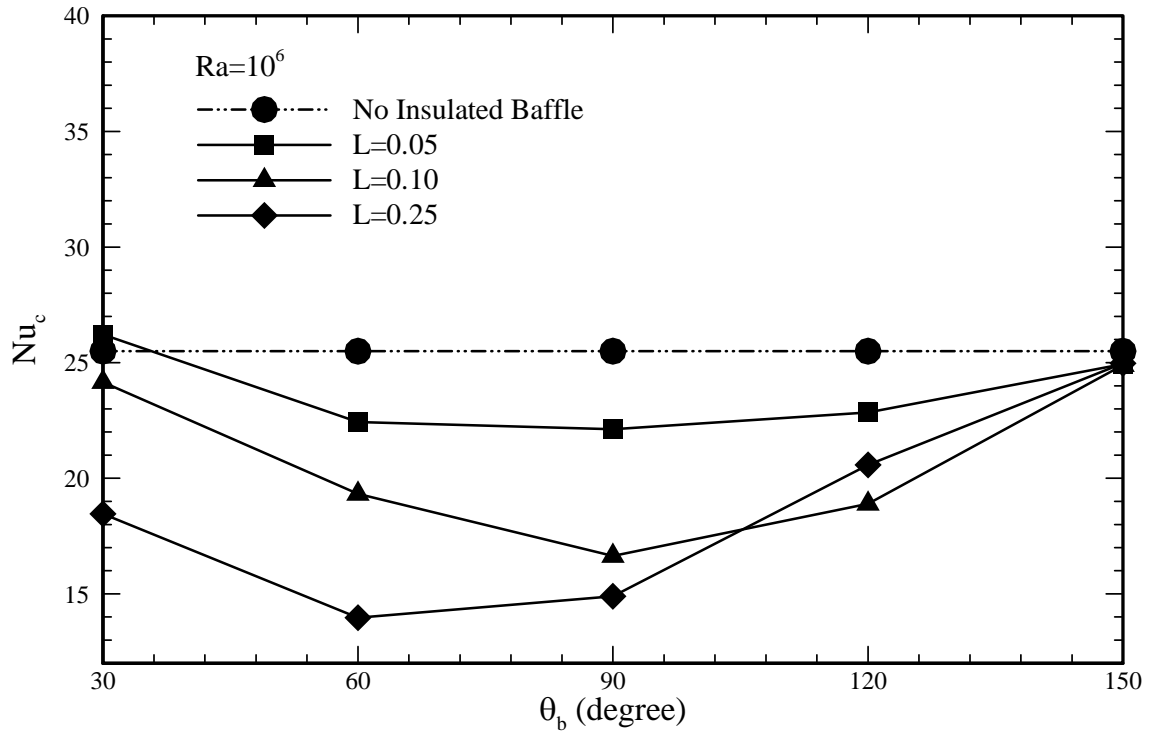


Figure 4.32 Dependence of the Nusselt number (Nu_c) on θ_b among a case without baffle and the cases with a thin insulated baffle of different lengths ($L=0.05, 0.10$ and 0.25) for $Ra=10^6$

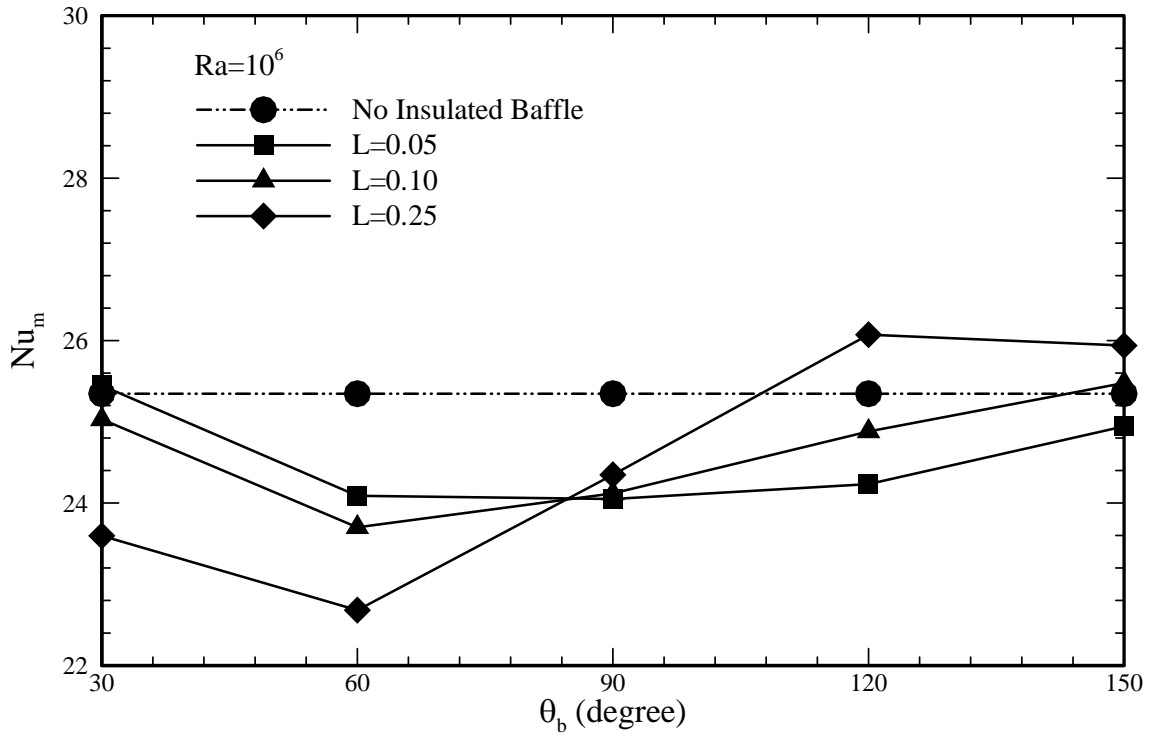


Figure 4.33 Dependence of the Nusselt number (Nu_m) on θ_b among a case without baffle and the cases with a thin insulated baffle of different lengths ($L=0.05$, 0.10 and 0.25) for $Ra=10^6$

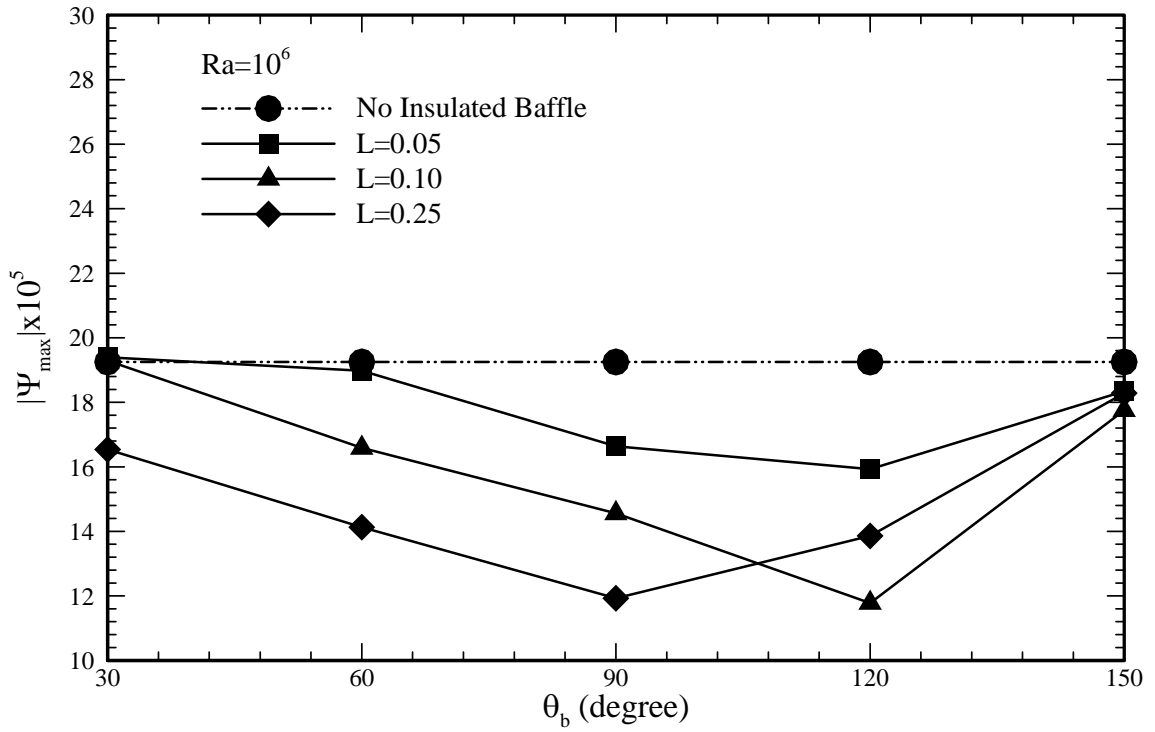


Figure 4.34 Dependence of the maximum stream function ψ_{\max} on θ_b among a case without baffle and the cases with a thin insulated baffle of different lengths ($L=0.05, 0.10$ and 0.25) for $Ra=10^6$

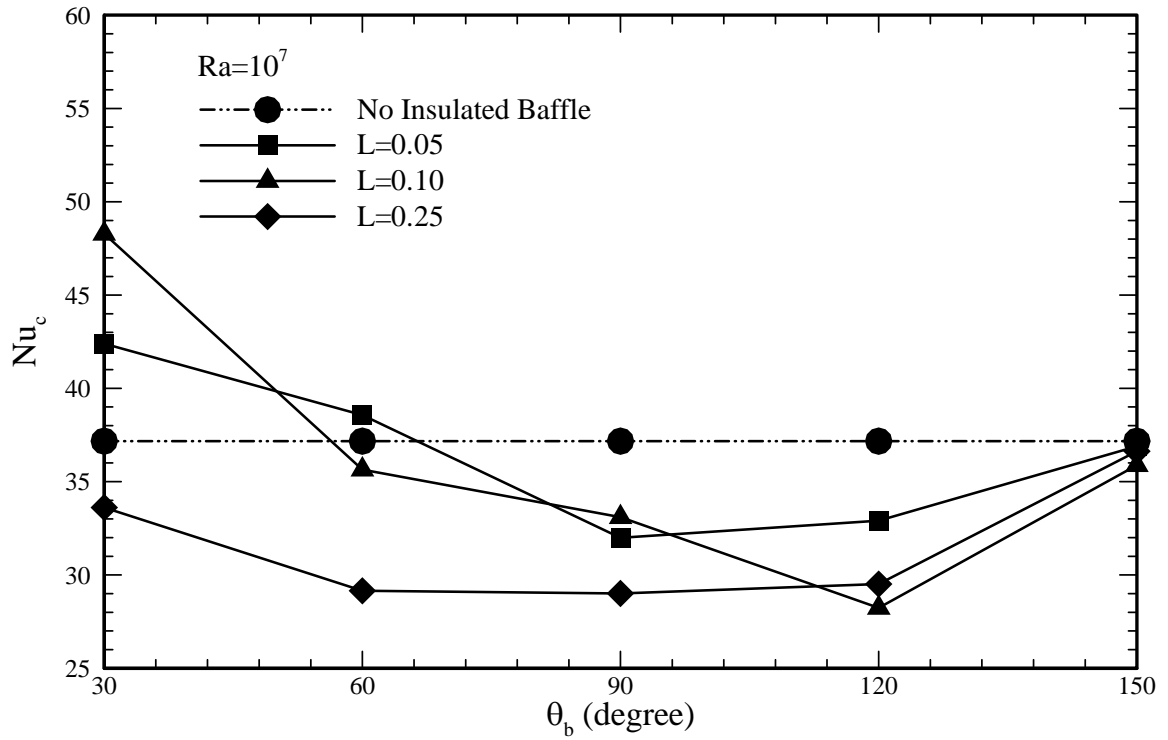


Figure 4.35 Dependence of the Nusselt number (Nu_c) on θ_b among a case without baffle and the cases with a thin insulated baffle of different lengths ($L=0.05, 0.10$ and 0.25) for $Ra=10^7$

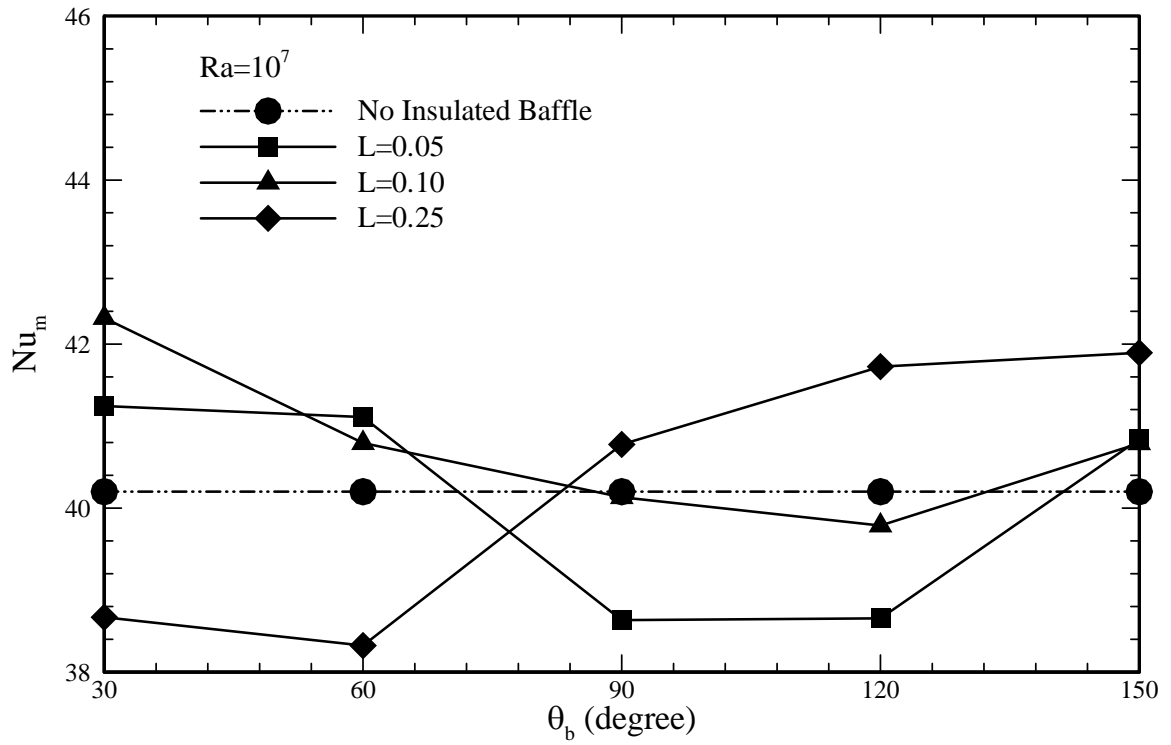


Figure 4.36 Dependence of the Nusselt number (Nu_m) on θ_b among a case without baffle and the cases with a thin insulated baffle of different lengths ($L=0.05, 0.10$ and 0.25) for $Ra=10^7$

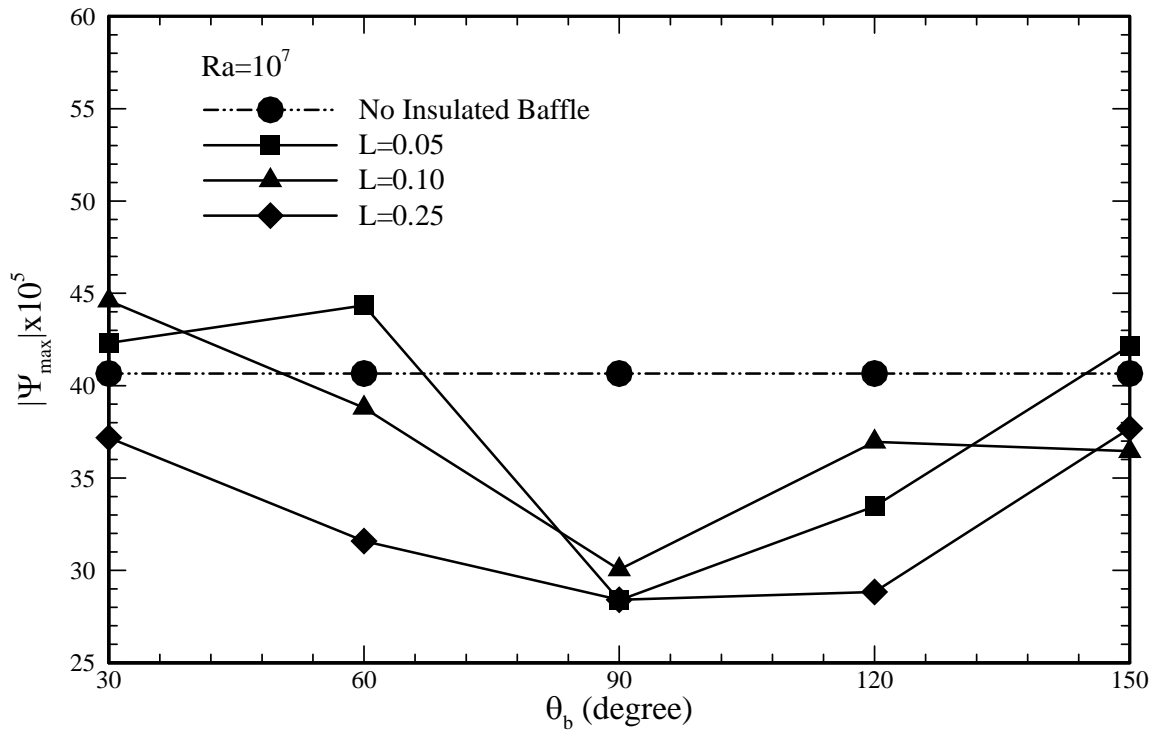


Figure 4.37 Dependence of the maximum stream function ψ_{\max} on θ_b among a case without baffle and the cases with a thin insulated baffle of different lengths ($L=0.05, 0.10$ and 0.25) for $Ra=10^7$

CHAPTER 5 EFFECT OF AN ISOTHERMAL BAFFLE ON PSEUDOSTEADY-STATE NATURAL CONVECTION INSIDE SPHERICAL CONTAINERS

Pseudosteady-state natural convection inside spherical containers with a thin insulated baffle was studied using a computational fluid dynamic package (FLUENT) in Chapter 4. In the absence of addition of extra thermal energy to the fluid by the thin insulated baffle, it was shown that the presence of a thin insulated baffle can generally degrade heat transfer due to blockage of fluid flow next to the wall of the sphere. Such a knowledge of management of heat transfer and fluid flow is of great interest in engineering applications. The insulated thermal condition of the baffle limits its use in some applications. Considering the other extreme limiting case, further research was conducted. The objective of this Chapter is to investigate the effect of a perpendicular-to-wall isothermal thin baffle on the flow field as well as heat transfer. Parametric studies were performed for a Prandtl number of 0.7. For Rayleigh numbers of 10^4 , 10^5 , 10^6 and 10^7 , baffles with 3 lengths positioned at 5 different locations were investigated. In effect, a parametric study involving 60 cases was performed.

5.1 Mathematical Formulation for the Pseudosteady-State Natural Convection inside Spherical Containers with a Thin Isothermal Baffle

A thin isothermal baffle is attached on the inside wall of a spherical container along the radial direction and points to the center. A schematic diagram for the posed problem is illustrated in Figure 5.1. Mathematically, an extra boundary condition is introduced due to the presence of a thin isothermal baffle, while the modeling assumptions are the same as Chapter 3.

5.1.1 Governing Equations and Boundary/Initial Conditions

Further research on the effect of a baffle on the flow and thermal fields is reported on the basis of Chapters 3 and 4, by switching from a thin insulated baffle to the case of a thin isothermal baffle. The governing equations are same as those formulated in Chapter 3 (Equations 3.1-3.5) and are not repeated here.

The no-slip boundary condition is imposed on the wall and two sides of the thin isothermal baffle. The thermal conductivity of the baffle is very high, so that its temperature is always same as the container's wall temperature. The applicable dimensionless boundary conditions on the wall ($r^* = 1$) and the two sides of the thin isothermal baffle ($(1 - 2L) \leq r^* < 1$ and $\theta = \theta_b$) are:

$$V_\theta^* = V_r^* = 0, \quad (5.1)$$

$$T_w^*(\tau) = T_c^*(\tau) + 1 \quad \text{for } \tau \geq 0. \quad (5.2)$$

On the symmetry axis ($\theta = 0$ and π):

$$V_\theta = \frac{\partial V_r^*}{\partial \theta} = \frac{\partial T^*}{\partial \theta} = 0. \quad (5.3)$$

A schematic drawing of the system, including the baffle is similar to Figure 4.2. Pseudosteady-state natural convection inside spherical containers with a thin isothermal baffle is driven by the temperature difference between the solid wall (including baffle) and center. A thin insulated baffle can not bring in any energy into the system, whereas a thin isothermal baffle can contribute heat flux to the fluid in the container. This distinct difference indicates that the flow field and heat transfer for cases with isothermal baffles can become more complicated than the cases with insulated baffles.

Pseudosteady-state natural convection inside spherical containers with thin isothermal baffles is governed by dimensionless parameters of the Rayleigh number, Prandtl number, baffle length and position. Hutchins and Marschall (1989) and Shen et al. (1995) have shown that numerical solution exhibits extremely weak dependence on the Prandtl number within the range of 0.7 to 8. Therefore, the Prandtl number is not taken as a variable but a constant equal to 0.7. Various Rayleigh numbers are investigated for different baffle parameters (L and θ_b).

5.1.2 Computational Details

Considering the particular difficulty associated with presence of a thin isothermal baffle in a sphere, the solution was handled by use of a commercial computational fluid dynamic (CFD) package. The mesh is generated using GAMBIT (version 2.2.30) and the commercial code FLUENT (version 6.2.16) is utilized for solving the governing equations. All the computations (60 cases) were performed on the Cray XD1 supercomputer of the Alabama Supercomputer Authority (Huntsville, Alabama).

The mesh generation procedures and FLUENT settings are same as the cases with thin insulated baffles that were discussed in Chapter 4 and the details are not repeated here.

5.1.3 Code Validation

The computational results were benchmarked against previous data available in the literature by comparing the heat transfer correlations, temperature distribution and streamline patterns for cases with no baffle. The code validation and verification procedures for the pseudosteady-state natural convection inside spherical containers without baffles are discussed in detail in Chapter 3. As for mathematical formulation, the presence of a thin isothermal baffle introduces an extra boundary condition on the baffle, while the governing equations are same as the case without baffles. Therefore, it is considered that the code validation reported in Chapter 3 has provided enough confidence in the appropriateness of pseudosteady-state natural convection inside spherical containers with isothermal thin baffles.

5.2 Grid and Time Step Size Independence Study

The grid density and the time step size exhibit extremely strong effects on the accuracy of numerical solution. The grid density and time step size independence tests have been studied in Chapter 4 for the pseudosteady-state natural convection inside spherical containers with a thin insulated baffle. When a thin isothermal baffle replaces a thin insulated baffle, the flow is expected to be more dynamic due to extra heating effect of the isothermal baffle. This indicates that the “proper mesh” suitable for the case with a

thin insulated baffle may not be suitable for the case with a thin isothermal baffle within the required accuracy. Therefore, independence studies for grid density and time step size were performed based on the grid information that is similar to the cases with insulated baffles. The case ($L=0.25$ and $\theta_b = \frac{\pi}{2}$) with an isothermal thin baffle for the Rayleigh number of 10^7 is selected for the sensitivity test. The schematic geometry employed for the grid independence study is illustrated in Figure 4.3(c). Time-averaged Nusselt numbers are employed as representative parameters to evaluate the accuracy of the numerical solution. Grid density and time step size are two independent variables, thus these two independence studies can not be done at the same time. The grid size independence is tested first, while the time step size is fixed to 2 seconds ($\Delta\tau = 1.57 \times 10^{-4}$). The effect of the spacing of the first row of the “boundary layer” mesh, number of nodes on the baffle and density of the “interior” nodes are studied. For convenience, a parameter called the “number of cells” is used to describe the overall grid density. The variations of the time-averaged Nusselt numbers (Nu_m and Nu_c) on the overall grid density along with the RMS values are illustrated in Figures 5.2 and 5.3, respectively. The tabulated values of these Nusselt numbers are also presented in Table 5.1. It is observed that the time-averaged Nusselt number values do not change markedly when the number of cells is greater than 10^4 . Considering both the accuracy of the solution and the computational time, the mesh with 13,868 cells is considered as a “proper” mesh and is shown in Figure 4.3(c). All the other grid systems were created based on the parameters of this “proper” mesh. Hence, it was concluded that the grid system suitable for cases with a thin insulated baffle is also suitable for cases with a thin isothermal baffle.

Table 5.1 Dependence of the time-averaged and RMS values of the Nusselt numbers on the number of cells for an isothermal case with $Ra=10^7$, $Pr=0.7$, $L=0.25$, $\theta_b = 90^\circ$ and

$$\Delta\tau = 1.57 \times 10^{-4}$$

Number of Cells	Nu_c	$RMS _{Nu_c}$	Nu_m	$RMS _{Nu_m}$
108	19.8663	5.90E-05	24.8261	2.80E-05
318	27.7329	1.4298	37.0698	0.7274
962	33.5458	3.8704	42.0646	1.7535
2,084	33.9722	7.4818	44.045	4.5685
5,200	32.4959	8.1602	40.3278	6.9394
6,790	32.4986	7.4417	39.3839	6.3753
8,972	31.8137	6.7483	39.9492	5.5549
9,500	31.7294	7.0372	39.9635	5.2822
10,998	32.3284	7.5086	39.7588	6.4909
13,868	32.1272	7.36998	40.2304	6.82308
15,618	32.1188	8.602	40.0673	7.4348
23,584	32.2059	8.5845	40.2089	7.424
29,218	33.0703	8.0383	40.352	6.923
35,744	32.3324	8.1451	40.2915	6.8855

Similar to what was discussed in the independence study of Chapter 4, the time step size independence was conducted. The variation of the time-averaged Nusselt numbers (Nu_m and Nu_c) on the time step size along with the RMS values for the same isothermal baffle discussed above is shown in Figures 5.4 and 5.5, respectively. The values of these quantities are also given in Table 5.2. Taking both the accuracy of the solution and the computational time into account, a time step size of 2 seconds ($\Delta\tau = 1.57 \times 10^{-4}$) is selected as a proper time step size for all 60 cases with thin isothermal baffles.

Table 5.2 Dependence of the time-averaged and RMS values of the Nusselt numbers on the time step size for an isothermal case with $Ra=10^7$, $Pr=0.7$, $L=0.25$, $\theta_b = 90^\circ$ and

13,868 cells

Δt (s)	Nu_c	$RMS _{Nu_c}$	Nu_m	$RMS _{Nu_m}$
0.1	32.3599	7.76638	40.2526	6.60545
0.2	33.0188	8.28112	40.2959	7.31774
1	32.6375	8.01251	40.2261	7.3654
2	32.1272	7.36998	40.2304	6.82308
3	31.2453	5.74914	40.026	5.29944
5	31.4553	6.79749	40.3208	7.0884
7	33.5314	6.86723	40.903	8.25014
8	33.2931	6.30238	40.8288	7.65948
10	32.3229	5.93448	40.7544	7.39692
15	28.8112	4.5176	39.7598	5.86457
30	25.4682	2.59521	38.4361	3.2171

5.3 Results and Discussion

The flow and temperature fields strongly depend on the Rayleigh number, isothermal baffle location and length. Temperature and stream function contours for 45 cases ($Ra=10^4$, 10^5 and 10^6) are presented for the pseudosteady-state condition, whereas the time-dependent flow and thermal fields of the high Ra cases ($Ra=10^7$) are discussed separately.

5.3.1 Pseudosteady-State Fluid Flow and Thermal Fields for $Ra=10^4$, 10^5 and 10^6

The composite diagrams of the streamlines and temperature contours for three isothermal baffles with lengths ($L=0.05$, 0.1 and 0.25) placed at various polar angle locations ($\theta_b = 30^\circ$, 60° , 90° , 120° and 150°) for a Rayleigh number of 10^4 are presented

in Figure 5.6. Diagrams in each row correspond to baffles of various lengths positioned at a fixed location, whereas for each column the effects of a baffle with a fixed length at various positions are given. By comparing the streamline patterns and temperature fields in this figure to the limiting case of no baffle in Figure 3.13 for the same Ra , the effect of a thin isothermal baffle can be elucidated. Focusing on the left column of Figure 5.6, it is clear that the presence of the shortest baffle ($L = 0.05$) does not alter the flow and thermal fields significantly, regardless of the angular position of the baffle. The distortions are restricted to minor alteration of the streamlines next to the short baffles as well as temperature field. For the cases corresponding to the $L = 0.1$ baffle that are shown in the middle column, the modifications to the flow and thermal fields are a bit more marked than the cases with the shortest baffle, however the changes are still observed to be next to the baffle. In contrast, marked changes to the flow field are observed in the right column of Figure 5.6 that correspond to the longest baffle ($L = 0.25$), specially for the cases when the baffle is located at $\theta_b = 60^\circ, 90^\circ$ and 120° . For these cases, two distinct recirculating vortices are observed on both sides of the baffle. These vortices rotate in the clockwise (CW) direction lifting heated fluid next to the wall to a higher elevation and bringing down colder fluid. The temperature fields have also been affected markedly by the longer length of the baffle and the pseudo-concentric ring contour patterns have been greatly modified in the vicinity of the isothermal baffle. It can clearly be stated that due to the isothermal condition of the baffle, this structure perturbs the thermal field dramatically to the extent that a marked temperature gradient next to the baffle is observed. In addition to modifying the flow paths, the isothermal baffle is responsible for bringing in heat into the sphere due to availability of a larger surface area.

For the Rayleigh number of 10^5 , streamlines patterns and temperature contours for three baffles with lengths ($L = 0.05, 0.1$ and 0.25) placed at various locations ($\theta_b = 30^\circ, 60^\circ, 90^\circ, 120^\circ$ and 150°) are shown in Figure 5.7. Diagrams are plotted going from left column to right column with the dimensionless baffle length increasing from 0.05 to 0.25. Comparing the streamline patterns and temperature fields on the left column of Figure 5.7 ($L = 0.05$) with the case of no baffle (Figure 3.13), the presence of the shortest thin isothermal baffle ($L=0.05$) modifies the thermal fields to some extent for various angular positions of the baffle. The flow field modifications are not very significant that is similar to the cases in Figure 5.6 ($Ra=10^4$), while modification of the thermal fields are also observed to be minimal. In general, the flow and thermal fields exhibit features similar to those discussed above for Figure 5.6.

Streamlines and temperature contours for three isothermal baffles with lengths ($L = 0.05, 0.1$ and 0.25) placed at various locations ($\theta_b = 30^\circ, 60^\circ, 90^\circ, 120^\circ$ and 150°) for a Rayleigh number of 10^6 are presented in Figure 5.8. Comparing the streamline patterns and temperature fields on the left column of Figure 5.8 ($L = 0.05$) with the case of no baffle (Figure 3.13), the presence of the shortest baffle modifies the flow and thermal fields to some extent for the various angular positions of the baffle. The flow modifications are confined to streamlines next to the short baffle through its interaction with the eye of the vortex that is closer to the wall compared to similar cases in Figures 5.6 and 5.7. For some positions of the short baffle, two eyes within the CW rotating vortex are observed. In regard to the effect of the shortest baffle on the temperature contours, the changes are more pronounced in comparison to similar cases of Figure 5.7, however they are still localized in the vicinity of the baffle. The flow modifications are

more pronounced for $L = 0.1$ baffles that are shown in the middle column of Figure 5.8, particularly when the baffle is located at $\theta_b = 90^\circ$, 120° and 150° . For these cases, the double CW rotating vortex structure is further complicated by appearance of a counter CW rotating vortex that is located partly on top of the baffle and very near the open end of the baffle. In contrast to a similar vortex that was observed for the same conditions but with an insulated baffle in Chapter 4, this vortex extracts heat from the isothermal baffle and is observed to be stronger and has a bigger spatial coverage. One can also note that the multi-vortex structure can clearly rearrange the thermal field when compared to the case of the shortest baffle that exhibited constant-temperature stratified layers in the vicinity of the symmetry axis of the sphere. In assessing the effect of the long baffle on the flow fields in the right column of Figure 5.8, modifications that are similar to the case of $Ra = 10^5$ in Figure 5.7 are observed. In general, two CW rotating vortices are clearly observed for all the cases. In addition, a fresh third counter CW rotating vortex with its eye at $\theta < \approx \theta_b$ is created for cases with $\theta_b \geq 90^\circ$. This vortex gains more spatial coverage as the baffle is placed deeper into the lower hemisphere and is sandwiched between the two CW rotating vortices when the baffle is located at $\theta_b = 120^\circ$ and 150° . The entire top surface of the baffle is in contact with this counter CW rotating vortex. Observing the marked temperature gradient next to the top surface of the baffle, this fresh vortex is clearly energized by the extra heat that is brought into the sphere from the top surface of the baffle. As for the effect of the longest baffle on the thermal field, if the baffle is located such that $\theta_b \leq 90^\circ$, parts of the interior of the sphere is composed of stable stratified constant-temperature layers. This suggests that the flow within these regions is not strong and conduction mode of transport is dominant. For other positions

of the baffle in the lower hemisphere, the remainder of the sphere is greatly affected by the extra heat that is brought into the sphere through the extended surface of the baffle. The extra heat coming through the baffle energizes a counter CW rotating vortex that directs hot fluid toward the center of the sphere, thus reducing thermal stratification. As a general observation, note that the baffle divides the thermal field into two zones. Both zones have areas of intense wall heat transfer that are located at the bottom of the sphere and angular positions $\theta < \approx \theta_b$. The top zone is generally a region of stable constant-temperature layers suggesting weak natural convection and its spatial coverage diminishes as the location of the baffle moves lower. The bottom zone is generally observed to be the site of strong natural convection that is brought about by the extra heating afforded by the baffle.

The effects of the Rayleigh number (10^4 , 10^5 , 10^6 and 10^7) and baffle's position ($\theta_b = 30^\circ$, 90° and 150°) on streamlines and temperature contours for the case of the longest baffle ($L=0.25$) are presented in Figure 5.9. With the baffle positioned near the top at $\theta_b = 30^\circ$ (left column), the increase of the Rayleigh number brings about stronger convection and fluid flow within the CW rotating vortex as indicated by the denser packing of the streamlines next to the surface. This is accompanied by lifting of the eye of the vortex and its migration outward. For the highest Ra number studied, a weak vortex is observed near the top within the cone, part of which is the baffle. The vortex at the bottom that is driven by the thermally unstable stratified layers is present. The temperature contours exhibit greater deviation from the concentric ring patterns as natural convection strengthens. With the baffle located at $\theta_b = 90^\circ$ (middle column), two CW rotating vortices occupy the two hemispherical regions with the lower half of the sphere

being the site of stronger convection. As the Ra number is raised, a third counter-CW rotating vortex is created above the top surface of the baffle and next to the free end of the baffle. For the highest Ra number studied, two vortices occupy the top hemisphere. For this case, the top hemisphere is partially stratified with stable constant-temperature layers occupying it, whereas the thermal field within the bottom hemisphere is heavily affected by the stronger rotating vortex that occupies it. The flow fields for the cases with the longest baffle positioned near the bottom at $\theta_b = 150^\circ$ (right column) exhibit many of the features with the baffle located at $\theta_b = 30^\circ$, but in reverse in addition to the appearance of another counter CW rotating vortex for a wide range of the Rayleigh number. The appearance of this counter CW rotating vortex is directly linked to the isothermal surface of the baffle and the resultant extra heat released into the fluid from this surface. A recirculating vortex that occupies the small space between the baffle and the symmetry line of the sphere is clearly observed. As for the temperature contours, the alterations appear to be generally confined to the lower hemisphere for all the Rayleigh numbers and more dramatically in the vicinity of the symmetry axis for the higher Ra numbers. Extremely pronounced modifications of the temperature fields are observed for the high Ra number cases showing that stratifications are generally eliminated and the extra heat added to the sphere is transported inside by a counter CW rotating vortex that is positioned next to the top surface of the baffle.

5.3.2 Time-Dependent Fluid Flow and Thermal Fields for Ra=10⁷

In order to illustrate the time-dependent nature of the flow for most of the Ra=10⁷ cases, a representative case of Ra=10⁷, L=0.25 and $\theta_b = 60^\circ$ was selected. The

instantaneous composite diagrams of the streamlines and temperature contour fields for this case during a “cycle” are shown in Figures 5.10 (a)-(i). In order to aid the reader, a companion diagram showing the variation of the instantaneous area-averaged Nusselt number is also shown in Figure 5.11. The cyclic nature of the instantaneous Nusselt number is clearly shown and the instants at which the composite streamlines and temperature contours of Figure 5.10 were shown are marked by letters a-i. An extremely dynamic flow field is observed within the cycle with distinct growth and decay of a multitude of vortices. Most notably, the primary vortex below the baffle decays early in the cycle (Figure 5.10 (a)-(c)) and then re-energizes during the remainder of the cycle. The vortex that is near the bottom of the sphere and is linked to the unstable stratified temperature layers is exhibiting dynamic behavior during the cycle. The temperature gradients next to the wall of the sphere and the baffle vary dramatically during the cycle and are clearly linked to the variation of the instantaneous averaged Nusselt number shown in Figure 5.11.

5.4 Nusselt Number Definitions and Other Parameters

Before further discussion, the important parameters used to characterize the flow field and heat transfer quantitatively are defined.

5.4.1 Definitions of the Nusselt Numbers

The Nusselt number represents the ratio of convection heat transfer to conduction heat transfer. Hence, it is used to characterize the strength of pseudosteady-state natural convection inside spherical containers with thin isothermal baffles. The Nusselt number

either can be derived directly from the temperature gradient at the wall and baffle, or can be obtained by performing an energy balance for the fluid within the container, which is similar to the work done by Hutchins and Marschall (1989). Theoretically, these two approaches should attain the same values of the Nusselt numbers when the pseudosteady-state is reached.

The presence of a thin isothermal baffle does not only modify the flow field but also contributes heat flux into the fluid within the spherical container. Thus, the effective heat transfer area is the area of the container's inner wall plus the surface area of the thin baffle. Obviously, the effective heat transfer area is greater than the case with a thin insulated baffle. The Nusselt number derived from the temperature gradients at the inner wall and baffle is illustrated first. Following that, the Nusselt number obtained by performing an energy balance is presented.

In order to get the area-averaged Nusselt number over the entire wall surface and baffle, the area-weighted heat flux should be derived. In fact, the Nusselt number can also be identified as a dimensionless form of the heat flux. Though the baffle is assumed to have zero thickness, it has two identical effective heat transfer surfaces, namely baffle's upper surface and baffle's lower surface, respectively (Figure 5.12). The heat flow on the baffle's lower surface (Q_{bl}) is:

$$Q_{bl} = \int_{R-l}^R dQ_{bl} = \int_{R-l}^R k \frac{\partial T}{\partial n^+} dA, \quad (5.4)$$

with n standing for the normal-to-surface direction:

$$\frac{\partial T}{\partial n^+} = \frac{1}{r} \frac{\partial T}{\partial \theta^+}, \quad (5.5)$$

$$dA = 2\pi r \sin \theta_b dr. \quad (5.6)$$

Finally, Q_{bl} is:

$$Q_{bl} = 2\pi k \sin \theta_b \int_{R-l}^R \frac{\partial T}{\partial \theta^+} dr. \quad (5.7)$$

The heat flow on the baffle's upper surface (Q_{bu}) is similarly given by:

$$Q_{bu} = \int_{R-l}^R dQ_{bu} = \int_{R-l}^R k \frac{\partial T}{\partial n^-} dA = 2\pi k \sin \theta_b \int_{R-l}^R \frac{\partial T}{\partial \theta^-} dr. \quad (5.8)$$

The total heat flow over the baffle (Q_b) can be calculated by combining Equations 5.7 and 5.8:

$$Q_b = Q_{bu} + Q_{bl} = 2\pi k \sin \theta_b \int_{R-l}^R \left(\frac{\partial T}{\partial \theta^+} + \frac{\partial T}{\partial \theta^-} \right) dr = 2\pi k \sin \theta_b \int_{R-l}^R \frac{\partial T}{\partial \theta} \Big|_e dr, \quad (5.9)$$

where the effective temperature gradient over the baffle is denoted as:

$$\frac{\partial T}{\partial \theta} \Big|_e = \frac{\partial T}{\partial \theta^+} + \frac{\partial T}{\partial \theta^-}. \quad (5.10)$$

The heat flow over the wall surface of the sphere (Q_w) is:

$$Q_w = \int_0^\pi k \frac{\partial T}{\partial r} \Big|_{r=R} 2\pi R \sin \theta R d\theta = 2\pi R^2 k \int_0^\pi \frac{\partial T}{\partial r} \Big|_{r=R} \sin \theta d\theta. \quad (5.11)$$

Therefore, the total heat (Q_t) conducted into the fluid within the spherical container is:

$$Q_t = Q_w + Q_b = 2\pi R^2 k \int_0^\pi \frac{\partial T}{\partial r} \Big|_{r=R} \sin \theta d\theta + 2\pi k \sin \theta_b \int_{R-l}^R \frac{\partial T}{\partial \theta} \Big|_e dr. \quad (5.12)$$

The effective heat transfer area (A_t) is:

$$A_t = 4\pi R^2 + 2(2\pi Rl - \pi l^2) \sin \theta_b. \quad (5.13)$$

Hence, the area-averaged heat flux for pseudosteady-state natural convection inside spherical containers with a thin isothermal baffle is:

$$\bar{q}(t) = \frac{Q_t}{A_t} = \frac{R^2 k \int_0^\pi \frac{\partial T}{\partial r} \Big|_{r=R} \sin \theta d\theta + k \sin \theta_b \int_{R-l}^R \frac{\partial T}{\partial \theta} \Big|_e dr}{2R^2 + (2Rl - l^2) \sin \theta_b}. \quad (5.14)$$

Then, the area-averaged instantaneous Nusselt number can be calculated by employing the general definition:

$$Nu(t) = \frac{hD}{k} = \frac{\bar{q}D}{k\Delta T} = \frac{D}{\Delta T} \frac{R^2 \int_0^\pi \frac{\partial T}{\partial r} \Big|_{r=R} \sin \theta d\theta + \sin \theta_b \int_{R-l}^R \frac{\partial T}{\partial \theta} \Big|_e dr}{2R^2 + (2Rl - l^2) \sin \theta_b}. \quad (5.15)$$

The choice of the temperature difference ΔT is arbitrary. Generally, the term ΔT is taken as $\Delta T = T_w - T_m$ that serves as the driving force. The dimensionless form of the RHS of Equation 5.15 is preferred. Hence, the following dimensionless parameters are introduced:

$$T^* = \frac{T - T_0}{T_w - T_c}, \quad (5.16)$$

$$r^* = \frac{r}{R}, \quad (5.17)$$

$$L = \frac{l}{D}. \quad (5.18)$$

Substituting these dimensionless parameters into the Nusselt number expression, Equation 5.15 is simplified as:

$$Nu_m(\tau) = \frac{1}{(T_w^* - T_m^*)} \frac{1}{[1 + 2(L - L^2) \sin \theta_b]} \left(\int_0^\pi \frac{\partial T^*}{\partial r^*} \Big|_{r^*=1} \sin \theta d\theta + \sin \theta_b \int_{1-2L}^1 \frac{\partial T^*}{\partial \theta} \Big|_e dr^* \right). \quad (5.19)$$

The term $\frac{1}{1 + 2(L - L^2) \sin \theta_b}$, named shape factor, is related to the location and length of a thin isothermal baffle. If $L=0$ (i.e. no baffle), the second integral vanishes and this term becomes equal to unity and the Nusselt number expression will be identical to Equation

3.21. Note that a subscript “m” is used for the area-averaged Nusselt number meaning that T_m (mean or bulk temperature) is used in the ΔT expression.

Considering that in this pseudosteady-state natural convection modeling, the temperature difference between the wall and center is maintained as a constant value, hence another logical Nusselt number that is based on the constant driving force $\Delta T = T_w - T_c$ can be introduced. This Nusselt number (Nu_c) is:

$$Nu_c(\tau) = \frac{1}{[1 + 2(L - L^2) \sin \theta_b]} \left(\int_0^\pi \frac{\partial T^*}{\partial r^*} \Big|_{r^*=1} \sin \theta d\theta + \sin \theta_b \int_{1-2L}^1 \frac{\partial T^*}{\partial \theta} \Big|_e dr^* \right). \quad (5.20)$$

Note that a subscript “c” is used for the surface-averaged Nusselt number meaning that T_c (container’s center temperature) is used in the ΔT expression. If $L=0$, the second integral vanishes and the shape factor equals unity. Expression 5.20 is then same as Equation 3.22.

As mentioned above, another approach to get the Nusselt number is to perform the energy balance for the fluid within the container. Under the pseudosteady-state condition, the heat transferred into the container will be exactly equal to the enthalpy change of the fluid inside the container. Mathematically, this can be written as:

$$\bar{q}(t) = \frac{mc_p \frac{dT_m}{dt}}{A_t} = \frac{\rho \frac{4}{3} \pi R^3 c_p \frac{dT_m}{dt}}{4\pi R^2 + 2(2\pi Rl - \pi l^2) \sin \theta_b} = \frac{\rho \frac{2}{3} R^3 c_p \frac{dT_m}{dt}}{2R^2 + (2Rl - l^2) \sin \theta_b}. \quad (5.21)$$

Taking the dimensionless form of area-averaged heat flux, the mathematical formula of the Nusselt number can be obtained:

$$Nu(t) = \frac{\bar{q}D}{k\Delta T} = \frac{D}{k\Delta T} \frac{\rho \frac{2}{3} R^3 c_p \frac{dT_m}{dt}}{2R^2 + (2Rl - l^2) \sin \theta_b} = \frac{1}{12\alpha\Delta T} \frac{D^4 \frac{dT_m}{dt}}{2R^2 + (2Rl - l^2) \sin \theta_b}. \quad (5.22)$$

Similarly, the term ΔT can either be taken as $\Delta T = T_w - T_m$ or $\Delta T = T_w - T_c$.

Correspondingly, two definitions of the Nusselt number are obtained as follows via introducing dimensionless time:

$$\tau = \frac{\alpha t}{R^2}, \quad (5.23)$$

$$Nu_m(\tau) = \frac{2}{3} \frac{1}{[1 + 2(L - L^2) \sin \theta_b]} \frac{1}{(T_w^* - T_m^*)} \frac{dT_m^*}{d\tau}, \quad (5.24)$$

$$Nu_c(\tau) = \frac{2}{3} \frac{1}{[1 + 2(L - L^2) \sin \theta_b]} \frac{dT_m^*}{d\tau}. \quad (5.25)$$

When $L=0$ (i.e. no baffle), the above equations return to the form of Equations 3.25 and 3.26, respectively.

The two Nusselt numbers that are based on the driving force of $\Delta T = T_w - T_m$ should equal each other. Similarly, the two Nusselt numbers which are based on the driving force of $\Delta T = T_w - T_c$ should be identical. All these four Nusselt numbers are evaluated for each case. The Nusselt number definitions of pseudosteady-state natural convection inside spherical containers with a thin isothermal baffle is more complicated in comparison with cases with no baffle or with a thin insulated baffle. They are not only dependent on dimensionless temperature gradient or time change of rate of dimensionless temperature, but also depend on shape factor that varies with the baffle length and location. Note that the shape factor can not be greater than unity. Therefore, there is a chance for some cases with a high time rate of change of bulk temperature that the shape factor can lead to a low Nusselt number. In effect, the presence of a thin isothermal baffle brings energy into the system and makes heat transfer more complex.

5.4.2 Time-Averaged Nusselt Numbers for Time-Dependent Cases

It is shown that for high Rayleigh numbers, the system can not be recognized to be stable and therefore is not considered to be strictly at pseudosteady-state. Determining whether the pseudosteady-state natural convection inside a spherical container with a thin isothermal baffle is reached is a critical step for our analysis. The oscillations in some cases are quite well-organized (Figure 5.13 (a)), while in other cases the oscillations are disorderedly and random (Figure 5.13 (b)).

Similar to the case with a thin insulated baffle, the time-averaged method is employed to monitor whether the flow and thermal fields can be considered to be statistically stationary and to calculate the mean or time-averaged value. The straight-line fitting curve equation is employed to quantitatively determine the pertinent values and judge the statistical stationary state. The least-squares method is utilized in the process. Equations 4.9 to 4.15 are not repeated here. More details can be found in Chapter 4.

The determination of whether the statistical stationary pseudosteady-state natural convection inside spherical container with a thin isothermal baffle is reached can be achieved by the approximated straight line. The slope of this straight line can determine the tolerance and was employed for statistical stationary state judgment. In the simulations when the slope is less than 10^{-6} , it is declared that the statistical stationary state has been reached.

5.4.3 Oscillation Strength of the Nusselt Numbers

The time-averaged Nusselt numbers are defined to characterize the mean magnitudes of the fluctuating Nusselt numbers. However, this can not reflect the strength of oscillations of the Nusselt numbers. Therefore, another parameter should be defined to quantitatively describe the strength of the fluctuations which can illustrate the strength of flow and thermal fields. The Root Mean Square (RMS) value is considered an appropriate parameter for such characterization and the process is similar to the case with a thin insulated baffle. More details can be found in Chapter 4.

5.4.4 Stream Function Field

In the previous section, the Nusselt number is introduced to characterize the pseudosteady-state natural convection inside spherical containers with a thin isothermal baffle. From its definition, it is known that the Nusselt number is directly related to the temperature field but not the flow field. The stream function is a parameter that is directly related to fluid flow. For example, the difference between the maximum and the minimum stream function values of a vortex can be employed to characterize the strength of a rotating flow field. Hence, it is necessary to study the stream function difference to determine the possible link to heat transfer due to the presence of a thin isothermal baffle. Stream function can also be employed to monitor whether the pseudosteady-state natural convection inside spherical containers with a thin isothermal baffle has reached the stationary state. The stream function ψ at the center of vortex is defined as zero. Therefore, the maximum stream function ψ_{\max} (value on the wall) can be taken as a characteristic value of the flow field.

Similar to the Nusslet number, the stream function $\psi_{\max}(\tau)$ is not a constant value but is a fluctuating quantity for most cases when the Rayleigh number is as high as 10^7 . Thus, the time-averaged stream function ψ_{\max} is defined for characterization. The RMS and relative RMS values are calculated for each case to describe the strength of the flow field. An approximated straight-line equation is solved to obtain the time-averaged stream function ψ_{\max} and to determine whether the statistical stationary state is reached. If the slope of the approximated line is less than 10^{-6} , it is considered that the statistical stationary state is reached. Therefore, there are two different ways to monitor the determination of statistical stationary state. In relation to this, equations 4.16 to 4.17 are not repeated here and more details can be found in Chapter 4.

5.5 Variations of Time-Averaged Nusselt Numbers and Maximum Stream Function

In Section 5.3, the streamline patterns and temperature contours were presented for different Rayleigh numbers varying from 10^4 to 10^7 for different baffle lengths and locations. In addition to affecting the thermal field directly by bringing heat into the fluid, the presence of a thin isothermal baffle disturbs the flow field and consequently modifies the temperature field indirectly. In order to describe these modifications quantitatively, the variations of the time-averaged Nusselt numbers and maximum stream function are studied. The Nusselt number is uniquely associated with the temperature field, whereas the stream function can characterize the flow field. Details on the definitions of the time-averaged Nusselt numbers were given in Section 4.4.2.

The variations of the time-averaged Nusselt numbers (Nu_c and Nu_m) and maximum stream function of the primary vortex (ψ_{\max}) with Ra for cases with a thin

isothermal baffle are presented in Figures 5.14 to 5.22. In each figure, the baffle length is fixed ($L=0.05, 0.10$ and 0.25) and baffle locations ($\theta_b = 30^\circ, 60^\circ, 90^\circ, 120^\circ$ and 150°) are identified with filled symbols, whereas the reference case with no baffle is shown with an open symbol. It must be emphasized that even though variations of the time-averaged Nusselt number (Nu_m) are presented, they will not be discussed in view of the complexity of their relation to the time rate of rise of the bulk temperature (Equation 5.24). The Nusselt numbers and maximum stream function strongly depend on the Rayleigh number and clearly exhibit the strengthening trend with the increase of Rayleigh number, irrespective of the baffle lengths and locations. For $Ra=10^4$, the flow and temperature fields do not change greatly due to the presence of the thin isothermal baffle. This is because conduction is dominant for this low range of the Rayleigh number. With increase of Ra , the effects of the thin isothermal baffle become more marked due to the increase of convective effects. For a given Rayleigh number, the extent of flow and thermal field modifications is directly related to the length of the thin isothermal baffle. It is evident (51 out of 60 cases) that by adding a thin isothermal baffle, the time-averaged Nusselt number (Nu_c) is lower than the reference case with no baffle. This Nusselt number is directly proportional to the heat that is transferred into the container from the surface of the sphere and both sides of the thin baffle. This quantity (Nu_c) is also very convenient since it is directly related to the time rate of rise of the bulk temperature according to Equation 5.25. This means that even though heat is transferred through the surface of the baffle, the presence of the baffle has adversely caused lowering of the heat input through the wall of the sphere. This control utility is related to the observed flow and thermal fields presented earlier in Chapter 4, where it was reasoned

that presence of an insulated baffle can lead to “confinement” or “compartmentalization” of the sphere. In other words, it was generally stated that the zone above the insulated baffle was dominated by conduction, whereas the lower region was dominated by convection. For the majority of the cases investigated in this Chapter (51 out of 60), it is clear that the extra heating of the fluid by the baffle is not sufficient to overcome the degraded heat transfer through the surface of the sphere due to compartmentalization.

Among the cases that were investigated, it can be observed that the Nusselt numbers and maximum stream function for some cases for which the baffle is located at 30° , 60° , 120° and 150° are higher than the reference case for $Ra=10^6$ and 10^7 . This is explained as follows. For all the cases with no baffle, the thermal boundary layer becomes thicker as the fluid from the bottom of the sphere rises along the inner wall. For cases with $Ra=10^7$, the presence of baffles near the top is beneficial to disturbing the thickened boundary layer, thus allowing extra heat to be drawn into the sphere. This effect is even maintained for longer baffles suggesting that the degrading effect of a long baffle through compartmentalization is overcome by extra heating. The enhancement of heat transfer that is observed due to presence of an isothermal baffle near the bottom of a sphere was seen to be limited to the high Ra number cases of 10^6 and 10^7 and the longest baffle ($L=0.25$) that was investigated. This observation is clearly linked to the creation of a counter CW rotating vortex on the upper surface of the baffle that was discussed in Figure 5.9 (2 bottom entries on the right column). Partly due to the orientation of the baffle and also its longer length, the counter CW rotating vortex that is created on the surface of the baffle due to heating directs the hot fluid toward the center of the sphere and penetrates higher into the sphere rising toward the top. This activity, in turn,

counteracts the compartmentalization of the baffle by introducing hot fluid into the stable stratified fluid layers above the baffle.

The behavior of the maximum stream function values that are shown in Figures 5.20-5.22 generally match the trends of Nusselt number (Nu_c) that were discussed. This indicates that the presence of thin isothermal baffles alters the temperature field through modification of the flow field. Of course, addition of heat through the surface of the baffle is important for high Ra numbers, however this can not be quantified directly from the dependence of the maximum stream function values.

Dependence of the time-averaged Nusselt numbers (Nu_c and Nu_m) and maximum stream function of the primary vortex (ψ_{\max}) on the position of the baffles (θ_b) are presented in Figures 5.23-5.25, 5.26-5.28, 5.29-5.31 and 5.32-5.34 for Ra= 10^4 , 10^5 , 10^6 and 10^7 , respectively. In each figure, the reference case with no baffle is identified with a filled circle, whereas various baffle lengths (L=0.05, 0.10 and 0.25) are identified with non-circular filled symbols. Again, it must be emphasized that even though variations of the time-averaged Nusselt number (Nu_m) are presented, they will not be discussed in view of the complexity of their relation to the time rate of rise of the bulk temperature (Equation 5.24).

For a given Ra number, as the location of baffle is lowered starting from the top of the sphere and moving toward the bottom, the Nusselt number Nu_c and maximum stream function exhibit trends suggesting that the confinement effect is minimal, when the baffle is placed near the two extremes. The location corresponding to the most marked confinement varies depending on the Ra and length of the baffle. For a fixed location of the baffle and Ra numbers lower than 10^7 , one can generally state that as the

length of the baffle is raised, the confinement effect becomes more enhanced. This behavior is not observed for the highest Rayleigh number studied.

The tabulated data for the Nusselt numbers (Nu_c and Nu_m) and maximum stream function (ψ_{\max}) of the primary vortex are listed in Tables 5.3, 5.4 and 5.5, respectively. In general, the relative RMS values are low suggesting that the pseudosteady-state is established, except for $Ra=10^7$, indicating that unsteady effects are promoted as the Ra number is raised.

It is found that the relative RMS values of the Nusselt numbers have strong dependence on the Rayleigh number. This is not unusual, because for higher Rayleigh numbers, convection heat transfer is stronger. However, there are four exceptions when $Ra=10^7$. These are $L = 0.05 | \theta_b = 30^\circ$, $L = 0.10 | \theta_b = 30^\circ$, $L = 0.25 | \theta_b = 30^\circ$ and $L = 0.25 | \theta_b = 150^\circ$, which are shaded in grey in Table 5.3. This indicates that the oscillation strength does not only depend on the Rayleigh number, but also depends on the combination of thin isothermal baffle location and length.

The results indicate that relative RMS values of the maximum stream function strongly depend on the Rayleigh number. When $Ra=10^7$, for most cases the oscillation effect is strong except three cases with relative RMS being less than 10^{-6} . These are $L = 0.05 | \theta_b = 30^\circ$, $L = 0.10 | \theta_b = 30^\circ$ and $L = 0.25 | \theta_b = 30^\circ$ which are shaded in grey in Table 5.5. It can be concluded that the relative RMS value does not only depend on the Rayleigh number but also depends on the combination of the baffle length and location.

Table 5.3 Nusselt numbers (Nu_c) and relative RMS ($RMS|_{rNu_c}$) for all 60 cases with thin isothermal baffles

Ra	θ_b	L=0.05		L=0.10		L=0.25	
		Nu_c	$RMS _{rNu_c}$	Nu_c	$RMS _{rNu_c}$	Nu_c	$RMS _{rNu_c}$
10^4	30°	5.5733	3.30E-04	5.4652	2.59E-04	5.8663	2.03E-04
	60°	5.304	2.56E-04	5.012	3.62E-04	5.425	2.15E-04
	90°	5.1474	3.62E-04	4.6801	3.03E-04	4.5801	3.30E-04
	120°	5.2647	2.41E-04	4.8007	1.76E-04	4.2544	3.75E-04
	150°	5.4984	3.53E-04	5.248	3.64E-04	4.6944	2.15E-04
10^5	30°	12.3137	1.36E-04	11.807	1.62E-04	11.5104	1.52E-04
	60°	11.476	1.71E-04	10.2345	1.79E-04	8.9583	1.73E-04
	90°	11.2919	1.71E-04	9.9437	1.47E-04	7.7898	9.57E-05
	120°	11.7066	1.57E-04	10.6524	1.54E-04	8.6384	1.85E-04
	150°	12.2407	1.36E-04	11.6042	1.59E-04	10.07	1.64E-04
10^6	30°	25.1747	8.05E-05	23.9844	5.01E-05	20.4738	7.40E-05
	60°	22.136	3.95E-05	20.3639	8.68E-05	17.777	7.00E-05
	90°	21.641	7.93E-05	16.8075	1.32E-04	16.0448	0.0283
	120°	22.1494	0.004	16.3173	0.182	15.8997	9.80E-05
	150°	23.9819	0.002	18.3277	0.2927	29.2267	4.37E-05
10^7	30°	37.8193	5.11E-05	39.1508	3.89E-05	40.6807	3.07E-05
	60°	39.1656	0.0216	38.995	0.0077	34.7519	0.0617
	90°	34.0939	0.1523	31.987	0.1609	32.1272	0.2294
	120°	32.8959	0.0172	27.506	0.2894	38.9514	0.3485
	150°	36.7836	0.0535	33.2905	0.4207	74.5868	8.20E-04

Table 5.4 Nusselt numbers (Nu_m) and relative RMS ($RMS|_{rNu_m}$) for all 60 cases with thin isothermal baffles

Ra	θ_b	L=0.05		L=0.10		L=0.25	
		Nu_m	$RMS _{rNu_m}$	Nu_m	$RMS _{rNu_m}$	Nu_m	$RMS _{rNu_m}$
10^4	30°	10.8826	3.00E-04	10.835	2.59E-04	11.4643	2.02E-04
	60°	10.6079	2.56E-04	10.539	3.61E-04	12.1179	2.15E-04
	90°	10.4532	3.62E-04	10.3222	3.02E-04	12.2986	3.29E-04
	120°	10.5258	2.41E-04	10.3532	1.76E-04	11.8568	3.75E-04
	150°	10.8477	3.53E-04	10.7599	3.63E-04	11.2307	2.14E-04
10^5	30°	15.5981	1.36E-04	15.4156	1.62E-04	15.7231	1.52E-04
	60°	15.1604	1.70E-04	14.8853	1.79E-04	15.8039	1.72E-04
	90°	14.8112	1.70E-04	14.7301	1.47E-04	16.0063	9.57E-05
	120°	14.9991	1.56E-04	14.7917	1.53E-04	15.6979	1.84E-04
	150°	15.5322	1.36E-04	15.2921	1.58E-04	15.3046	1.64E-04
10^6	30°	24.597	8.03E-05	24.1461	4.99E-05	23.6414	7.38E-05
	60°	23.1803	3.95E-05	22.7097	8.66E-05	23.2855	6.98E-05
	90°	23.0235	7.91E-05	23.2071	1.09E-04	23.6109	0.0201
	120°	23.3297	0.0033	23.4176	0.0749	24.9867	9.77E-05
	150°	24.2325	0.0035	23.1952	0.1939	25.8978	4.03E-05
10^7	30°	39.2061	5.15E-05	39.0203	3.87E-05	39.316	3.07E-05
	60°	39.8818	0.0192	39.2148	0.0076	39.0198	0.0507
	90°	37.5667	0.1124	38.5192	0.102	40.2304	0.1696
	120°	37.5437	0.0181	38.715	0.2009	42.7318	0.2304
	150°	40.427	0.044	39.5723	0.3388	47.0156	5.52E-04

Table 5.5 Maximum Stream function (ψ_{\max}) and relative RMS ($RMS|_{r\psi_{\max}}$) for all 60 cases with thin isothermal baffles

Ra	θ_b	L=0.05		L=0.10		L=0.25	
		ψ_{\max}	$RMS _{r\psi_{\max}}$	ψ_{\max}	$RMS _{r\psi_{\max}}$	ψ_{\max}	$RMS _{r\psi_{\max}}$
10^4	30°	1.52E-05	2.91E-06	1.48E-05	1.81E-07	1.37E-05	1.22E-06
	60°	1.48E-05	1.08E-07	1.37E-05	1.11E-06	1.06E-05	3.46E-06
	90°	1.36E-05	8.87E-08	1.12E-05	6.58E-07	5.90E-06	3.59E-06
	120°	1.38E-05	9.44E-07	1.19E-05	1.25E-06	8.64E-06	8.10E-08
	150°	1.52E-05	7.16E-07	1.48E-05	1.37E-06	1.26E-05	1.21E-06
10^5	30°	7.43E-05	2.17E-14	7.23E-05	1.81E-07	6.61E-05	3.12E-07
	60°	7.44E-05	4.62E-08	7.02E-05	6.96E-08	5.36E-05	1.28E-07
	90°	7.10E-05	4.61E-08	6.63E-05	3.04E-08	3.92E-05	1.10E-08
	120°	6.94E-05	4.68E-08	6.07E-05	4.70E-08	5.01E-05	3.20E-08
	150°	7.34E-05	3.50E-08	7.04E-05	5.43E-08	6.00E-05	2.66E-08
10^6	30°	1.93E-04	2.24E-06	1.88E-04	3.56E-07	1.69E-04	1.24E-07
	60°	1.87E-04	1.02E-07	1.72E-04	7.43E-08	1.39E-04	6.24E-06
	90°	1.71E-04	1.49E-06	1.41E-04	2.07E-04	1.25E-04	0.0236
	120°	1.67E-04	0.0051	1.62E-04	0.1201	1.28E-04	4.79E-08
	150°	1.83E-04	0.0062	1.80E-04	0.1809	1.84E-04	1.66E-07
10^7	30°	4.12E-04	1.22E-07	4.06E-04	3.82E-08	3.77E-04	2.51E-07
	60°	4.34E-04	0.0802	3.95E-04	0.0284	3.18E-04	0.0465
	90°	4.34E-04	0.1523	3.27E-04	0.1874	2.59E-04	0.2029
	120°	3.63E-04	0.019	3.74E-04	0.1705	4.30E-04	0.1296
	150°	4.21E-04	0.0733	3.43E-04	0.1393	4.96E-04	0.0352

5.6 Closure

The effect of an isothermal baffle that is attached on the inner wall of a sphere on the pseudosteady-state natural convection was investigated in this Chapter. For low Rayleigh numbers, pseudosteady-state with minimal fluctuations of the flow and thermal fields was observed. For higher Ra, strong fluctuations were promoted. In general, because of compartmentalization, attaching an isothermal baffle degrades the amount of heat that can be added to the stored fluid. When an isothermal baffle is placed at the top or bottom of a sphere, the disturbance of the boundary layer next to the wall and extra heating were shown to overcome the compartmentalization.

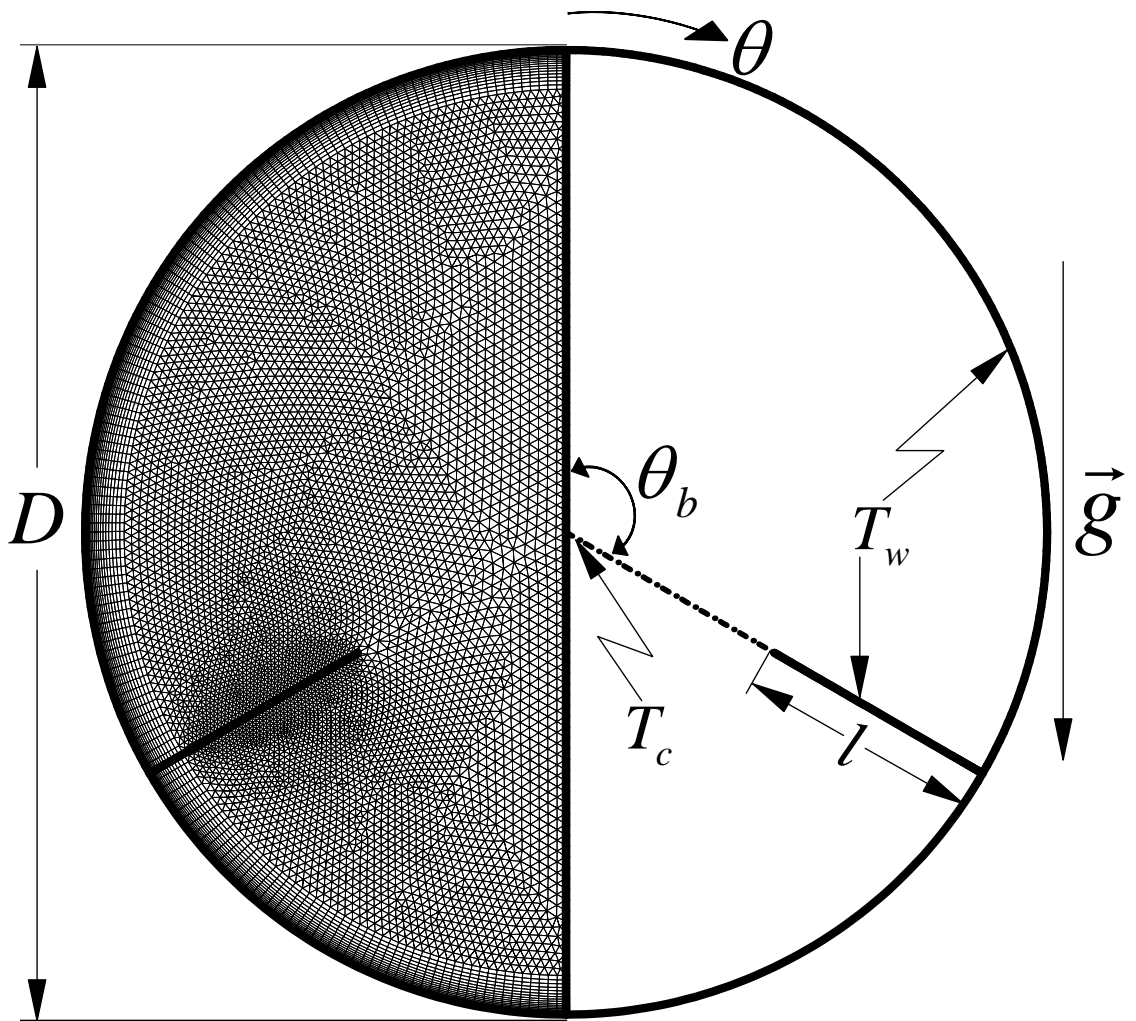


Figure 5.1 Schematic diagram of a spherical container with a thin isothermal baffle

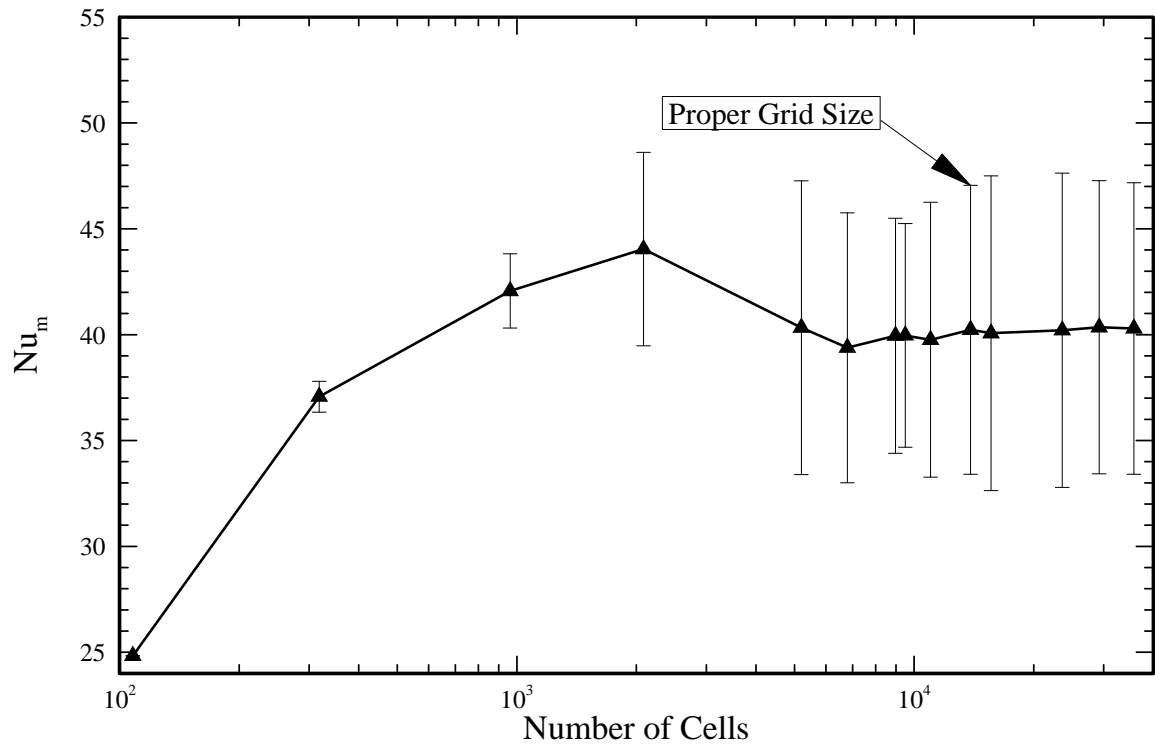


Figure 5.2 The time-averaged and RMS values of the Nusselt number Nu_m (based on $\Delta T = T_w - T_m$) as a function of grid size for a case with isothermal baffle ($L=0.25$, $\theta_b = 90^\circ$ and $Ra=10^7$)

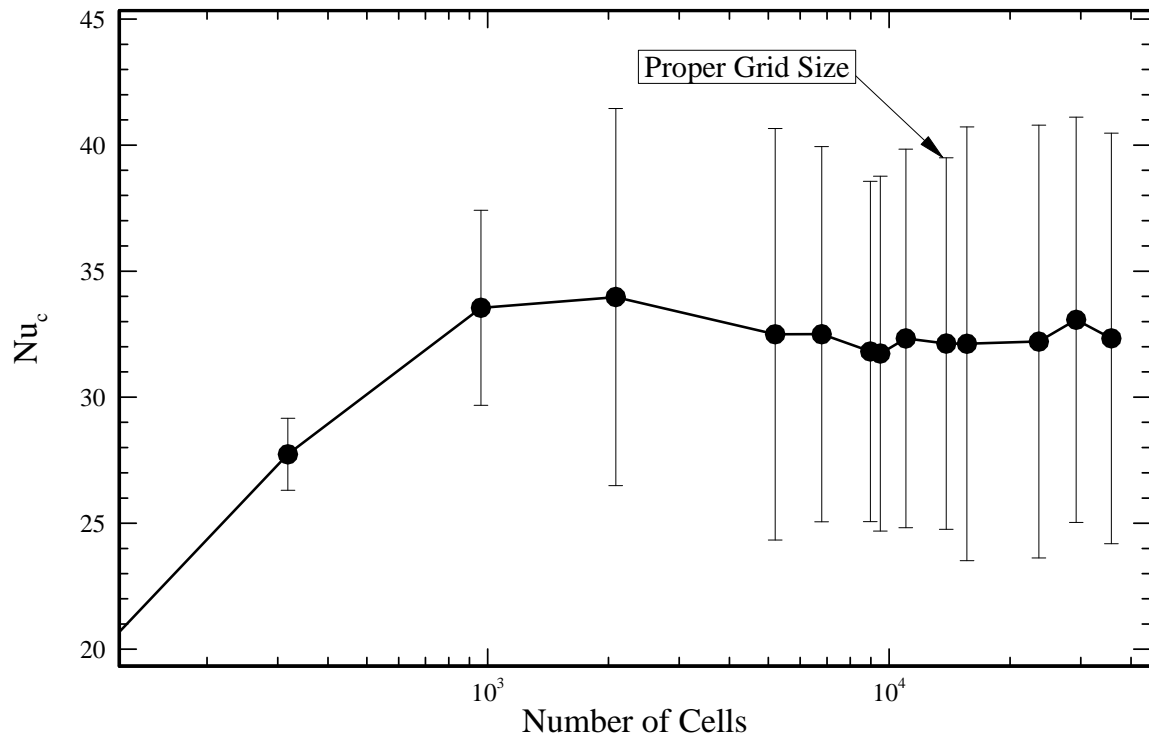


Figure 5.3 The time-averaged and RMS values of the Nusselt number Nu_c (based on $\Delta T = T_w - T_c$) as a function of grid size for a case with isothermal baffle ($L=0.25$, $\theta_b = 90^\circ$ and $Ra=10^7$)

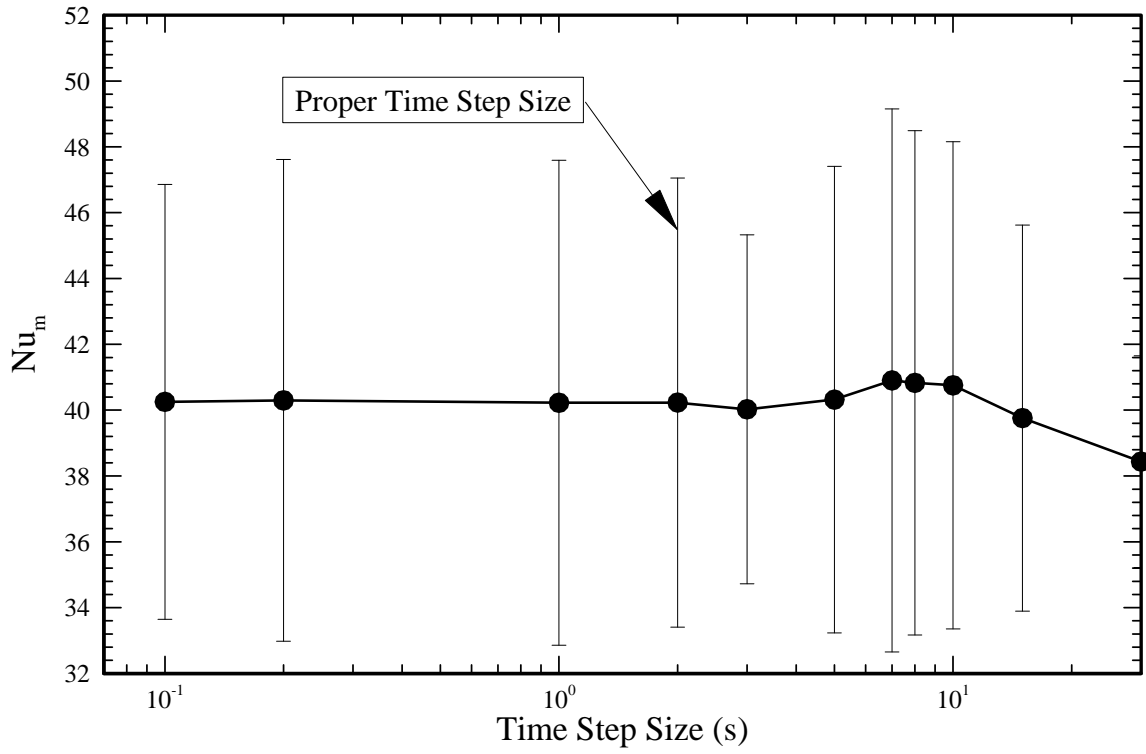


Figure 5.4 The time-averaged and RMS values of the Nusselt number Nu_m (based on $\Delta T = T_w - T_m$) as a function of time step size for a case with isothermal baffle ($L=0.25$, $\theta_b = 90^\circ$ and $Ra=10^7$)

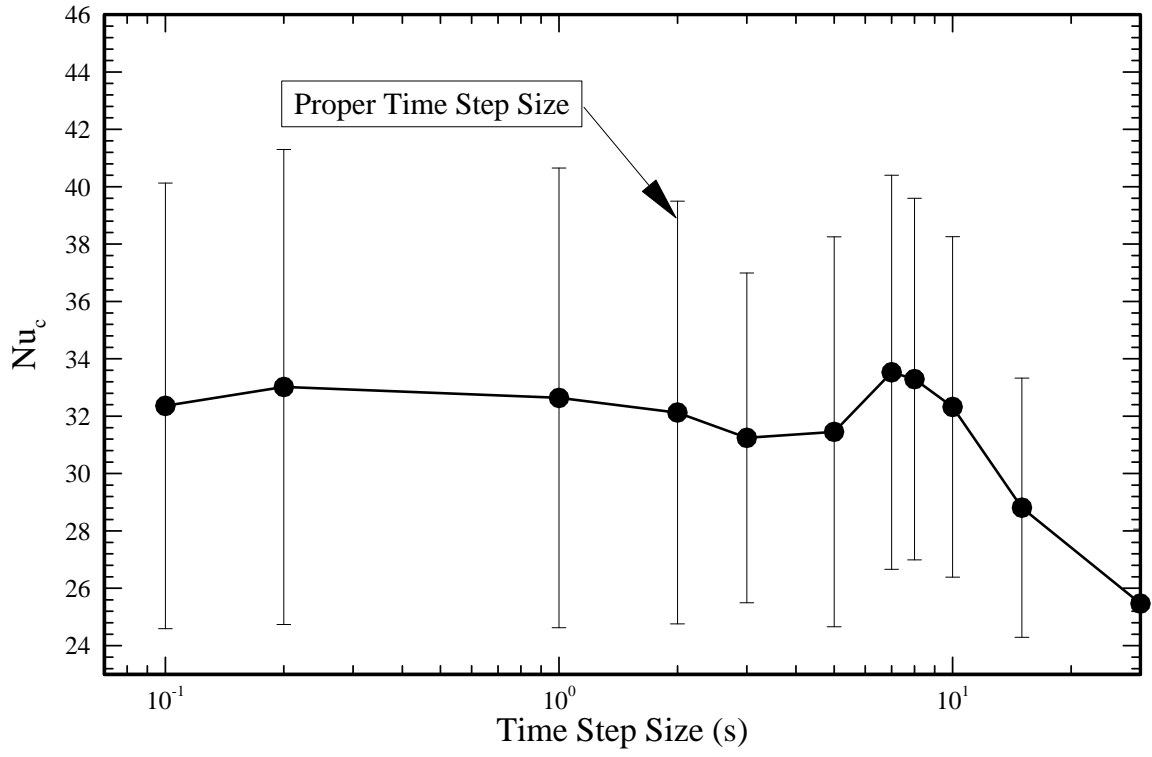


Figure 5.5 The time-averaged Nusselt number Nu_c (based on $\Delta T = T_w - T_c$) as a function of time step size

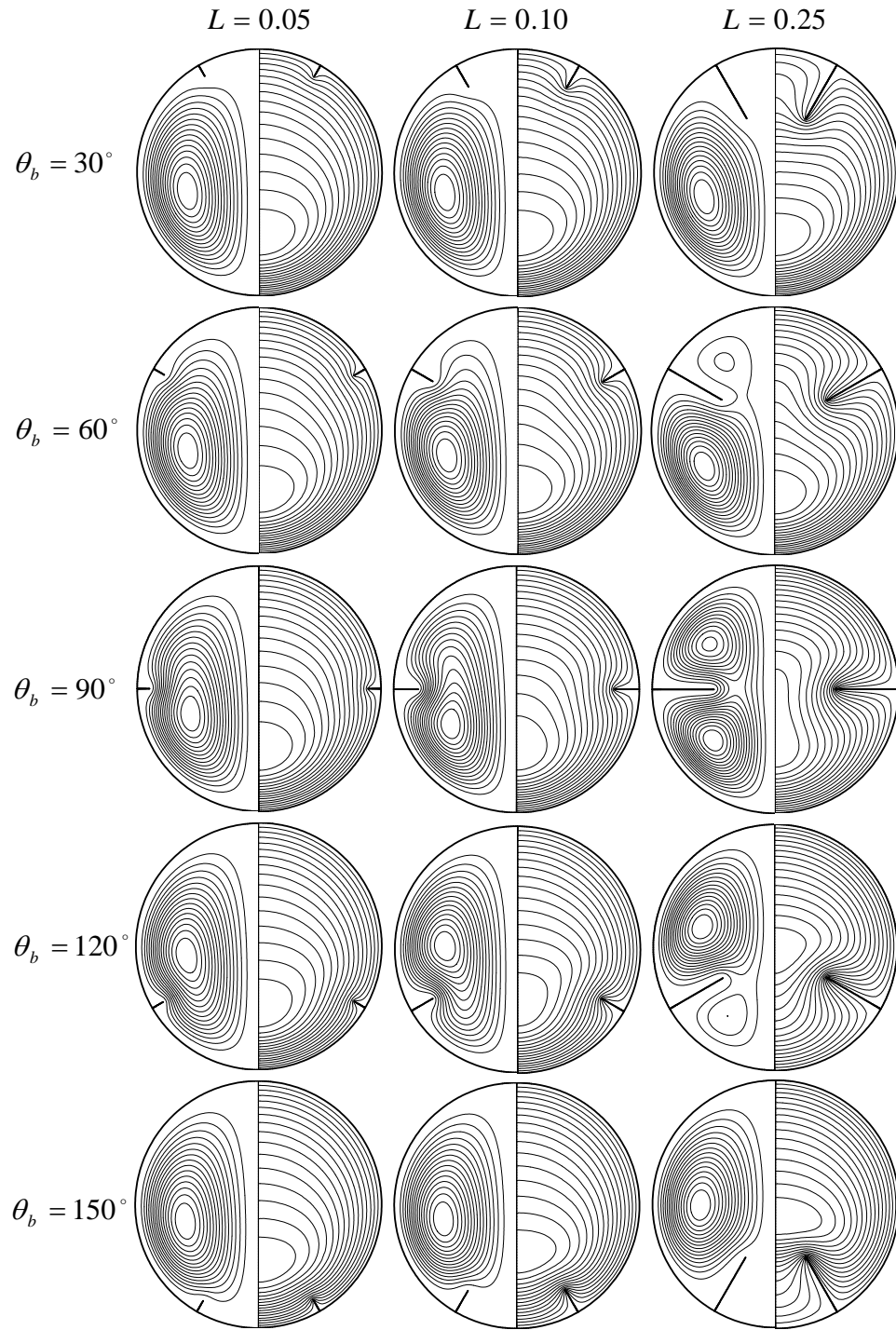


Figure 5.6 Pseudosteady-state streamline patterns and temperature contours for three isothermal baffles ($L = 0.05, 0.10$ and 0.25) placed at various locations ($\theta_b = 30^\circ, 60^\circ, 90^\circ, 120^\circ$ and 150°) for $Ra = 10^4$

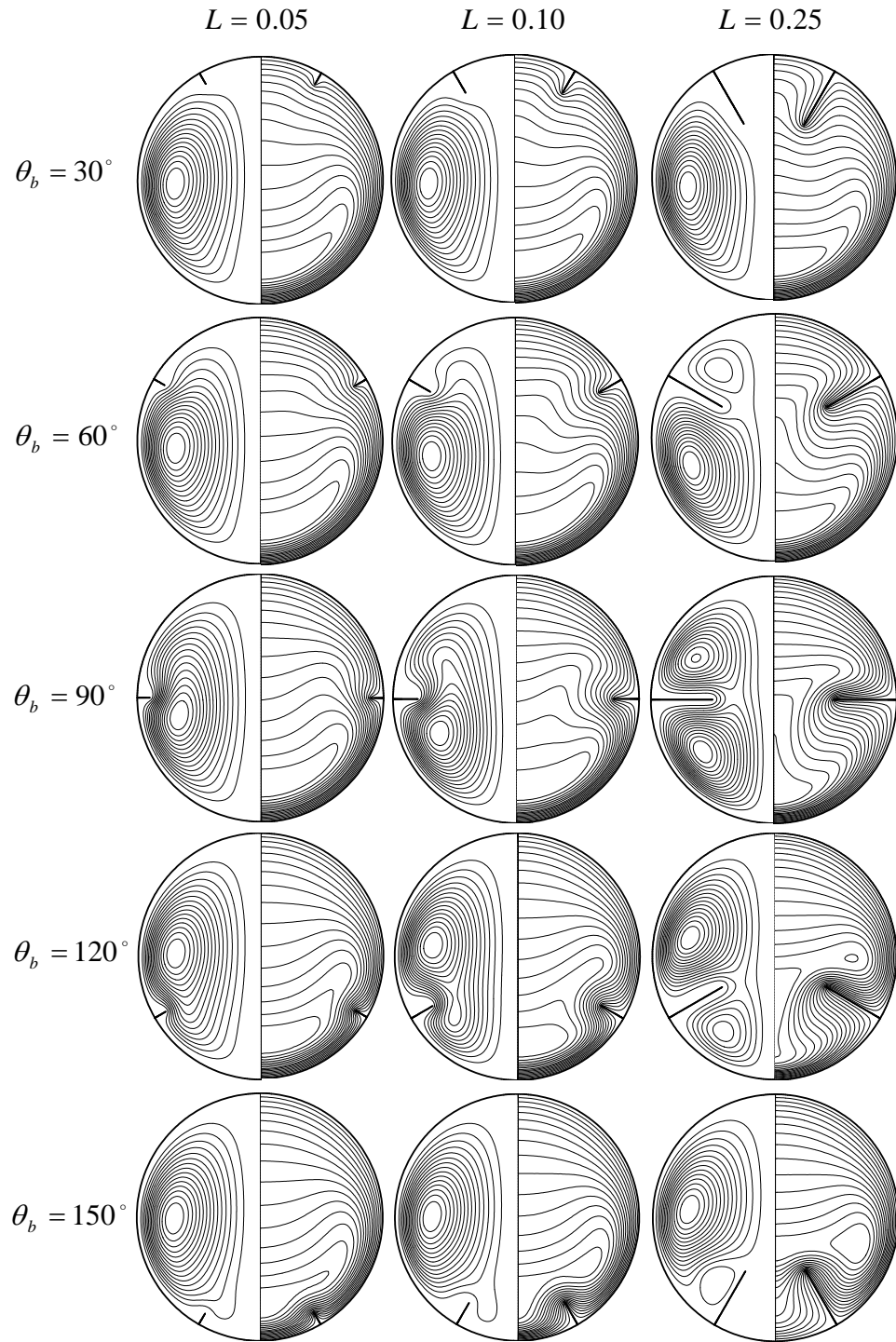


Figure 5.7 Pseudosteady-state streamline patterns and temperature contours for three isothermal baffles ($L = 0.05, 0.10$ and 0.25) placed at various locations ($\theta_b = 30^\circ, 60^\circ, 90^\circ, 120^\circ$ and 150°) for $Ra = 10^5$

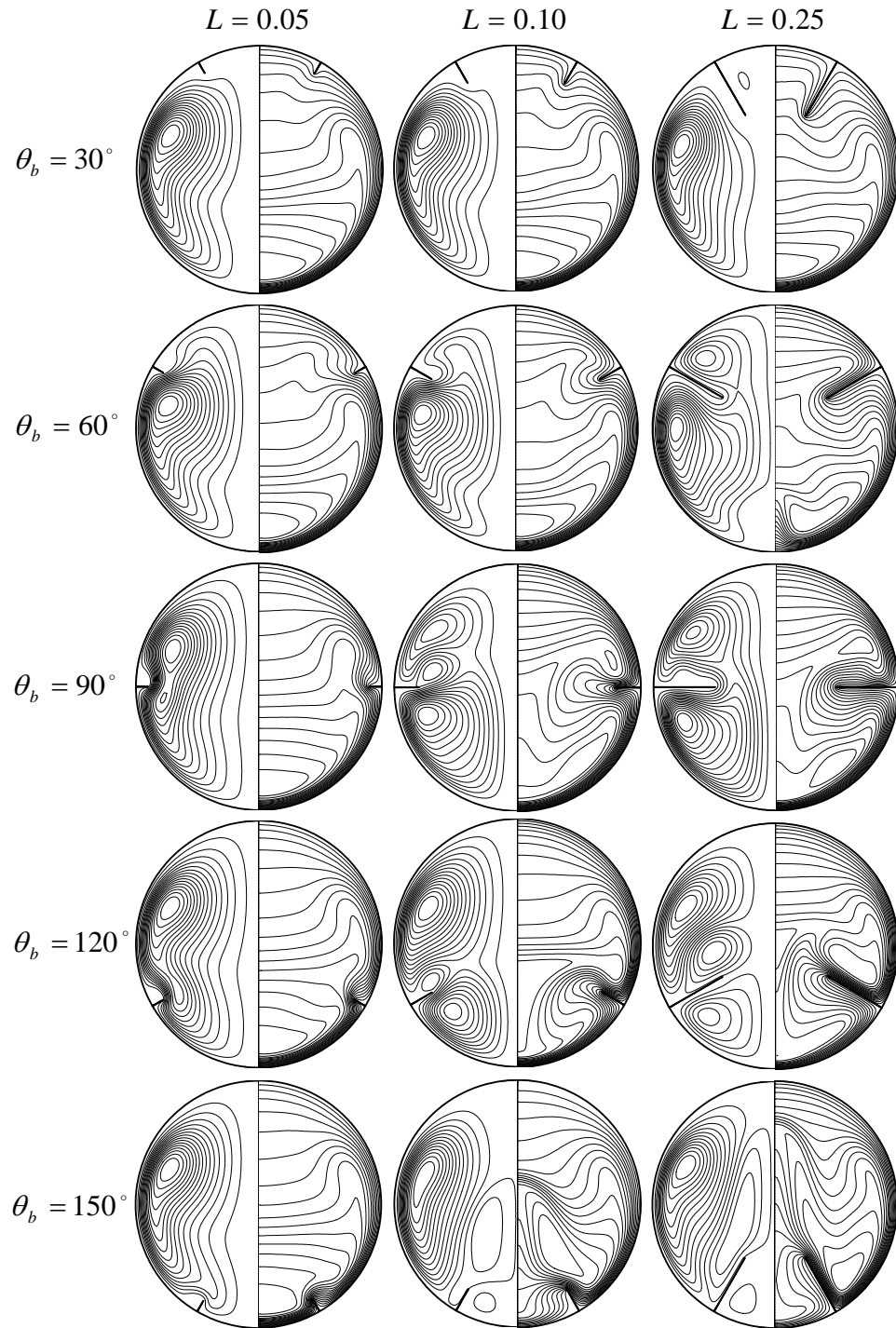


Figure 5.8 Pseudosteady-state streamline patterns and temperature contours for three isothermal baffles ($L = 0.05, 0.10$ and 0.25) placed at various locations ($\theta_b = 30^\circ, 60^\circ, 90^\circ, 120^\circ$ and 150°) for $Ra = 10^6$

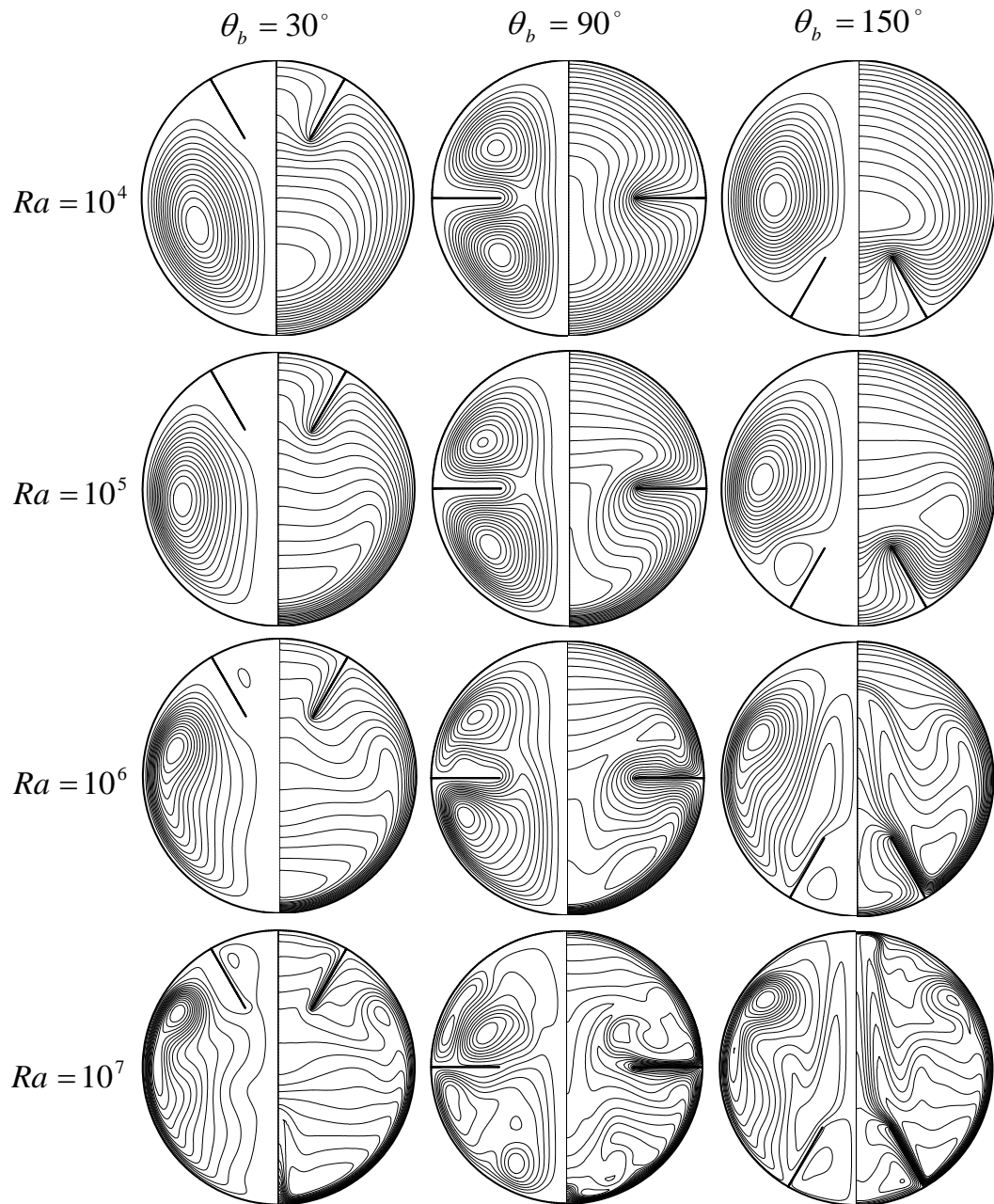


Figure 5.9 Pseudosteady-state streamline patterns and temperature contours with an isothermal baffle ($L = 0.25$) placed at various locations ($\theta_b = 30^\circ, 90^\circ$ and 150°) for $Ra = 10^4, 10^5, 10^6$ and 10^7

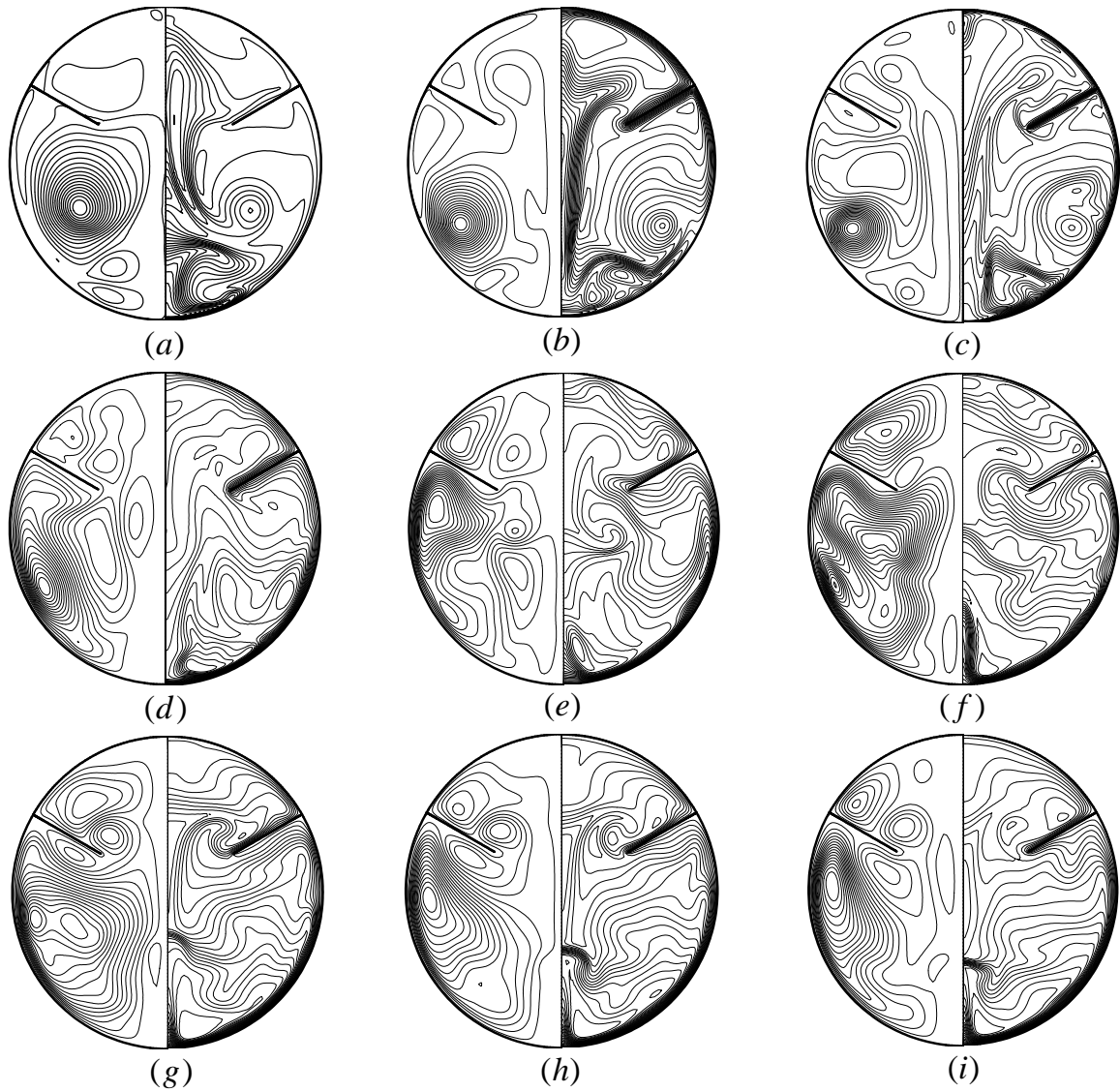


Figure 5.10 Time-dependent streamline patterns and temperature contours in one cycle (a→i) for a case with a thin isothermal baffle ($L=0.25$, $\theta_b=60^\circ$) for $Ra=10^7$

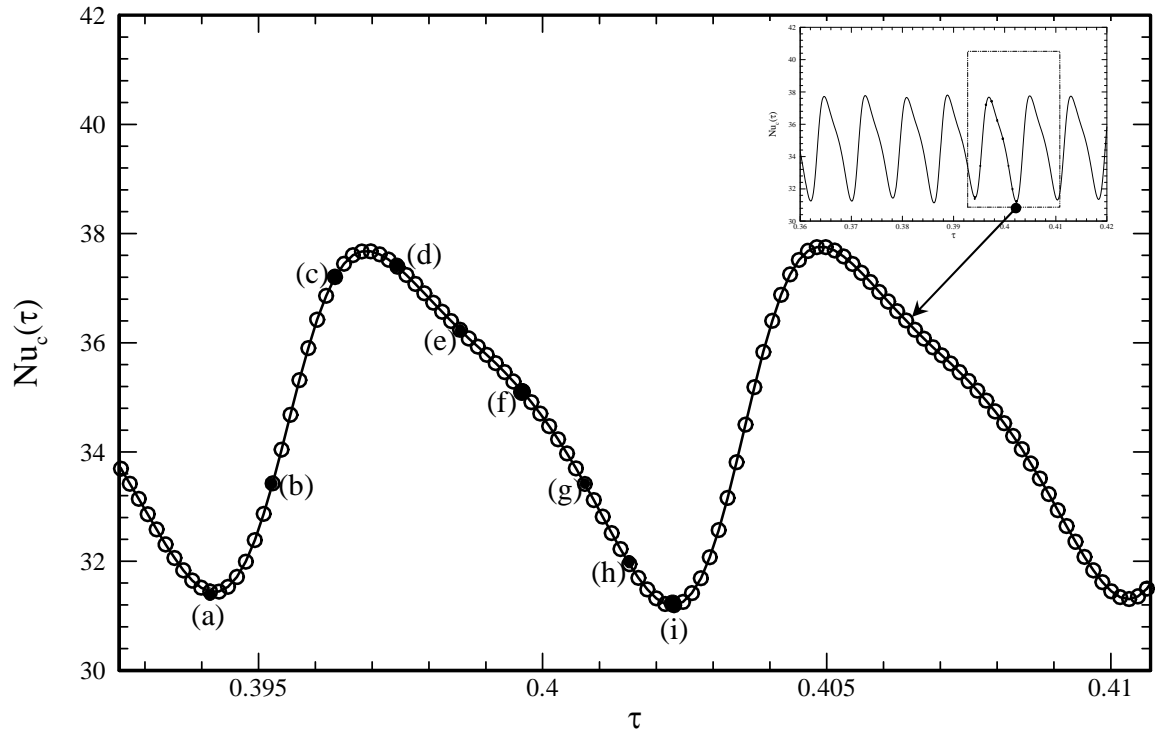


Figure 5.11 Cyclic variation of the instantaneous area-averaged Nusselt number for a case with a thin isothermal baffle ($L=0.25$, $\theta_b=60^\circ$) for $Ra=10^7$ (Corresponding to Figure 5.10)

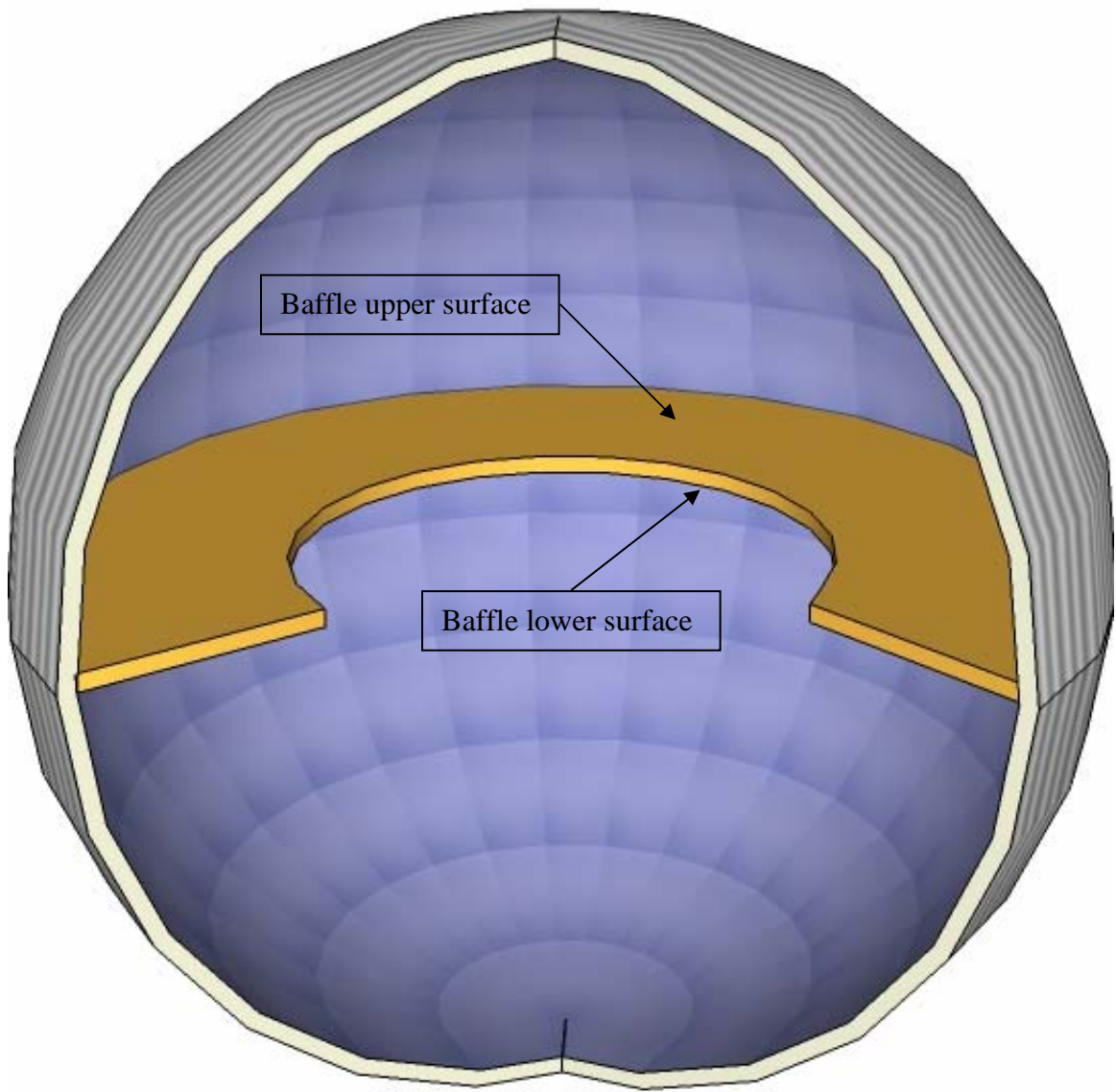
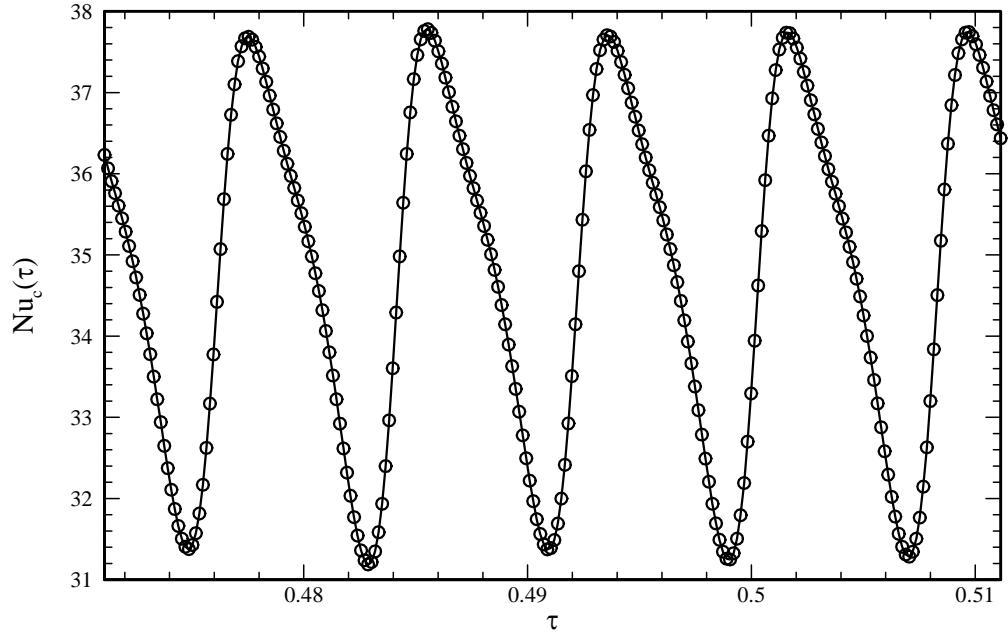
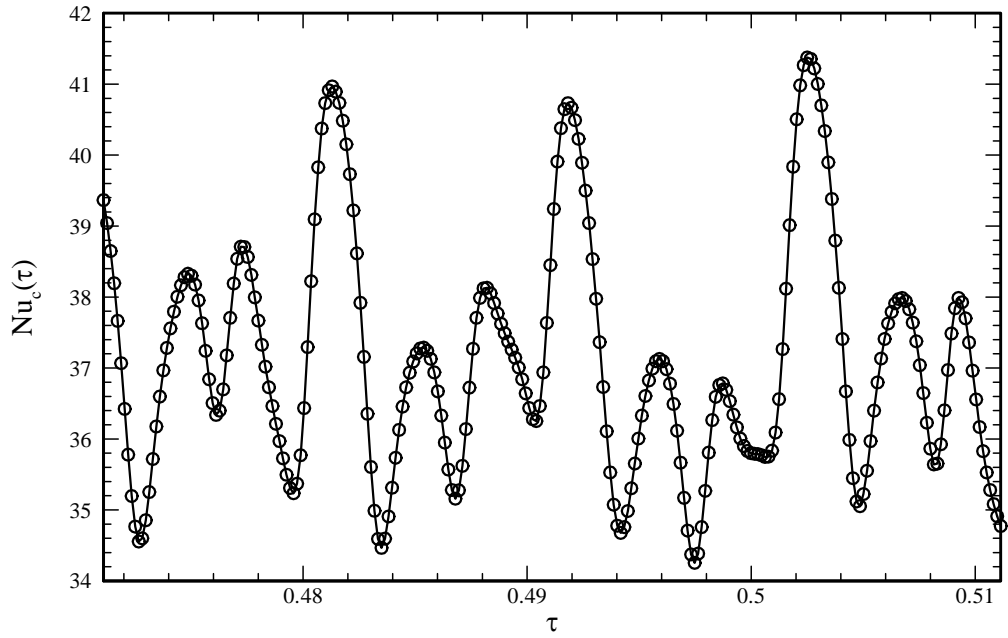


Figure 5.12 Detailed drawing of an isothermal baffle surface



(a)



(b)

Figure 5.13 Instantaneous area-averaged Nusselt number oscillation with dimensionless time for case (a) with a thin isothermal baffle ($L=0.25$, $\theta_b = 60^\circ$, $Ra=10^7$) and case (b) with a thin isothermal baffle ($L=0.05$, $\theta_b = 150^\circ$, $Ra=10^7$)

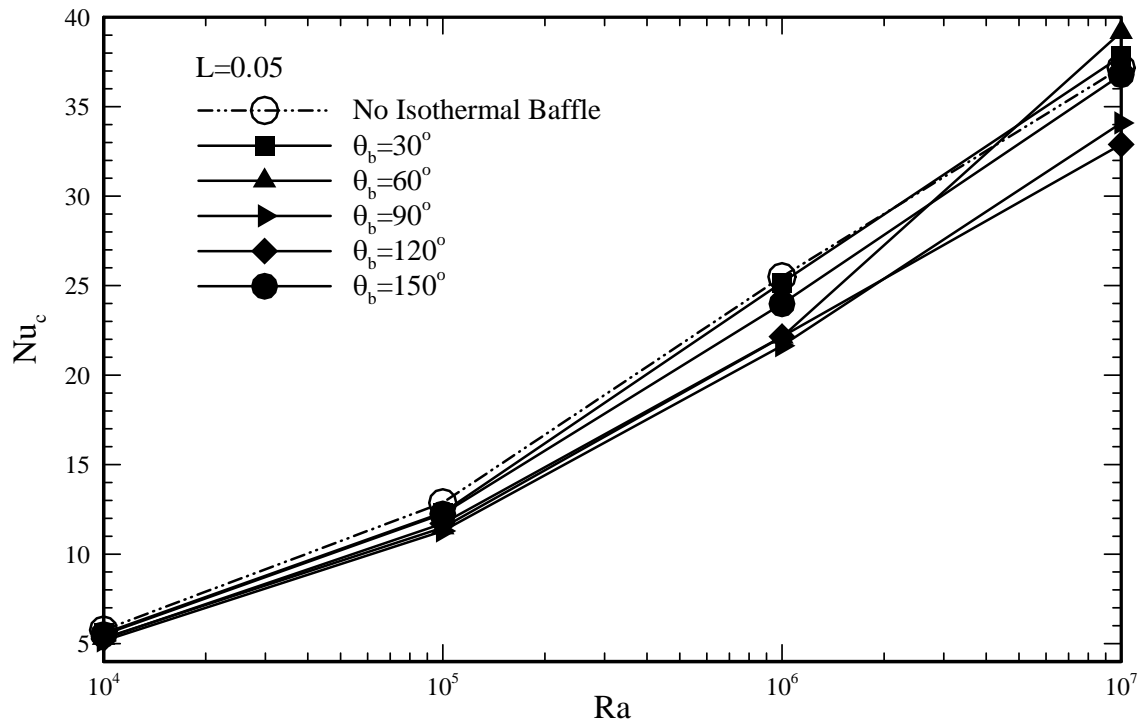


Figure 5.14 Dependence of the time-average Nusselt number (Nu_c) on Ra among cases with a fixed thin isothermal baffle ($L=0.05$) at various locations ($\theta_b = 30^\circ, 60^\circ, 90^\circ, 120^\circ$ and 150°) and the case without baffle

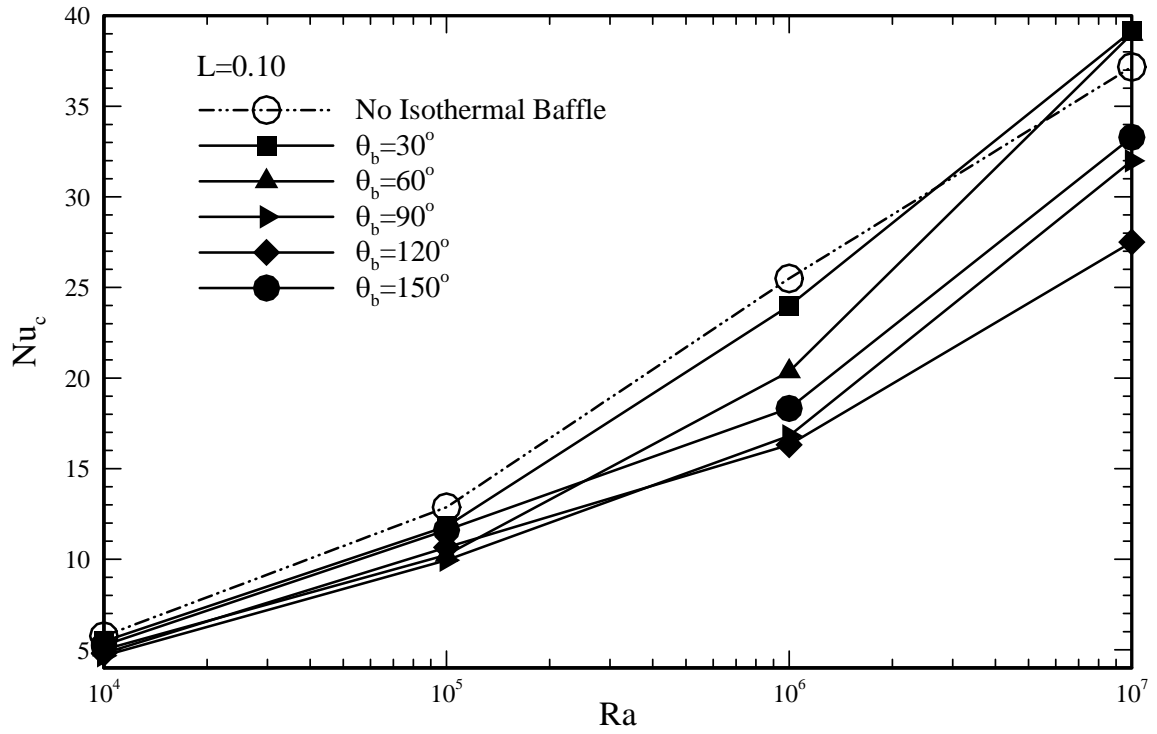


Figure 5.15 Dependence of the time-average Nusselt number (Nu_c) on Ra among cases with a fixed thin isothermal baffle ($L=0.10$) at various locations ($\theta_b = 30^\circ, 60^\circ, 90^\circ, 120^\circ$ and 150°) and the case without baffle

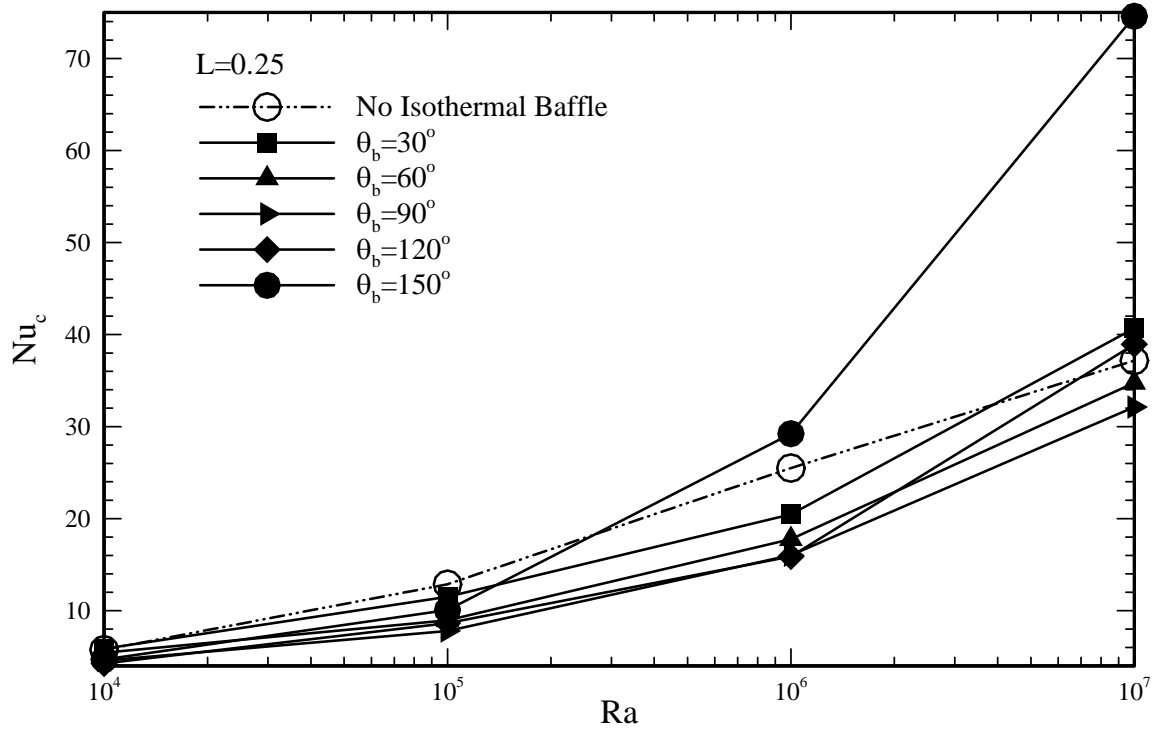


Figure 5.16 Dependence of the time-average Nusselt number (Nu_c) on Ra among cases with a fixed thin isothermal baffle ($L=0.25$) at various locations ($\theta_b = 30^\circ, 60^\circ, 90^\circ, 120^\circ$ and 150°) and the case without baffle

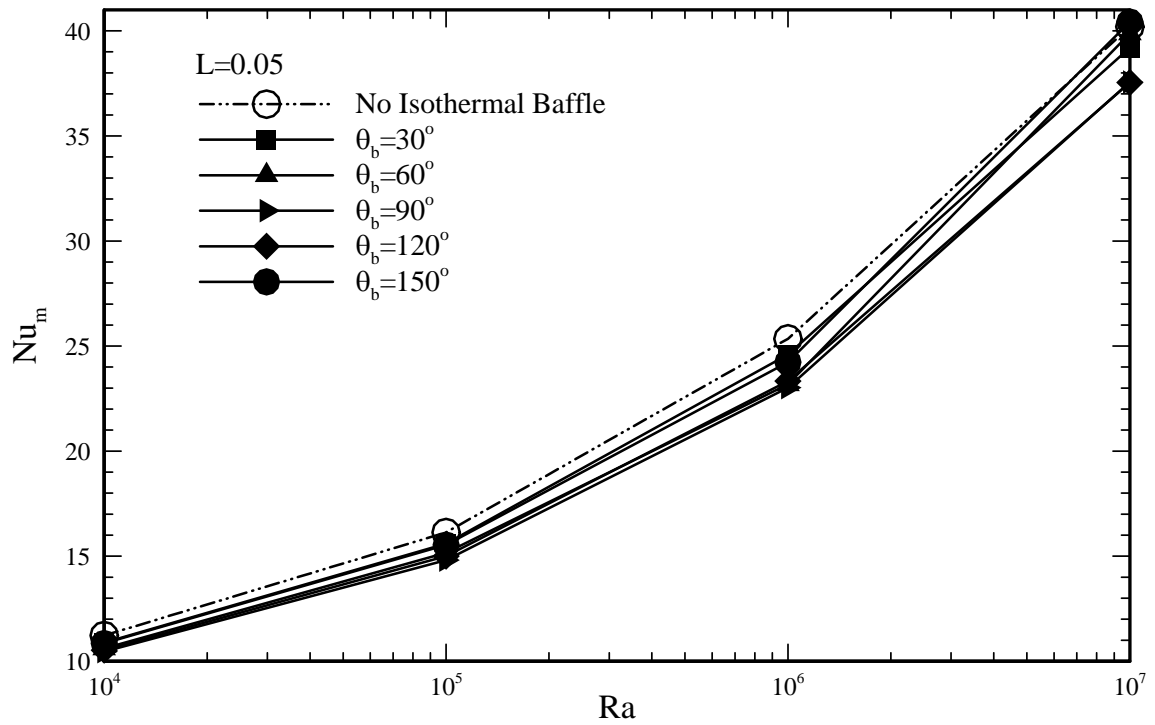


Figure 5.17 Dependence of the time-average Nusselt number (Nu_m) on Ra among cases with a fixed thin isothermal baffle ($L=0.05$) at various locations ($\theta_b = 30^\circ, 60^\circ, 90^\circ, 120^\circ$ and 150°) and the case without baffle

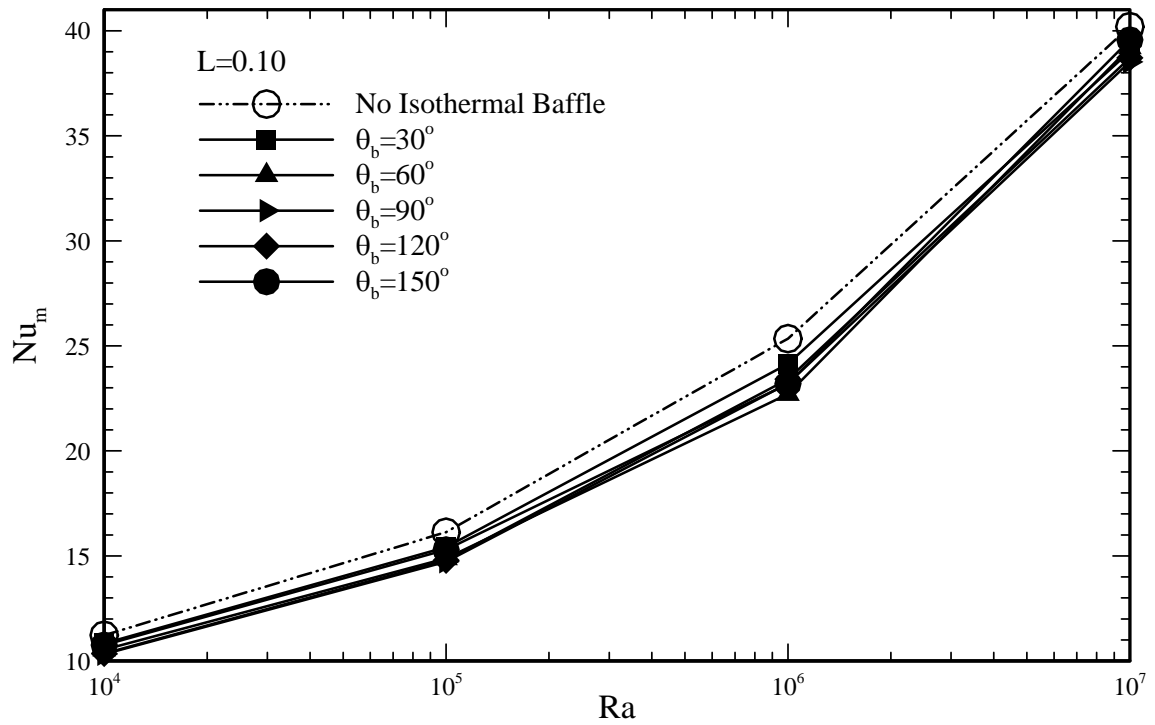


Figure 5.18 Dependence of the time-average Nusselt number (Nu_m) on Ra among cases with a fixed thin isothermal baffle ($L=0.10$) at various locations ($\theta_b = 30^\circ, 60^\circ, 90^\circ, 120^\circ$ and 150°) and the case without baffle

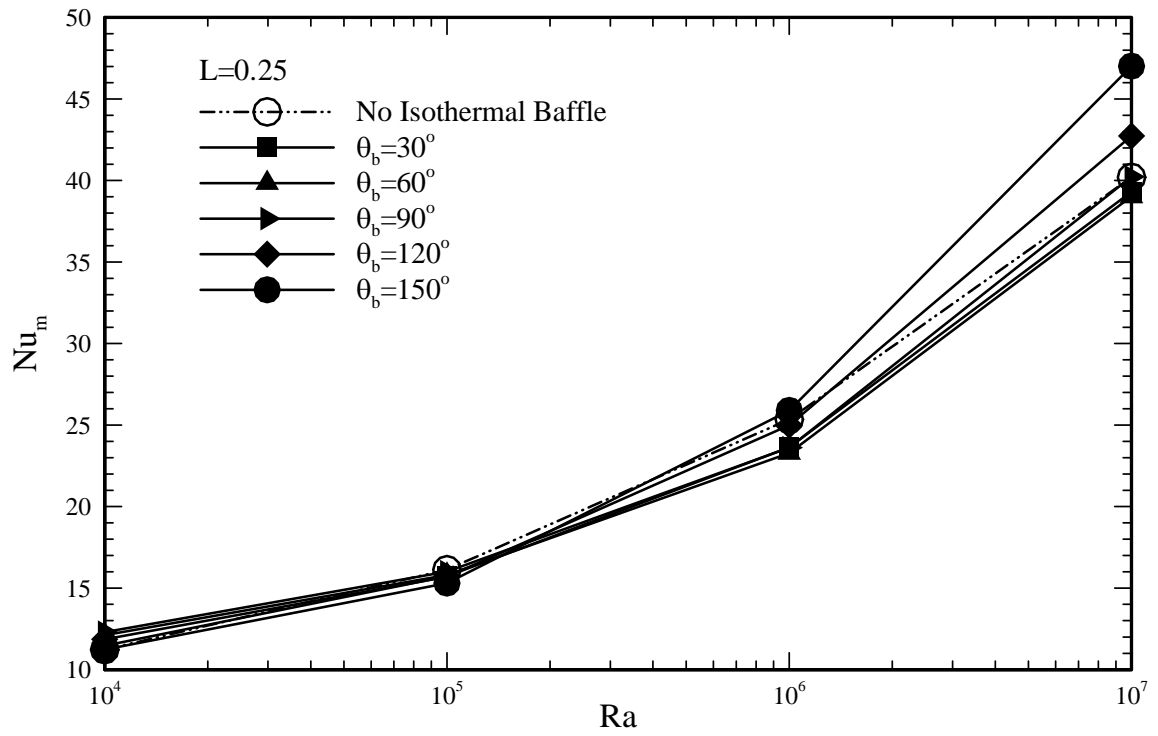


Figure 5.19 Dependence of the time-average Nusselt number (Nu_m) on Ra among cases with a fixed thin isothermal baffle ($L=0.25$) at various locations ($\theta_b = 30^\circ, 60^\circ, 90^\circ, 120^\circ$ and 150°) and the case without baffle

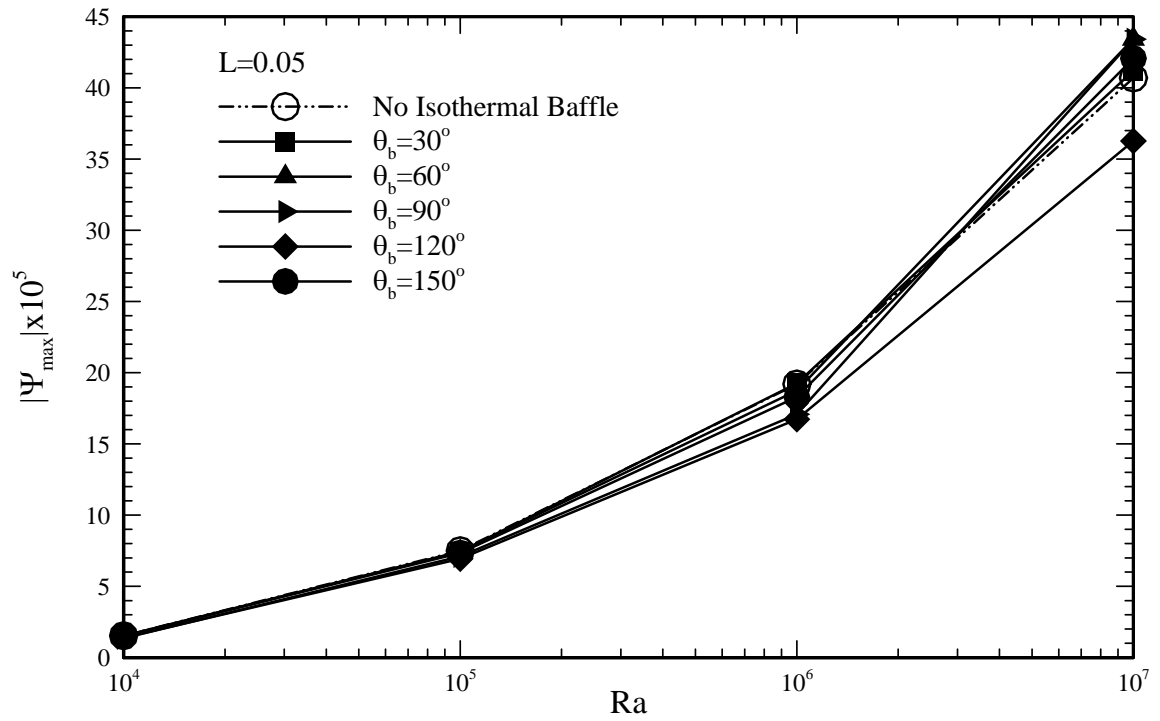


Figure 5.20 Dependence of the maximum stream function ψ_{\max} on Ra among cases with a fixed thin isothermal baffle ($L=0.05$) at various locations ($\theta_b = 30^\circ, 60^\circ, 90^\circ, 120^\circ$ and 150°) and the case without baffle

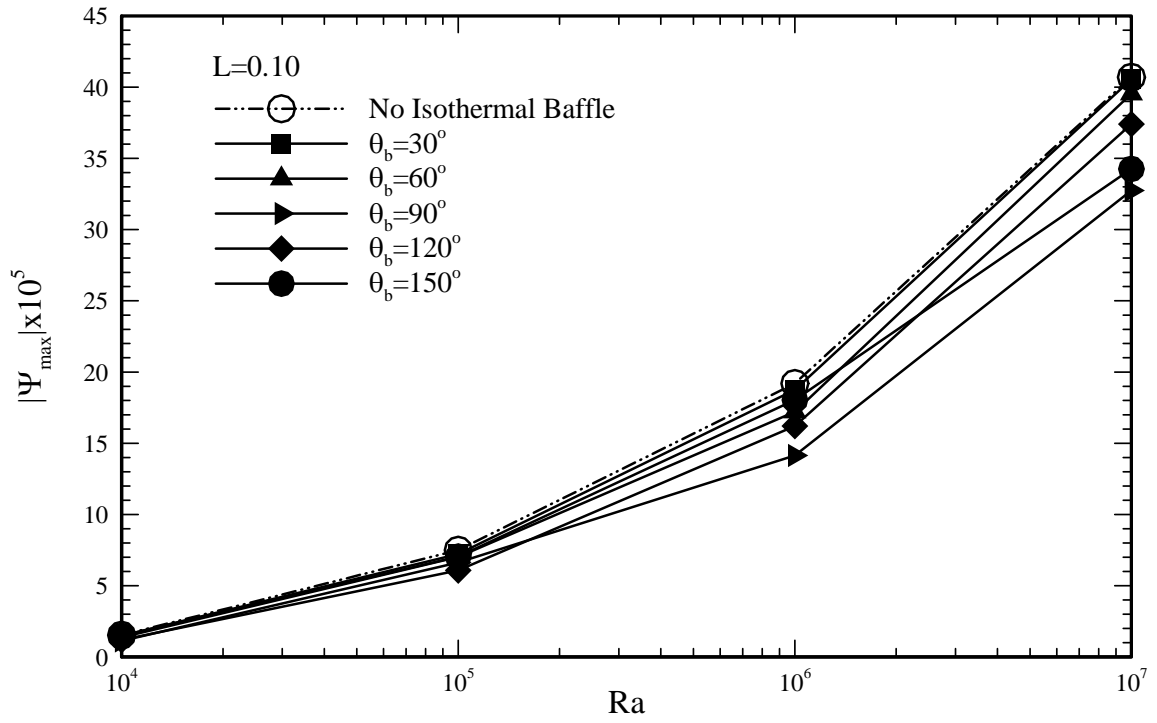


Figure 5.21 Dependence of the maximum stream function ψ_{\max} on Ra among cases with a fixed thin isothermal baffle ($L=0.10$) at various locations ($\theta_b = 30^\circ, 60^\circ, 90^\circ, 120^\circ$ and 150°) and the case without baffle

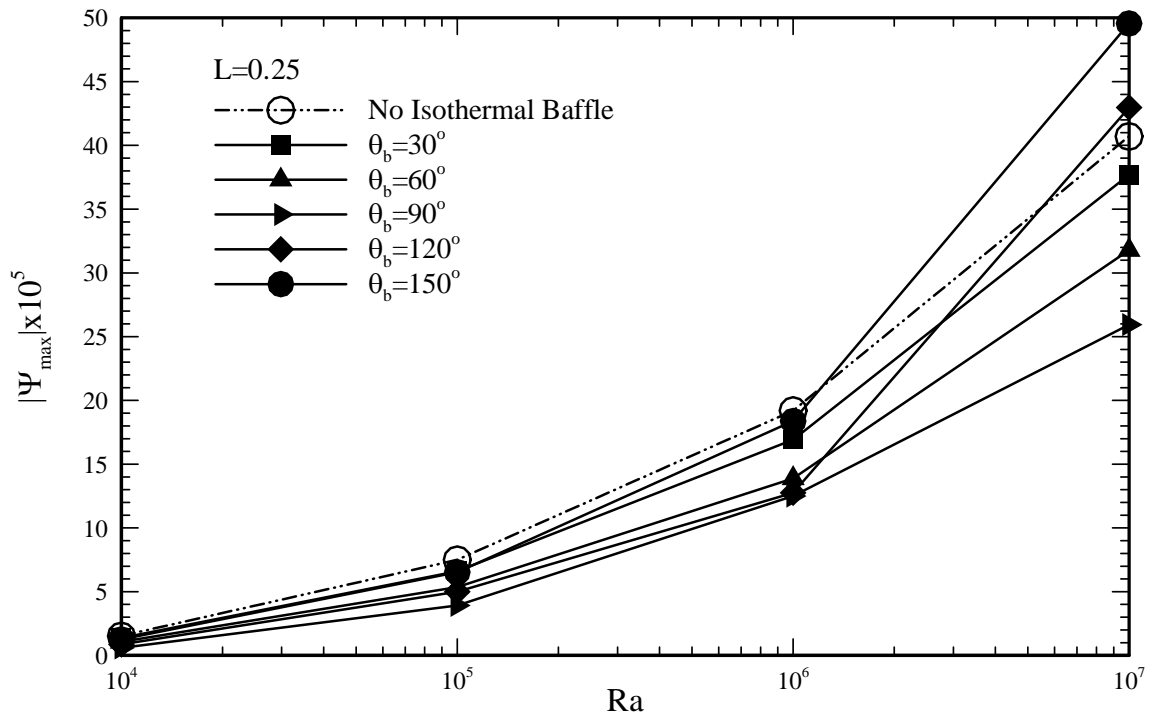


Figure 5.22 Dependence of the maximum stream function ψ_{\max} on Ra among cases with a fixed thin isothermal baffle ($L=0.25$) at various locations ($\theta_b = 30^\circ, 60^\circ, 90^\circ, 120^\circ$ and 150°) and the case without baffle

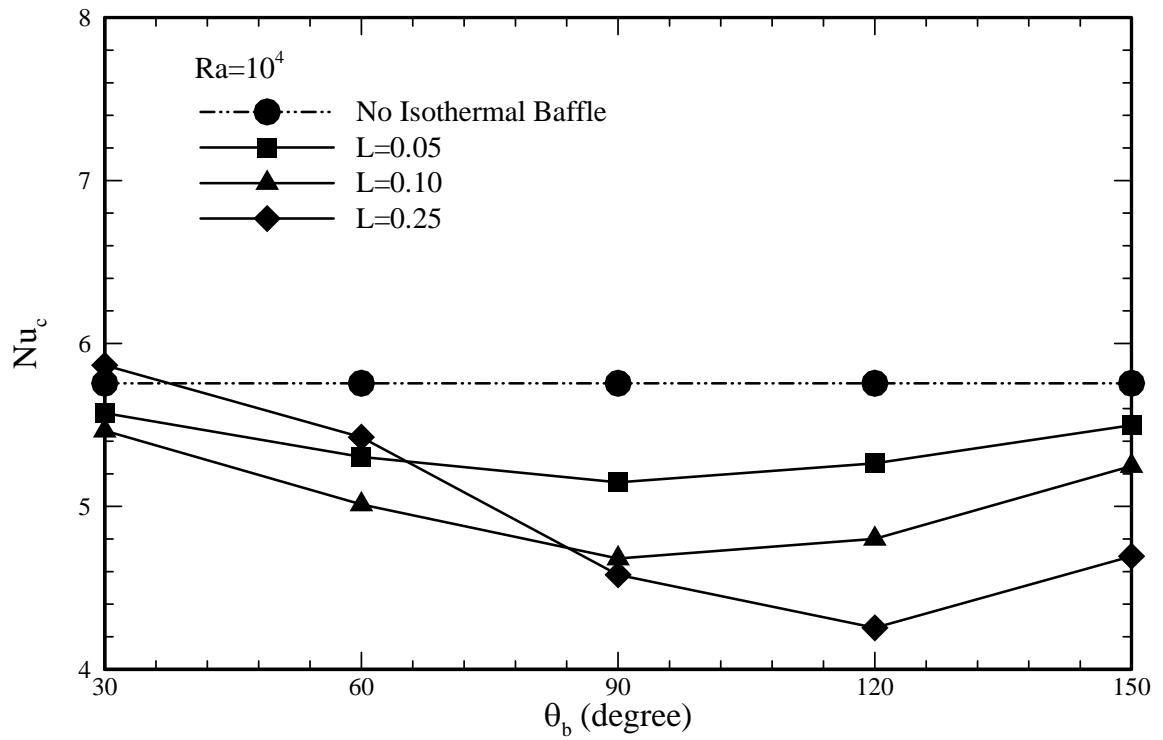


Figure 5.23 Dependence of the Nusselt number (Nu_c) on θ_b among case without baffle and cases with a thin isothermal baffle of different lengths ($L=0.05, 0.10$ and 0.25) for $Ra=10^4$

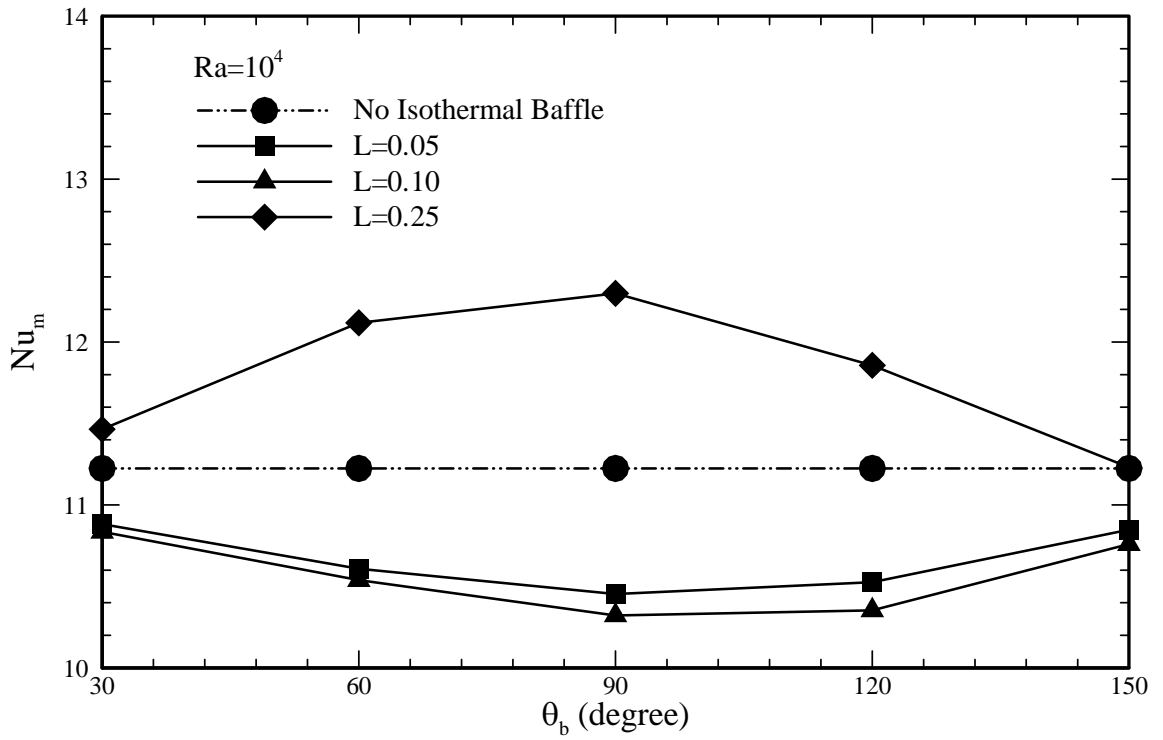


Figure 5.24 Dependence of the Nusselt number (Nu_m) on θ_b among case without baffle and cases with a thin isothermal baffle of different lengths ($L=0.05, 0.10$ and 0.25) for $Ra=10^4$

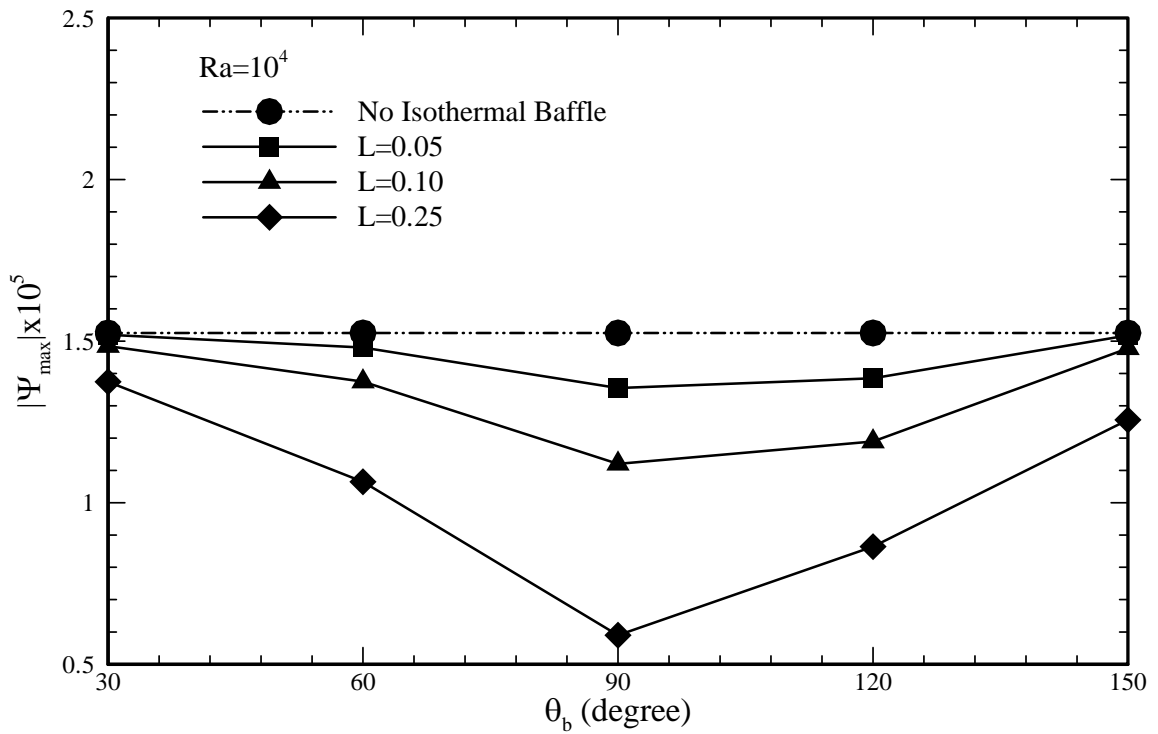


Figure 5.25 Dependence of the Maximum stream function (ψ_{\max}) on θ_b among case without baffle and cases with a thin isothermal baffle of different lengths ($L=0.05, 0.10$ and 0.25) for $Ra=10^4$

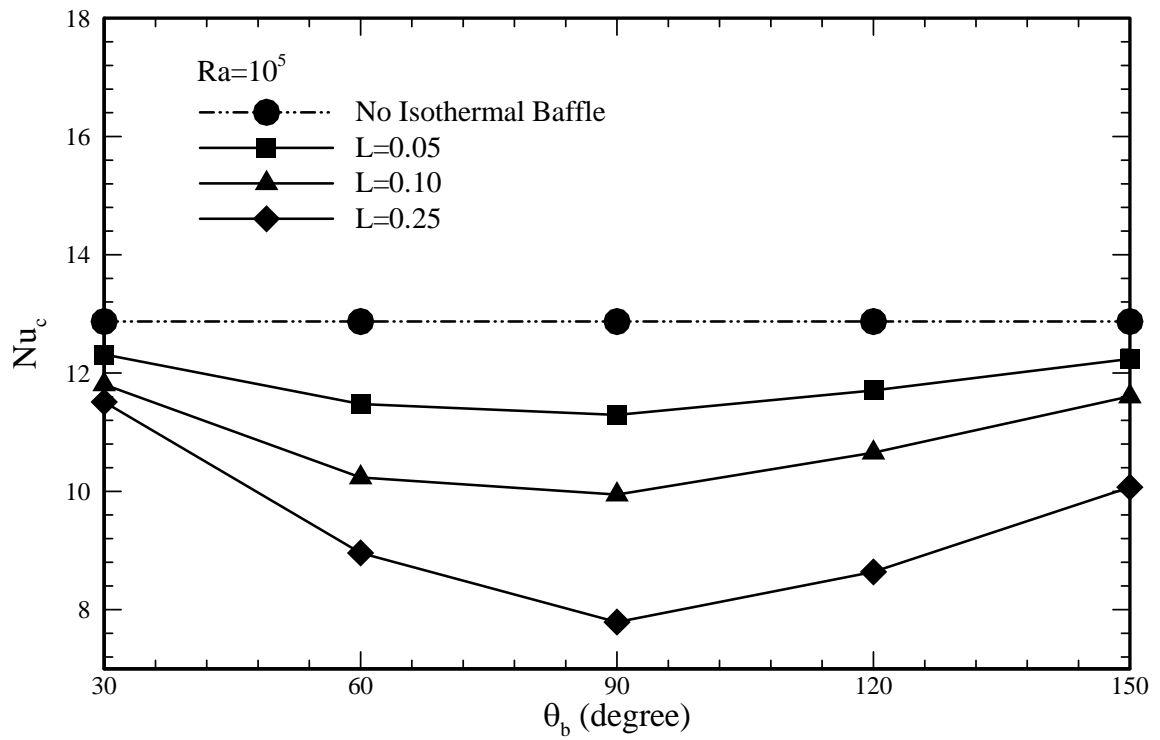


Figure 5.26 Dependence of the Nusselt number (Nu_c) on θ_b , among case without baffle and cases with a thin isothermal baffle of different lengths ($L=0.05, 0.10$ and 0.25) for $Ra=10^5$

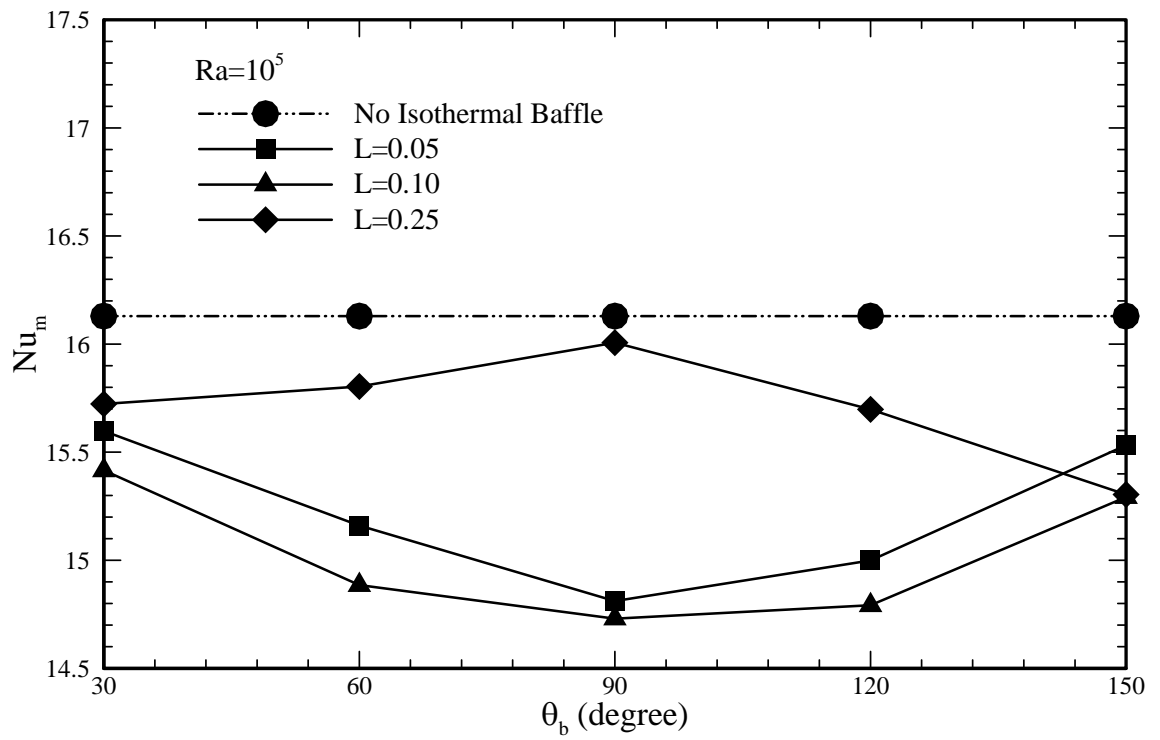


Figure 5.27 Dependence of the Nusselt number (Nu_m) on θ_b among case without baffle and cases with a thin isothermal baffle of different lengths ($L=0.05, 0.10$ and 0.25) for $Ra=10^5$

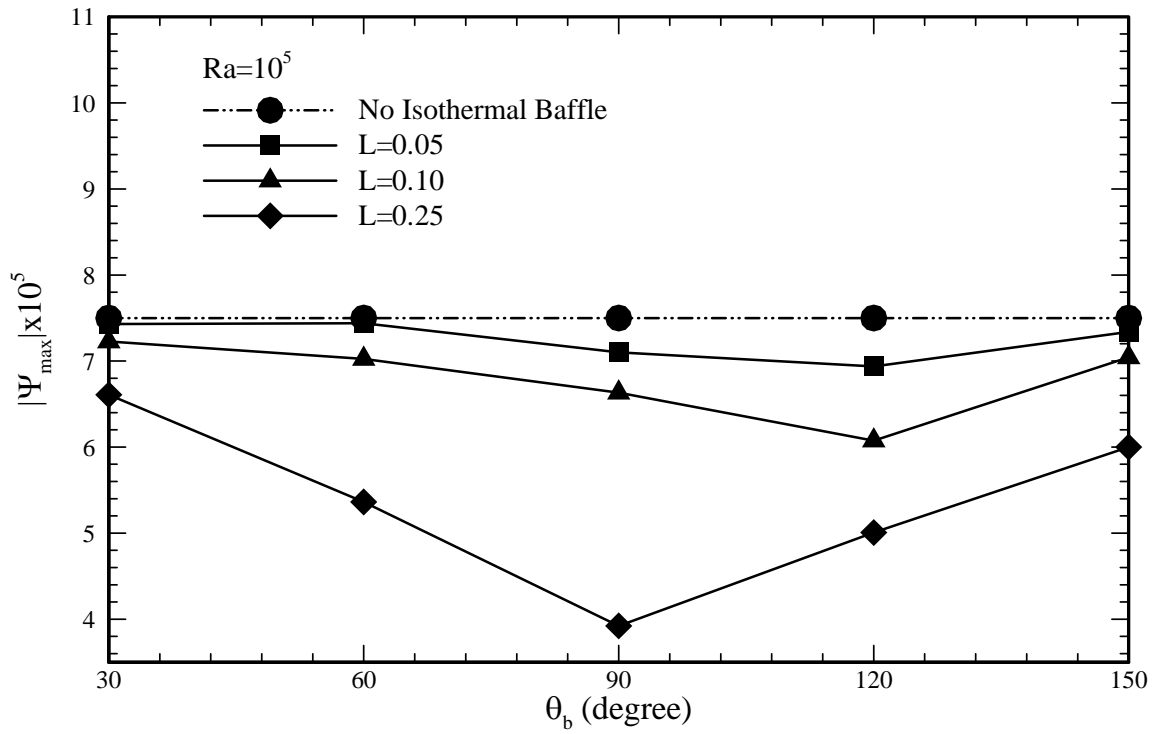


Figure 5.28 Dependence of the Maximum stream function (ψ_{\max}) on θ_b among case without baffle and cases with a thin isothermal baffle of different lengths ($L=0.05$, 0.10 and 0.25) for $Ra=10^5$

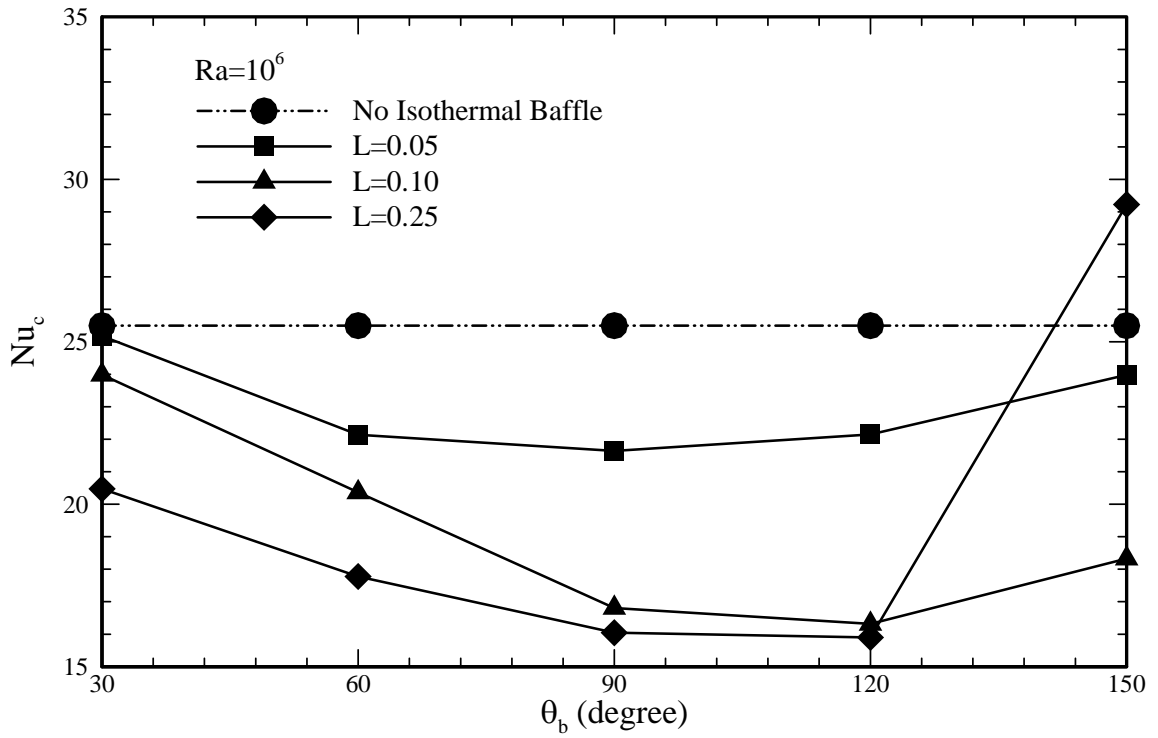


Figure 5.29 Dependence of the Nusselt number (Nu_c) on θ_b among case without baffle and cases with a thin isothermal baffle of different lengths ($L=0.05, 0.10$ and 0.25) for $Ra=10^6$

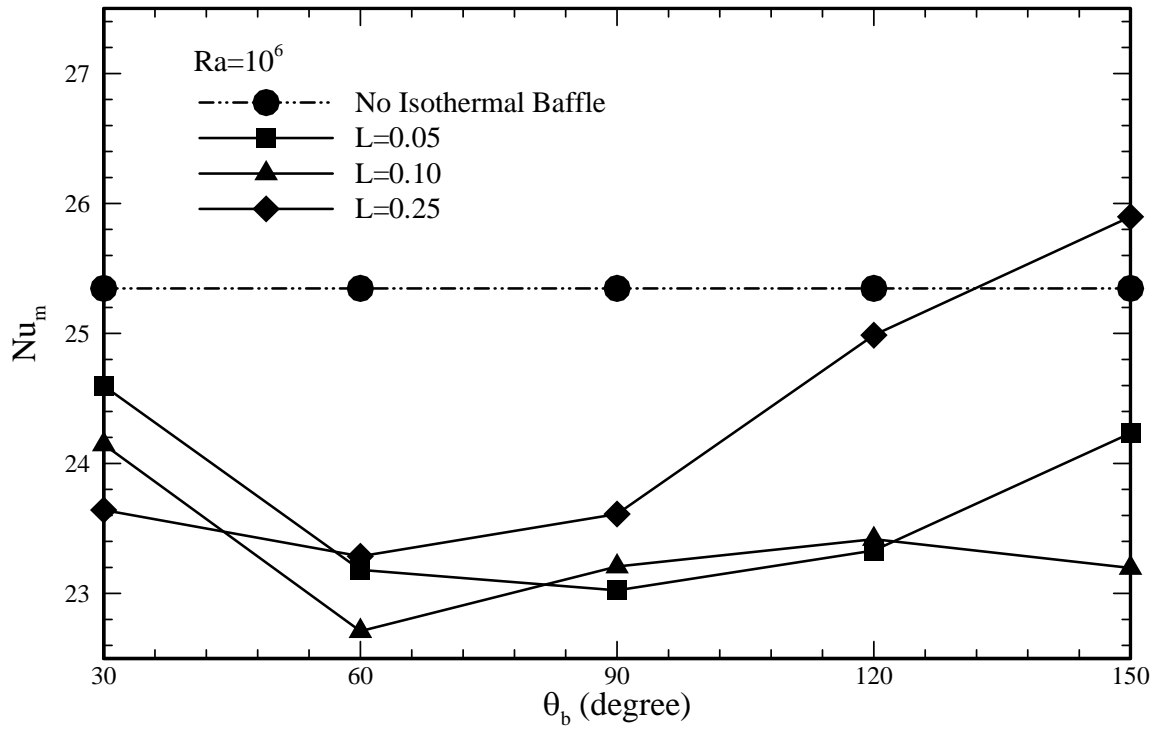


Figure 5.30 Dependence of the Nusselt number (Nu_m) on θ_b among case without baffle and cases with a thin isothermal baffle of different lengths ($L=0.05, 0.10$ and 0.25) for $Ra=10^6$

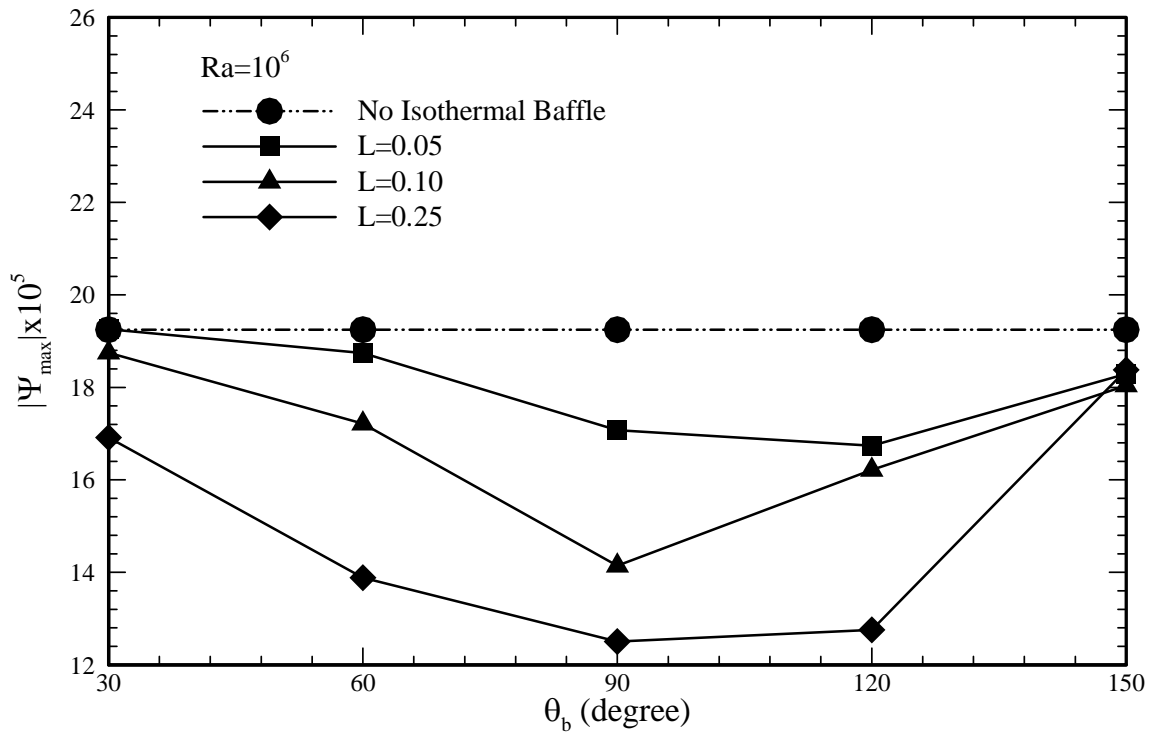


Figure 5.31 Dependence of the Maximum stream function (ψ_{\max}) on θ_b among case without baffle and cases with a thin isothermal baffle of different lengths ($L=0.05, 0.10$ and 0.25) for $Ra=10^6$

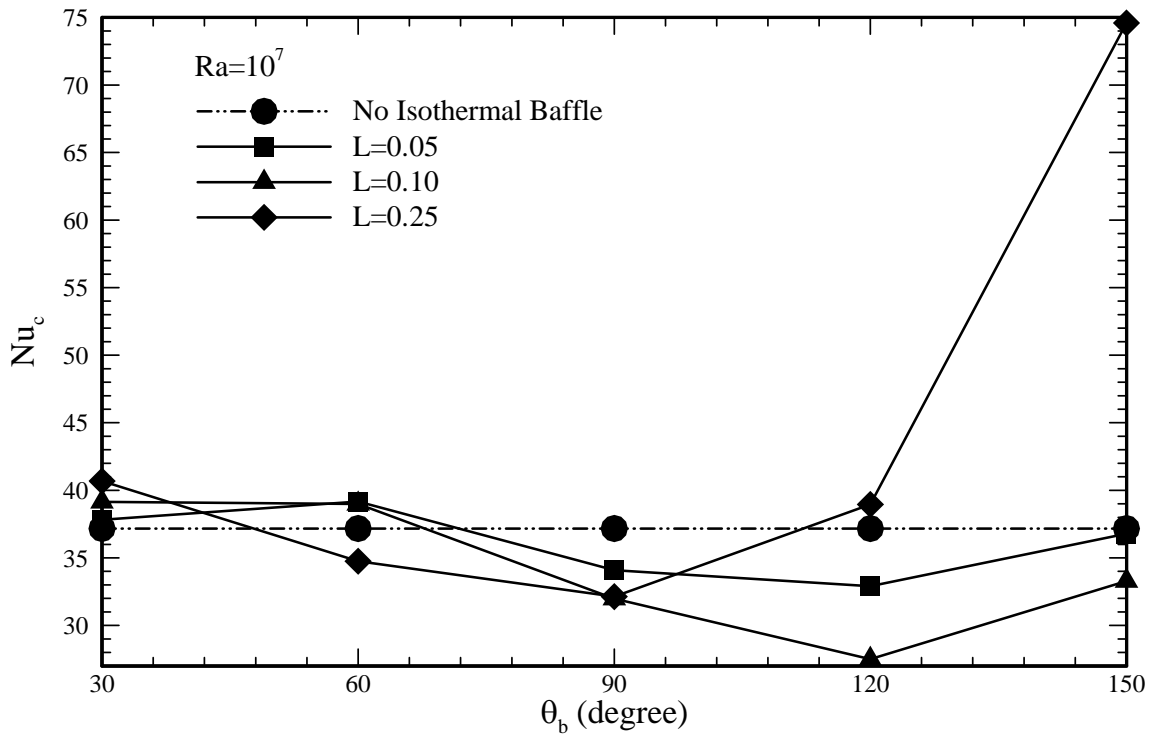


Figure 5.32 Dependence of the Nusselt number (Nu_c) on θ_b among case without baffle and cases with a thin isothermal baffle of different lengths ($L=0.05, 0.10$ and 0.25) for $Ra=10^7$

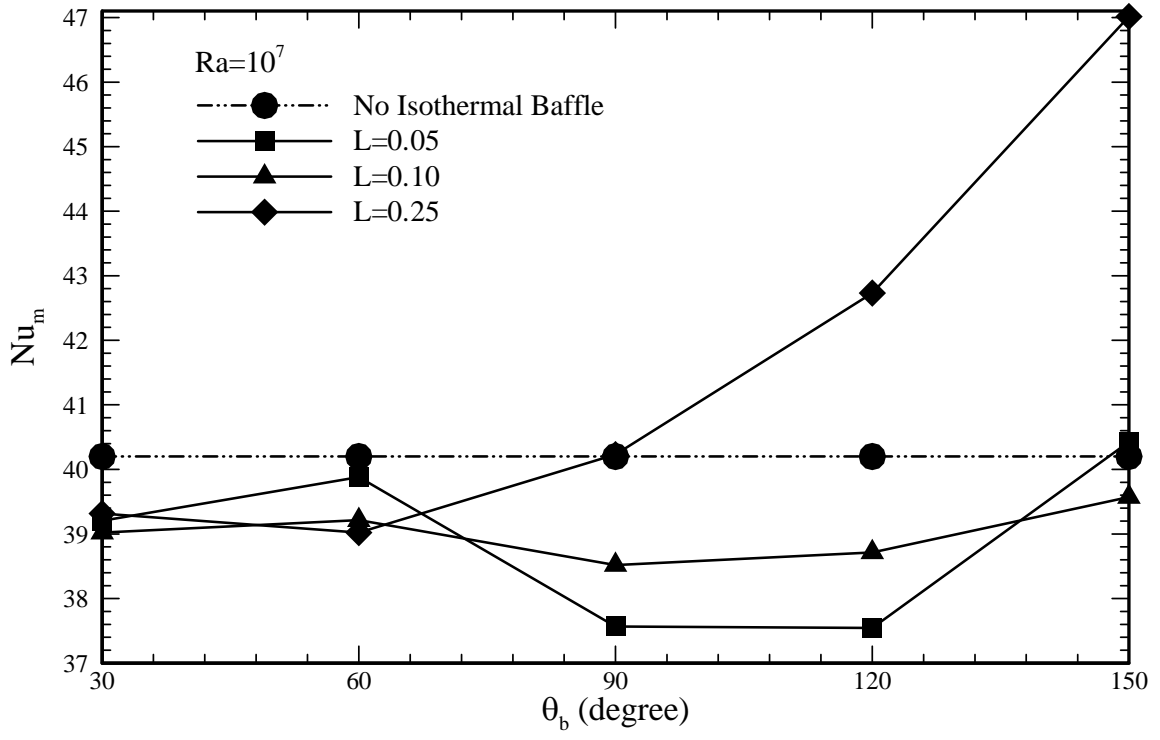


Figure 5.33 Dependence of the Nusselt number (Nu_m) on θ_b among case without baffle and cases with a thin isothermal baffle of different lengths ($L=0.05, 0.10$ and 0.25) for $Ra=10^7$

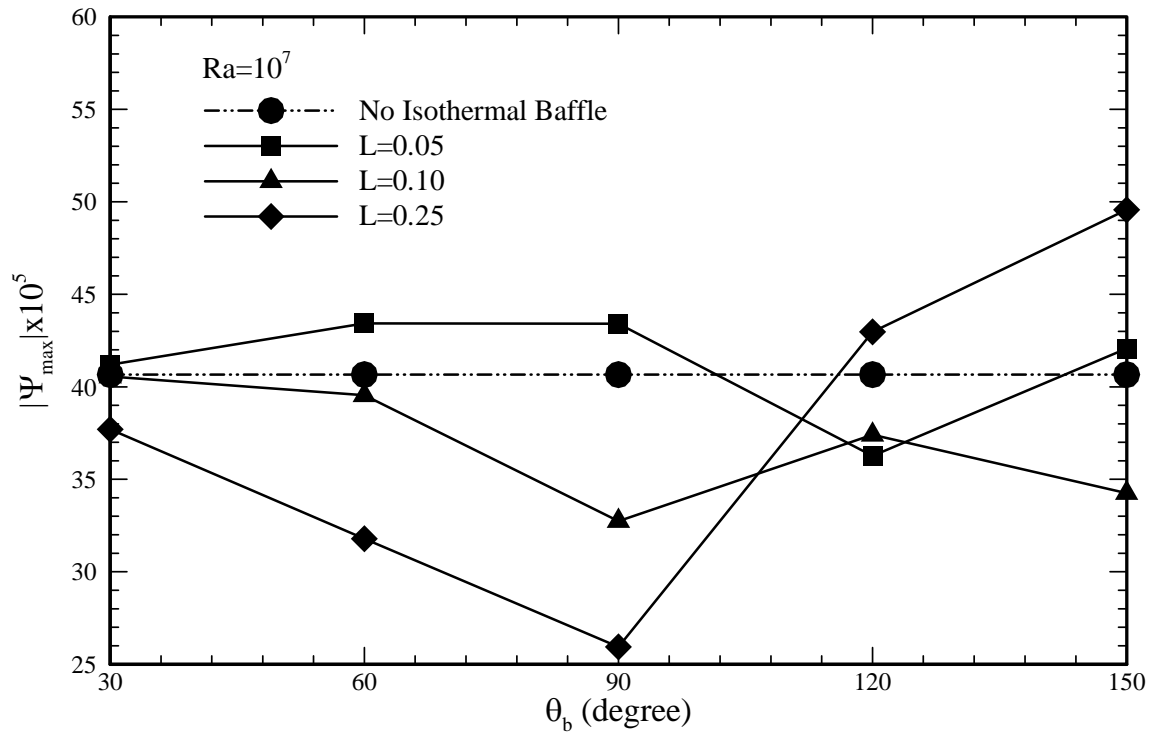


Figure 5.34 Dependence of the Maximum stream function (ψ_{\max}) on θ_b among case without baffle and cases with a thin isothermal baffle of different lengths ($L=0.05$, 0.10 and 0.25) for $Ra=10^7$

CHAPTER 6 CONCLUSIONS AND RECOMMENDATIONS

In order to passively manage fluid flow and natural convection heat transfer under the pseudosteady-state condition inside spherical containers, a thin baffle (insulated or isothermal) was attached to the inner wall of the container. The baffle is positioned such that it points along the radial direction. For Rayleigh numbers of 10^4 , 10^5 , 10^6 and 10^7 , baffles with 3 lengths positioned at 5 different locations were investigated. Elaborate grid size and time step size independence tests were performed. The solution of the governing equations was obtained by use of a commercial computational fluid dynamic (CFD) package.

6.1 Conclusions

Based on the results of the computational study conducted during the course of this research, the main conclusions are:

1. Code validation was carried out by comparing the simulated results for the flow and thermal fields with no baffle to previous experimental and computational data. The comparison among the various approaches was satisfactory. For the four Rayleigh numbers that were studied, the pseudosteady-state condition was clearly established and no noticeable fluctuations of the Nusselt numbers were observed. Specifically, two correlations for the Nusselt number (Nu_m and Nu_c) were proposed. Both thermally stable and unstable layers are present in this problem and for the higher Rayleigh

numbers, the onset of instabilities was observed in this system. Within the thermally unstable layer near the bottom of the spherical container, an active small vortex was formed for $Ra=10^7$. This flow pattern has not been reported to date by others.

2. In the absence of extra heating, it was observed that introduction of a thin insulated baffle on the inner wall of the spherical container directly leads to modification of the velocity field, which in turn affects the temperature field. It can generally be stated that an insulated baffle gives rise to “confinement” or “compartmentalization”, by which the fluid above the baffle is generally characterized by stable constant-temperature layers that are slow moving and dominated by heat conduction. In contrast, the fluid below the baffle is subjected to strong natural convection currents. Regardless of the Ra number, the short baffle ($L = 0.05$) alters the flow field and temperature contours to a minor extent in comparison to the corresponding Ra number cases with no baffle. The modifications are limited to the vicinity of the baffle and a possible interaction with the eye of the primary CW rotating vortex. The changes in the flow and thermal fields are observed to be more dramatic for the $L = 0.1$ baffle. Multi-vortex structures rotating in opposite directions were observed. The modifications of the flow and thermal fields were more pronounced for the longest baffle ($L = 0.25$) for which two CW rotating vortices are clearly observed when the baffle is positioned at or in the vicinity of the mid-plane. The Nusselt numbers and maximum stream function of the primary vortex were generally lower than the reference cases with no baffle. In general, placing a baffle in the mid-plane of the container can lead to the lowest time rate of change of the bulk temperature, that is equivalent to Nu_c . The degree of degradation of the Nusselt number has a strong dependence on the position and length of the insulated baffle. In contrast to the general

reduction of heat transfer trends exhibited by the insulated baffles, placing it near the top of the sphere for high Ra number cases can lead to heat transfer enhancement in comparison to the reference case with no baffle. The extra heat that is brought in the fluid through the surface of the sphere is linked to the disturbance of the thermal boundary layer by the thin baffle.

3. In light of the extra heating afforded by a thin isothermal baffle, the velocity and temperature fields were more complicated than the case with a thin insulated baffle. Modified expressions for the Nusselt numbers were derived by introducing a “shape factor” that depends on the length and position of the isothermal baffle. The effect of the baffle’s length on the flow and thermal fields was observed to be similar to the trends exhibited by the insulated baffles. In addition to confinement, a strong counterclockwise (CCW) rotating vortex that was created due to the extra heating of the baffle was present for high Ra numbers and baffle positions on or below the mid-plane. The hot fluid in this vortex was observed to be transported toward the center of the sphere, thus disturbing the stable stratified layers. The Nusselt number and maximum stream function values were dependent on Ra, baffle length and baffle location. In comparison to the cases with no baffles, most Nusselt numbers and maximum stream function values were lower indicating that the confinement effect of the baffle still persists for the isothermal baffles in spite of the extra heating. By placing an isothermal baffle near the top of the sphere and with high Ra numbers, heat transfer enhancement can be realized that is due to disturbance of the thermal boundary layer by the thin baffle. In contrast to insulated baffles, placing isothermal baffles near the bottom for high Ra number cases also gave

rise to heat transfer enhancement due to disturbance of the stratified layers by the CCW rotating vortex that is energized by the heated baffle.

4. Regardless of the thermal state of the baffle, its length and position, the pseudosteady-state condition was achieved for the three lower Ra numbers that were investigated. For the highest Rayleigh number case, strong fluctuations of the velocity and temperature fields were clearly recorded. Even though the instantaneous Nusselt numbers exhibit marked fluctuations, the corresponding time-averaged values were shown to exhibit the pseudosteady-state behavior.

6.2 Recommendations for Future Work

The results obtained in this study greatly enrich the knowledge base of management of flow field and natural convection heat transfer in spherical containers.

The recommendations for future work are summarized as follow:

- I. Explore the effect of an oscillating thin insulated and isothermal baffle,
- II. Study the effect of multiple baffles pointing to the center,
- III. Investigate a single insulated or isothermal baffle pointing away from the center.

REFERENCES

Bird, R. B., Stewart, W. E. and Lightfoot, E. N., 1960, *Transport Phenomena*, John Wiley and Sons, New York, NY.

Chow, M. Y. and Akins, R. G., 1975, "Pseudosteady-State Natural Convection inside Spheres," *Transactions of the ASME, Journal of Heat Transfer*, Vol. 97, pp. 54-59.

FLUENT 6.1 User's Guide, Fluent, Inc., Lebanon, NH, 2003.

Hutchins, J. and Marschall, E., 1989, "Pseudosteady-State Natural Convection Heat Transfer Inside Spheres," *International Journal of Heat and Mass Transfer*, Vol. 32, No. 11, pp. 2047-2053.

Khodadadi, J. M., Li, W. and Shi, X., 1999, "Pseudosteady-State Mixed Convection inside Rotating Spherical Containers," *Proceedings of the 5th ASME/JSME Thermal Engineering Joint Conference (CD ROM)*, Paper AJTE99-6264, San Diego, California, 10 pages.

Nguyen, H. D., Paik, S. and Pop, I., 1997, "Transient Thermal Convection in a Spherical Enclosure Containing a Fluid Core and a Porous Shell," *International Journal of Heat and Mass Transfer*, Vol. 40, pp. 379-392.

Owen, I. and Jalil, J. M., 1986, "Transient Heat Transfer in a Liquid Sphere," in *Heat Transfer 1986: Proceedings of the Eight International Heat Transfer Conference*, Taylor & Francis, Vol. 4, pp. 1889-1893.

Patankar, S. V., 1980, *Numerical Heat Transfer and Fluid Flow*, Hemisphere Publishing Corporation, Washington, DC.

Pustovoit, S. P., 1958, "Transient Thermal Convection in a Spherical Cavity," *P. M. M. (Journal of Applied Mathematics and Mechanics)*, Vol. 22, No. 4, pp. 568-572.

Roy, C., 2006, *CFD Course Notes*, Auburn University, Alabama.

Schmidt, E., 1956, "Versuche zum Wärmeübergang bei natürlicher Konvektion," *Chemie Ingenieur Technik*, Vol. 28, No. 3, pp. 175-180.

Shen, F., Khodadadi, J. M. and Zhang, Y., 1995, "Pseudosteady-State Natural Convection inside Spherical Containers," *Proceedings of the 4th ASME/JSME Thermal Engineering Joint Conference*, Volume 1, Lahaina, Maui, Hawaii, pp. 209-216.

Val'tsiferov, Yu. V. and Polezhaev, V. I., 1975, "Convective Heat Transfer and Temperature Stratification in a Sphere Completely Filled with a Liquid, with a Given Heat Flux," *Fluid Dynamics*, Vol. 10, No. 5, pp. 828-832.

Whitley, H. G. III, and Vachon, R. I., 1972, "Transient Laminar Free Convection in Closed Spherical Containers," *Transactions of the ASME, Journal of Heat Transfer*, Vol. 94, pp. 360-366.

Zhang, Y., Khodadadi, J. M. and Shen, F., 1999, "Pseudosteady-State Natural Convection inside Spherical Containers Partially Filled with a Porous Medium," *International Journal of Heat and Mass Transfer*, Vol. 42, No. 13, pp. 2327-2336.